

Depth Resolved Structural and Chemical Studies of Nanostructured Materials using Synchrotron Radiation

By
Gangadhar Das
PHYS03201204013

Raja Ramanna Centre for Advanced Technology, Indore

A thesis submitted to the
Board of Studies in Physical Sciences
In partial fulfilment of requirements
For the Degree of
DOCTOR OF PHILOSOPHY
of
HOMI BHABHA NATIONAL INSTITUTE



October, 2017

Homi Bhabha National Institute

Recommendations of the Viva Voce Board

As members of the Viva Voce Board, we certify that we have read the dissertation prepared by Gangadhar Das entitled Depth Resolved Structural and Chemical Studies of Nanostructured Materials using Synchrotron Radiation and recommend that it maybe accepted as fulfilling the dissertation requirement for the Degree of Doctor of Philosophy.

Rawalhas Date: 13.4.18

Chair - Prof. Rama Chari

BM Date: 13.04.2018

Guide/Convener - Prof. M. K. Tiwari

Anjan K. Gupta Date: 13.04.2018

Examiner - Prof. Anjan K. Gupta

N. L. Misra Date:

External Member - Prof. N. L. Misra

Tapas Ganguli Date: 13/04/2018

Member 1 - Prof. Tapas Ganguli

T. K. Sharma Date: 13.04.2018

M. H. Modi Date: 13.4.18

S. M. Gupta Date: 13.4.18

M. K. Chattopadhyay Date: 13/04/2018

Member 5 - Prof. M. K. Chattopadhyay

Final approval and acceptance of this dissertation is contingent upon the candidate's submission of the final copies of the dissertation to HBNI.

I hereby certify that I have read this dissertation prepared under my direction and recommend that it may be accepted as fulfilling the dissertation requirement.

Date: 13-04-2018

Place: Indore

Guide

A handwritten signature in blue ink, consisting of a stylized first name followed by a surname, all enclosed within a rectangular box drawn with the same ink.

STATEMENT BY AUTHOR

This dissertation has been submitted in partial fulfilment of requirements for an advanced degree at Homi Bhabha National Institute (HBNI) and is deposited in the Library to be made available to borrowers under rules of the HBNI.

Brief quotations from this dissertation are allowable without special permission, provided that accurate acknowledgement of source is made. Requests for permission for extended quotation from or reproduction of this manuscript in whole or in part may be granted by the Competent Authority of HBNI when in his or her judgement the proposed use of the material is in the interests of scholarship. In all other instances, however, permission must be obtained from the author.


Gangadhar Das

DECLARATION

I, hereby declare that the investigation presented in the thesis has been carried out by me.
The work is original and has not been submitted earlier as a whole or in part for a degree
/ diploma at this or any other Institution / University.

Gangadhar Das
Gangadhar Das

List of Publications arising from the thesis

In Journals

1. Depth resolved chemical speciation of a W-B₄C multilayer structure
Gangadhar Das, A. G. Karydas, Haranath Ghosh, M. Czyzycki, A. Migliori, and M. K. Tiwari
Physical Review B, **2017**, 96, 155444
2. Probing nanostructured materials using x-ray fluorescence analysis
Gangadhar Das, A. Khooha, A. K. Singh, and M. K. Tiwari
X-Ray Spectrometry, **2017**, 46, 448-453
3. Exploring interface morphology of a deeply buried layer in periodic Multilayer
Gangadhar Das, Ajay Khooha, A. K. Singh, A. K. Srivastava, and M. K. Tiwari
Applied Physics Letters, **2016**, 108, 263109
4. An interactive graphical user interface (GUI) for the CATGIXRF program - for microstructural evaluation of thin film and impurity doped surfaces
M. K. Tiwari and Gangadhar Das
X-Ray Spectrometry, **2016**, 45, 212-219
5. X-ray standing wave analysis of nanostructures using partially coherent radiation
M. K. Tiwari, Gangadhar Das, and M. J. Bedzyk
Applied Physics Letters, **2015**, 107, 103104
6. Simultaneous measurements of X-ray reflectivity and grazing incidence fluorescence at BL-16 beamline of Indus-2
Gangadhar Das, S. R. Kane, Ajay Khooha, A. K. Singh, and M. K. Tiwari
Review of Scientific Instruments, **2015**, 86, 055102
7. Effect of Synchrotron Polarization in Grazing Incidence X-ray Fluorescence analysis
Gangadhar Das, M. K. Tiwari, A. K. Singh, and Haranath Ghosh
Journal of Analytical Atomic Spectrometry, **2014**, 29, 2405-2413

In Conferences/Symposiums

1. Depth resolved chemical speciation in a Multilayer
Gangadhar Das, A. Khooha, A. K. Singh, and M. K. Tiwari
66th Annual Denver X-ray Conference (DXC-2017), Montana, U.S.A., August-2017

Attested
[Signature]

Gangadhar Das

2. Determination of surface morphology of TiO₂ nanostructure using Synchrotron Radiation
Gangadhar Das, Manoj Kumar, A. K. Biswas, Ajay Khooha, Puspun Mondal, and M. K. Tiwari
61st Solid State Physics Symposium (SSPS-2016), Odisha, India, December-2016
AIP Conference Proceedings, 2017, 1832, 050025
3. X-ray standing wave assisted depth resolved chemical speciation in periodic multilayer structures
Gangadhar Das, A. G. Karydas, Haranath Ghosh, M. Czyzycki, A. Migliori and M. K. Tiwari
European Conference on X-Ray Spectrometry (EXRS-2016), Gothenburg, Sweden, June-2016
4. Characterization of laser synthesized TiO₂ nanostructures by synchrotron X-ray standing wave technique
Gangadhar Das, M. Kumar, A. K. Biswas, Ajay Khooha, Puspun Mondal, and M. K. Tiwari
24th National Laser Symposium (NLS-24), Madhya Pradesh, India, December-2015
5. Surface and Interface analysis of Nanomaterials at Microfocus Beamline (BL-16) of Indus-2
Gangadhar Das, Ajay Khooha, S. R. Kane, A K Singh and M K Tiwari
International Conference on Condensed Matter Physics (ICC-2015), Rajasthan, India, October-2015
AIP Conference Proceedings, 2016, 1728, 020142
6. Azimuthal Anisotropy of the Scattered Radiation in Grazing Incidence X-ray Fluorescence
Gangadhar Das, M K Tiwari, A K Singh, and Haranath Ghosh
59th Solid State Physics Symposium (SSPS-2014), Tamil Nadu, India, December-2014
AIP Conference Proceedings, 2015, 1665, 080039
7. Synchrotron Total Reflection X-ray Fluorescence at BL-16 Microfocus Beamline of Indus-2
M K Tiwari, A K Singh, Gangadhar Das, Anupam Chowdhury, and G S Lodha
58th Solid State Physics Symposium (SSPS-2013), Punjab, India, December-2013
AIP Conference Proceedings, 2014, 1591, 642-643
8. Higher European Research Course for Users of Large Experimental Systems, Hercules European School 2017
Grazing incidence x-ray fluorescence studies of nanostructured materials using Synchrotron Radiation
Grenoble, France, 27th February-30th March, 2017

Attested


Gangadhar Das

9. Joint ICTP-IAEA School on Novel Experimental Methodologies for Synchrotron Radiation Applications in Nano-science and Environmental Monitoring
Trieste, Italy, 17-28th November, 2014

Others (Not included in the thesis)

In Journals

1. Direct Determination of Oxidation States of Uranium in Mixed Valent Uranium Oxides using TXRF-XANES
K. Sanyal, A. Khookha, Gangadhar Das, M. K. Tiwari, and N. L. Misra
Analytical Chemistry, **2017**, 89, 871
2. Observation of dopant-profile independent electron transport in sub-monolayer TiO_x stacked ZnO thin films grown by atomic layer deposition
D. Saha, P. Misra, Gangadhar Das, M. P. Joshi, and L. M. Kukreja
Applied Physics Letters, **2016**, 108, 032101
3. Structural and electronic properties of Fe(Al_xGa_{1-x})₃ system
D Mondal, C. Kamal, S Banik, A. Bhakar, A Kak, Gangadhar Das, V. R .Reddy, A. Chakrabarti, and T. Ganguli
Journal of Applied Physics, **2016**, 120, 165102
4. Size effect on the structural, magnetic and magnetotransport properties of electron doped manganite La_{0.15}Ca_{0.85}MnO₃
Rini Thomas, Gangadhar Das, Rajib Mondal, Rabindra N. Mahato, R. Nirmala, A. V. Morozkin, J. Lamsal, W. B. Yelon, A. K. Nigam and S. K. Malik
Journal of Applied Physics, **2012**, 111, 07D729

In Conferences

1. Analytical capabilities and applications developed at the IAEA multi-purpose X-ray spectrometry end-station at the XRF beamline of Elettra Sincrotrone Trieste
M. Czyzycki, J. J. Leani, A. Migliori, M. Bogovac, P. Wrobel, N. Vakula, J. Osan, M. K. Tiwari, D. Gangadhar, R. B. Kaiser and A. G. Karydas
European Conference on X-Ray Spectrometry (EXRS-2016), Gothenburg, Sweden, June-2016
2. Theoretical analysis of X-ray propagation in Waveguides
Nikhil Das .S, Gangadhar Das, A. K. Biswas, S. K. Sudheer, and M. K. Tiwari
60th Solid State Physics Symposium (SSPS-2015), Uttar Pradesh, India, December-2015

AH 15/10/16


Gangadhar Das

Dedicated to My Late Grandfather

Krishnakinkar Das

ACKNOWLEDGEMENTS

First and foremost, I would like to extend my sincere gratitude and deep sense of indebtedness to my thesis supervisor Manoj Kumar Tiwari for his invaluable guidance, endless encouragement and his continuous support paired with stimulating enthusiasm. Due to his kind nature, various helpful advices and interesting discussions, I could remain focus and not stray away from the essence of my work. Under his leadership I have proceeded into the field of experimental condensed matter physics. I am highly thankful to him for his invaluable suggestions at every point which lead me to complete my thesis work successfully.

I am extremely indebted to N. L. Misra, Bhabha Atomic Research Centre for his valuable advice, constructive criticism and his extensive discussions around my work. I am highly obliged to Haranath Ghosh, Abhik K. Biswas, S. R. Kane, Manoj Kumar, S. K. Rai, A. K. Sinha, M. H. Modi, Arvind K. Srivastava, Parasmani Rajput and Maheswar Nayak for their valuable suggestions and keen interest in my work. My gratitude in particular to Haranath Ghosh for being my major mentor. Abhik K. Biswas deserve special mention here for his constant support and motivation. Haranath Ghosh and Abhik K. Biswas gave me the moral support and encouragement I needed to move on.

I express my gratitude to Tapas Ganguli and Aparna Chakrabarti for providing uninterrupted support and constant encouragement. I sincerely appreciate the efforts made by Aparna Chakrabarti for correcting and improving these pages during the intensive writing period.

I wish to express my gratitude to Arup Banerjee, Avijit Chowdhury, and other Training School members for their support and advice rendered to me during my entire PhD career.

I would like to thank the Doctoral Committee for their constructive criticism and suggestions which led me to an unprecedented insight to my thesis work.

It is my pleasure to thank my colleagues Ajit K. Singh and Ajay Khooha of BL-16

beamline for spending their valuable time with me during measurements especially during early days of my work. I still remember all-night-long measurement sessions with Ajit K. Singh and Ajay Khooha at BL-16 beamline.

I express my sincere thanks to Head of the departments of Laser Surface & Material Treatment Laboratory and Microscopy Laboratory of RRCAT, Indore for allowing me to utilise their facilities. I also place my thanks to lab members especially, Puspen Mondal, Mahendra Babu, Sudheer and others for their help. I am also grateful to Shrikrishna Sartale, SP Pune University, Pune who had provided me permission to work in his laboratory and use the facilities available at his laboratories.

This thesis work would not have been possible without the extended co-operation and support of Indus beamline control members. I am especially grateful to Indus operation team members. I am also extremely thankful to Suraj Das and Ramesh Patil for their help provided during the design & fabrication of Goniometer components and various beamline instruments.

I am very grateful to HBNI, Mumbai for providing me with the opportunity to pursue my research at RRCAT Indore. I am also grateful to various national and international organisation namely The Abdus Salam International Centre for Theoretical Physics (ICTP)-Italy, Science and Engineering Research Board (SERB)-India, Fostering Science-France, Homi Bhabha National Institute -India, and The International Centre for Diffraction Data (ICDD) - U.S.A. for providing the financial support to participate in various International Symposiums/conference during my PhD work.

I also would like to extend my thanks to Arijit Chakraborty, Tufan Roy, Debashis Mondal, Paresh Chandra Pradhan, Smritijit Sen, Dipankar Jana, Subhomoy Halder, Mangalika Sinha, Nitish Paul, Ayushi Trivedi, Debabrata Saha, Tirtha Mandal for their continuous support and help during my PhD period. A special thanks goes to all my friends who provided me various resources. I learned a lot from them through discussions and friendly chats. Here, I mention many thanks to Rajib Mondal, Joy Narayan Mukherjee, Yasin and Arup Ratan Jana for their help and support. In addition, I

would like to convey my sincere thanks to one and all who have helped me during my PhD research work.

I express my life long indebtedness to my parents, Priya, Sukumar, Madhu, and Kartik for their love, affection and stimulating encouragement throughout my career. My deepest regard goes to my late grandfather Krishnakinkar Das. Your warm memories are still fresh in my heart. You are always there for me. Last of all lots of love and affection for Riju, Brishti and Sudha for listening my every little problem and cheering me up.

Contents

Synopsis	vi
List of Figures	xvi
List of Tables	xxx
1 Introduction	1
1.1 Introduction	2
1.2 Importance of Nanostructured Materials and their role in real device applications	2
1.3 Analytical technique for surface-interface analysis of nanostructured materials	6
1.3.1 Scanning Electron Microscopy (SEM) & Energy Dispersive X-ray Analysis (EDAX)	6
1.3.2 Transmission Electron Microscopy (TEM)	8
1.3.3 Atomic Force Microscopy (AFM)	9
1.3.4 Secondary Ion Mass Spectrometry (SIMS)	9

1.4	Various x-ray based techniques for characterisation of Nanostructured Materials	10
1.4.1	X-ray Photoelectron Spectroscopy (XPS)	11
1.4.2	X-ray Diffraction Technique (XRD)	11
1.4.3	X-ray absorption fine structure (XAFS)	13
1.4.4	X-ray reflectivity (XRR)	14
1.4.5	Total reflection x-ray Fluorescence (TXRF) and Grazing incidence x-ray fluorescence (GIXRF)	15
1.5	Combined XRR-GIXRF technique	18
1.6	XSW compared with other analytical technique	19
1.7	Scope of present work	21
1.7.1	XSW characterisation of thin layered materials	22
1.7.2	XSW characterisation of nanoparticle	23
2	Instrument development and Experimental details	25
2.1	Introduction	26
2.2	Details of the source and beamline	28
2.2.1	Indus-2 source	28
2.2.2	Synchrotron based XRF: a microfocus XRF beamline of Indus-2 (BL-16)	29
2.3	Details of the XRR-GIXRF experimental station	32
2.4	Thin film Deposition system: Magnetron sputtering	35

2.5	Photon Flux Measurements at BL-16	36
2.6	Various x-ray spectroscopy probes at BL-16 beamline	37
2.6.1	XRF and TXRF	38
2.6.2	μ -XRF and Microfluorescence mapping	39
2.7	Analysis of thin layered materials by using simultaneous XRR and GIXRF measurements	39
2.8	Summary	48
3	Effect of Synchrotron Polarization on grazing incidence excited fluorescence emission	49
3.1	Introduction	50
3.2	Physical background on the scattering density profile	52
3.2.1	Theoretical simulation	55
3.3	Experimental	57
3.4	Results and discussions	59
3.4.1	Applications to a few methodological samples	62
3.4.2	Effect on the Detection sensitivity	65
3.4.3	Effect of azimuthal anisotropy of scattered radiation on the fluorescence signal strength	68
3.4.4	Determination of degree of Polarization of the Synchrotron beam	70
3.5	Summary	71
4	Depth resolved structural and chemical analysis of thin layered materials	73

4.1	Introduction	74
4.2	Standing wave - grazing incidence x-ray fluorescence	76
4.3	Development of a GUI-CATGIXRF program	78
4.3.1	Program Methodology	78
4.3.2	GUI-CATGIXRF Interface	86
4.3.3	Program internals	87
4.3.4	Main features and utilities of the CATGIXRF program	88
4.4	Some example studies	93
4.4.1	An x-ray wave guide structure	93
4.4.2	Applicability of GUI-CATGIXRF for the characterisation of thin layered materials	96
4.5	Analysis of interface morphology of a deeply buried layer in a multilayer structure	101
4.5.1	Numerical simulation to understand the depth profiling of buried layer	102
4.5.2	Probing buried interfaces	103
4.5.3	Determination of in depth Electron density profile	105
4.6	Depth resolved chemical speciation in a multilayer structure	108
4.6.1	Probing various depth of a multilayer structure	110
4.6.2	Determination of optical constant of W near the absorption edge	115
4.6.3	Depth resolved chemical analysis of a multilayer structure	118
4.6.4	X-ray diffraction study	123

4.7	Summary	125
5	Analysis of nanoparticles using XSW	127
5.1	Introduction	128
5.2	Analysis of Au nanoparticle on flat substrate	130
5.3	Effect of temporal coherence on surface x-ray standing wave measurements	136
5.3.1	Theoretical background	139
5.3.2	Numerical simulations	141
5.3.3	Analysis of Au nanoparticles and Langmuir-Blodgett thin film structure using partially coherent SR radiation	143
5.4	Characterization of TiO ₂ nano-composites	146
5.4.1	Synthesis of TiO ₂ nanoparticles	148
5.4.2	Studies on growth kinetics and crystalline phase of TiO ₂ nanoparticles	149
5.4.3	Determination of surface morphology of TiO ₂ nano-composites .	151
5.5	Summary	160
6	Summary and Future scope	163
6.1	Development of an x-ray reflectometer	164
6.2	Grazing incidence x-ray fluorescence studies	164
6.3	XSW analysis of thin layered medium	165
6.4	XSW analysis of nanocomposite	166
6.5	Future scope	166

Synopsis

In recent years, precise structural characterization of nanostructured materials is becoming increasingly important as they find widespread usages in various fields of science and nano-technological applications. Numerous advantages of functionalized patterned nanostructures especially in medical physics, chemistry, biology and their applicability as catalyst for solar energy applications have rapidly driven the growth of this field in the last two decades. In particular, for applications involving biomedical imaging, the nanostructured materials have attracted perhaps the greatest attention as they provide a direct interface at the subcellular length scale. The performance of a nanostructured device strongly depends on its microstructural properties. Presence of any unwanted impurity even at micro or trace level may lead to change in the physical properties and may deteriorate the overall performance of a nanostructured device. Quantitative analysis of nanomaterials is often very challenging because currently available methods are not suitable for probing large depth of the order of 100 nm or more, moreover, it requires high depth resolution of a nano-probe method (of the order of sub-nanometer length scale) to distinguish internal structure of a nanoscale thin film device [1–4].

In a similar vein, periodic synthetic multilayer structures consisting of alternating thin layers of high Z and low Z elements or compounds, offer unique structural, magnetic, and electronic, properties with a wide range of applications. Multilayers as an x-ray optical element are used in many technological applications like x-ray astronomy, microscopy and fluorescence spectroscopy. They are also employed as filters and

monochromators in synchrotron beamlines and free-electron x-ray lasers. The performance of a multilayer structure strongly depends on its microstructural properties such as thickness of individual high Z and low Z layers, interface roughness and interlayer formation between the two mediums [5–7].

In the literature, most commonly available surface microscopy methods (e.g. - scanning electron microscopy, scanning tunneling microscopy, atomic force microscopy) and compositional analysis methods (e.g. - x-ray photoelectron spectroscopy, secondary ion mass spectrometry etc.) allow nanometer length scale resolution for probing nanomaterials, however, these techniques suffer from the serious disadvantages of relatively poor probing depths as well as inferior detection sensitivities for elements that are present at low concentrations. Moreover, these techniques do not provide any depth resolved physical and chemical nature of a nanostructured material.

The x-ray reflectivity (XRR) technique is another reliable method to measure structural properties such as thickness and interface roughness at sub-nanometer length scale, as demonstrated for several metallic, intermetallic, semiconducting and ceramic thin film mediums. The conventional XRR technique however, has the intrinsic limitation of analyzing non-reflecting (non-continuous) layers. Moreover, it does not provide any element-specific information. It only gives the thickness and roughness values for the high and low Z layer mediums, and thus sometimes it becomes quite difficult to determine true microstructural parameters of the periodic multilayer thin film structures [8, 9].

Using grazing incidence x-ray fluorescence (GIXRF) analysis, it is possible to unfold depth resolved physical and chemical properties of a nanostructured material. GIXRF analysis not only provides dimensional visualization for a nanostructured material but also offers depth resolved localization for a foreign impurity element (if any) embedded inside the nanostructured thin film medium. GIXRF technique provides information both for the non-reflecting layer as well as for the reflecting thin layer medium. The inherent characteristics features of GIXRF allow us to even analyze multielement nanostructured

materials. However, it has less sensitivity to surface roughness effects in a thin layered material as compared to that of the XRR technique. In addition, small density variations in a thin film structure cannot be truly described by using the GIXRF technique alone [10–12].

In the present thesis work, it has been shown that the XRR analysis, in combination with GIXRF measurements allows angstrom level ($\sim 5 \text{ \AA}$) depth resolved sensitivities for nondestructive determination of microstructural parameters of a thin layered material. The most significant advantage of the combined XRR and GIXRF analysis is that it reduces the limitations of the individual techniques thereby improving the reliability of the estimated parameters (such as thickness, roughness, density variations, and interface diffusion) of a thin film medium. Synchrotron radiation based instrumentation as well as computational analysis methodologies developed for the combined XRR-GIXRF analysis of the nanostructured materials are described in this thesis.

A brief description of the individual Chapters of the present thesis work is given below.

Chapter 1: Introduction

Chapter 1 describes a general overview, importance and role of thin film nanostructured materials as optics for synchrotron mirrors, monochromators as well as a catalyst for energy applications. The limitations and advantages of various x-ray based techniques over the conventional methods have been presented. Various characterization techniques available for the structural and chemical analysis of nanostructured materials are also briefly described. Various advantages of the combined XRR-GIXRF analysis approach over other conventional methods have been highlighted in detail. Finally, the scope of present work in light of existing literature is described.

Chapter 2: Instrument development and Experimental details

An x-ray reflectometer station has been developed and set-up on the BL-16 microfocus beamline of Indus-2 synchrotron facility. This Chapter describes the mechanical details and various salient features of the BL-16 reflectometer station. The reflectometer station facilitates surface-interface characterization of thin layered materials by using x-ray reflectivity and x-ray standing wave induced grazing incidence x-ray fluorescence measurements. The performance of the reflectometer has been evaluated by analyzing several thin layered structures having different surface interface properties. In addition, a brief description of the various experimental stations available at the BL-16 beamline for characterization of bulk materials is also presented in this Chapter.

Contents of this Chapter are published in Review of Scientific Instruments 86, 055102 (2015) and AIP Conference Proceedings 1728, 020142 (2016).

Chapter 3: Effect of Synchrotron Polarization on grazing incidence excited fluorescence emission

The effect of synchrotron beam polarization in grazing incidence excited x-ray fluorescence analysis has been investigated in Chapter 3. Theoretical computations carried out explain how scattering probability densities of the Compton and elastic scattering radiations depend on the scattering angle (θ) and azimuthal angle (ϕ) in the polarization plane of the synchrotron radiation beam. The computation results closely corroborate with the experimental total reflection x-ray fluorescence (TXRF) measurements carried out on several standard reference materials (SRMs). The results further explain that one can achieve approximately one order of magnitude enhancement in the spectral signal strength of various elements in synchrotron assisted TXRF analysis

by utilizing anisotropic nature of the primary scattered radiation in the horizontal detection geometry ($\theta = \pi/2$, $\phi = 0$). Interestingly, the azimuthal anisotropy of the scattered photons shows its vital role on the significance of observed x-ray fluorescence detection sensitivities.

Contents of this Chapter are published in Journal of Analytical Atomic Spectrometry 29, 2405 (2014), AIP Conference Proceedings 1591, 642 (2014), and AIP Conference Proceedings 1665, 080039 (2015).

Chapter 4: Depth resolved structural and chemical analysis of thin layered materials

In this Chapter, the underlying physical aspects of x-ray standing wave technique and development of the GUI-CATGIXRF program, as a solution to provide non-destructive evaluation of nanostructured materials are described. The GUI-CATGIXRF program allows combined analysis capabilities for both XRR and GIXRF data simultaneously, thus enabling us an improved reliability for the determination of microstructural parameters of a thin film medium. The potential utility and various salient features of the GUI-CATGIXRF program are described by providing example calculations as well as by analyzing several thin film structures comprising of different surface-interface properties. Applicability of the combined XRR and x-ray standing wave (XSW) analysis approach for probing deep buried interfaces inside a W-B₄C multilayer structure has also been demonstrated. The cross sectional transmission electron microscopy results obtained on the same W-B₄C multilayer structure provide overall reliability and accuracies of the XSW technique. It has been demonstrated that XRR investigation together with the GIXRF measurements can be used as a sensitive probe to quantitatively evaluate the presence of a buried interface structure or any thickness non-uniformity inside a periodic multilayer structure. It has been further demonstrated that the technique offers capability

to distinguish density variations of the order of 6 % or any atomic migration occurring in any layer, deep inside a multilayer medium.

To study nondestructive chemical speciation inside a W-B₄C multilayer structure, XSW assisted depth resolved near edge x-ray absorption measurements have been carried out. Interestingly, results presented in Chapter 4 show existence of some unusual electronic states for W at the surface-interface boundary of the W-B₄C multilayer structure as compared to that of the bulk W. Grazing incidence x-ray diffraction analysis carried out on the same multilayer structure provides valuable insights on the local crystalline environment of W in the multilayer medium and supports conclusions drawn from the XSW results.

Contents of this Chapter are published in X-Ray Spectrometry 45, 212 (2016), Applied Physics Letters 108, 263109 (2016).

Chapter 5: Analysis of nanoparticles using XSW

In Chapter 5, potential applicability of the combined XRR-GIXRF approach has been demonstrated for the reliable and precise characterization of surface morphology of metal nanoparticles, dispersed on a flat surface. Appropriate theoretical models have been developed that take into account an effect of average particle size, particle's shape, nature of particle's dispersion and their agglomeration on top of a substrate surface during computation of XSW assisted fluorescence profile of a nanostructured material. The effect of temporal coherence of the primary x-ray beam on the total reflection assisted x-ray standing wave (TR-XSW) fluorescence analysis of nanostructured materials is also evaluated in detail.

In the subsequent sections of the Chapter 5, applicability of the XSW assisted fluorescence methodology for the determination of surface morphology of different types of nanostructured materials (e.g. Au nanoparticles and TiO₂ nanoparticles dispersed on top of a Si substrate surface) has been described. A novel synthesis procedure for the

fabrication of low dimensional TiO₂ nanoparticles using gas phase CO₂ laser pyrolysis method is described. Laser based pyrolysis method provides nearly mono - dispersed, and narrow size distribution of the TiO₂ nanoparticles over large surface area of a Si substrate surface. Atomic force microscopy measurements along with the transmission electron microscopy measurements were also carried out to correlate findings of the XSW investigations. Grazing incidence x-ray diffraction and electron diffraction measurements were performed to investigate the crystalline nature of the TiO₂ nanoparticles.

Contents of this Chapter are published in Applied Physics Letters 107, 103104 (2015), AIP Conference Proceedings 1832, 050025 (2017), and X-Ray Spectrometry (2017).

Chapter 6: Summary and Future scope

Chapter 6 summarizes the results and conclusions of the present thesis work. A grazing incidence x-ray reflectometer station has been developed and set up on the BL-16 microfocus x-ray fluorescence beamline of Indus-2 synchrotron facility for the microstructural characterization of nanostructured materials using combined XRR-GIXRF analysis approach. Effect of polarization properties of synchrotron radiation and correction for nonzero wavelength dispersion of the incident x-ray wave field have been taken into account in the model computations of x-ray reflectivity and XSW assisted angle dependent fluorescence profiles originated from a thin nanostructured material. It has been shown that the combined XRR - GIXRF technique allows precise determination of depth resolved structural and chemical informations about a nanostructured material in a nondestructive manner.

For future work, two developments that seem promising are: I) vacuum compatibility of the reflectometer for light element detection and, II) in-situ studies of nanostructured materials at various sample environments (with change of temperature and magnetic field). Other interesting applications that can be pursued using combined XSW-XANES

technique are - depth resolved x-ray absorption studies on electrolyte interfaces of solid state batteries, and chemical speciation of buried interfaces in thin film solar cell structures. Furthermore, the combined XRR-GIXRF technique can also be applied to study structural and chemical properties of the core-shell nanoparticles. Such kinds of studies have not been performed so far and therefore may yield valuable informations on novel physical properties of the core-shell nanoparticles.

References

- [1] N. Nakagawa, H. Y. Hwang, and D. A. Muller, *Nature Materials*, **2006**, 5, 204.
- [2] J. Chakhalian, J. W. Freeland, H. U. Habermeier, G. Cristiani, G. Khaliullin, M. van Veenendaal, and B. Keimer, *Science*, **2007**, 318, 1114.
- [3] B. Revaz, M. C. Cyrille, B. L. Zink, I. K. Schuller, and F. Hellman, *Phys. Rev. B*, **2002**, 65, 094417.
- [4] E. Benckiser et al., *Nature Materials*, **2011**, 10, 189; P. Yu et al., *Phys. Rev. Lett.*, **2010**, 105, 027201; G. Jackeli and G. Khaliullin, *Phys. Rev. Lett.*, **2008**, 101, 216804.
- [5] B. G. Kelly, A. Loether, K. M. Unruh, and M. F. DeCamp, *Phys. Rev. B*, **2017**, 95, 064301.
- [6] A. F. Kravets, D. M. Polishchuk, Yu. I. Dzhezherya, A. I. Tovstolytkin, V. O. Golub, and V. Korenivski, *Phys. Rev. B*, **2016**, 94, 064429.
- [7] M. Charilaou, C. Bordel, P.E. Berche, B. B. Maranville, P. Fischer, and F. Hellman, *Phys. Rev. B*, **2016**, 93, 224408.
- [8] G. Ju, M. Tabuchi, Y. Takeda, and H. Amano, *Appl. Phys. Lett.*, **2017**, 110, 262105.
- [9] G. Bhattacharya, R. P. Giri, H. Saxena, V. V. Agrawal, A. Gupta, M. K. Mukhopadhyay, and S. K. Ghosh, *Langmuir*, **2017**.
- [10] F. Meirer, A. Singh, G. Pepponi, C. Streli, T. Homma and P. Pianetta, *J. Anal. At. Spectrom.*, **2010**, 29, 479.

[11] R. S. Becker, J. A. Golovchenko, and J. R. Patel, Phys. Rev. Lett., **1983**, 50, 153.

[12] D. K. G. de Boer, Phys. Rev. B, **1991**, 44, 498.

List of Figures

1.1	Schematic diagram of a scanning electron microscope	7
1.2	A schematic diagram of Atomic force microscope system.	8
1.3	A schematic diagram for geometric construction of Bragg Law.	12
1.4	(a) Schematic representation of reflection phenomena from a thin film on top of a Si substrate, where multiple reflections can take place in thin film medium. (b) Simulated x-ray reflectivity spectra of a Cr thin film of thickness 500 Å and 100 Å respectively on Si substrate at incident x-ray energy of 8 keV. The figure clearly demonstrate the dependency of the oscillation frequency on the film thickness.	15
1.5	Computed GIXRF profiles for (a) bulk-like, (b) particle like, and (c) thin layer like structures. The calculations were carried out at incident x-ray energy of 8 keV. The critical angle position in all cases are marked by dotted lines.	17
2.1	A schematic optical layout of the BL-16 beamline showing different components of the beamline.	29
2.2	Annotated photograph of the developed x-ray reflectometer station at BL-16 beamline.	33

2.3	A snapshot of the “XSWBL16” control software of the BL16 beamline, showing different windows for remote data acquisition and alignment of the x-ray reflectometer station.	34
2.4	A picture of DC magnetron sputtering system, utilized for the deposition of different single and multilayer thin film structure.	35
2.5	Variation of photon flux with energy at BL-16 beamline of Indus-2 SR facility.	37
2.6	(a) Measured and fitted XRR profile of a W thin film structure measured at 10.0 keV incident x-ray energy. In the inset of the figure, the effective electron density profile of the three layer medium is shown, calculated from the best fit results of XRR and W-L α fluorescence measurements. A Schematic diagram of the W thin film on a Si substrate is delineated in the inset of figure. (b) Measured and fitted XRR and XSW induced W-L α fluorescence profiles of the W layer at 12.0 keV x-ray energy. The scattered points show the experimental data while the solid lines are the best fits to the measured profiles. The fluorescence yield of W-L α has been normalized at an incidence angle $\theta=1.2^\circ$	41
2.7	(a) Measure and fitted XRR profiles of a TiO ₂ thin film medium at 10.0 keV incident x-ray energy. The inset of figure (a) shows the effective electron density distribution of TiO ₂ thin film medium on top of a Si substrate. (b) Measured and fitted XSW induced Ti-K α fluorescence and XRR profiles of the TiO ₂ structure at 8.0 keV x-ray energy. The scattered points are the experimental data while the solid lines represent the best fit curves to the measured data. The Ti-K α fluorescence yield has been normalized at an incidence angle $\theta \sim 1.0^\circ$	43

2.8	(a) Measured x-ray reflectivity profile of the W-B ₄ C multilayer structure using a laboratory reflectometer (BRUKER D-8 system) at Cu-K α wavelength ($\lambda = 1.54 \text{ \AA}$). The multilayer structure consists of N = 15 bilayers of the W and B ₄ C layers deposited on Si (100) substrate, as shown schematically in the inset of the figure. (b) Measured XRR profile of the same W-B ₄ C multilayer structure using BL-16 reflectometer station at incident x-ray energy of 10.0 keV. The scattered points indicate the experimental data while the solid lines show the best fit curves for the measured data.	45
2.9	XSW induced W-L α fluorescence and XRR profiles measured for the W-B ₄ C multilayer structure at incident x-ray energy of 12.0 keV. The scattered points shows the experimental data while the solid lines are the best fits to the measured profiles. The W-L α fluorescence yield has been normalized at an incidence angle $\theta=1.2^\circ$	46
3.1	Experimental geometry used for the angle dependent XRF measurements. The spectroscopy detector is placed in the vertical geometry (<i>i.e.</i> , $\theta = \pi/2$ and $\phi = \pi/2$) as well as in the horizontal geometry (<i>i.e.</i> , $\theta = \pi/2$ and $\phi = 0$) to collect the XRF spectra.	53
3.2	Angular distribution of the scattered photon for (a) Compton and (b) elastic scattering as a function of scattering angle (θ) and azimuthal angle (ϕ) at incident x-ray energy of 15 keV.	55
3.3	Variation of Compton scattered radiation as a function of scattering angle (θ) and incident energy.	56
3.4	Angular distribution of the Compton scattered photon as a function of scattering angle (θ) and azimuthal angle (ϕ) at the 1 MeV monochromatic incident x-ray beam.	56

3.5	Annotated photograph of the TXRF experimental station of the BL-16 beamline. The inset shows a recorded image at the x-ray CCD in TXRF excitation geometry. In this figure the incident and reflected x-ray beam are marked.	58
3.6	Measured TXRF spectra of a NIST-1640 reference material in vertical geometry ($\theta = \pi/2$ and $\phi = \pi/2$) and horizontal geometry ($\theta = \pi/2$ and $\phi = 0$). Here, Ga (100 ppb) is used as an internal standard reference element. Scattered points are experimental data, solid lines are the fitted spectrum in the two measurement geometries.	59
3.7	Recorded TXRF spectra for an ICP-IV Merck reference standard (containing 50.35 ppm wt. concentration of each elements) in vertical ($\theta = \pi/2$ and $\phi = \pi/2$) and horizontal ($\theta = \pi/2$ and $\phi = 0$) geometry. In this figure, scattered points are experimental data, solid lines are fitted spectrum in the two geometries. Figure 3.7(b) shows extended view of the encircle region of Fig. 3.7(a), where Tl-L γ_1 peak is individually fitted in the presence of large Compton scattered background. It can be seen that the visibility of Tl-LL γ_1 peak gets enhanced in the horizontal detection geometry due to the reduced spectral background.	60
3.8	Measured TXRF spectra of the Au nanoparticles distribution on the Si substrate at monochromatic x-ray energy of $E_0 = 15$ keV in the horizontal and vertical detection geometries respectively. Scattered points are experimental data, solid lines are fitted spectrum in the two measurement geometries. Inset gives AFM image for the Au nanoparticles distribution on the Si Substrate surface.	62

3.9	Measured TXRF spectrum of coconut water sample at monochromatic x-ray energy of $E_0 = 15$ keV in the horizontal and vertical geometries respectively. Ga (35 ppm) was used as an internal standard. Scattered points are experimental data, solid lines are fitted data in the two geometries.	63
3.10	Variation of elemental detection sensitivities for (a) NIST-1640 (in ppb) and (b) ICP-IV (in ppm) standard reference samples as a function of atomic number Z in the vertical ($\theta = \pi/2$ and $\phi = \pi/2$) and horizontal ($\theta = \pi/2$ and $\phi = 0$) detector mounting geometry.	67
3.11	Variation of the Compton and elastic scattered radiations at different azimuthal angles in the TXRF measurements. Scattered points are experimental data, solid lines are the fitted data at different angles. The inset illustrates the scattered radiation intensity variation at different azimuthal angles.	68
3.12	Variation of fluorescence signal to scattered Compton intensity ratios for different elements present in the NIST-1640 standard reference material at 15 keV as a function of azimuthal angle (ϕ). The inset illustrates the experimental geometry used for the Phi- scan measurements. The arrow shows the scanning direction of the detector in the horizontal mounting geometry. The detector was placed at a distance ≈ 30 mm from the centre of beam footprint on the sample surface.	70
4.1	(a) Refraction of x-rays through an inhomogeneous medium (material). (b) The formation of x-ray standing wave on top of a reflecting surface due to the interference of incident and reflected x-ray beams of wave length λ . Enhanced fluorescence x-rays are emitted from those parts of the sample volume that present at the locations of XSW field antinodes.	76

4.2	Multiple refraction and reflection of x-rays in a multilayer thin film structure on a thick infinite substrate. The transmitted and reflected field intensity in different media has been demonstrated by respective subscripts.	80
4.3	Schematic of various concentration profiles for an impurity element in a layer of thickness d.	84
4.4	A snapshot of the main window of the GUI-CATGIXRF program, showing different command tools and buttons for input and output of the data. To allow model based fitting of the thin film medium, one can define the structure type by selecting options; ‘multilayer structure’ or ‘independent structure’, as described in the text.	86
4.5	A schematic illustration for the beam foot print effect in the grazing incidence x-ray fluorescence measurements. On the right hand side, a snapshot of the sub-program window of the GUI-CATGIXRF program is shown that takes different input parameters from a user to define excitation geometry for a thin film specimen for the correction of beam foot print effect in the computed GIXRF profile.	90
4.6	Computed XRR and GIXRF (Cr-K α fluorescence) profiles of a Cr (55 Å) / B ₄ C (400 Å) / Cr (250 Å) trilayer structure, deposited on a Si substrate surface. The computations are performed using the GUI-CATGIXRF program assuming an incident x-ray energy of 12 keV. (a) XRR profile, (b) GIXRF (Cr-K α fluorescence) profile, showing various transverse electric field excitation modes (TE ₀ , TE ₁ and TE ₂) that excite inside low Z material (B ₄ C) at specific incidence angles. In the inset of figure (a) we have also shown an extended view of the XRR profile in the vicinity of critical angle, showing location of the incidence angle for various excited modes.	95

4.7 Electric field intensity (EFI) distribution computed inside the Cr (55 Å) / B₄C (400 Å) / Cr (250 Å) trilayer structure on a Si substrate surface using GUI-CATGIXRF program. The formation of different transverse electric field modes (TE₀, TE₁ and TE₂) can be clearly observed in the B₄C medium at distinct incidence angles. (b) Computed effective electron density profile for the trilayer medium. 96

4.8 (a) Measured XRR and GIXRF (W-L α fluorescence) profiles along with fitted curves for the W (276 Å) - B₄C (304 Å) bilayer structure at incident x-ray energy of 12 keV. The fitted results also reveal the presence of a SiO₂ layer of thickness ~ 12.7 Å at the interface of W layer and Si substrate, as illustrated in the inset of the figure. Scattered points are the measured data while solid lines represent best fit curves to the experimental data. The fit residuals of the respective profiles are shown below. (b) Effective electron density profile for the bilayer medium computed from the best fit results. 97

4.9 Measured and fitted XRR and GIXRF (W-L α fluorescence) profiles along with the fit residuals for a W-B₄C periodic multilayer structure of parameters $d = 48.5 \pm 0.8$ Å and, number of bilayers $N = 15$ on a Si (100) substrate surface at incident x-ray energy of 12 keV. (a) XRR profile, (b) GIXRF (W-L α fluorescence) profile in the vicinity of Bragg region. Scattered points are the measured data while solid lines represent best fit curves to the experimental data. 99

4.10 (a) calculated XRR and GIXRF profiles of a W-B ₄ C multilayer structure at 12.0 keV incident x-ray energy assuming a thickness asymmetry in the bilayer period of ~ 5 Å at 4 th , 8 th , and 12 th bilayer location respectively. (b) Simulated XRR and GIXRF profiles of the W-B ₄ C multilayer structure assuming a thickness variation of ± 5 Å in the W layer at 4 th bilayer location.	102
4.11 Measured (scattered points) and fitted (solid lines) x-ray reflectivity profiles of W-B ₄ C multilayer structure at two different incident x-ray energies of (a) 10.0 keV and (b) 12.0 keV. On the right hand side, a schematic illustrations depict two layer and buried layer model of the W-B ₄ C multilayer. In this layer model, a low-density C layer is also marked on top of the W-B ₄ C multilayer medium.	104
4.12 (a) Measured and fitted W-Lα fluorescence and XRR profiles for the W-B ₄ C multilayer structure at an incident x-ray energy of 12.0 keV. The inset shows an extended view of the XRR and GIXRF profiles in the vicinity of the 1 st order Bragg peak. (b) Computed x-ray field intensity (EFI) distribution inside a W-B ₄ C periodic multilayer structure at 12.0 keV x-ray energy.	106
4.13 (a) Cross-sectional TEM micrograph of the W-B ₄ C multilayer structure. (b) A line scan profile derived from the cross section TEM micrograph. (c) Derived effective electron density profile (EDP) of the multilayer structure.	108
4.14 A schematic representation showing the x-ray reflection from a W-B ₄ C periodic multilayer structure consisting of N=15 bilayer repetitions. In this figure we have also depicted a buried interface layer of W inside the multilayer medium, on top of a Si substrate.	111

4.15 Measured and fitted (a) XRR and (b) W-L α fluorescence profiles for W-B ₄ C multilayer structure comprising of N=15 bilayer repetitions at an incident x-ray energy of 10230 eV.	112
4.16 X-ray field intensity (EFI) distribution inside a W-B ₄ C periodic multilayer structure computed using best fitted parameters obtained from the XRR and W-L α fluorescence measurements at an incident x-ray energy of E=10230 eV. In this figure, we have also marked various dotted vertical lines showing different incident angles that have been opted for depth selective XANES measurements of W-B ₄ C multilayer structure.	114
4.17 Measured and fitted XRR profiles for W-B ₄ C multilayer structure comprising of N=15 bilayer repetitions in the incident x-ray energies of 10192-10230 eV.	115
4.18 Determined optical constants (a) δ ,(b) β , and (c) the ratio β/δ of W from the x-ray reflectivity measurements in a W-B ₄ C multilayer structure comprising of N=15 bilayer repetitions in x-ray energy region of 10192-10230 eV. The values of optical constants calculated from the Henke table are also given for comparison.	117
4.19 X-ray field intensity (EFI) distribution inside a W-B ₄ C periodic multilayer structure computed using best fitted parameters obtained from the XRR and W-L α fluorescence measurements and determined optical constants (δ,β) at incident x-ray energy of (a)10205 eV,(b) 10207 eV,(c) 10212 eV and (d) 10218 eV. One clearly observed the proving depth volume of XSW wave field inside W-B ₄ C multilayer structure across the W-L ₃ absorption edge energy preserves a more or less constant volume, except a angular shift $\theta \sim 0.01^\circ$ at high energy side ($E \sim 10230eV$) of the W-L ₃ edge.	119

4.20	X-ray standing wave induced XANES profiles of the W-B ₄ C multilayer structures measured at L ₃ edge of W. (a) Measured XANES profile of a multilayer structure consisting of N=15 bilayer repetitions using BL-16 beamline of Indus synchrotron facility, and (b) W-B ₄ C multilayer structure with N=10 bilayer repetitions measured at the International Atomic Energy Agency (IAEA) GIXRF-XRR experimental facility operated at the XRF beamline of Elettra Sincrotrone Trieste (BL-10.1L).	120
4.21	X-ray standing wave induced XANES profiles of (a) W-B ₄ C bilayer and (b) W single thin film structures at L ₃ edge of W. In the inset of Figs. (a) and (b) a schematic model structure of the W-B ₄ C bilayer and W single thin film structures are given. On the right hand side, computed x-ray field distribution near W-L ₃ edge energy (E ~ 10208 eV) is shown inside the two mediums.	122
4.22	Measured GIXRD pattern of W-B ₄ C multilayer consisting of N=15 bilayer repetitions at incident x-ray energy of 15.5 keV. During the measurements the incidence angle of the primary x-ray beam was fixed at 1.0°.	124
5.1	Computed XSW assisted (a) XRR and (b) Au-L α fluorescence profiles for 10 nm Au nano-spheres of various densities (0.005 to 19.3 g/cm ³). During the calculation we have assumed Au nano-spheres dispersed on top of a Si surface at incident x-ray energy of 15.0 keV.	132

5.2	Computed Au-L α fluorescence profiles for the Au nano-spheres dispersed on top of a Si surface at incident x-ray energy of 15.0 keV. The Au-L α fluorescence yield has been calculated by assuming an average particle size of \sim 30 nm and considering different r. m. s. variations (σ) in the particle size distribution (a) $\sigma = 2$ nm, (b) $\sigma = 8$ nm, and (c) $\sigma = 12$ nm respectively. The insets show the computed distribution profiles of the Au nanoparticles (NF) vs. their size. On the upper right location of the figure we have depicted a schematic illustration for the distribution of nanoparticles on a Si surface. (d) Computed contour plot for x-ray field intensity distribution at 15 keV x-ray energy on a Si substrate.	133
5.3	Computed GIXRF profiles (Au-L α fluorescence yields) for different shapes of Au nanoparticles distributed on the Si surface at 15.0 keV x-ray energy. (a) Nano-sphere (dia.= 30 nm), (b) Nanorod (height = 30 nm). In the above calculations, we have assumed a r. m. s. variation (σ) in the particle size distributions $\sigma = 2$ nm. (c) Computed form factor profiles for the spherical and cylindrical shapes nanoparticles.	134
5.4	(a) Measured and fitted Au-L α fluorescence profiles obtained for the Au nano-spheres, deposited on top of the Si surface at 15.0 keV x-ray energy. The scattered points show the experimental data while the solid line is the best fitted profile to the measured data. The Au-L α fluorescence yield has been normalized at an incidence angle of $\theta = 0.5^\circ$. (b) Particle size distribution profile obtained for the Au nanoparticles on top of the Si surface using GIXRF measurements. On the right side, measured AFM images for the distribution of Au nanoparticles on the Si surface acquired at different locations are shown.	137
5.5	A schematic illustration describing formation of XSW field under total external reflection of x-rays on a mirror surface.	138

5.6 Variation of $Re [\gamma(\Delta)]$ and computed x-ray field intensity distribution above the Si substrate surface for the 15 keV x-rays at two different spectral resolutions. (a) and (b) show simulation results obtained at spectral resolution of $\lambda_o/\delta\lambda \approx 5000$. While (c) and (d) depict simulation results obtained at low spectral resolution of $\lambda_o/\delta\lambda \approx 6.22$. (a) and (c) are calculated at the critical angle $\theta_c \approx 0.114^\circ$ 140

5.7 (a) Computed XSW induced fluorescence profiles for spherical Au nanoparticles distribution on a Si substrate surface at different spectral resolution widths of the incoming x-ray beam. The angle dependent fluorescence profiles are simulated using eqn. (5.1) and the formula $I_{FY}(\theta) = \int_0^d I(\theta, z) \times \exp(-\frac{\mu_{Au}}{\sin\phi}) \times F(z) dz$, where μ_{Au} describes the linear absorption coefficient of Au for the outgoing fluorescent x-ray photons, ϕ is the take off angle of emitted fluorescent photons and d is the diameter of the nanoparticle, $F(z) = 4z \frac{(d-z)}{d^2}$ represents the normalized density profile for a spherical nanoparticle as a function of height z above the substrate surface. (b) Comparison of measured to calculated Au fluorescence yields. AFM image of Au nanoparticles distribution on Si surface is shown in upper right along with enlarged image of a single nanoparticle. 142

5.8	Experimental demonstration of the applicability of the partially coherent radiation for TR-XSW analysis. (a-c) Measured and fitted angle-dependent x-ray fluorescence profiles for the Zn atomic layer embedded in a LB film structure at different spectral widths of the incident x-ray photons. The relative uncertainty in the Zn yield is less than 5% for data above 0.45° and less than 2% below 0.45° . (d) Measured and fitted x-ray reflectivity profiles for the LB thin film structure at x-ray energy of 10.162 keV with spectral resolution of $\lambda_0/\delta\lambda \approx 5000$ corresponding to (a). (e) Effective electron density profile of the LB thin film structure determined from the best fit results using combined XRR and TR-XSW analysis, which clearly reveals the presence of Zn atomic layer at a mean height $\langle z \rangle = 90.3$ nm, from Au surface layer.	145
5.9	A photograph of the deposition set up (based on the laser pyrolysis process).	148
5.10	Total reflection x-ray fluorescence (TXRF) measurements were performed at incident x-ray energy of 8 keV. The grazing incidence angle $\theta \sim 0.22^\circ$ was fixed during the measurements. Si, Ti-fluorescence intensity, and Scattered light intensity are plotted with vapour pressure of TTIP as a function of temperature.	150
5.11	(a) Grazing incidence x-ray diffraction profile of synthesised TiO_2 nanoparticles deposited on Si substrate. (b) XRD profile of standard TiO_2 powder (P25) at Cu- $K\alpha$ wavelength ($\lambda = 1.54 \text{ \AA}$).	151
5.12	Calculated XSW assisted GIXRF profiles at 8 keV incident x-ray energy for two cases: (a) TiO_2 nano-spheres of various sizes, and (b) TiO_2 thin films of different thicknesses on top of Si substrate.	152

5.13 Measured and simulated (a) XRR and (b) XSW induced GIXRF profiles of TiO ₂ nanostructures at 8 keV incident x-ray energy. The inset shows a three layer model of TiO ₂ nano-structure opted for the fitting of measured experimental data.	153
5.14 Combined XRR and GIXRF measurements at 8 keV incident x-ray energy. Measured and fitted (a) XRR , and (b) XSW induced GIXRF profiles of the TiO ₂ nano-structure. (c) The contour plot of x-ray field intensity distribution on a Si substrate as a function of depth of layer medium and incidence angle calculated with the best fit results of XRR and Ti-K α fluorescence measurements. The scatter points are the experimental data and the solid lines are the simulated data. The fluorescence yield of Ti- K α has been normalized at $\theta = 0.45^\circ$	156
5.15 (a) Measured and fitted GIXRF profiles of TiO ₂ nanostructures deposited on a W thin film at 8 keV incident x-ray energy. (b) The contour plot of x-ray field intensity distribution on a W thin film as a function of depth of layer medium and incidence angle. The EFI was calculated from best fit results of GIXRF. The scatter points are the experimental data and the solid lines are the fitted data. The fluorescence yield of Ti- K α has been normalized at $\theta = 0.85^\circ$	157
5.16 (a) TEM micrograph, and (b) Electron diffraction (ED) profile of TiO ₂ nanoparticle deposited on Cu grid.	159

List of Tables

1.1	Overview of various analytical techniques available for the analysis of nanostructured material. * SAXS-small angle x-ray scattering.	20
2.1	Parameters of Indus-2 electron storage ring.	28
2.2	Main parameters of BL-16 Beamline.	30
2.3	The measured photon flux at 100 mA ring current at BL-16 beamline. . .	38
2.4	Best fitted microstructural parameters of the W thin film obtained using XRR and GIXRF measurements.	42
2.5	Best fitted microstructural parameters of the TiO ₂ thin film obtained using XRR and GIXRF measurements.	43
2.6	Best fitted microstructural parameters of the W-B ₄ C multilayer obtained using laboratory and synchrotron based XRR and GIXRF measurements.	47
3.1	Determined relative signal strengths and concentrations of various trace elements in the coconut water.	65
3.2	Measured relative signal strength of various elements in different samples.	66
3.3	Measured degree of Polarization for SR beam at the BL-16 beamline. . .	71

4.1	Structural parameters used in the GUI-CATGIXRF program for the computation of XRR and GIXRF (Cr-K α fluorescence) profiles for a Cr/B ₄ C/Cr trilayer structure.	94
4.2	Fitted microstructural parameters of the W-B ₄ C bilayer structure, determined from the GUI-CATGIXRF program using combined XRR and GIXRF (W-L α fluorescence) analysis at incident x-ray energy of 12 keV.	98
4.3	Microstructural parameters of the W-B ₄ C periodic multilayer structure consisting of N = 15 bilayers of the B ₄ C and W materials. These parameters were determined from the GUI-CATGIXRF program using combined XRR and GIXRF (W-L α fluorescence) analysis.	101
4.4	Fitted microstructural parameter of the W-B ₄ C multilayer structure obtained by using XRR and XSW analysis. d = thickness (Å), ρ = density (g/cm ³), σ = roughness (Å), All the error values in the determined microstructural parameters of multilayer structure are lies between 2-6 %.	105
5.1	Optimum parameters for the low dimensional TiO ₂ nanoparticle deposition.	149
5.2	Best fitted microstructural parameters of the TiO ₂ nanostructured obtained from the combined XRR and GIXRF measurements.	158

Chapter 1

Introduction

This chapter gives a general overview and importance of the nanostructured materials in different areas of science and technology. The limitations and advantages of various x-ray based techniques over the conventional analytical methods have been presented. As a non-destructive probe, the combined x-ray reflectivity and grazing incidence-ray fluorescence (XRR-GIXRF) technique for the structural and chemical analysis of nanostructured materials is briefly described. Finally, the scope of present work has been highlighted.

1.1 Introduction

X-rays play a significant role in understanding the internal structural details of an atom. The history of x-ray spectroscopy dates back to the accidental discovery of x-rays in 1895 by the German physicist Wilhelm Conrad Roentgen. This discovery had opened up a new window of research not only in the area of physics and chemistry but also in various branches of science and technology. In 1970, the lithium drifted silicon detector was developed for the first time and that technology is still in use today. There are several possible atomic and molecular resonances, that allow absorption of x-ray radiation in a very short wavelength range of the order of a few nanometer to angstrom in the electromagnetic spectrum. All these resonances can be used to identify the specific chemical states of an atom in a given material. By carefully controlling the incident photon energies one can probe atomic and molecular resonances in various physical states of a material (solid, liquid or gas). For instance, in magnetic microscopy one can determine the contents of two neighbouring elements (i.e, Fe or Co) distinctly. Similarly, there is a great potential to work in the water window region to determine the absorption of O and C edges that has lot of applications in the biological field [1, 2].

1.2 Importance of Nanostructured Materials and their role in real device applications

Usually Nanomaterials can be defined as an arrangement of structure having characteristic dimension between the microscopic and molecular length scale. Nanostructured materials show various novel physical and chemical properties as compared to that of the bulk. Their unique structural, electronic and magnetic properties play an important role in understanding many correlated and uncorrelated physical phenomenon, such as electronic and magneto transport properties and interlayer exchange coupling properties of various compound materials [3, 4]. Numerous

advantages of functionalised patterned nanostructures especially in medical physics, chemistry, biology and their applicability as catalyst for solar energy applications have rapidly driven the growth of this field in the last two decades. In particular, for applications involving biomedical imaging, the nanostructured materials have attracted perhaps the greatest attention as they provide a direct interface at the subcellular length scale [5].

Lack of adequate knowledge about the growth kinetics such as nucleation of atoms, formation of a layer structure etc. makes it difficult to tune the overall fabrication processes from the point of view of practical device applications of low dimensional nanomaterials [6]. Furthermore, presence of any unwanted impurity even at micro or trace level may lead to change in the physical properties and therefore may deteriorate the overall performance of a nanostructured device. For example, the presence of transition elements like Cr, Fe, Co, Ni, Cu and Zn may cause increased leakage current of a thin film transistor device [7, 8]. Therefore, precise structural and interface knowledge about a nanostructured material is often necessary to tailor the physical properties of a thin film based semiconductor device. Any unwanted structural non-uniformity in the layer thickness or formation of a buried layer interface structure can lead to malfunction and may change the overall characteristic features of a nanostructured device. Similarly, long term durability of a thin film based device is also strongly correlated with the nature of interface structure associated between different constituent layers [9]. Electronic states at the surface and interface boundary of a thin film medium significantly differ from that of the bulk due to strong orbital reconstruction or hybridization of near surface atoms [10, 11]. Such hybridization extensively modulates the physical properties of a thin film medium. Alteration of surface and interface properties due to atomic scale modulation of the orbital occupation has been a major obstacle that hinder further progress in real device applications of the nanostructured materials. Interface reconstruction due to diffusion or atomic migration is an active area of research to unravel insights of many physical phenomena [12–14].

Despite immense progress in this direction, no appropriate technique is available that can provide depth resolved localised chemical information about a thin layered material.

The constructive interference of the x-rays produced by crystalline materials opens a new window of research to understand many basic problems in condensed matter physics [15]. It has been demonstrated that periodic synthetic multilayer structures comprising of alternating thin layers of the high-Z and low-Z elements or compounds might expand the range of utility of this phenomenon into various spectral domains, which are not usually accessible using naturally occurring crystalline materials. Such synthetic periodic multilayer structures are primarily employed as artificial x-ray Bragg reflectors in synchrotron beamlines, and their reflection efficiency predominantly dictated by the nature of the buried interfaces between different layers. Recently, an increasing interest has grown on the synthesis of such periodic multilayer materials. Similarly an x-ray optical system based on the total external reflection phenomena has been used in many applications for the optimization and conditioning of an x-ray beam [16]. Every optical system has its own advantages and limitations. On the other hand multilayer optics can be used as a bandpass filter and they provide energy resolution about two orders of magnitude wider as compared to that of single crystals. Another significant benefit of multilayer optics is that they provide Bragg angle values which is typically 2 to 3 times higher than the critical angle of a reflecting mirror based on totally reflection phenomena. Thus, the photon flux transported by a multilayer optics is significantly higher compared to both the single crystals and reflecting mirror optics. In addition to that, multilayer optics also provides an opportunity to tailor ‘*d*’ period laterally, satisfying the Bragg condition at each point on a curved surface. Such graded multilayer optics are usually fabricated with elliptical or parabolic shapes. They provides enhanced photon flux and improved beam collimation properties [17–19].

Quantitative analysis of such nanostructured optics is often very challenging because currently available methods are not particularly suitable for probing large depths of the order of 100 nm or more, moreover, it requires high depth resolution of a nano-probe

method (of the order of sub-nanometer length scale) to distinguish internal structure of a nanoscale thin film device. However, currently available techniques suffer from the serious disadvantages of relatively poor probing depths as well as inferior detection sensitivities for elements that are present at low concentrations. Moreover, these techniques do not provide any depth resolved physical and chemical nature of a nanostructured material. Therefore, it is important to explore non-destructive analytical methods that can provide precise structural properties of the nanostructures. The recent advances in the field of surface-interface analysis of nanostructured materials have spurred new experimental efforts to develop methodologies that can provide depth resolved structural and chemical information of a nanostructured material non-destructively.

In this thesis work, special emphasis has been given on the development of suitable analytical techniques for the depth resolved structural and chemical characterisation of nanostructured materials. To bridge the missing gap, synchrotron radiation based instrumentation has been developed to perform combined XRR-GIXRF analysis of the nanostructured materials. Analytical methods have been developed to determine surface-interface characterisation of nanostructured materials in a non-destructive manner. The present thesis work also provides solutions to a number of unsolved issues that are not addressed so far. For examples, in one of the case it discusses in detail the effect of polarization of synchrotron beam during grazing incidence excited x-ray fluorescence analysis. Similarly, effect of temporal coherence properties of a synchrotron x-ray beam on the total reflection assisted x-ray standing wave fluorescence analysis of the nanostructured materials has been studied in detail.

1.3 Analytical technique for surface-interface analysis of nanostructured materials

A number of analytical methods are employed for the characterisation of surface-interface properties and chemical composition of a nanostructured material. A single analytical technique cannot be applied to each branch of science to obtain complete details about a system. Each technique has its own advantages and limitations. Depending on the capability and sensitivity a measuring technique, reliable characterisation results can be obtain about a specimen [20]. In this section, various microscopy techniques used for the characterisation of a nanostructured material are briefly summarized. The principle mechanism of a technique and its applicability to various fields of science are also discussed.

1.3.1 Scanning Electron Microscopy (SEM) & Energy Dispersive X-ray Analysis (EDAX)

Scanning electron microscopy (SEM) is one of the most commonly used technique for the determination of surface morphology of a nanostructured material over a wide range of magnification. In this technique, a high energy accelerated electron beam is allowed to focus onto a solid sample. The interaction between the incident electron beam and the atoms in the sample reveals the information about the surface topography and chemical composition of the specimen. Magnification of the SEM technique can be controlled over a wide range (up to six orders of magnitude). The energy exchange between the incident electron beam and the orbital electrons of an atom gives rise to back-scattered electrons (BSE), secondary electrons and characteristic x-rays. BSE are reflected electrons from the sample due to elastic scattering and they provide information about the distribution of different elements in the sample. BSE signal is strongly correlated with the atomic

number (Z) of the specimen. The secondary electrons come from a very shallow depths in the specimen because of inelastic scattering between the incident electrons and the atoms. It provides information about surface topography and a three dimensional image of the scanned area of the sample. Figure 1.1 demonstrates a schematic diagram of a SEM system.

Energy Dispersive x-ray (EDX) technique is used to identify the elemental composition

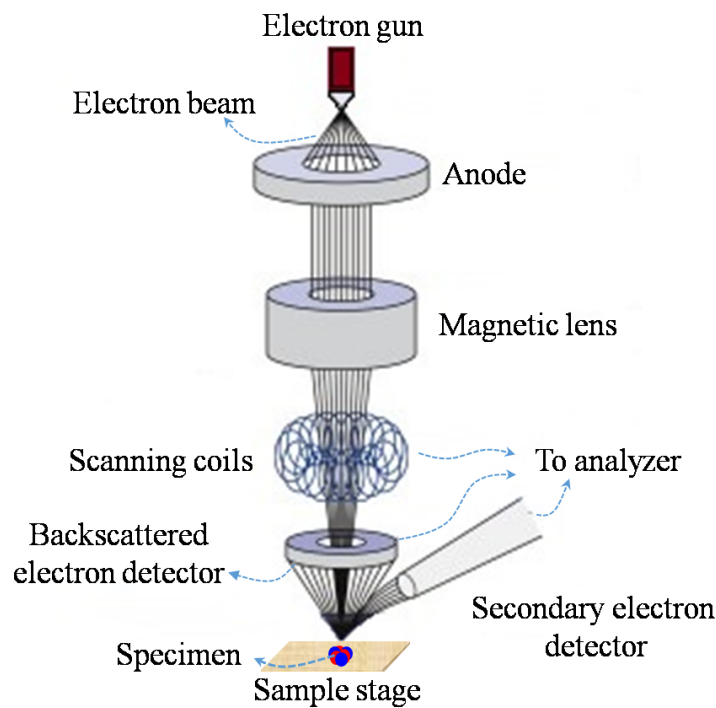


Figure 1.1: Schematic diagram of a scanning electron microscope .

of a specimen. Usually EDX is combined with SEM technique. In this technique high energy electrons are allowed to bombard on a specimen, knocking the inner shell electrons of an atom. The vacancies created in the inner shells are then filled by the upper shell electrons. Such transition of orbital electrons results the emission of characteristic x-rays. Characteristic x-rays are detected by solid state detector. It provides the composition of the constituent elements in a specimen.

1.3.2 Transmission Electron Microscopy (TEM)

The basic working principle of TEM is similar to SEM as discussed in the previous section. The TEM technique provides much higher spatial resolution as compared to the SEM. The TEM technique is very useful in understanding various informations of material such as surface morphology, crystal structure, strain, defects and chemical information down to atomic level. TEM image of a sample is formed due to the deflection of electrons that passes through the specimen. The technique provides a lattice resolution of ~ 1 nm. It has disadvantage that it can be used only for analysing thin specimen.

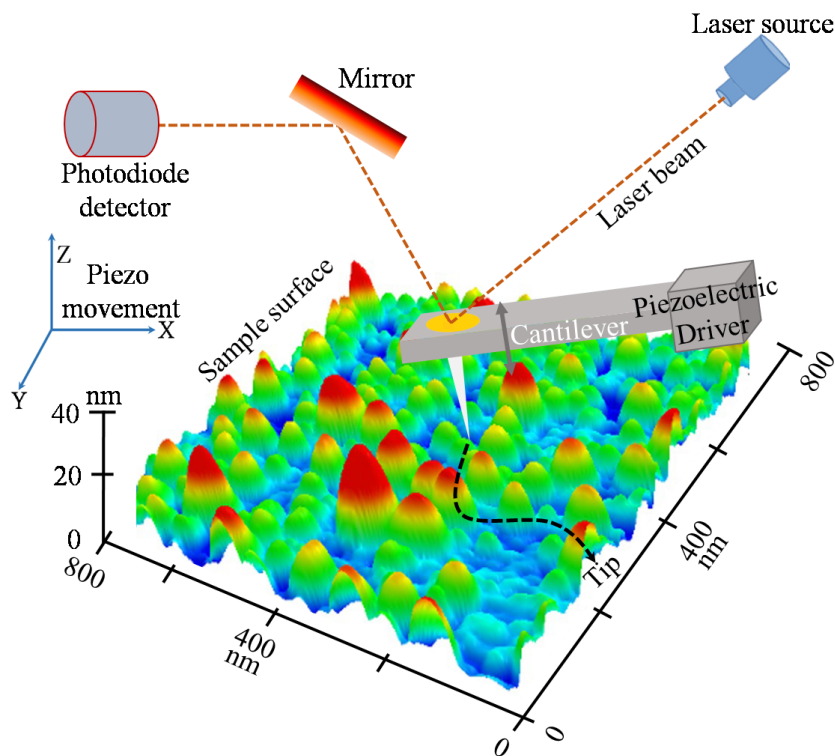


Figure 1.2: A schematic diagram of Atomic force microscope system.

1.3.3 Atomic Force Microscopy (AFM)

Atomic Force Microscopy (AFM) is a high resolution scanning microscopy technique. It finds widespread applications for the determination of surface morphology of nanostructured materials having dimension in the range of 100 Å to few microns [21]. The working mechanism of AFM is based on the principle of a cantilever. In this technique, a sharp tip is scanned over the sample surface in a very precise manner. The van der Waals forces between the atoms of probe tip and sample surface cause the cantilever to deflect on the sample surface according to its surface morphology. The short range attractive forces cause the cantilever to bend and measure fine changes in the surface morphology. A piezoelectric actuator provides very accurate and precise movement of the tip element on the sample surface. A schematic diagram of AFM system is shown in Fig. 1.2. The AFM technique allows various modes of operation. The contact mode also known as static mode of AFM, allows one to measure surface morphology of the solid surfaces. This mode of operation is largely affected by frictional and adhesive forces compared to non-contact or tapping mode. In the non-contact operation mode, the AFM tip is placed very close to the sample surface, such that it measures the attractive van der Waals forces between sample and AFM tip. The non-contact operation mode of AFM is preferred to measure surface morphology of soft biological and organic thin film samples. AFM provide a three dimensional surface visualization of a specimen. Using AFM one can image a maximum surface area of $150 \times 150 \mu\text{m}^2$ and a maximum height variation of 10-20 μm . The lateral resolution of the AFM technique is limited by the tip size of the cantilever.

1.3.4 Secondary Ion Mass Spectrometry (SIMS)

Secondary Ion Mass Spectrometry (SIMS) is used to probe the chemical state of an element inside the solid and thin film surfaces. The SIMS technique is primarily a

destructive probe. It is mainly used for the determination of depth profiling of dopants and impurity atoms inside a solid surface. In this technique, a sample is exposed by a primary ion beam of energy ranging from 1-30 keV in the vacuum environment. The secondary ions generated from the specimen are then detected and analysed by a mass spectrometer. The elemental detection sensitivities of the SIMS technique are in ppm range for most of the ($Z=6-10$) trace elements. The technique has the limitation that it can not be used to analyse soft matters and biological specimens.

1.4 Various x-ray based techniques for characterisation of Nanostructured Materials

X-ray based spectroscopy techniques are very useful for the analysis of nanomaterials because K, L and M absorption edges of most of the elements lie in the x-ray region. X-ray offers large penetration depths in most of the materials. When a specimen is exposed by x-ray, some of the x-ray photons interact with the atoms of the matter and their energy can be absorbed selectively or can be scattered. The number of x-ray photons transmitted by a material depends on its thickness, density and atomic number. The absorption of x-ray in the material is caused due to the photoelectric effect, fluorescence and auger effect; whereas the scattering of an x-ray photon may occurs due to elastic and inelastic scattering effects. All these processes have finite probability. It depends on the energy of the incident x-ray photon and atomic number of the irradiated material. Various interaction mechanisms allow a number of analytical techniques for the characterisation of a material [1, 2, 22].

1.4.1 X-ray Photoelectron Spectroscopy (XPS)

Photoelectron spectroscopy is based on the photoelectric effect. Electrons in an atom are tightly bound in their orbital by the characteristic binding energies. The binding energy of an orbital electron strongly depends on the atomic number, orbital type and the nature of neighbouring atoms. In the XPS technique, an incident photon of sufficient high energy is absorbed by the atom with the emission of a photoelectron. The kinetic energy of the emitted photoelectrons is evaluated by a concentric hemispherical electron analyser. XPS is primarily a surface sensitive technique because the electrons that are ejected from deep inside the surface are unable to escape from the surface of a material. Therefore, only few mono layers of the sample can be probed. The XPS experiments are performed under ultra high vacuum ($< 10^{-9}$ torr) environment. The technique provides the information about chemical state as well as concentration of different elements present in the material [23].

Both x-ray absorption near-edge spectroscopy (XANES) and XPS are complementary technique and can be used with equal ease to determine chemical nature of bulk and surface region of a nanostructure. XPS can be used to obtain information about the occupied electronic states below the Fermi level, whereas, XANES provides determination of density of unoccupied electronic states above the Fermi level.

1.4.2 X-ray Diffraction Technique (XRD)

X-ray diffraction is a widely used technique for the structural characterisation of materials. In this technique x-rays are allowed to diffract from a specimen. The diffracted x-rays carry the structural details of a material. Since the atoms are arranged periodically in the lattice, therefore x-rays diffracted from the different planes comprise of definite phase relationship between them, which leads to constructive and destructive interference pattern in the reflected x-ray beam. The Bragg's law for the diffraction of

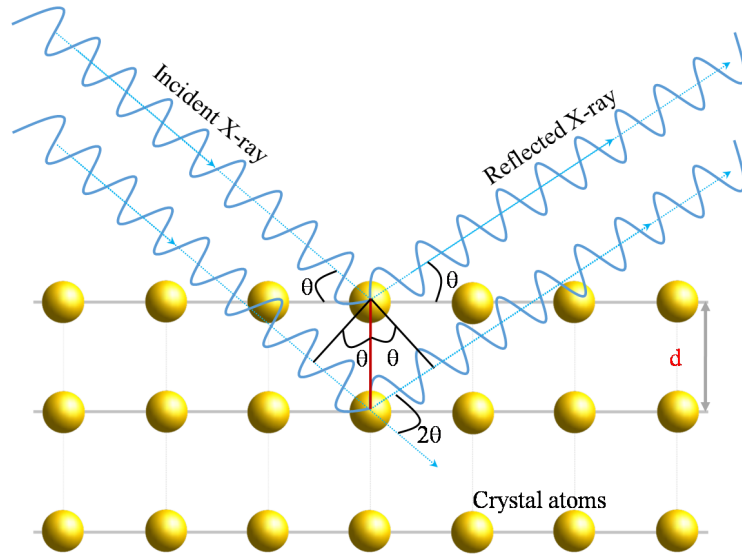


Figure 1.3: A schematic diagram for geometric construction of Bragg Law.

x-rays is given by

$$2d \sin \theta = n\lambda \quad (1.1)$$

where n =order of diffraction, d = interplanar spacing, θ =glancing angle, λ =wave length of the incident x-ray beam. The schematic representation of the Bragg's law is shown in Fig. 1.3. According to this law, the incident x-rays are reflected from the different parallel crystal planes (or Bragg planes), which contain a large number of atoms. These atoms scatter the primary x-ray beam coherently and produce the intensity Bragg peaks in the XRD spectrum. At certain incidence angles, the reflections from particular parallel Bragg plane are in phase. Hence, they reinforce constructive interference and produce maximum of intensity. For those angles where reflections from different planes are out of phase one obtains destructive interference pattern (i.e, zero or feeble reflected intensity) [24]. The lattice spacing (or the interplanar spacing) can be expressed as,

$$d_{hkl} = \frac{1}{\sqrt{\left(\frac{h}{a}\right)^2 + \left(\frac{k}{b}\right)^2 + \left(\frac{l}{c}\right)^2}} \quad (1.2)$$

where, a, b, c are lattice parameters and h, k, l are Miller indices for the corresponding parallel plane. When a beam of monochromatic x-rays is incident on a crystal surface

then each atom present in the crystal becomes the source of scattering radiation. X-ray diffraction technique is primarily used for the phase identification, impurity or secondary phase identification and to find out the crystallite size. The diffraction pattern can also be used to determine the crystallite size of nanomaterials using Scherrer formula. Crystals which are in size less than 1000 Å cause the broadening of the diffraction peaks. This broadening is usually related to the particle size which can be calculated using Scherrer formula, given as

$$D = \frac{K\lambda}{B\cos\theta} \quad (1.3)$$

where λ is the wavelength of the x-ray used, B is the broadening of the diffraction peak measured at its half maximum intensity, θ is the angle corresponding to the Bragg peak position, D is the diameter of crystalline particle, K is the shape factor. For various shapes of particles, it can be evaluated. For example, for spherical shape particles, $K = (4/3)(\pi/6)^{1/3}$. It is important to consider instrumental broadening factor during the calculation of particle size. The broadening factor can be expressed as $B^2 = B_M^2 - B_S^2$, where B_M is the measured breadth of the diffraction line of the sample and B_S is the corresponding width of a peak of the standard material. In general, low Bragg angle peaks are used for the determination of crystallite size as the broadening of a Bragg peak increases at higher incidence angles.

1.4.3 X-ray absorption fine structure (XAFS)

X-rays can be absorbed by an atom, that present isolated on top of a surface or inside a material at energies near and above the core-level binding energies. The x-ray absorption fine structure (XAFS) spectrum is typically divided into two regimes: x-ray absorption near-edge spectroscopy (XANES) and extended x-ray absorption fine structure spectroscopy (EXAFS). The XAFS signal is specifically sensitive to the coordination chemistry (e.g., octahedral, tetrahedral coordination) of the absorbing atom, neighbour distances, and types of the atoms in the near surroundings of the atom under

investigation. XANES measurements are strongly sensitive to formal oxidation state of an atom. Therefore one can obtain the information about local surroundings and the chemical state of an atom by fitting XAFS signal [25].

1.4.4 X-ray reflectivity (XRR)

X-ray reflectivity (XRR) is basically a scattering technique for the determination of microstructural properties of a thin layered material [15, 26, 27]. It provides information about thickness, density, and surface/interface roughness of the reflecting layers extending from few nanometers to some hundreds of nanometers with angstrom resolution. In case of a material that is deposited on a substrate surface and forms a continuous layer, there will be two interfaces *viz.* vacuum/film and film/substrate that are separated by the thin film of thickness ‘*d*’ (see Fig. 1.4(a)). Let the Fresnel reflected amplitudes of the top and bottom interfaces be r_{12} and r_{23} respectively. The amplitude of x-ray reflection from the thin film structure can be expressed as,

$$r = \frac{r_{12} + r_{22}exp(2i\Phi)}{1 + r_{12}r_{22}exp(2i\Phi)} \quad (1.4)$$

where $\Phi = \frac{2\pi}{\lambda} \times (n2dS \sin\theta)$ is the phase difference between the scattered amplitude from the two interfaces, which give rise to the oscillatory behaviour in the measured reflectivity pattern, n is the index of refraction. The oscillation frequency of the XRR pattern determines the thickness of the film medium; if Δq is the difference in wave vector transfer between the two successive maxima/minima, then $2\pi/\Delta q$ gives the thickness ‘*d*’ of the thin film medium. If only the single scattering events from the two interfaces are considered, then the denominator term in eqn. 1.4 can be neglected and resultant reflectivity can be described by the numerator of the eqn. 1.4 alone. However, the multiple scattering effects give rise to higher order terms and the denominator term in eqn. 1.4 becomes significant. Another important aspect is the relation between the film

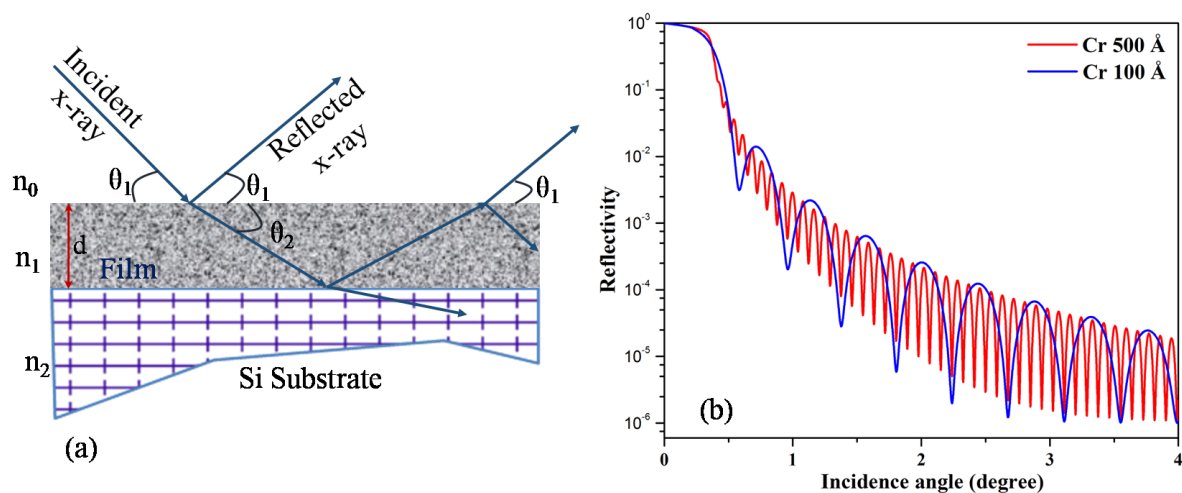


Figure 1.4: (a) Schematic representation of reflection phenomena from a thin film on top of a Si substrate, where multiple reflections can take place in thin film medium. (b) Simulated x-ray reflectivity spectra of a Cr thin film of thickness 500 Å and 100 Å respectively on Si substrate at incident x-ray energy of 8 keV. The figure clearly demonstrate the dependency of the oscillation frequency on the film thickness.

thickness and the oscillation frequency of XRR pattern. As the thickness of the film increases, the angular separation between two successive peaks decreases. This can be understood by the fact that the reflectivity is the Fourier transform of the electron density variation in the real space. This is illustrated in Fig. 1.4, where the simulated XRR curves for a 100 Å and 500 Å thick Cr film on a Si substrate are shown.

1.4.5 Total reflection x-ray Fluorescence (TXRF) and Grazing incidence x-ray fluorescence (GIXRF)

X-ray fluorescence (XRF) spectroscopy is a non-destructive analytical tool for the spectrochemical determination of almost all the elements present in a specimen. The emission of fluorescence photons occurs when a vacancy in an inner shell of an atom is formed due to ejection of a core shell electron by the incident x-ray photon. As a result an outer orbit electron makes a transition to that vacant core shell state. Due to this

electronic transition the atom undergoes with the emission of characteristic fluorescence photon. The energy of this photon is equal to the difference in energies of the initial and final electronic states of an atom.

TXRF is a variant of energy dispersive x-ray fluorescence spectrometry. It has been shown that the reflectivity of a polished surface is strongly increased at very low grazing incidence angle (critical angle). The angular region below which the incident x-ray is reflected completely from a surface is known as total reflection region. Therefore, the XRF measurements carried out under total reflection condition of a flat substrate is referred as total reflection x-ray fluorescence (TXRF). The main advantage of TXRF technique is that the spectral background generated due to Compton and elastic scattering of the primary x-ray beam is reduced to a great extent. The matrix effects are also eliminated completely in TXRF. The technique is highly suitable for multi element ultra-trace element analysis. In addition to trace elemental analysis, the TXRF technique finds widespread applications for surface and near-surface characterisation of thin layered materials. A detail description of TXRF technique has been provided in Chapter 3. The elemental depth sensitivity inside a nanostructured material can be enlarged to nanometer regime by measuring grazing incidence angle dependent x-ray fluorescence emitted from a thin layered material. In grazing incidence x-ray fluorescence (GIXRF) technique, a primary x-ray beam impinges on a smooth reflecting surface, a part of the radiation is specularly reflected and part of it is refracted and transmitted inside the sample surface. In the condition of total external reflection ($\theta < \theta_c$), the incoming and reflected beams interfere and form an x-ray standing wave (XSW) field pattern on the substrate surface. This XSW field also expands below the substrate surface up to a certain depth (3 nm to 0.1 μm). Enhanced fluorescence radiation is emitted from those parts of the sample volume that are present at the locations of XSW field antinodes. By changing the grazing incidence angle in the vicinity of the critical angle θ_c , the position of XSW antinodes can be moved inside the sample material and the corresponding changes in the fluorescence intensity can be recorded. The XSW technique provides the

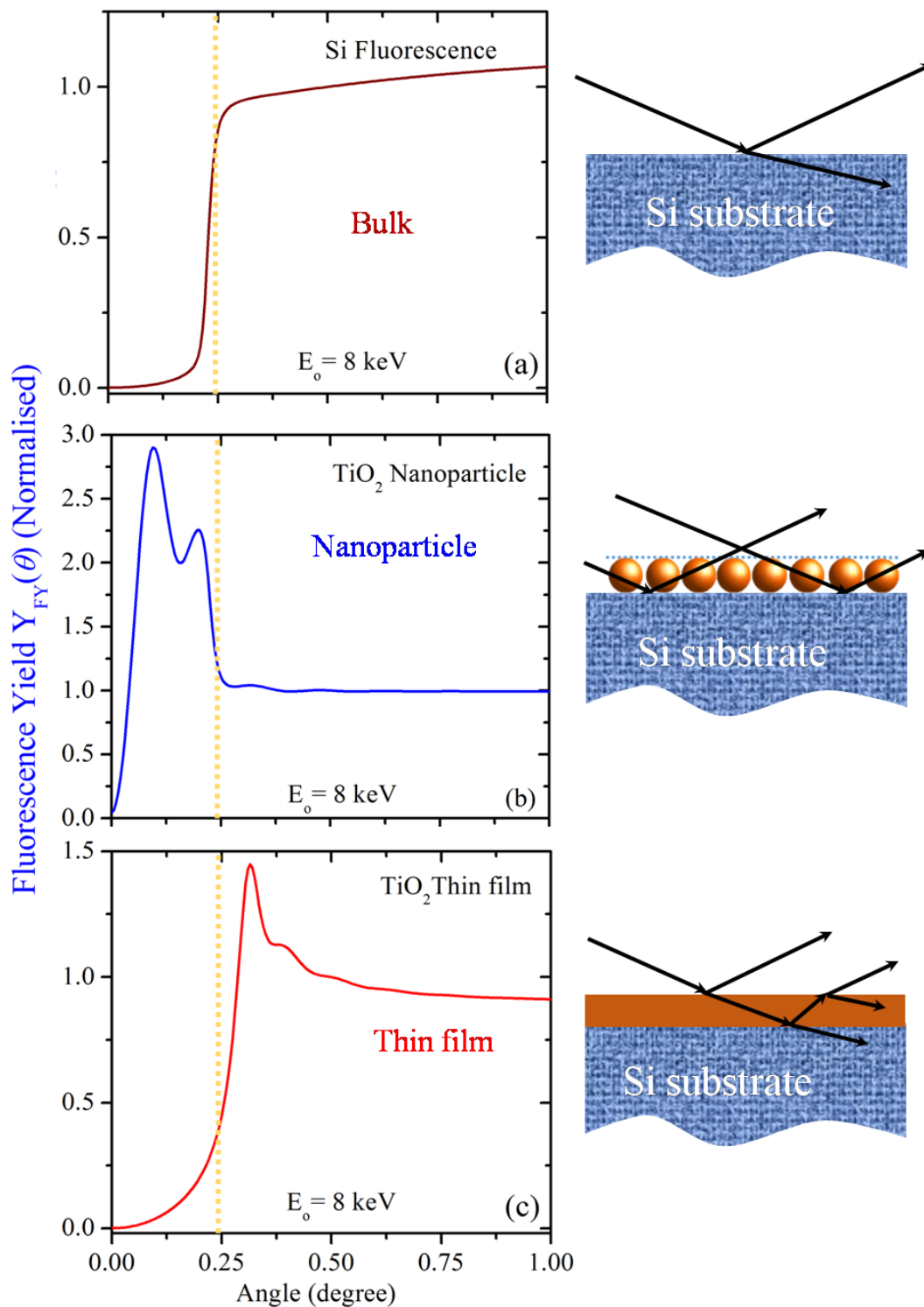


Figure 1.5: Computed GIXRF profiles for (a) bulk-like, (b) particle like, and (c) thin layer like structures. The calculations were carried out at incident x-ray energy of 8 keV. The critical angle position in all cases are marked by dotted lines.

determination of microstructural parameters like-roughness, thickness effects, and density variations in a thin film structure [28–32]. Figure 1.5 represents the computed GIXRF profiles for the bulk, nanoparticle, and thin film like structures. It can be seen from the Fig. 1.5 that GIXRF technique has the potential to distinguish the various types of nanostructure materials. In Chapter 4, the basic principles of XRR & GIXRF techniques have been explained in detail.

1.5 Combined XRR-GIXRF technique

XRR technique is a widely used technique for the surface-interface characterisation of nanostructured materials. It provides precise determination of depth resolved microstructural properties like density, thickness, roughness, etc. of a thin layered medium. However, one of the drawbacks of this technique is that it does not provide element specific information. The inherent characteristic features of GIXRF allow one to analyse multi-element nanostructured materials. Therefore by combining the two techniques in a simultaneous approach, one can reveal more or less complete informations about a nanostructure. The most significant advantage of the combined XRR-GIXRF analysis is that it reduces the limitations of the individual techniques thereby improving the reliability of the estimated parameters (such as thickness, roughness, density variations, and interface diffusion) of a thin film medium.

XAFS is a very promising technique to obtain chemical state and electronic structure of a material. However, the technique has a inherent technical limitation that it does not allow the analysis of a nanostructured material using the conventional fluorescence measurement geometry. Furthermore, it does not provide the depth resolved information about a nanostructured material. On the other hand XSW has the characteristic property to unfold depth resolve elemental information about a nanostructured material. Thus, by combining the x-ray absorption fine structure measurements in XSW geometry, it is possible to obtain the depth resolved physical and chemical properties of a

nanostructured material with angstrom depth resolution. Various attractive features of the combined XRR-GIXRF technique has been described in Chapter 2.

1.6 XSW compared with other analytical technique

It would be imperative to discuss the relative advantages and limitations of the available conventional microscopy techniques with respect to the XSW technique. The most significant advantage of XSW technique is that it allow large area of investigation as compared to the conventional surface analysis techniques. The inspected or sampled areas in electron probe microscopy (EM) and scanning probe microscopy techniques are in the range of few square micrometers, whereas the sampled area in the x-ray based techniques in grazing incidence geometry vary in several square millimetres (~ six orders of magnitude larger than the irradiated area of a conventional microscopic technique). As a result, XSW technique offers better measurement statistics as compared to the conventional microscopy techniques. In many cases, it is very time-consuming to record several images to improve of statistics of a measurement in EM and scanning microscopic techniques. Electron and scanning microscopic techniques provide direct information about the surface morphology of a nanostructured material with spatial resolution down to ~50 nm. Whereas, the XSW technique do not offer determination of surface resolved structural properties of a thin layered specimen. All the conventional techniques described above, however, do not have the capability to obtain information about a nanoparticle if it is embedded inside a bulk matrix or if several impurities are absorbed inside a nanostructured material. Moreover, the conventional surface characterisation techniques do not offer depth resolved information on the physical and chemical nature of the nanostructured materials and their localisation with respect to the substrate surface. Table 1.1 summarizes various advantages and disadvantages of the most common surface characterisation techniques.

Table 1.1: Overview of various analytical techniques available for the analysis of nanostructured material. * SAXS-small angle x-ray scattering.

Technique	Application	Advantages	limitations
SEM	surface morphology	provides magnification up to 6 orders and three dimensional appearance	offers limited depth resolution
TEM	surface morphology	provides high in depth resolution (cross section mode)	applicable to thin samples
AFM	surface morphology	offers lateral height of 100 Å to some microns with a resolution of sub-angstrom	limited lateral resolution, no in-depth information
SIMS	depth or impurity profiling	offers high elemental detection sensitivity	limited lateral resolution
XPS	elemental composition or chemical state	provides occupied electronic states	surface sensitive technique
XRD	structural characterisation	crystalline phase	in-depth chemical nature
XAFS	local surroundings and the chemical state	provides unoccupied electronic states	applicable to thin samples
SAXS*	microstructure, chemical composition, texture	particle systems of structure in the nanoscale to microscale	sensitive to electron density contrast
XRR	microstructural parameters	offers high depth resolution	no element specific information
TXRF	surface characterisation	offers high elemental detection sensitivity	surface sensitive technique
GIXRF	structural and chemical analysis	offers depth resolved analysis	low sensitivity for surface roughness effects and low density variations

1.7 Scope of present work

To overcome the limitations and advantages of individual XRR and GIXRF techniques, a combined XRR-GIXRF technique has been proposed in the present thesis work for depth resolved structural and chemical analysis of the nanostructured materials. Keeping in view the diverse applicability and several attractive merits of XRR & GIXRF, we have designed and constructed a x-ray reflectometer experimental station on the BL-16 microfocus beamline of Indus-2 synchrotron facility. The details of the BL-16 reflectometer along with its measured performance for the characterisation of nanostructured materials are described in detail in Chapter 2. The BL-16 XRR station allows various measurement modes *e.g.* total reflection XRF, combined as well as individual XRR and GIXRF measurements, XSW assisted x-ray absorption fine structure measurements of thin film structure, grazing incidence x-ray diffraction etc. During the XRR-GIXRF characterisation, the structure of a thin film specimen is usually evaluated by comparing the experimental XRR and GIXRF profiles with the model fit calculations. Therefore, a GUI based computer program (GUI-CATGIXRF) has been developed to examine angle dependent x-ray reflectivity and fluorescence intensities emitted from thin film medium.

Detection and precise quantification of elements that are present at trace and ultra-trace level in a specimen is important in many applications. Synchrotron radiation based XRF and SR-TXRF measurements are the examples of such trends. In the present thesis work systematic study has been carried out to investigate the influence of synchrotron polarization on the x-ray fluorescence emission at grazing incidence angles. The effect of anisotropic nature of Compton and elastic scattered x-rays on the spectral background and observed detection sensitivities are discussed in detail in Chapter 3. It has been shown that one can achieve approximately one order of magnitude enhancement in the spectral signal strength of an element under the grazing incidence excitation condition. We could observe detection sensitivity ~ 93 ppb - 3 ppb for elements of atomic number

Z ranging from 14 to 33 in synchrotron assisted TXRF analysis. The present thesis work describes the feasibility to determine the concentration as well as location of various trace embedded impurities at different depth inside a nanostructured material using GIXRF analysis technique. The applicability of GIXRF technique for the determination of shape and size distribution of metal nanoparticles has been demonstrated in detail.

1.7.1 XSW characterisation of thin layered materials

Precise structural and interface knowledge about a thin film medium is often necessary to tailor the physical properties of a thin film based semiconductor device or integrated circuits (ICs), magneto-electronics, and spintronics devices. Moreover, depth resolved studies on the chemical nature and electronic properties of a thin film medium are also important in many technological applications to understand and correlate the overall efficiency of a thin film based device. The formation of various chemical phases at various depths inside a thin film medium can strongly modify their physical properties. X-ray offers a large penetration depths in most of the materials. As a nondestructive probe, XSW induced fluorescence measurements at grazing incidence angles provide atomic scale depth resolution inside a thin film medium. We have discussed this issue in detail in Chapter 4 with respect to our results. Despite the recent advances in thin film growth methodology, the interface boundary between two materials in a thin film medium can not be realised distinctly due to atomic migration or diffusion of atoms at the interface region. The XSW induced GIXRF measurements along with XRR can be applied to quantitatively evaluate structural morphology of an underneath buried layer inside a periodic multilayer structure. Our results also reveal that the combined analysis approach has the capability to determine slight density variations or any atomic migration occurring in any layer, deep inside a thin layer medium. We have further demonstrated that the XANES characterisation along with the combined XRR-GIXRF analysis can be used as a sensitive probe to perform depth resolved chemical speciation

of a thin film medium. Our combined XSW-EXAFS analysis scheme has led to the first observation of the surface states at the surface-interface boundary inside a periodic multilayer structure. The understanding of distribution of surface states as a function of depth in thin films is often necessary to correlate their electronic, magnetic and transport properties.

1.7.2 XSW characterisation of nanoparticle

Dispersion of metal nanoparticles on flat surfaces has attracted considerable interest in many nanotechnology, biotechnology, and semiconductor quantum dot applications. Adequate characterisation of nanoparticle's distribution over a flat surface is important in many applications. In particular study of composite nanostructures (nanoparticle doped thin film structure and core-shell nanoparticles) has become an important area of research in last few years. Because, such nanostructures find variety of application in diverse fields as catalysts in industry, biomedical applications like biomolecular imaging, drug delivery, localised cancer therapy etc. Using conventional electron microscopy (EM) and atomic force microscopy (AFM) measurements it is not possible to obtain depth resolved chemical and physical properties of the nanostructured materials and their localization with respect to the substrate surface. In Chapter 5, we have addressed these issues related to the analysis of nanoparticles on top of flat a surface. The potential applicability of the combined XRR-GIXRF approach has been demonstrated for the reliable and precise characterisation of surface morphology of metal nanoparticles, dispersed on top of a flat surface. Appropriate theoretical models have been developed that take into account the effect of average particle size, particle's shape, nature of particle's dispersion and their agglomeration on top of a substrate surface during computation of XSW assisted fluorescence profile of a nanostructured material. It has also been demonstrated that the present approach can be successfully applied to determine the structure of a composite nanostructure. Furthermore, it has been shown

that the longitudinal coherence properties of a partially coherent x-ray source has a strong influence on the XSW analysis of a nanostructure material. To resolve this issue a systematic study has been carried out and the effect of temporal coherence of the primary x-ray beam on the XSW analysis of nanoscale materials has been investigated. The method developed by us opens up various new important applications *such as* enabling structural studies of large dimensioned nanostructures using conventional laboratory based partially coherent sources, which was inaccessible due to their inherent technical limitations. Chapter 6 summarizes the results and conclusions of present thesis work along with the future directions to carry out further research work in the area surface-interface analysis of thin nanostructured materials.

Chapter 2

Instrument development and Experimental details

In this chapter, details of various experimental stations available at the BL-16 microfocus x-ray fluorescence beamline of Indus-2 synchrotron facility for surface-interface characterisation of nanostructured materials and x-ray spectroscopy analysis of bulk materials are presented. A multipurpose x-ray reflectometer station has been developed and augmented at the BL-16 beamline to facilitate synchronous measurements of specular x-ray reflectivity and grazing incidence x-ray fluorescence radiation emitted from a nanostructured material. The design aspects and various salient features of the BL-16 x-ray reflectometer station are discussed in detail. Advantages and various salient features of the combined measurements of x-ray reflectivity and grazing incidence fluorescence on a single x-ray reflectometer station for the determination of true microstructural parameter of a thin layered materials are described in details.

2.1 Introduction

Recently, combined grazing incidence x-ray reflectivity (XRR) and x-ray fluorescence (GIXRF) analysis technique is gaining a remarkable momentum, because of its various salient features. The technique allows one to determine microstructural parameters of a thin layered material reliably down to atomic resolutions. Precise determination of depth resolved micro-structural parameters of the thin layered material has been a focus of interest in many applications (*viz.* distribution of impurities in magnetic thin layered materials, characterisation of δ -doped semiconductor materials, etc.).

X-ray reflectivity (XRR) is a well established nondestructive tool for the micro structural characterisation of thin layered materials. The XRR technique, allows one to evaluate micro-structural parameters *such as* thickness, surface and interface roughnesses and density variations in thin reflecting layers extending from few nanometers to some hundreds of nanometers with angstrom resolution. The technique offers high accuracy for the determination of thickness of a thin medium as it offers large dynamic range (Q_z range) for XRR measurements. The XRR technique however has the limitation that it does not provide any elemental specific information. In addition, the technique suffers from a serious limitation of its non-applicability for ultra thin layers of sub-nanometers, or very thick layers (>100 nm), as well as laterally inhomogeneous layers or non-reflecting layers, and multielemental composite thin film systems. Thus, sometimes it becomes quite difficult to ascertain real microstructural parameters of a thin layer medium using XRR technique alone.

X-ray fluorescence (XRF) spectrometry is another widely used non-destructive technique for the trace elements analysis of materials. It has been shown that by measuring grazing incidence angle dependent x-ray fluorescence intensities, the elemental depth sensitivity inside a thin film medium can be enlarged to nanometer regime [33]. GIXRF measurements alone have been employed for variety of applications including determination of roughness, thickness effects and density variations in the thin

film structures. Nevertheless, the GIXRF technique offers less sensitivity for the surface roughness effects and low density variations in the thin layered medium as compared to that of XRR technique.

The XRR technique, in combination with the GIXRF measurements, has shown to be a very powerful probe for non-destructive microstructural evaluation of thin layered materials [34]. The combined analysis approach offers determination of consistent microstructural parameters (*such as* thickness, roughness, density variations and interface diffusion) for a thin film medium with improved accuracies [35, 36]. In many cases, it is not possible to completely reveal the structure of a complex nanostructured material that comprises of both reflecting and nonreflecting layers, using only one of the techniques (XRR or GIXRF) [37, 38]. Recently, a few x-ray reflectometer stations have been installed at various synchrotron radiation facilities worldwide to facilitate combined XRR and GIXRF analysis for the thin nano-structured materials [39–42].

The BL-16 beamline on the Indus-2 synchrotron facility was initially set-up with a primary aim to perform trace elements analysis and micro-fluorescence mapping applications of various materials in condensed matter research [43–45]. Considering the numerous advantages of the SR based advanced spectroscopy methodologies in the area of surface condensed matter physics and to meet the current requirements of advanced analytical probes for the analysis of nanostructured materials, an in-house developed x-ray reflectometer station has been set-up on the BL-16 beamline. It has the capabilities to perform simultaneous XRR and GIXRF measurements of a thin layered structure. The combined XRR - GIXRF analysis features of the BL-16 reflectometer also allow a novel capability to perform GIXRF assisted depth resolved x-ray absorption fine structure (XAFS) studies to investigate the chemical state and electronic structure of the nanostructured materials.

In this chapter, details of the combined XRR-GIXRF experimental station of the BL-16 beamline are presented along with the measured performance. Appropriate computer softwares have also been developed for remote data acquisition control and

alignment of BL-16 XRR station. The BL-16 XRR-GIXRF experimental station has been equipped in a manner that allows users to perform XRR and GIXRF measurements of the thin layered materials independently with a minimal set-up time and without affecting the operations of other installed experimental stations at the beamline. The BL-16 reflectometer station beamline also provides a novel capability to perform x-ray standing wave assisted XAFS measurements to study in-depth chemical speciation inside a thin layered material.

Table 2.1: Parameters of Indus-2 electron storage ring.

SI. No.	Parameter	Value
1	Stored beam energy	2.5 GeV
2	Beam current	200 mA
3	Circumference	172.47 m
4	Critical wavelength	1.98 Å
5	Beam emittance (x, y)	: 5.8×10^{-8} mrad : 5.8×10^{-10} mrad
6	No. of operational beamline	: 13

2.2 Details of the source and beamline

2.2.1 Indus-2 source

Indus-2 is a 2.5 GeV, 200 mA third-generation synchrotron radiation source, with a critical wavelength of ~ 2 Å. It comprises of a double-bend-achromat lattice with zero dispersion function along the straight sections. This allows to get a low-emittance and high-brightness photon source size for the bending magnets. The estimated photon source size (FWHM) for the Indus-2 bending magnets is $\sim 120 \mu\text{m}$ (V) \times 546 mm (H) at 10 keV x-ray energy. Table 2.1 provides the various parameters of Indus-2 storage ring. Three different types of ports at 0° , 5° and 10° respectively have been provided at each bending magnet to take out synchrotron radiation into the beamlines. At present there

are 13 operational beamlines which are devoted for different applications including x-ray spectroscopy measurements. More details about Indus-2 SR facility and available experimental facilities at different beamlines can also be obtained online.

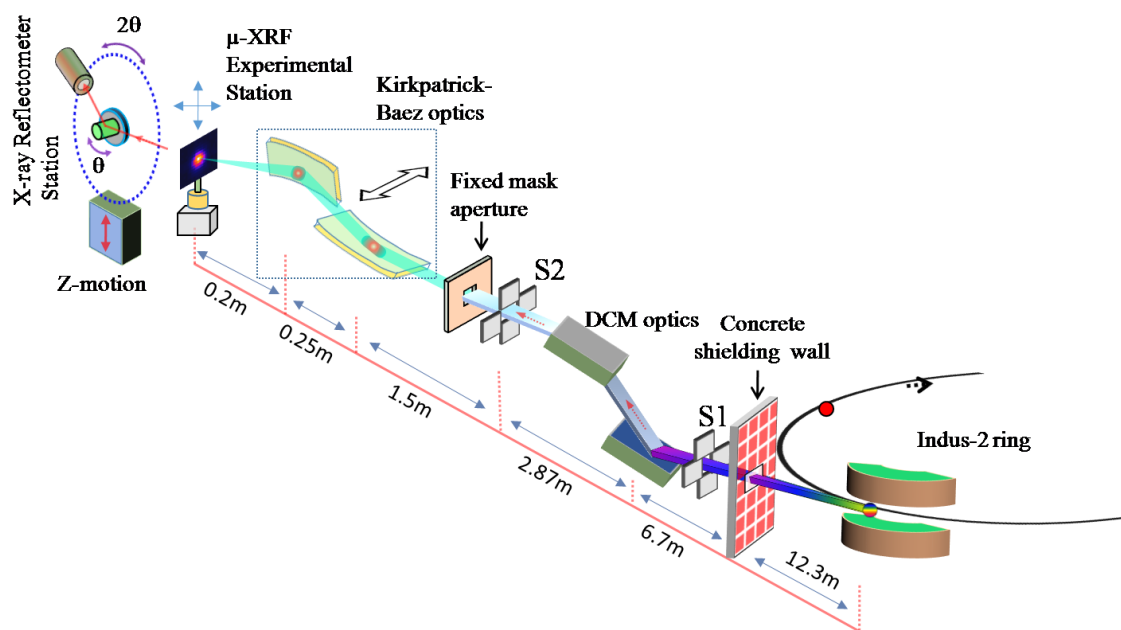


Figure 2.1: A schematic optical layout of the BL-16 beamline showing different components of the beamline.

2.2.2 Synchrotron based XRF: a microfocus XRF beamline of Indus-2 (BL-16)

Synchrotron based x-ray absorption and x-ray fluorescence measurements are shown to be very powerful analytical probes for the investigation of chemical environment of a material. These techniques can be applied with an equal ease to analyse bulk materials as well as samples that comprise of various elements in picograms or femtogram range. Modern third generation synchrotron source allows us a possibility to precisely investigate the distribution and concentration profile of different elements inside a sample simultaneously at sub-micrometer scale resolutions. A microfocus x-ray fluorescence spectroscopy beamline (BL-16) at the Indian synchrotron radiation facility

Table 2.2: Main parameters of BL-16 Beamline.

SI. No.	Parameter	Value
1	Source	Bending magnet
2	Working energy range	4-25 keV
3	Beam acceptance	0.2 mrad (V) \times 1.0 mrad (H)
4	Energy resolution	$\sim 10^{-3}$ - 10^{-4}
5	Beam spot size (at the sample position)	: ~ 4.3 mm (V) \times 7.5 mm (H) (Focused mode) : ~ 5 mm (V) \times 22 mm (H) (Collimated beam mode)
6	Photon flux (at 10 keV x-rays/100 mA ring current)	: Flux $\sim 3 \times 10^7$ photons s^{-1} (Focused mode) : Flux $\sim 2 \times 10^8$ photons $s^{-1} mm^{-2}$ (Collimated mode)
7	Experimental stations	: 4-axis sample manipulator (for TXRF and TXRF based XANES applications) : 5-axis sample manipulator (for micro XRF scanning applications) : Two circle (theta-2theta) Goniometer (for XSW, XRR, GIXRF and XSW assisted XAS applications)

Indus-2 has been constructed with an experimental emphasis on environmental, archaeological, biomedical and material science applications involving heavy metal speciation and their localization [46]. The BL-16 has been installed on the 5^o port of an Indus-2 bending magnet. Figure 2.1, illustrates a schematic optical layout of the BL-16 beamline. The beamline offers a combination of different analytical probes, *e.g.* x-ray fluorescence mapping, x-ray microspectroscopy and total-external-reflection fluorescence characterisation. BL-16 beamline has been designed to work in the x-ray energy range of 4 - 25 keV. Its main components are: a double crystal monochromator(DCM) and a Kirkpatrick-Baez (KB) focusing optics. In addition, there are several other components such as water cooled 4-blade slit (S1), an un-cooled 4-blade slit (S2), fluorescence screens etc. The combination of slits allows shaping of the x-ray beam dimensions as per the requirements of various experiments. The beamline radiation shielding hutch and the built-in personal safety interlock system allow safe

operation of the beamline. The beamline operates under high-vacuum conditions ($\sim 1 \times 10^{-6}$ mbar). The experimental station of the BL-16 beamline consists of a 4-axis sample manipulator for total reflection x-ray fluorescence (TXRF) analysis, 5-axis sample manipulator for microprobe XRF- scanning applications and a 2-circle goniometer for x-ray reflectivity and grazing incidence x-ray fluorescence measurements. A number of detectors (Ionization chamber, photodiode, Vortex spectroscopy detector and VHR x-ray CCD cameras) are also available on the beamline that makes it possible to record good quality data. The main parameters of BL-16 beamline are given in Table 2.2. In the subsequent section, the various key elements of the BL-16 beamline are described briefly.

Monochromator

A monochromator is an important optics of a synchrotron beamline. It provides a monochromatic x-ray beam (a beam of photons of single wavelength) from the white spectrum of incident synchrotron beam radiation. A double crystal monochromator (DCM) provides the monochromatic SR beam at fixed exit and therefore it eliminates the requirement to move the vertical position of an experimental station at different incident x-ray energies. BL-16 beamline uses a DCM system manufactured by FMB, Berlin, Germany. It contains a pair of symmetric and asymmetric Si (111) crystals. In BL-16 beamline the DCM is placed at ~ 19 m from the source. The first crystal of the DCM selects beam of x-ray with a particular wavelength corresponding to a Bragg angle θ_B . The second crystal is placed in downward looking direction and it also satisfies the same Bragg condition, which in turn allows to transmit the x-ray beam monochromatized by the first crystal. The purpose of the second crystal in the DCM is to ensure that the SR beam exits at a fixed height on to the experimental station. In BL-16 DCM flexibility has been provided to select either two pairs of symmetrical or asymmetrical Si (111) crystals. An asymmetry angle of 5° has been chosen for asymmetric Si (111) crystals.

The selection of asymmetric crystals provides ~ 1.5 to 2 times higher photon flux compared to symmetric Si (111) crystals.

Kirkpatrick-Baez (KB) optics

To investigate a two dimensional focussed beam of synchrotron x-rays a Kirkpatrick-Baez (KB) (Xradia, USA) optics has been installed on the vibration free table. The KB optics provides a stable two dimensional x-ray focal spot over the entire working energy range of BL-16 beamline. It comprises of a pair of Pt coated (25 nm) elliptical bendable mirrors of size ~ 30 mm (W) \times 200 mm (L). The mirrors have been mounted inside the KB vacuum chamber housing. The vacuum chamber of the KB system comprises of two beryllium windows of thickness ~ 75 μ m at the entrance and exit ends. The shape of the mirrors can be adjusted by the bender mechanism. The grazing incidence on the KB mirrors was set to be ~ 3.9 mrad to get a focused beam of maximum energy of 20 keV. The KB focusing optics of BL-16 beamline is placed at ~ 4.7 m upstream of the DCM. The KB optics of the BL-16 beamline provides a microfocus beam of dimension ~ 4.3 μ m (V) \times 7.5 μ m (H) for x-rays ranging from 5-20 keV.

2.3 Details of the XRR-GIXRF experimental station

The BL-16 x-ray reflectometer is also installed on a vibration free optics table before the Kirkpatrick-Baez focusing optics. Figure 2.2 depicts a photograph of the BL-16 x-ray reflectometer station. The reflectometer station has been equipped with several motion stages to facilitate different modes of XRR and GIXRF investigations. The BL-16 XRR station comprises of a 2-circle goniometer mounted on solid base. It is equipped with incident and detector arms. On the incident arm of the goniometer, an additional slit S3 is placed followed by a miniature ionization chamber (micro-IC) to monitor incident beam photon flux variations. Slit S3 allows adjustable vertical openings for the incoming

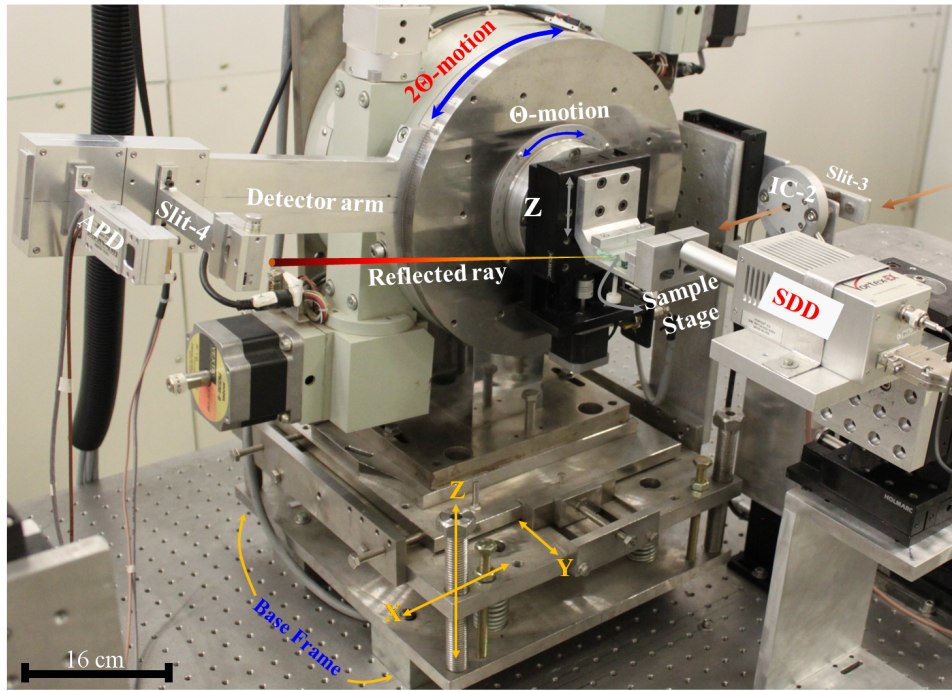


Figure 2.2: Annotated photograph of the developed x-ray reflectometer station at BL-16 beamline.

x-rays. The sample holder of the x-ray reflectometer station has been provided vertical motion with a minimum translation step size of $\sim 5 \mu\text{m}$ in order to facilitate precise alignment of the sample with respect to the incident x-ray beam path. The angular resolution of the BL-16 reflectometer station is $\sim 0.002^\circ$. The detector arm of the reflectometer station consists of an Avalanche Photo Diode (APD) detector followed by a slit S4 to monitor specularly reflected x-rays from a sample. The APD detector was placed at $\sim 350 \text{ mm}$ away from the sample rotation axis. The low noise and high dynamic range of the APD detector allow one to measure XRR pattern with a dynamic range up to ~ 7 orders. For the XRR and GIXRF measurements, it is possible to select different x-ray energies monochromatized from a Si (111) double crystal monochromator of the BL-16 beamline. To measure grazing angle dependent x-ray fluorescence emission from a thin film structure, a vortex spectroscopy detector (SDD) comprising an active surface area of 50 mm^2 and an energy resolution of $\sim 140 \text{ eV}$ at 5.9 keV (Mn- $K\alpha$ x-rays) was installed on the BL-16 x-ray reflectometer station. The SDD detector was placed in the plane of sample substrate (*i.e.*, in the plane of s-polarized

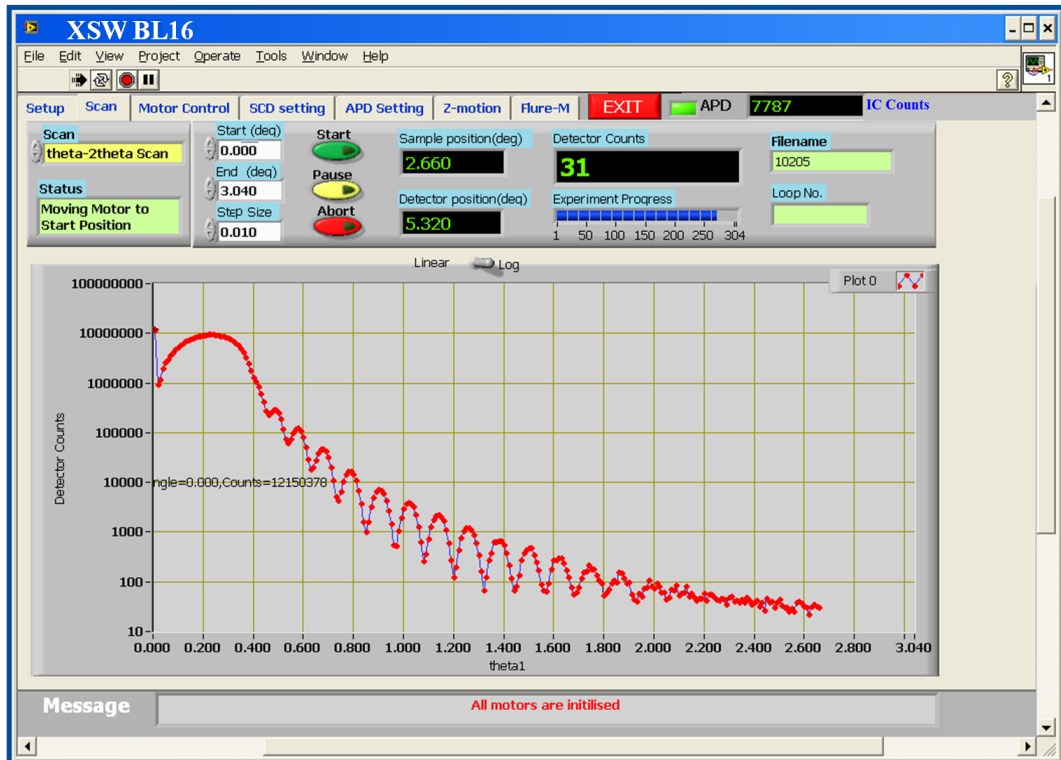


Figure 2.3: A snapshot of the “XSWBL16” control software of the BL16 beamline, showing different windows for remote data acquisition and alignment of the x-ray reflectometer station.

electric vector of the synchrotron beam) in order to obtain better signal to noise ratio for the emitted fluorescent x-rays [47]. Fluorescence x-rays were measured through a 1-mm Al pinhole collimator to maintain a constant solid angle of the SDD detector on the sample surface at various incidence angles [48]. The SDD was placed at ~ 25 mm distance from the sample. A computer software “XSWBL16” was developed for remote data acquisition and control of the BL-16 reflectometer station. Figure 2.3 shows a snapshot of the control software of BL-16 reflectometer station. “XSWBL16” software allows simultaneous measurements of the XRR and GIXRF profiles for a nanostructured material.

2.4 Thin film Deposition system: Magnetron sputtering

Thin film structures consisting of W and B₄C materials were deposited on the polished Si(100) substrate at room temperature using a DC magnetron sputtering system (Fig. 2.4). The deposition system consists of two parts; the main processing chamber and load-lock chamber. It is possible to load a Si substrate in the loadlock chamber and then it can be transferred in to the main deposition chamber through a mechanical rail platform. Pressures in main and load lock chambers were maintain to be $\sim 1 \times 10^{-8}$ and



Figure 2.4: A picture of DC magnetron sputtering system, utilized for the deposition of different single and multilayer thin film structure.

8×10^{-8} mbar, respectively. Two rectangular magnetron cathodes having a dimension of 500 mm (L) \times 100 mm (W) have been provided in the deposition system. Different types of masking arrangements were also installed in the deposition system to control the spatial variation of deposition rate of different targets. All the safety and interlock features in the deposition system were provided through a programmable logic controller. The power supplied to the W and B₄C target are 158 and 700 watts

respectively. W and B₄C based thin film samples were deposited using argon, as a sputtering gas medium at constant pressure of $\sim 5 \times 10^{-3}$ mbar, whereas the base vacuum of the chamber was maintained to be $\sim 2 \times 10^{-8}$ mbar before start of the deposition process. During the fabrication of W-B₄C multilayer structures, the deposition rates were kept constant for different targets (W ~ 4 Å/s and B₄C ~ 4.2 Å/min respectively, at a working pressure of 5×10^{-3} mbar). Several synthetic test thin film samples have been also prepared prior to optimizing various deposition parameters (*such as* gas flow rate, pressure, power, target-substrate distance and substrate velocity etc.) to obtain good quality thin film structures. The details of the deposition system are given elsewhere [49, 50]. Before deposition, the r.m.s. roughness of the Si substrate was examined by laboratory based x-ray reflectivity measurements using BRUKER D-8 x-ray reflectometer system at Cu-K α wavelength ($\lambda = 1.54$ Å). The average roughness for a polished Si substrate was found to be $\sim 5 \pm 1$ Å.

2.5 Photon Flux Measurements at BL-16

Photon flux available at the experimental station for the sample excitation, is an important characteristic parameter of a SR beamline. Monochromatic photon flux available at the XRR experimental station of BL-16 beamline was measured by using a calibrated silicon photodiode. An Mo aperture of ~ 1 mm \times 1 mm was placed in front of the photodiode. The photodiode current generated at a given incident photon energy was converted to photon flux (per mm²) using the responsivity curve of the photon diode. Based on the dispersion relation in vacuum $f\lambda = C$ or $\omega = kC$, where C is the velocity of light in vacuum and, the product of photon energy $\hbar\omega$ and wavelength λ is given by $\hbar\omega \times \lambda = 1239.842$ eV nm. The number of photons required for one joule of energy, with wavelength given in nanometers (nm), is 1 joule $\implies 5.034 \times 10^{15} \lambda(\text{nm})$ photons and 1 watt $\implies 5.034 \times 10^{15} \lambda(\text{nm})(\text{photons}/\text{second})$. Power of one watt corresponds to a photon flux of 5.034×10^{15} photons/s, each photon having an energy $E \cong 1240$ eV. So

energy of one photon = $1.987 \times 10^{-16} / \lambda(\text{nm})$ watt. The photon flux can be expressed as

$$\text{Photon flux} = \frac{\text{Photo current in A/responsivity (A/W)}}{\text{Energy of a single photon (W)}}$$

Table 2.3 gives the values of the photon flux at the BL-16 XRR experimental station at different incident photon energies at Indus-2 operation of 100 mA ring current. Responsivity of the photodiode and observed photodiode current (nA) at different incident x-rays are also shown in Table 2.3. Figure 2.5 depicts the measured photon flux at the BL-16 beamline as a function of incident photon energy.

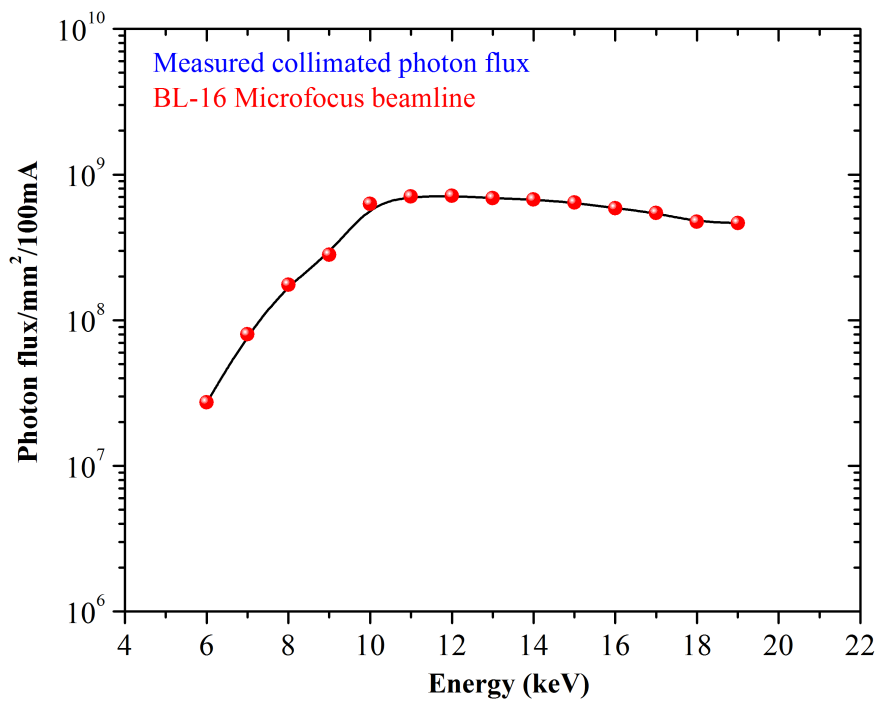


Figure 2.5: Variation of photon flux with energy at BL-16 beamline of Indus-2 SR facility.

2.6 Various x-ray spectroscopy probes at BL-16 beamline

The BL-16 beamline offers different modes of operation for the x-ray fluorescence and scattering measurements. In the subsequent sections, salient features of various

Table 2.3: The measured photon flux at 100 mA ring current at BL-16 beamline.

Energy (keV)	Responsivity (A/W)	Photodiode current (nA)	Photon flux per 100 mA ring current
6	0.17027	2.7185	2.72E+07
7	0.20188	10.919	8.00E+07
8	0.2201	34.42	1.76E+08
9	0.23287	64.92	2.82E+08
10	0.23712	156.99	6.29E+08
11	0.22998	186.49	7.06E+08
12	0.22599	200.99	7.14E+08
13	0.21418	197.99	6.91E+08
14	0.19821	190.99	6.72E+08
15	0.1793	175.49	6.41E+08
16	0.1637	155.99	5.88E+08
17	0.14344	133.99	5.46E+08
18	0.13683	116.99	4.74E+08
19	0.11245	98.99	4.66E+08

experimental stations available at the BL-16 are briefly described.

2.6.1 XRF and TXRF

A 4-axis sample manipulator system has been installed on the vibration-free optics table of BL-16 beamline for XRF and TXRF analysis of various types of samples [29, 43, 51, 52]. The detection sensitivity of the BL-16 beamline XRF experimental station ranges from a few $\sim \mu\text{g/g}$ (ppm) to sub ppm levels for a wide range of elements with atomic numbers (Z) ranging from 14 (Si) to 92 (U). On the other hand detection sensitivities of BL-16 TXRF station were found to be in the range ~ 2 ppb to 156 ppb for elements of atomic number Z ranging from 19 to 33 [47, 53]. Nevertheless, since the fluorescence efficiency of an element strongly depends on the excitation energy E_0 ; hence, by properly selecting the excitation energy close to the absorption edge of an element and optimizing the detector-to-sample distance down to ~ 15 mm, detection sensitivity can be improved further down to sub ppb level for some of the high Z

elements. In TXRF geometry, it is possible to mount a fluorescence detector either in the plane of the synchrotron radiation beam or perpendicular ($\sim 90^\circ$) to the substrate surface. In addition various state of the art instrumentations available at BL-16 beamline allows one to perform novel measurements, such as study of trace elements in biological specimen as well as elements that are embedded inside a solid surface.

2.6.2 μ -XRF and Microfluorescence mapping

BL-16 beamline also includes a third experimental station that allows one to perform elemental mapping in multi-element samples using a microfocused x-ray beam generated from a KB mirror optics. In the μ -XRF measurements, a specimen is scanned through a microfocused x-ray beam and fluorescence radiation emitted is recorded as a function of sample movements. Micro-XRF measurements allow one to visualize compositional variation and spatial distribution of different elements in a sample. The BL-16 beamline has already been used for variety of micro-XRF applications for the study of distribution of elements in uranium (U), thorium (Th) compounds and trace elements distribution in biological samples [44, 45].

2.7 Analysis of thin layered materials by using simultaneous XRR and GIXRF measurements

An x-ray reflectometer station is also installed at the BL-16 beamline for the simultaneous characterisation of nanostructured materials. The details of the BL-16 reflectometer are described in section 2.3. The performance of the BL-16 x-ray reflectometer station was evaluated thoroughly by performing combined XRR and GIXRF measurements on several thin film and multilayer structures comprising of different surface interface properties. Figure 2.6(a) shows the measured grazing

incidence angle dependent XRR profile along with fitted profile for a W thin film layer structure, deposited on a Si substrate surface at the incident x-ray energy of 10.0 keV. It can be seen from Fig. 2.6(a), that the periodic Kiessig interference oscillations in the measured XRR profile appear up to the large grazing incidence angle of $\sim 4.0^\circ$. The location and amplitude of these oscillations match quite well with the computed XRR profile. The Kiessig interference oscillations in the XRR profile appear as a result of a fixed path difference encountered by the incident and reflected x-ray beams and their period is closely related with the thickness of the thin film medium. The best fit XRR curve to the experimental data was obtained assuming a three layer model comprising of a native oxide layer on top of Si substrate surface (between W-layer and Si substrate), a bare W-layer and a low density C-layer on top of the W layer (see the inset of Fig. 2.6(a)). The computations were performed using the CATGIXRF program [34]. The reflectivity data have been analysed by using Parratt formalism [54] and the effect of surface roughness has been taken into account using Novet-Croce model [55]. The details about the CATGIXRF program and the internal physical mechanism is described in Chapter 4. The best fit XRR curve to the experimental data yields a thickness of the bare W-layer $\sim 116.7 \pm 3.0 \text{ \AA}$, roughness and mass density to be $\sim 4.8 \text{ \AA}$ and 17.3 g/cm^3 respectively. The electron density profile of the W thin film structure derived from the best fit structural parameters is depicted in the inset of Fig. 2.6(a). In this EDP profile, the depth $z=0$ is defined as the top surface of the thin film medium (air-Carbon interface).

To evaluate the reliability and reproducibility of determined microstructural parameters of the W thin film medium we have performed x-ray standing wave (XSW) induced x-ray fluorescence and XRR measurements simultaneously at incident x-ray energy of 12.0 keV. The measurements are presented in Fig. 2.6(b) wherein, the normalized W- $L\alpha$ fluorescence yield emitted from the W layer is plotted as a function of incidence angle θ along with the measured XRR data. For the GIXRF measurements, W- $L\alpha$ fluorescence counts were collected for an data acquisition live time of 3 s at each

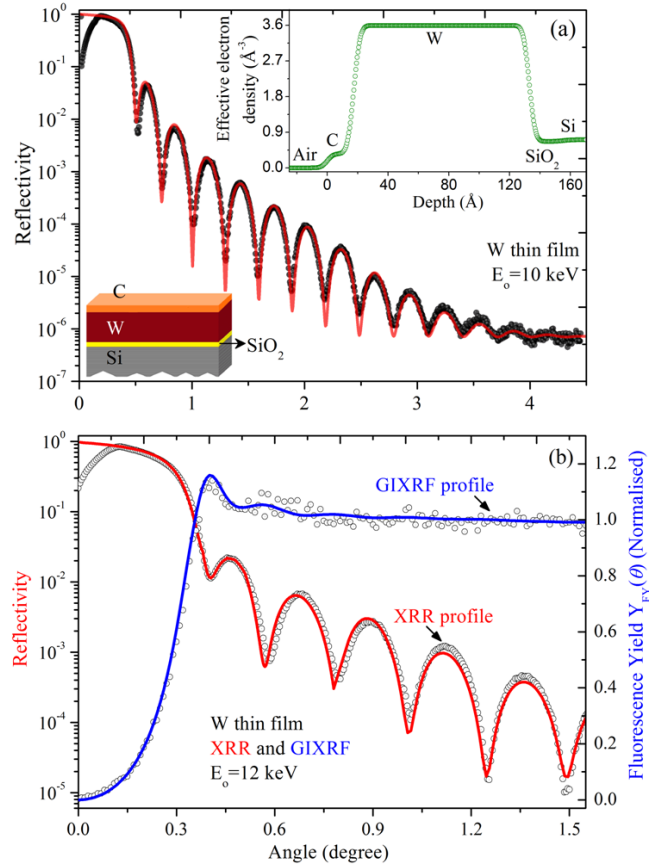


Figure 2.6: (a) Measured and fitted XRR profile of a W thin film structure measured at 10.0 keV incident x-ray energy. In the inset of the figure, the effective electron density profile of the three layer medium is shown, calculated from the best fit results of XRR and W- $L\alpha$ fluorescence measurements. A Schematic diagram of the W thin film on a Si substrate is delineated in the inset of figure. (b) Measured and fitted XRR and XSW induced W- $L\alpha$ fluorescence profiles of the W layer at 12.0 keV x-ray energy. The scattered points show the experimental data while the solid lines are the best fits to the measured profiles. The fluorescence yield of W- $L\alpha$ has been normalized at an incidence angle $\theta=1.2^\circ$.

angular position of the W thin film sample. The net W- $L\alpha$ fluorescence peak intensity was then derived using non linear least square fitting of a Gaussian profile, after subtracting linear background from the W- $L\alpha$ peak. From the Fig. 2.6(b), it can be observed that the periodic Kiessig interference fringes in the XRR and GIXRF profiles are anticorrelated in nature. The W- $L\alpha$ fluorescence intensity is minimum at very small incidence angles and it starts increasing rapidly as the incidence angle crosses the critical angle $\theta_c=0.26^\circ$ of the W film medium. Above θ_c ($\sim 0.26^\circ$), fluorescence intensity reaches to a maximum value (~ 1.2) due to the formation of XSW field inside the thin

Table 2.4: Best fitted microstructural parameters of the W thin film obtained using XRR and GIXRF measurements.

Incident x-ray energy	Layer Material	Density (g/cm ³)	Thickness (Å)	Roughness (Å)	chi ²
10 keV (XRR measurements only)	C	1.1±0.1	17.5±0.4	3.2±0.2	0.82
	W	17.3±0.6	116.7±3.0	4.8±0.2	
	SiO ₂	2.2±0.1	22.3 ±3.0	3.2 ±0.2	
12 keV (XRR and XSW measurements)	C	1.1±0.1	16.5 ±0.2	3.2±0.2	0.11
	W	17.3±0.5	115.5±1.8	4.6±0.2	
	SiO ₂	2.2±0.1	21.6±2.0	3.2 ±0.2	

film medium. At higher incidence angles, the W-L α fluorescence intensity more or less remains constant, because the W material is excited only with the direct x-ray beam. For fitting of the XSW induced W-L α fluorescence and XRR profiles we have taken microstructural parameters of the W layer medium, determined from the XRR measurements at 10.0 keV as an initial guess. The thickness, roughness and density of the individual layers in the three layer model were then varied systematically to obtain best fit results for the measured XRR and W-L α fluorescence profiles simultaneously. The fitted microstructural parameters of the W thin film sample at two different x-ray energies are summarized in Table 2.4. It may be noted here that the two profiles (XRR and W-L α fluorescence) are quite sensitive to the structural parameter of the W thin film medium. The combined XRR and GIXRF analysis allows us to reduce the uncertainties in the individual fitting procedures and offers more precise microstructural parameters of a thin film medium. The combined fitting of the measured XRR and GIXRF profiles was performed using the CATGIXRF program. An encouraging level agreement obtained between measured and fitted profiles gives us a confidence about the accuracy of the determined microstructural parameters of the W thin film medium.

In the next section, the microstructural characterisation of a thin TiO₂ layer grown using

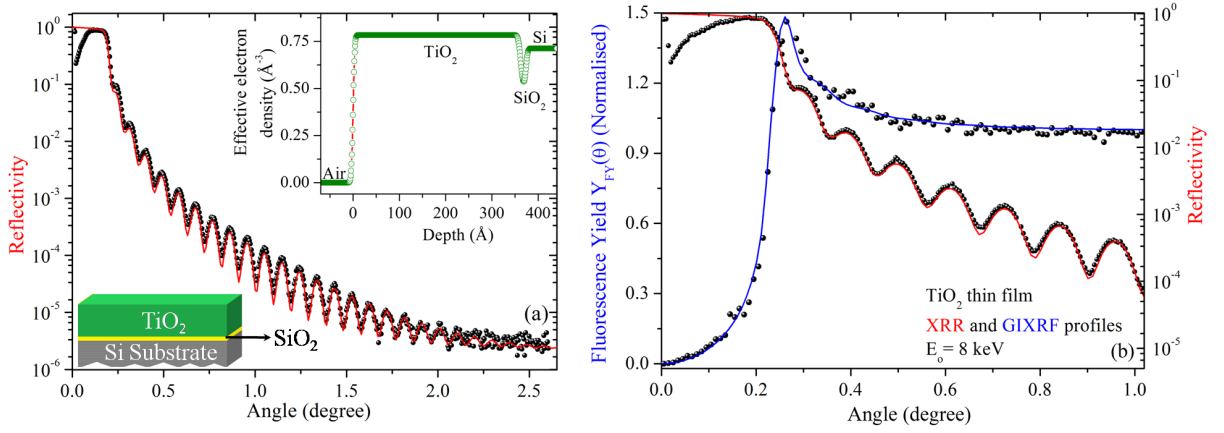


Figure 2.7: (a) Measure and fitted XRR profiles of a TiO_2 thin film medium at 10.0 keV incident x-ray energy. The inset of figure (a) shows the effective electron density distribution of TiO_2 thin film medium on top of a Si substrate. (b) Measured and fitted XSW induced $\text{Ti-K}\alpha$ fluorescence and XRR profiles of the TiO_2 structure at 8.0 keV x-ray energy. The scattered points are the experimental data while the solid lines represent the best fit curves to the measured data. The $\text{Ti-K}\alpha$ fluorescence yield has been normalized at an incidence angle $\theta \sim 1.0^\circ$.

Table 2.5: Best fitted microstructural parameters of the TiO_2 thin film obtained using XRR and GIXRF measurements.

Energy	Layer Material	Density (g/cm^3)	Thickness (\AA)	Roughness (\AA)	χ^2
10.0 keV	TiO_2	2.71 ± 0.2	356 ± 7.0	3.4 ± 0.2	0.73
XRR	SiO_2	1.6 ± 0.1	22.0 ± 3.0	4.8 ± 0.2	
8.0 keV	TiO_2	2.71 ± 0.15	362.0 ± 4.0	3.0 ± 0.2	0.12
XRR and XSW	SiO_2	1.7 ± 0.1	21.0 ± 2.0	4.0 ± 0.2	

atomic layer deposition (ALD) technique is discussed. Figure 2.7(a) shows the measured and fitted XRR profiles of the TiO₂ thin film medium deposited on a Si(100) substrate at incident x-ray energy of 10.0 keV. From this figure, one can clearly distinguish various periodic Kiessig oscillations up to an incidence angle of $\theta \sim 2.2^\circ$. The experimental XRR profile has been fitted by considering a two layers model comprising of a TiO₂ layer and a native oxide layer of Si (i.e. SiO₂) on top of the Si substrate surface (refer to the inset of Fig. 2.7(a)). Table 2.5 describes the determined microstructural parameters of TiO₂ thin film medium obtained from the best fitted XRR results at 10.0 keV energy. To verify the reproducibility of the determined microstructural parameters, we have carried out simultaneous XRR and x-ray standing wave (XSW) induced XRF measurements near the K-absorption edge of Ti. The measured and fitted XRR and normalized Ti-K α fluorescence profiles of the TiO₂ thin film medium are plotted in Fig. 2.7(b). The computations were carried out using the CATGIXRF program and the best fitted microstructural parameters are summarized in Table 2.5. The effective electron density profile calculated from the best fitted results is given in the inset of Fig. 2.7(a).

In the proceeding an example of structural analysis of a bit complicated thin film medium is described. Figure 2.8(a) demonstrates the XRR measurements for a periodic W-B₄C multilayer structure obtained using a commercial BRUKER D-8 x-ray reflectometer station at Cu-K α wavelength ($\lambda = 1.54 \text{ \AA}$). It can be seen from the Fig. 2.8(a) that the periodic Kiessig oscillations and Bragg peaks up to 4th diffraction orders are clearly visible, which suggests a uniform and distinct formation of the bilayer period boundaries in the multilayer stack. The best fitted XRR results yield a bilayer period thickness of the W-B₄C multilayer $d \sim 46.9 \text{ \AA}$. The thickness and roughness of the individual W and B₄C layers are summarized in Table 2.6.

The same periodic multilayer structure was further analyzed using the BL-16 x-ray reflectometer station, at incident x-ray of energy of 10 keV. The measurements are depicted in Fig. 2.8(b). From the measured XRR profile one can clearly observed various Bragg peaks up to the 5th diffraction orders. In the inset of Fig. 2.8(b) we have

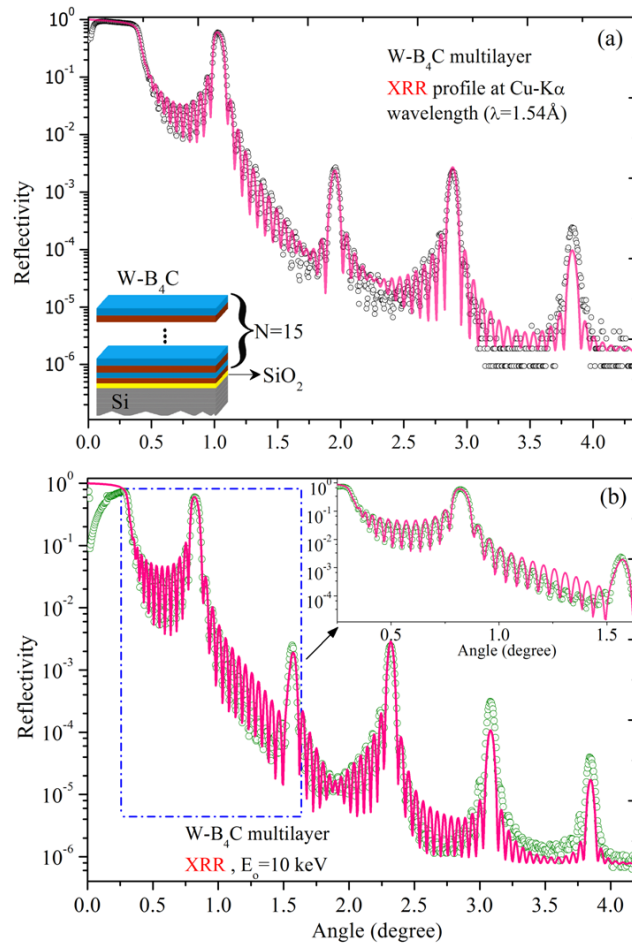


Figure 2.8: (a) Measured x-ray reflectivity profile of the W-B₄C multilayer structure using a laboratory reflectometer (BRUKER D-8 system) at Cu-K α wavelength ($\lambda = 1.54 \text{ \AA}$). The multilayer structure consists of $N = 15$ bilayers of the W and B₄C layers deposited on Si (100) substrate, as shown schematically in the inset of the figure. (b) Measured XRR profile of the same W-B₄C multilayer structure using BL-16 reflectometer station at incident x-ray energy of 10.0 keV. The scattered points indicate the experimental data while the solid lines show the best fit curves for the measured data.

shown an extended view of the reflectivity pattern in the vicinity of first and second Bragg peaks. The measured reflectivity profile was fitted using CATGIXRF program by considering determined structural parameters from the laboratory source data as initial guess. It can be seen that measured reflectivity pattern obtained using synchrotron x-rays matches quite well with the fitted profile in the θ range of 0 to 4 $^\circ$ except a small deviation at higher θ values. This deviation attributes to the nonlinear diffuse scattered background produced from the thin film sample due to presence of high energy orders contamination from beamline double crystal monochromator optics. The best fit XRR profile yields

multilayer period thickness $d = 46.3 \text{ \AA}$ ($d_W=23.7 \text{ \AA} + d_{B_4C} = 22.6 \text{ \AA}$). The roughness values of the W and B_4C layers were found to be $\sim 4.8 \text{ \AA}$ and 3.2 \AA respectively. Determined microstructural parameters of the W- B_4C multilayer structure are given in Table 2.6. By comparing tabulated results it can be clearly seen that the structural parameters obtained from synchrotron reflectivity measurements match reasonably well to the parameters evaluated from a commercial laboratory instrument.

To further validate determined microstructural parameters of the W- B_4C multilayer,

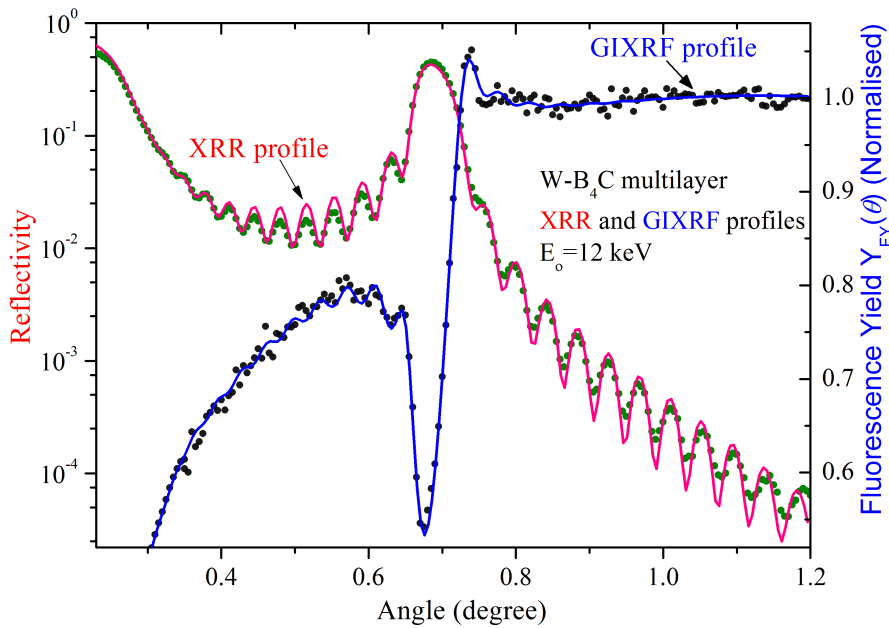


Figure 2.9: XSW induced W- $L\alpha$ fluorescence and XRR profiles measured for the W- B_4C multilayer structure at incident x-ray energy of 12.0 keV. The scattered points shows the experimental data while the solid lines are the best fits to the measured profiles. The W- $L\alpha$ fluorescence yield has been normalized at an incidence angle $\theta=1.2^\circ$.

we have performed combined XRR and XSW induced fluorescence measurements at 12.0 keV x-ray incident energy. In Fig. 2.9, normalized W- $L\alpha$ fluorescence yield and XRR profiles in the vicinity of the 1st Bragg order were plotted. It can be seen that the W- $L\alpha$ fluorescence intensity shows a strong XSW induced modulation across the Bragg region. One can also observe the characteristics Kiessig oscillations at low and high angle side of the Bragg peak. These Kiessig oscillations are anticorrelated with Kiessig oscillations of the reflectivity profile. While fitting the XRR and W- $L\alpha$ fluorescence

profiles at 12.0 keV x-ray energy we considered best fit results obtained from XRR measurements at 10.0 keV, as the initial guess. The fitting was carried out in an iterative way using the CATGIXRF program. During the fitting, we allowed to vary thickness, roughness and density of individual high Z and low Z layers until one gets best fit curves to the experimental data. The results obtained from the combined XRR and GIXRF analysis are summarized in the Table 2.6. It can be seen from Table 2.6, that the determined microstructural parameters roughly agree in all three cases within observed experimental error values. The error values in the parameters estimation were derived from the measurement accuracy, which comprises the statistical fluctuations in the W-L α fluorescence and XRR counts as well as repeatability of a measurement. The quality of fits in the combined XRR and GIXRF analysis gives us a confidence about accuracy of the determined microstructural parameters of the W-B₄C multilayer structure.

Table 2.6: Best fitted microstructural parameters of the W-B₄C multilayer obtained using laboratory and synchrotron based XRR and GIXRF measurements.

Incident x-ray energy	Layer Material	Density (g/cm ³)	Thickness (Å)	Roughness (Å)	chi ²
8.047 keV (Cu-K α) (XRR measurements only)	B ₄ C	2.1±0.1	22.7±0.7	3.2±0.5	0.75
	W	17.3±0.7	24.2±0.7	4.8±0.5	
	SiO ₂	2.2±0.1	25 ±3.5	3.2 ±0.5	
10.0 keV (XRR measurements only)	B ₄ C	2.1±0.1	22.6±0.5	3.2±0.2	1.5
	W	17.3±0.6	23.7±0.5	4.8±0.2	
	SiO ₂	2.2±0.1	25 ±3.0	3.2 ±0.2	
12.0 keV (XRR and XSW measurements)	B ₄ C	2.1±0.1	22.3 ±0.3	3.2±0.2	0.13
	W	17.3±0.5	23.5±0.3	4.6±0.2	
	SiO ₂	2.2±0.1	22±2.0	3.2 ±0.2	

2.8 Summary

The different key experimental stations that are available at the BL-16 beamline for the material characterisation are presented in this chapter. The BL-16 beamline offers various re-configurable operation modes for normal XRF, TXRF and μ -XRF measurements. This allows one to perform a wide range of experiments for the presence of trace elements and their distribution inside a specimen. A grazing incidence x-ray reflectometer station has also been designed and installed on the BL-16 microfocus beamline of Indus-2 synchrotron facility for surface-interface investigation of nanostructured materials. The reflectometer offers combined as well as individual measurement modes for specular x-ray reflectivity and grazing incidence x-ray fluorescence analysis of thin nanostructured materials. The performance of the BL-16 reflectometer has been evaluated by analysing some real thin layered (W film, TiO₂ film and W-B₄C periodic multilayer structures) materials. The results obtained evince a good accuracy and agreement with the standard lab source data. The BL-16 reflectometer provides an attractive platform for a variety of research activities especially in the fields of surface condensed matter physics applications and characterisation of nanoscale thin layered materials.

Chapter 3

Effect of Synchrotron Polarization on grazing incidence excited fluorescence emission

In this chapter, the effect of synchrotron beam polarization in total external reflection x-ray fluorescence (TXRF) analysis has been investigated. The effect of anisotropic Compton and elastic scattered x-rays on spectral background and detection sensitivities has been demonstrated. Theoretical computations have been performed to study the role of the Compton and elastic scattered radiation on the spectral background of a fluorescence spectrum. The numerical calculations explain how scattering probability densities of the Compton and elastic scattering radiations depend on the scattering angle (θ) and azimuthal angle (ϕ) in the polarization plane of the synchrotron radiation beam. The computation results closely corroborate with the experimental TXRF measurements carried out using standard reference samples. The results further reveal that one can achieve approximately one order of magnitude enhancement in the spectral signal strength of synchrotron radiation (SR) based TXRF technique by utilizing anisotropic nature of the scattered synchrotron radiation in the horizontal detection geometry ($\theta = \pi/2, \phi = 0$).

3.1 Introduction

Understanding the nature of x-ray scattering and its influence on the XRF detection sensitivities in case of plane polarized x-ray beam provide an opportunity to improve the elemental sensitivities of the technique. Despite the emergence of new technologies and high brilliance synchrotron radiation sources, the requirements of high detection sensitivities of various elements is a crucial prerequisite in many technological applications *viz.* magnetic thin layered materials, semiconductors and integrated circuit technologies etc, where process control and physical failure analysis are mostly dominated by elemental impurity infiltration [29, 56]. In conventional XRF technique, the element detection sensitivities are largely limited to the $\mu\text{g/g}$ (ppm) range due to large spectral background produced by the Compton scattered x-rays from the specimen. TXRF spectroscopy is another variant of the energy dispersive-XRF (EDXRF) technique, which has seen a remarkable progress over the past few years. Numerous applications in basic and applied sciences prove its importance. In this technique the complexity of the large spectral background gets eliminated to a great extent owing to the high reflectivity of the flat surface and low penetration depth of the primary x-ray beam in the substrate material, on which the incident x-rays are allowed to impinge at glancing incidence angles. So, in the total external reflection region the sample surface is excited by the evanescent wave. The extinction depth of the x-ray beam at this condition is around $\sim 2\text{-}5$ nm for most of the substrate materials. These characteristics of the TXRF technique significantly eliminate the matrix effects and the complexity of large spectral background of the fluorescence process. All the above mentioned features improve the detection sensitivities of TXRF to $\sim 2\text{-}3$ orders of magnitude or better compared to the conventional XRF, typically in the range of parts per billion (ppb) levels for most of the elements [52, 53]. Another approach to reduce the spectral background in x-ray fluorescence measurements is to utilize linearly polarized primary radiation for excitation [29, 57]. Based on the classical dipole oscillator approach, it is well

understood that the emission profile of scattered radiation is anisotropic in nature in case of a polarized x-ray beam. For synchrotron x-rays, the azimuthal anisotropy of the scattered photon imposes an important constraint for the excitation and detection geometry of the XRF experimental set-up. Maximal signal to noise ratio can be realized if fluorescence signal is measured in a position, where the contribution of anisotropic scattered radiation is minimal [51, 58–62].

In literature, several attempts have been made earlier that report significant reduction of the spectral background and hence improved detection sensitivities of the XRF technique. Embong *et al.* [63] have reported sub-ppm level detection sensitivities using three-dimensional polarization dependent excitation geometry for the multielement sediment samples by means of varying experimental parameters like excitation geometry, x-ray energy, secondary targets, operating voltage and current of the x-ray tube source, and thickness of the filters installed in the XRF spectrometer. Spolnik *et al.* [64] highlighted that the use of three-dimensional polarizing optical geometry in combination with secondary targets is highly beneficial to reduce the scattered background and they achieved nearly one order of magnitude improved detection sensitivities as compared to that of the conventional EDXRF measurements. It may be mentioned here that a small molecule in solution is excited by polarized x-ray, then it emits partially polarized fluorescence light. This polarized fluorescence x-ray is then used as a tool to find the structural binding, orientation or motion of a small molecule or protein.

In this chapter, we have described the effect of the linear polarization of the SR radiation in the grazing incidence x-ray fluorescence analysis. It has been shown that the Compton and elastic scattering probability densities strongly depend on the scattering angle (θ) and the azimuthal angle (ϕ) in the plane of synchrotron polarization. The analytical treatment described in this chapter considered the effect of incident x-ray energy as well as the spatial distribution of the scattered x-ray photons. The results show that the Compton and elastic scattered x-rays have an optimal intensity contrasts for

some particular positions of θ and ϕ because of the anisotropic emission characteristics of the scattered radiation. Interestingly, the azimuthal anisotropy of the scattered photon is shown to have a vital role on the improvement of the x-ray fluorescence detection sensitivities. The effect of SR beam polarization on spectral background is demonstrated by carrying out TXRF measurements on standard reference materials as well as using a few TXRF methodological samples. The results reveal that one obtains approximately one order of magnitude enhancement in the spectral signal strength, if the spectroscopy detector is placed in the plane of polarization of synchrotron beam ($\theta = \pi/2$ and $\phi = 0$) in contrast to the conventional mounting geometry ($\theta = \pi/2$ and $\phi = \pi/2$).

3.2 Physical background on the scattering density profile

The number density of scattered photons in a well defined solid angle strongly depends on the plane of polarization of the incident x-ray beam. However, if the excitation radiation is unpolarized in nature then the isotropic behaviour of the scattered radiation allows us to choose detector collimator geometry randomly. Figure 3.1 illustrates a typical geometrical configuration used in the x-ray fluorescence measurements. For the convenience the propagation of x-ray beam is considered along the z-axis and the electric field vibrations are constrained parallel to the x-axis (*i.e.*, s-polarized synchrotron beam). The scattering angle (θ) and azimuthal angle (ϕ) are measured from the z-axis and from the plane of vibrations of electric field respectively. The differential Compton scattering cross section can be readily obtained from the Klein Nishina formula [65]. The theory of Compton and elastic scattering cross sections for polarized x-rays including the effect of the detector aperture has already been investigated in detail by A. L. Hanson [66, 67]. In case of the linearly polarized x-ray beam of energy E, the differential Compton and elastic scattering cross sections can be expressed as function of polar angle θ and

azimuthal angle ϕ , from a scattering centre (i.e. atom of atomic number Z)

$$\frac{d}{d\Omega}\sigma_{Comp}(\theta, \phi, E) = \frac{r_e^2}{2}\gamma^2\left(\gamma + \frac{1}{\gamma} - 2S \sin^2\theta \cos^2\phi\right)S(X, Z) \quad (3.1)$$

and

$$\frac{d}{d\Omega}\sigma_{elas}(\theta, \phi, E) = r_e^2(1 - S \sin^2\theta \cos^2\phi)F^2(X, Z) \quad (3.2)$$

where, $S(X, Z)$ is the incoherent scattering factor, $F(X, Z)$ is the atomic form factor, X is defined as $S \sin(\theta/2) \times (E/1.239852 \text{ keV nm})$, r_e represents the classical electron radius, and the dimensionless quantity γ can be defined as

$$\gamma = \left(1 + \frac{\Delta\lambda_{Comp}}{\lambda}\right)^{-1} \quad (3.3)$$

Here, $\Delta\lambda_{Comp}$ describes the wavelength shift in the Compton scattering process and λ is the wavelength of the incident x-ray beam. The scattering probability density for a photon of

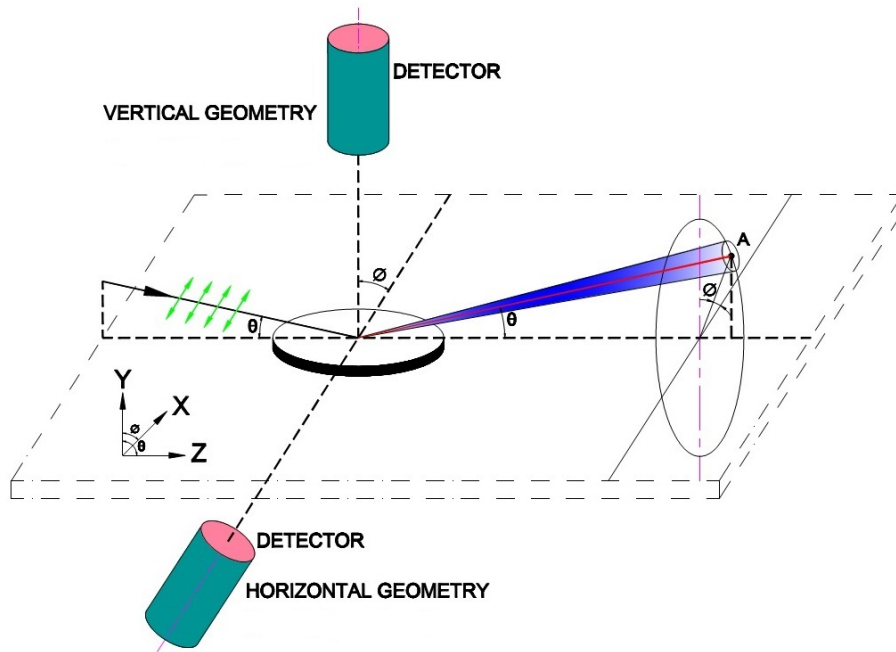


Figure 3.1: Experimental geometry used for the angle dependent XRF measurements. The spectroscopy detector is placed in the vertical geometry (i.e., $\theta = \pi/2$ and $\phi = \pi/2$) as well as in the horizontal geometry (i.e., $\theta = \pi/2$ and $\phi = 0$) to collect the XRF spectra.

energy E , which scatters within the finite polar angle domain of ϕ and $\phi+d\phi$, at a specific scattering angle θ , can be expressed as

$$f(\theta, \phi, E) = \frac{1}{\sigma(\theta, \phi, E)} \frac{d}{d\Omega} \sigma(\theta, \phi, E) = \frac{d}{d\Omega} \sigma(\theta, \phi, E) \left[\int_0^{2\pi} \frac{d}{d\Omega} \sigma(\theta, \phi, E) d\phi \right]^{-1} \quad (3.4)$$

To estimate the Compton and elastic scattering density profiles it is required to substitute the differential scattering cross-sections [68, 69] in eqn. (3.4). This substitution allows one to arrive at a relation

$$f(\theta, \phi, E) = \frac{1}{2\pi} \left[1 - \frac{S \sin^2 \theta}{G(\theta)} \cos 2\phi \right] \quad (3.5)$$

where, the mathematical term G for Compton scattering is expressed as

$$G(\theta) = \gamma + \frac{1}{\gamma} - S \sin^2 \theta \quad (3.6)$$

and for elastic scattering

$$G = 2 - S \sin^2 \theta \quad (3.7)$$

From eqn. (3.5), it is evident that the scattering probability densities are independent of the incoherent scattering form factor $S(X,Z)$ and atomic form factor $F(X,Z)$. For unpolarized x-ray beam of energy E , the differential Compton and elastic scattering cross sections can be expressed as function of polar angle θ and azimuthal angle ϕ , as

$$\frac{d}{d\Omega} \sigma_{Comp}(\theta, E) = \frac{r_e^2}{2} \gamma^2 \left(\gamma + \frac{1}{\gamma} - S \sin^2 \theta \right) S(X, Z) \quad (3.8)$$

$$\frac{d}{d\Omega} \sigma_{elas}(\theta, E) = \frac{r_e^2}{2} (1 + \cos^2 \theta) F^2(X, Z) \quad (3.9)$$

From eqns. (3.8) and (3.9), it can be seen that the differential Compton and elastic scattering cross sections are isotropic in nature for a unpolarized x-ray beam.

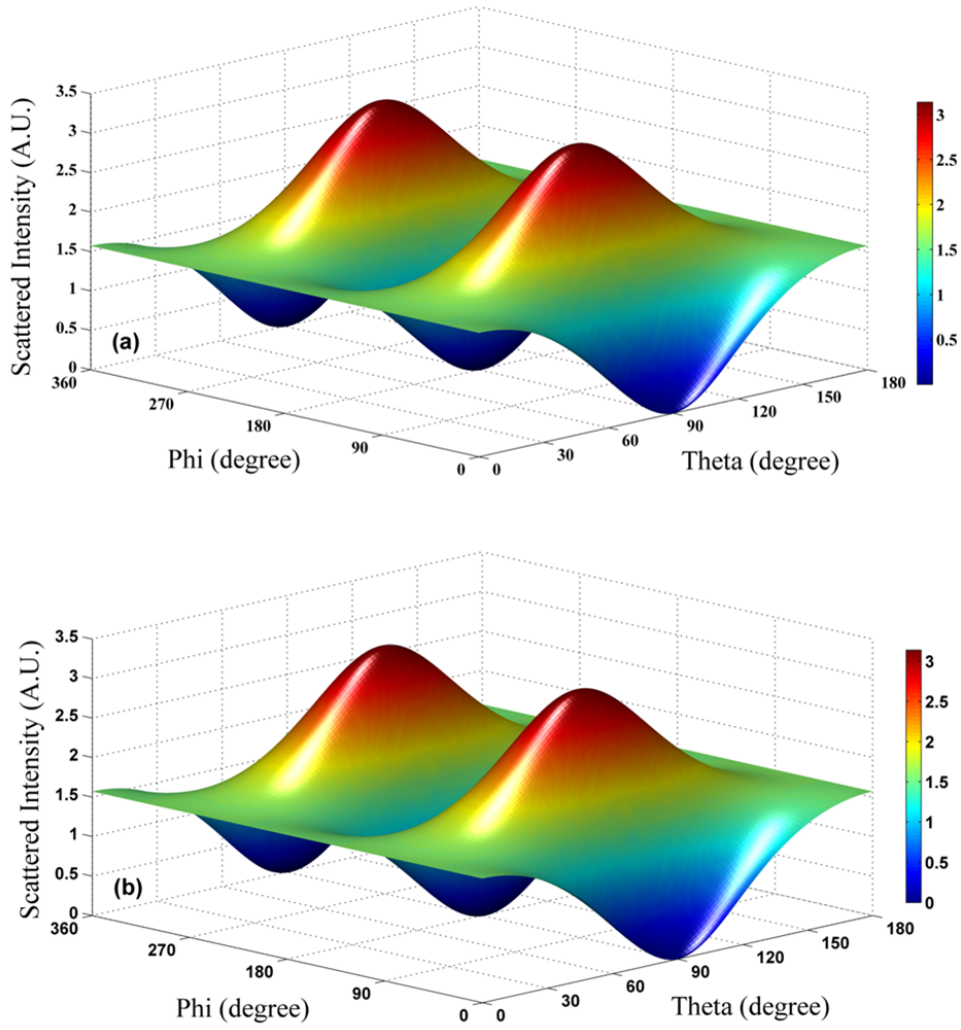


Figure 3.2: Angular distribution of the scattered photon for (a) Compton and (b) elastic scattering as a function of scattering angle (θ) and azimuthal angle (ϕ) at incident x-ray energy of 15 keV.

3.2.1 Theoretical simulation

Numerical simulations have been carried out to investigate the effect of angular dependence of the scattered photons. Figure 3.2 depicts scattering probability densities (eqn. (3.5)) for the (a) Compton and (b) elastic scattered x-rays as a function of scattering angle θ and azimuthal angle ϕ assuming an incident x-ray energy of 15 keV.

It can be seen from Fig. 3.2, that both the Compton and elastic scattered x-ray photons show strong angular anisotropy with respect to angles θ and ϕ . The scattered intensity is maximum at angular positions $\theta = \pi/2$ and $\phi = \pi/2$ and minimum at $\theta = \pi/2$ and $\phi = 0$.

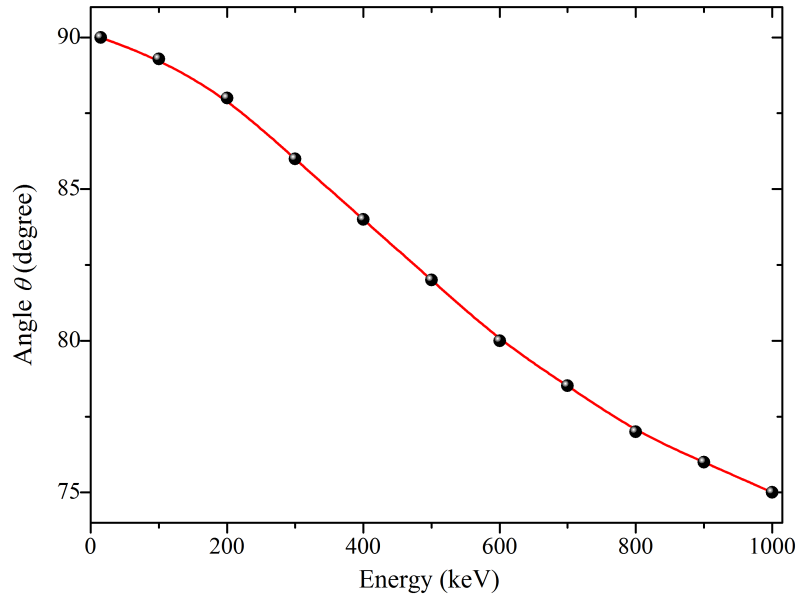


Figure 3.3: Variation of Compton scattered radiation as a function of scattering angle (θ) and incident energy.

These angular positions have been referred as vertical and horizontal geometry respectively. It can be realized that if the spectroscopy detector is placed in the horizontal geometry (*i.e.*, $\theta = \pi/2$ and $\phi = 0$) one will observe minimum spectral background in the fluorescence spectrum.

The behaviour of angular dependence of the scattered photons at higher incident x-ray

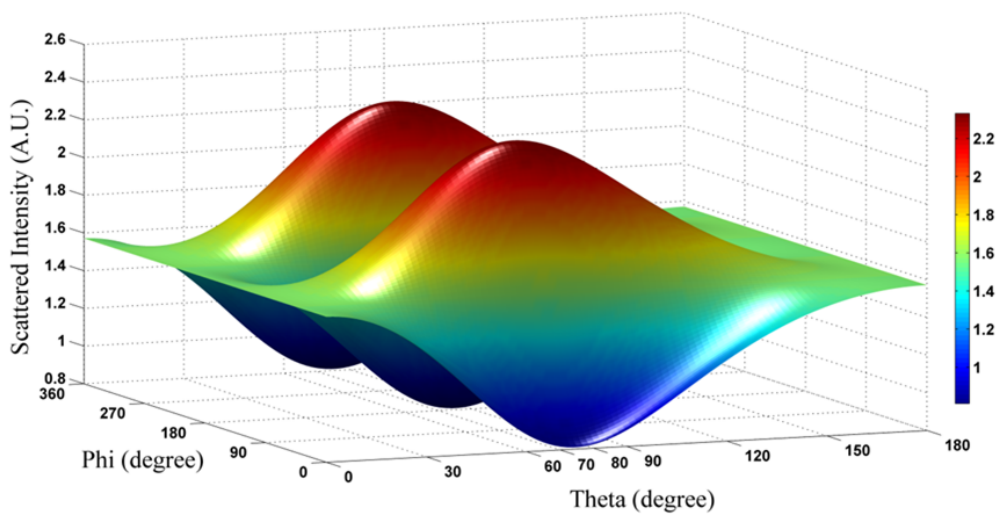


Figure 3.4: Angular distribution of the Compton scattered photon as a function of scattering angle (θ) and azimuthal angle (ϕ) at the 1 MeV monochromatic incident x-ray beam.

energies was also evaluated by theoretical simulations. The results are presented in Fig. 3.3. It has been realized from simulations that energy dependence does not have much influence on the angular distribution of the scattered photons especially in the medium energy range (10-100 keV). However, if the energy of the incident x-ray photon is greater than 100 keV then the angular profile of scattered photon changes considerably. Fig. 3.4 shows computed angular distribution profile for the Compton scattered x-rays as a function of θ and ϕ at incident x-ray energy of 1 MeV. It can be observed from this figure that minima and maxima of the Compton scattering distribution are shifted towards the lower scattering angle side ($\theta \approx 75^\circ$). However, the azimuthal angle (ϕ) remains unchanged. On the other hand, the angular distribution of elastically scattered intensity nearly remains unchanged at lower as well as at higher incident x-ray energies.

The scattering measurements also allow one to determine degree of polarization P , of the incident x-ray beam using following formula [70]

$$P = \frac{I_{\perp} - I_{\parallel}}{I_{\perp} + I_{\parallel}} \quad (3.10)$$

where I_{\perp} and I_{\parallel} are the intensities of the scattered radiations (Compton or elastic) in the parallel and perpendicular planes respectively with respect to the plane of incident electric field vibrations.

3.3 Experimental

The TXRF measurements using various standard reference samples were carried out at the microfocus x-ray fluorescence (BL-16) beamline of the Indus-2 synchrotron radiation facility. The BL-16 beamline is designed to work in the x-ray energy range of 4 - 25 keV. The details of the beamline and different experimental stations installed on this beamline are described in Chapter 2 [46, 53]. Figure 3.5 shows the photograph of the TXRF experimental station of BL-16 beamline. The BL-16 TXRF set-up comprises of

an in-house developed 4-axes motorized sample manipulator installed on a vibration free optics table. It provides vertical as well as horizontal movement to a sample with respect to the x-ray beam with a minimum step size resolution ~ 1 micrometer. Two independent angular motions (Tilt and Roll) were also provided for the alignment of the sample as well as to set small grazing incidence angle to achieve total external reflection condition on sample reflector surface with a minimum step size resolution of $\sim 0.001^\circ$. Monochromatic x-rays of energy 15keV monochromatized from a Si (111)

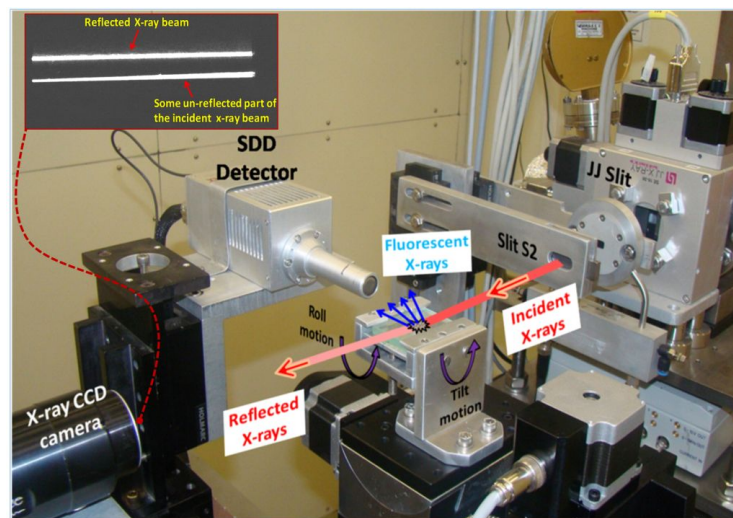


Figure 3.5: Annotated photograph of the TXRF experimental station of the BL-16 beamline. The inset shows a recorded image at the x-ray CCD in TXRF excitation geometry. In this figure the incident and reflected x-ray beam are marked.

double-crystal monochromator (DCM) were used for excitation of the samples at grazing incidence angle. For the total reflection x-ray fluorescence measurements an incident x-ray beam of size ~ 10 mm (H) $\times 100$ μ m (V) was allowed to impinge on the sample surface at grazing incidence angle of 0.102° . Provisions have been made to mount the solid state spectroscopy detector (Vortex, USA) in the horizontal plane as well as in the vertical plane with respect to the substrate surface (see Fig. 3.1). The spectroscopy detector (SDD) has an active surface area of 50 mm² and an energy resolution of ~ 140 eV at 5.9 keV (Mn-K α) x-rays. The SDD was placed at ~ 30 mm distance from the centre of beam footprint on the sample surface. An x-ray CCD camera was also employed to confirm the TXRF condition by observing reflected x-ray beam from the

sample. The inset of Fig. 3.5 depicts a recorded CCD image of the reflected x-ray beam, which clearly demonstrates total external reflected part of the incident x-ray beam. For the TXRF investigations, NIST-1640 standard reference material (*Trace elements in natural water*), ICP-IV Merck multielement standard sample were used. Aliquots of $\sim 20 \mu\text{L}$ volume of standards were micropipetted on polished Si (100) substrates. Instead of using a single element standard we used multielement reference materials to investigate detection sensitivities of different elements over the full spectral background.

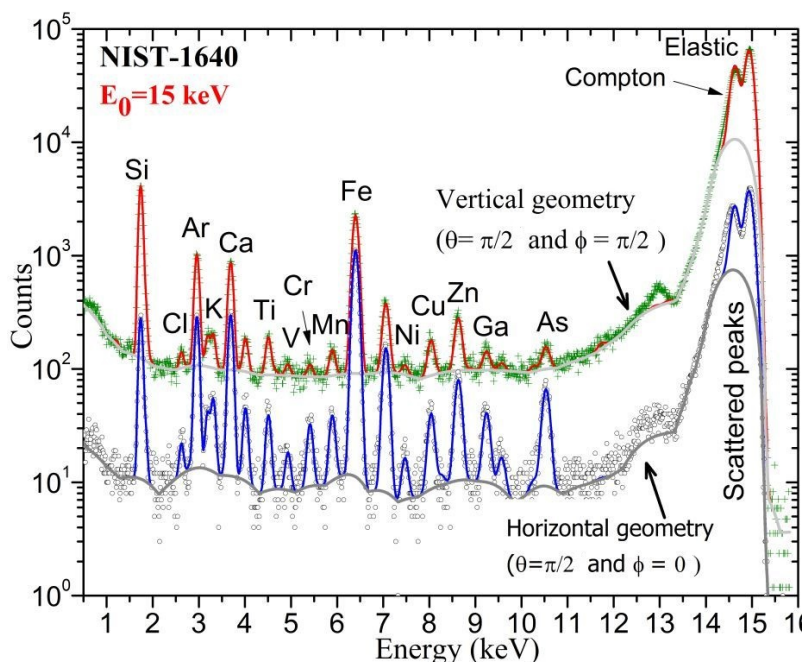


Figure 3.6: Measured TXRF spectra of a NIST-1640 reference material in vertical geometry ($\theta = \pi/2$ and $\phi = \pi/2$) and horizontal geometry ($\theta = \pi/2$ and $\phi = 0$). Here, Ga (100 ppb) is used as an internal standard reference element. Scattered points are experimental data, solid lines are the fitted spectrum in the two measurement geometries.

3.4 Results and discussions

Figure 3.6 represents the measured TXRF spectra of the NIST-1640 reference material at 15 keV monochromatic x-ray energy in the vertical ($\theta = \pi/2$ and $\phi = \pi/2$) and horizontal ($\theta = \pi/2$ and $\phi = 0$) geometries. The figure clearly shows the presence of

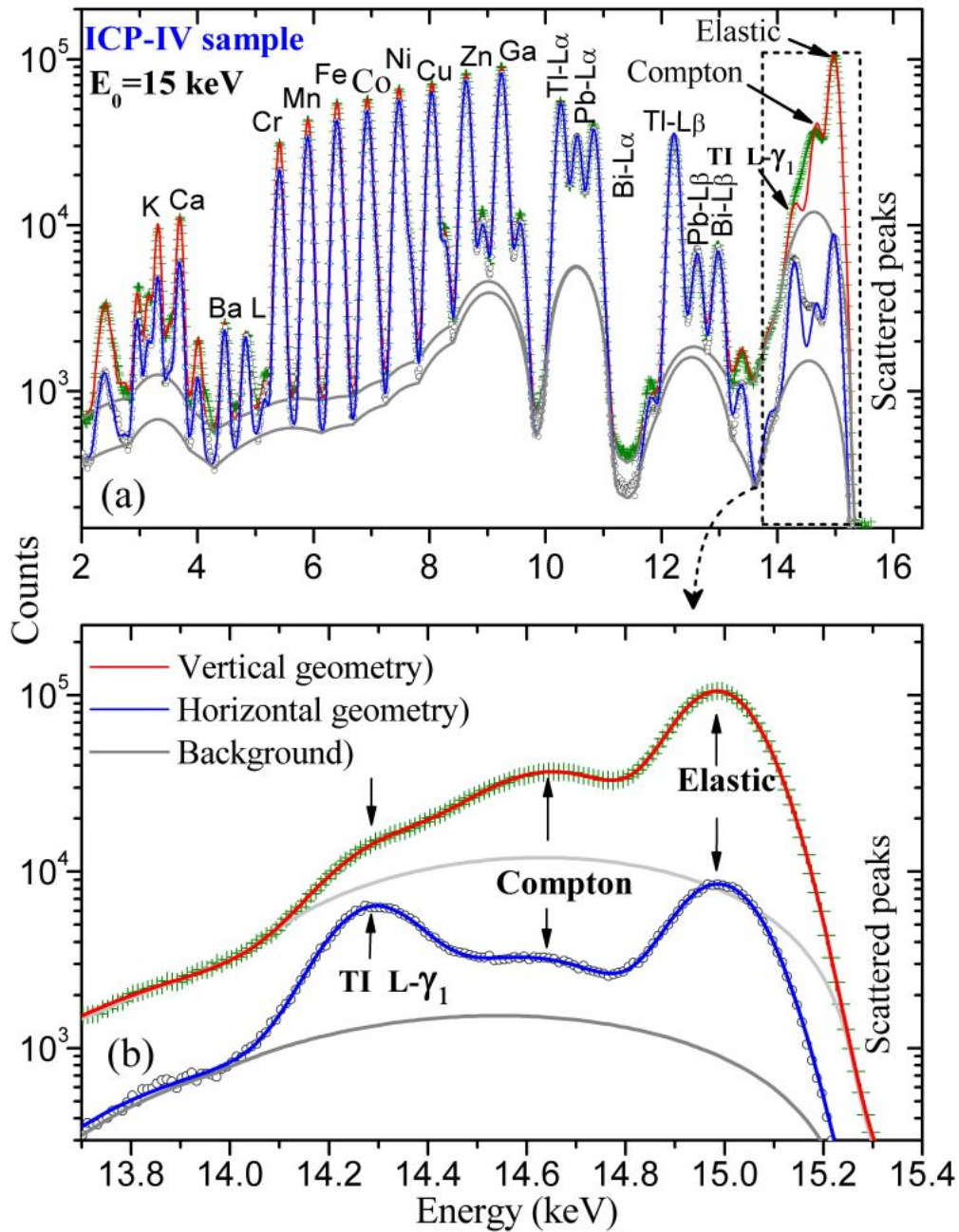


Figure 3.7: Recorded TXRF spectra for an ICP-IV Merck reference standard (containing 50.35 ppm wt. concentration of each elements) in vertical ($\theta = \pi/2$ and $\phi = \pi/2$) and horizontal ($\theta = \pi/2$ and $\phi = 0$) geometry. In this figure, scattered points are experimental data, solid lines are fitted spectrum in the two geometries. Figure 3.7(b) shows extended view of the encircle region of Fig. 3.7(a), where Tl-L γ_1 peak is individually fitted in the presence of large Compton scattered background. It can be seen that the visibility of Tl-L γ_1 peak gets enhanced in the horizontal detection geometry due to the reduced spectral background.

various elements in the NIST reference material of atomic number Z ranging from 19 (K) to 33 (As). The fluorescence peaks of Ar and Si were also observed from the Si substrate and atmosphere respectively. It can be noticed from the Fig. 3.6 that the signal to noise ratio is unambiguously higher in the horizontal geometry compared to that of the vertical geometry. As a result, one can detect an analyte, which is present at very low concentration in the NIST specimen with an encouraging level of confidence limit (for example, As 26.67 ppb). In case of vertical detection geometry, the peak height for the same element is very small compared to the horizontal geometry. This is mainly because of the reduction of (Compton and elastic) scattered background originated from the specimen. To validate above observations, similar measurements were also carried out using another reference standard material (ICP-IV sample) containing different elements at ppm level. Figure 3.7(a) illustrates measured TXRF spectrum of the ICP-IV standard reference material containing 50.35 ppm of each elements at 15 keV monochromatic x-ray energy in the vertical geometry ($\theta = \pi/2$ and $\phi = \pi/2$) as well as horizontal geometry ($\theta = \pi/2$ and $\phi = 0$). From this figure, it can be seen that the effect of spectral background is not very significant as recognized in case of NIST-1640 standard reference sample because most of the elements in the ICP-IV standard sample are present in the ppm range. Nonetheless, we could observe similar kind of behaviour for the spectral background in the case of the ICP-IV as well. The effect of spectral background on the fluorescence signal becomes obvious if we give attention to the TI $L\text{-}\gamma_1$ peak. The fluorescence peak of TI $L\text{-}\gamma_1$ could only be observed clearly in the horizontal geometry, as a result of significant reduction of the Compton scattered background (see Fig. 3.7(b)). This suggests that the influence of spectral background on the fluorescence signal is more significant if the analytes are present (in ppb level) at the tailing background of the Compton scattered peak. These results are consistent with the observations of Sakurai *et al.* [71].

3.4.1 Applications to a few methodological samples

To further demonstrate the effect of SR polarization on the spectral background of TXRF a few methodological samples were analysed using TXRF measurements. In one case, the distribution of self assembled Au nanoparticles, on top of a polished Si substrate surface was analysed. For this, Au nanoparticles of average heights of ~ 90 nm were dispersed into the water solution. The Si substrate was then directly dipped into the Au nanoparticles solution to deposit nanoparticles on the substrate surface and then taken out. The nanoparticle sample was then heated to $\sim 50^\circ\text{C}$ for 30 minute to remove the water component from the nanoparticle film. This generates a uniform distribution of Au nanoparticles over a large surface area on the Si substrate. Figure 3.8 compares the

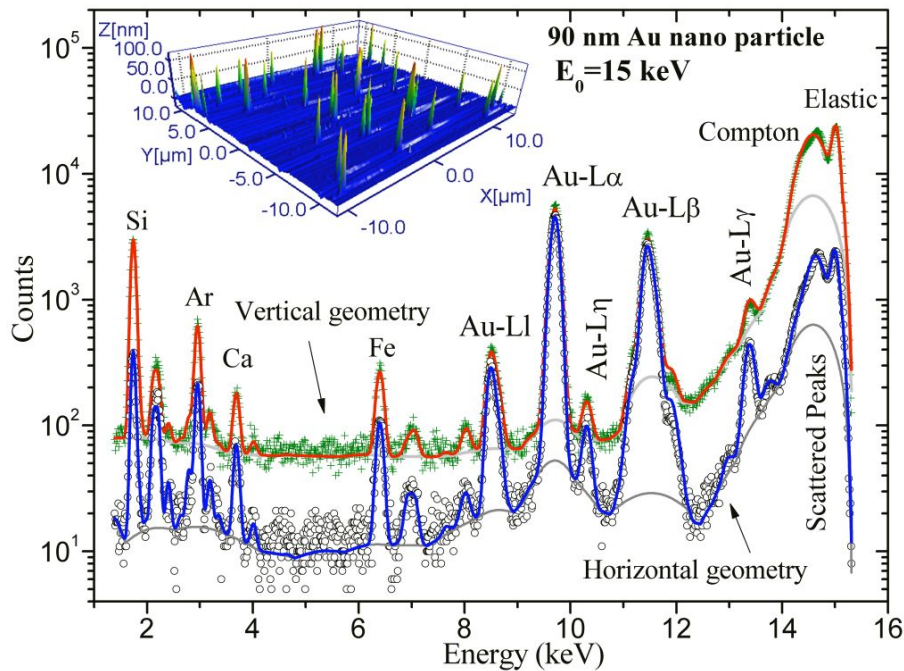


Figure 3.8: Measured TXRF spectra of the Au nanoparticles distribution on the Si substrate at monochromatic x-ray energy of $E_0 = 15$ keV in the horizontal and vertical detection geometries respectively. Scattered points are experimental data, solid lines are fitted spectrum in the two measurement geometries. Inset gives AFM image for the Au nanoparticles distribution on the Si Substrate surface.

measured TXRF spectra of the self assembled Au nanoparticles distribution in the two measurement geometries. From Fig. 3.8, it can be clearly observed that the spectral

background reduced significantly in the horizontal detection geometry. Moreover, the net area intensities of various Au-L α fluorescence lines also increased considerably as compared to that of the vertical detection geometry. These measurements clearly demonstrate the effect of signal potency of the fluorescence peaks in the horizontal detection geometry. From TXRF measurement, we could also determine the presence of Fe and Ca impurities in the distribution of Au nanoparticles on the Si substrate surface. These impurities are expected to originate from the dried water residue and from the ambient dust particles that get deposited during sample preparation. To confirm the surface morphology of the Au nanoparticles on the Si substrate surface, we have performed AFM measurements. Inset of Fig. 3.8, shows the AFM image for the Au nanoparticles distribution. The AFM investigations reveal a monodispersed distribution of the Au nanoparticles on the Si substrate surface with an average particle height of about $\sim 90 \pm 2$ nm. In another study, we performed TXRF measurement to determine

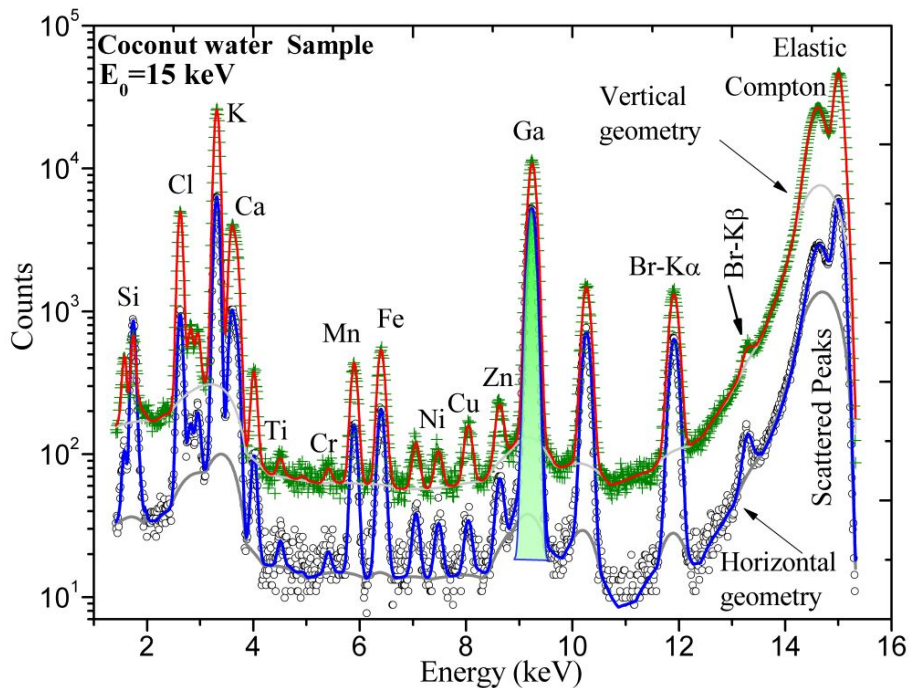


Figure 3.9: Measured TXRF spectrum of coconut water sample at monochromatic x-ray energy of $E_0 = 15$ keV in the horizontal and vertical geometries respectively. Ga (35 ppm) was used as an internal standard. Scattered points are experimental data, solid lines are fitted data in the two geometries.

the presence of various trace elements in Coconut water. For this, $\sim 10 \mu\text{L}$ volume of coconut water was pipetted on a cleaned quartz glass substrate after adding Ga internal standard (35 ppm) and without employing any dilution procedure. The dried residue of Coconut water was then employed for TXRF measurements in the vertical ($\theta = \pi/2$ and $\phi = \pi/2$) and horizontal ($\theta = \pi/2$ and $\phi = 0$) geometries. Figure 3.9 shows the measured TXRF spectra of the coconut water in two different geometries. From Fig. 3.9, it can be seen that the relative signal strengths (signal to noise ratio) of various fluorescence peaks grow noticeably in the horizontal geometry as compared to that of the vertical detection geometry owing to effective reduction of spectral background. The enhanced signal efficiency in the horizontal geometry is especially helpful for analysing fluorescence peaks that lie on the tailing background of Compton and elastic scattered peaks. For example, the Br-K β line is not clearly visible in the vertical geometry. In such a situation, sometimes it is quite difficult to analyse an element, if it is present in a very low concentration, in the sample. These results clearly prove the effectiveness of the horizontal geometry measurement. We define the relative signal strength as a ratio of the signal to noise ratios ($S/B = \text{net peak area intensity} / \text{background}$) in horizontal to vertical detection geometry. Table 3.1 summarise determined concentrations and relative signal strength of various trace elements present in the coconut water sample in the two excitation geometries. To evaluate the advantages of horizontal geometry measurement more quantitatively, the relative fluorescence signal strength was calculated for all the samples. The results are summarised in Table 3.2. These tabulated data clearly show that the signal strength enhancement in horizontal geometry is about one order of magnitude higher as compared to that of the vertical detection geometry especially for the specimens that contain trace concentrations of the elements. This enhanced signal strength greatly influences the observed detection sensitivities of various elements if TXRF excitation is made in the horizontal detection geometry.

Table 3.1: Determined relative signal strengths and concentrations of various trace elements in the coconut water.

Element	Z	S/B (vertical geom- etry)	S/B (horizontal ge- ometry)	Relative signal strength	Determined Concentration (ppm)
Cl	17	3.3	3.9	1.2	265 ± 6
K	19	12.16	13.72	1.1	1367 ± 14
Ca	20	3.89	5.62	1.4	68 ± 2
Ti	22	0.06	0.08	1.4	130 ± 6 ppb
Cr	24	0.09	0.22	2.4	23 ± 1 ppb
Mn	25	2.24	3.18	1.4	2 ± 0.1
Fe	26	1.88	4.29	2.3	2 ± 0.1
Ni	28	0.43	0.89	2.1	158 ± 8 ppb
Cu	29	0.44	0.83	1.9	91 ± 7 ppb
Zn	30	0.76	1.12	1.5	258 ± 7 ppb
Ga	31	21.8	44.95	2.1	35 ± 2
Br	35	3.47	8.19	2.4	4 ± 0.2

3.4.2 Effect on the Detection sensitivity

The term “detection limit” (DL) is an important aspect of any technique because it is an indication of the sensitivity of the technique. The detection limit is a measure of the minimum quantity that can be detected by an instrument or technique under the given experimental conditions (sample geometry, sample matrix, analysis time, etc).

The minimum detection limits (MDLS) in the XRF technique can be described using the formalism $C_{DL} = \frac{3\sqrt{I_B}}{I_A/C_A}$, where I_B is the integrated linear background intensity under the fluorescence peak of analyte element A, I_A is the net area intensity of the analyte, and C_A is the weight concentration of the analyte. Figure 3.10 shows the measured detection sensitivities of various elements in the vertical and horizontal geometries for the (a) NIST-1640 and (b) ICP-IV standard reference samples. From Fig. 3.10(a), it can be seen that the detection sensitivities in the horizontal geometry range ~ 234 ppb to 2 ppb for elements of atomic number Z ranging from 19 to 33 for the NIST-1640 standard reference material. On the other hand, in the vertical detection geometry these detection sensitivities have been found to be diminished by a factor of 2. Furthermore, we

Table 3.2: Measured relative signal strength of various elements in different samples.

Element	Z	S/B (vertical geometry)	S/B (horizontal geome- try)	Relative signal strength
NIST-1640				
K	19	0.43	1.55	3.6
Ca	20	2.99	9.80	3.3
V	23	0.02	0.10	7
Cr	24	0.13	1.15	9.4
Mn	25	0.30	1.38	4.7
Fe	26	7.33	36.00	5
Ni	28	0.13	0.90	6.7
Cu	29	0.45	1.83	4
Zn	30	0.72	3.12	4.4
Ga	31	0.25	1.60	6.6
As	33	0.30	2.29	7.5
Au nano particles				
Au L- γ	79	0.19	1.47	7.7
Au L- β	79	4.87	22.1	4.5
Au L- α	79	14.14	33.53	2.4
Au L-L1	79	1.51	5.09	3.4
Fe	26	0.98	2.78	2.8
Ca	20	0.54	1.47	2.7
ICP-IV standard reference sample				
Cr	24	11.25	14.32	1.3
Mn	25	13.94	18.19	1.3
Fe	26	17.35	21.00	1.2
Co	27	17.34	21.17	1.2
Ni	28	15.38	18.60	1.2
Cu	29	11.48	12.86	1.1
Zn	30	7.54	8.15	1.1
Ga	31	6.38	6.68	1.1

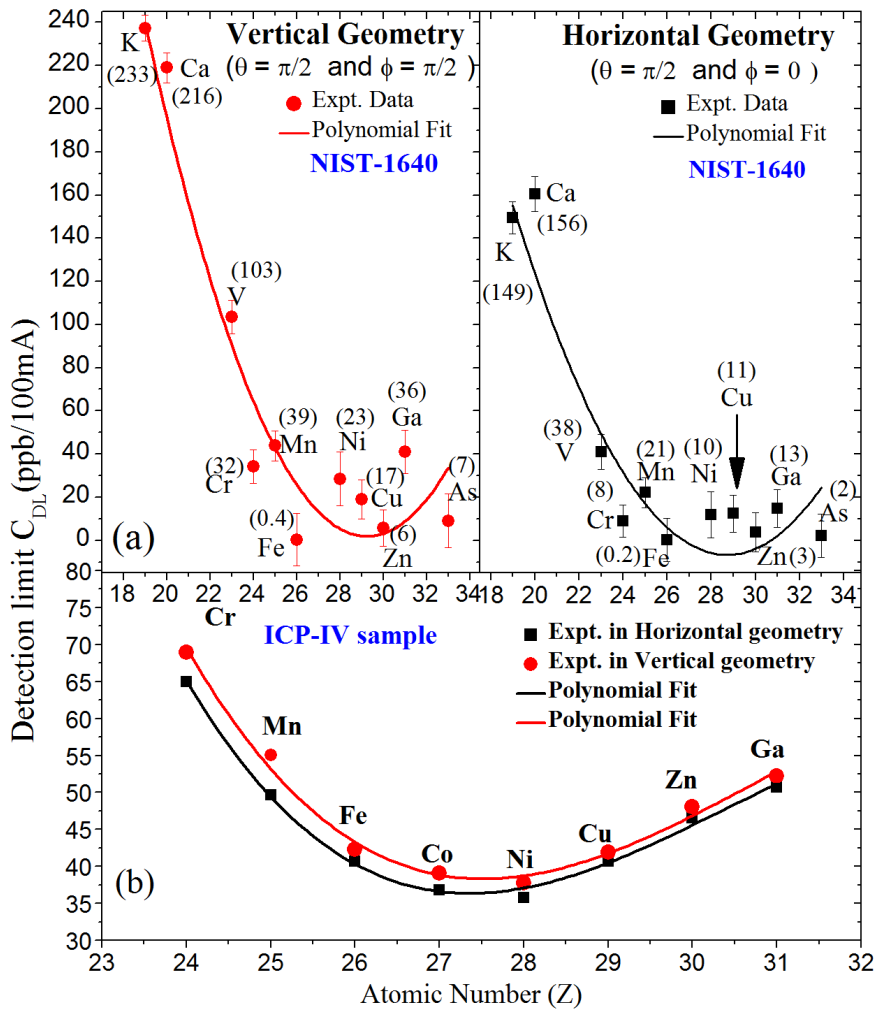


Figure 3.10: Variation of elemental detection sensitivities for (a) NIST-1640 (in ppb) and (b) ICP-IV (in ppm) standard reference samples as a function of atomic number Z in the vertical ($\theta = \pi/2$ and $\phi = \pi/2$) and horizontal ($\theta = \pi/2$ and $\phi = 0$) detector mounting geometry.

obtained an analogous conclusion in case of ICP-IV standard reference sample. The detection sensitivities of various elements in the horizontal detection geometry were found superior compared to that off the vertical detection geometry as depicted in Fig. 3.10(b). The higher C_{DL} values were found for different elements in case of ICP-IV sample as compared to that of the NIST-1640 sample because of higher concentration of analyte present in the ICP-IV sample. The minimum detection sensitivity of an element in the x-ray fluorescence technique strongly depends on the analyte mass present in the specimen [72]. These findings are consistent with the experimental observations reported

by Margui *et al.* [73]. They showed that the quantification of Cadmium in 100 mL aqueous samples in the range of 1-20 μg is only practicable by using polarized energy dispersive x-ray fluorescence instrument (P-EDXRF) in contrast to the conventional EDXRF and WDXRF spectrometers.

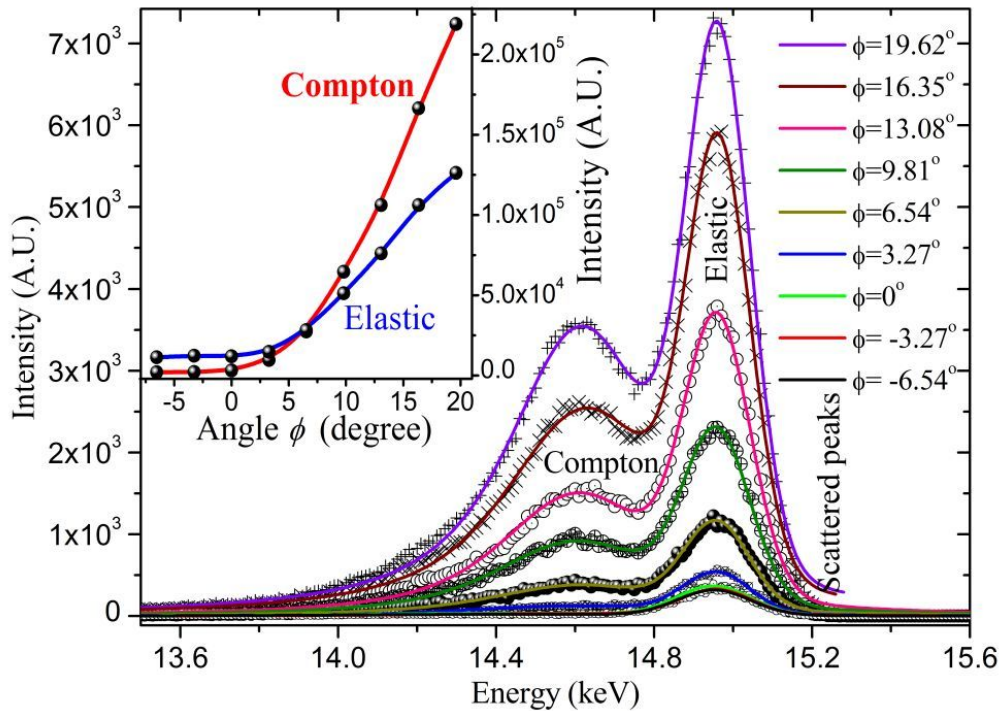


Figure 3.11: Variation of the Compton and elastic scattered radiations at different azimuthal angles in the TXRF measurements. Scattered points are experimental data, solid lines are the fitted data at different angles. The inset illustrates the scattered radiation intensity variation at different azimuthal angles.

3.4.3 Effect of azimuthal anisotropy of scattered radiation on the fluorescence signal strength

The azimuthal anisotropy of the scattered radiation plays significant role in obtaining improved elemental detection sensitivities in a TXRF measurement. For precise determination of effect of azimuthal anisotropy of the Compton and elastic scattering cross sections in the horizontal plane, TXRF measurements were carried out for the NIST-1640 standard reference sample at different shallow azimuthal angles. In order to

accomplish this, first, the SDD detector axis was aligned in the horizontal plane at $\phi = 0$ and then it was moved in the azimuthal plane (ϕ - plane) to acquire fluorescence spectrum at different shallow azimuthal angles (please refer to the inset of Fig. 3.12). Figure 3.11 illustrates a comparison of the scattered radiations (Compton and elastic radiations) in the TXRF spectrum of NIST-1640 at different azimuthal angles. It is evident that tailing part of the Compton and elastic scattered peaks has a significant extent towards the lower energy side in the fluorescence spectrum and this tailing spectral background increases monotonously as one increases azimuthal angle (ϕ). From these measurements it can be clearly realized that one gets improved fluorescence signal strength (signal-to-background ratio) at smaller azimuthal angles. The inset of Fig. 3.11 shows the intensity variation of the Compton and elastic scattered peaks as a function of azimuthal angles. Figure 3.12 shows the variation of fluorescence to Compton intensity ratios for different elements present in the NIST-1640 standard sample for azimuthal angles ranging from -7° to 20° . The inset of Fig. 3.12 pictorially describes experimental arrangement used for the ϕ -scan measurements. It may be noted from the Fig. 3.12 that the maximum of the fluorescence to Compton intensity ratio lies in the angular region of $\phi = 3^\circ$ to $\phi = 6^\circ$ for all the elements. This azimuthal angular region is basically dictated by the effective geometrical active area of the detector element and detector-to-sample distance. For the BL-16 TXRF spectrometer fluorescence signal strength (signal to noise ratio) was found to be maximum for the detector take-off angle values of $\phi \sim 5^\circ$. If detector is moved further away at higher take-off angles, the spectral background due to Compton scattered radiation starts increasing rapidly, thus decreasing the signal to noise ratio monotonously at higher values of the azimuthal angles. This azimuthal anisotropy is directly related to the scattering density profile of the Compton and elastic scattering intensity distributions.

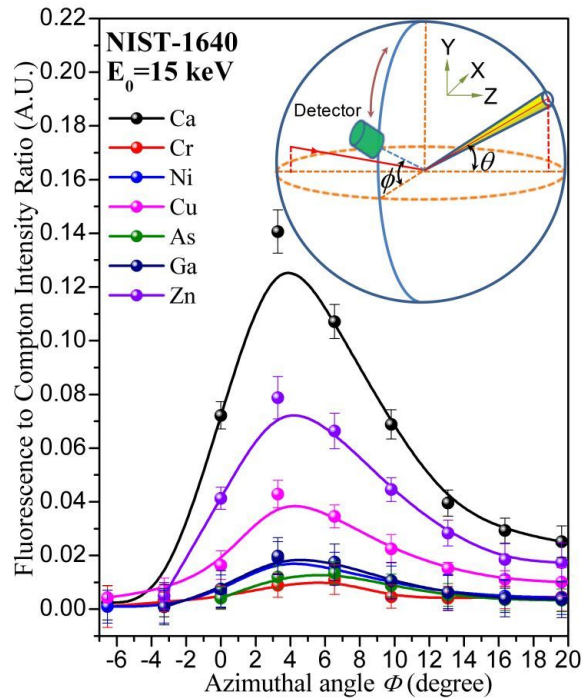


Figure 3.12: Variation of fluorescence signal to scattered Compton intensity ratios for different elements present in the NIST-1640 standard reference material at 15 keV as a function of azimuthal angle (ϕ). The inset illustrates the experimental geometry used for the Phi- scan measurements. The arrow shows the scanning direction of the detector in the horizontal mounting geometry. The detector was placed at a distance ≈ 30 mm from the centre of beam footprint on the sample surface.

3.4.4 Determination of degree of Polarization of the Synchrotron beam

It is also possible to estimate the degree of polarization of the incoming SR beam using the Compton and coherently scattered radiations observed in a TXRF spectrum. The Compton and elastic scattered intensities were calculated from the measured TXRF spectra in the vertical ($\theta = \pi/2$ and $\phi = \pi/2$) and horizontal detection ($\theta = \pi/2$ and $\phi = 5^\circ$) geometries. The polarization factor is then calculated following eqn. 3.10. The values obtained are tabulated in Table 3.3. During the polarization measurements the SDD detector was placed at a distance ≈ 30 mm from the centre of beam footprint on the sample surface. The observed degree of polarization is $\sim 88 \pm 2 \%$ for the incoming synchrotron x-ray beam for TXRF excitation at the BL-16 beamline.

Table 3.3: Measured degree of Polarization for SR beam at the BL-16 beamline.

Radiation	I_{\perp}	I_{\parallel}	Polarization (P)
Compton	3182085	212829	0.87
Elastic	1563135	95212	0.88

3.5 Summary

The effect of synchrotron beam polarization in grazing incidence x-ray fluorescence excitation was examined experimentally by performing TXRF measurements of several samples. It was realized that the anisotropic nature of the scattered radiation imposes a constraint to place an x-ray spectroscopy detector in a condition where the contribution of the scattered background is minimal. The computation results obtained using reported literature [66–69] closely corroborate with the experimental TXRF measurements performed on various standard reference materials as well as for few TXRF methodological samples. It is realized that the horizontal detection geometry provides approximately one order of magnitude better signal to noise ratio, in contrast to the conventional vertical detection geometry, thus improving TXRF detection sensitivities $\sim 20 - 60\%$ for most of the elements. In addition, it also gives the benefit of reducing detector dead time and thus improves the real time spending ($\sim 20\%$) considerably, for the acquisition of spectra. The ϕ -dependent anisotropy of the scattering cross section in the horizontal plane can be understood in terms of the detector geometry for different elements. For the BL-16 TXRF set-up best signal to Compton background contrast was obtained in the angular region of $\phi = 2^\circ$ to $\phi = 8^\circ$. It may be worth mentioning here that the results described here provide a general guideline for mounting of a spectroscopy detector, especially, for the synchrotron based grazing incidence x-ray fluorescence (GIXRF) and total reflection x-ray fluorescence (TXRF) measurements to achieve better signal to spectral background contrast and will be of vital importance to the field of ultra-trace element analysis.

Chapter 4

Depth resolved structural and chemical analysis of thin layered materials

In this chapter the underlying physical aspects of x-ray standing wave (XSW) technique and development of GUI-CATGIXRF program, as a solution to provide non-destructive evaluation of nanostructured materials have been described. The potential utility and various salient features of the GUI-CATGIXRF program are described by providing example calculations as well as by analysing experimentally a few thin film structures comprising of different surface-interface properties.

We demonstrate the applicability of combined XRR-XSW analysis approach for probing deeply buried interfaces inside a W-B₄C multilayer structure. X-ray standing wave field generated under Bragg reflection condition is used to probe the different constituent layers of the W-B₄C multilayer structure. To provide various insights on chemical speciation of a W-B₄C multilayer structure, XSW assisted depth resolved near edge x-ray absorption measurements have been carried out. Various depth resolved localized chemical states of W in the W-B₄C multilayer structure were probed. Interestingly, the results show the existence of some unusual electronic states at the surface-interface boundary of the W-B₄C structure as compared to that of the bulk thin film medium.

4.1 Introduction

Nanostructured materials deposited on a flat smooth surface find widespread applications in many branches of science, especially in the semiconductor industry, x-ray optics and integrated circuits (ICs) fabrication technology etc. Their unique structural, [74, 75] electronic [76, 77] and magnetic properties [78–80] play an important role in understanding many correlated and uncorrelated physical phenomenon such as electronic and magneto transport properties, interlayer exchange coupling and magneto-transport properties of various compound materials [77, 79, 81]. Periodic multilayer structures consisting of alternating thin layers of the high-Z and low-Z elements or compounds are used as an x-ray optical element in many technological applications like x-ray astronomy, microscopy, synchrotron beamlines and free-electron x-ray lasers [81–84]. In all these applications, microstructural properties of the thin film medium such as thickness, roughness, presence of unwanted impurities, (*if any*), buried interfaces and interface diffusion between the constituent layers play an important role in obtaining overall performance of a thin film device [85–87]. Precise structural and interface knowledge about a thin film medium is often necessary to tailor the physical properties of a thin film based semiconductor device or ICs, magneto-electronics and spintronics devices [88, 89]. Any unwanted structural inhomogeneity in the layer thickness or formation of a buried layer interface structure can lead to malfunction and deteriorate the overall performance of a thin film device. This is because the anisotropic intermixing or the mechanical strain developed between different layers in a thin film medium significantly alters the physical properties e.g. magnetization, tunneling spin polarization, and band alignment etc. of a thin film semiconductor device [90–93]. In such cases, it is often necessary to use characterisation technique that are non-destructive in nature and it is not advisable to abrade or add any unwanted impurities into the sample during the analysis.

In literature, several conventional methods; *such as* secondary ion mass spectrometry,

soft x-ray emission spectroscopy, auger electron spectroscopy, x-ray photoelectron spectroscopy, etc., have been proposed and used for the structural analysis of nano-scaled thin layered materials [94–96]. Most of the techniques described above however offer probing depths up to few nanometers (~ 10 nm), and therefore they are not particularly suitable for probing of nano-structured materials of large dimensions or buried interfaces that are present in the form of a deeply buried layer inside a thin film medium.

X-ray offers large penetration depths in most of the materials. The depth sensitivity of the x-ray inside a thin film medium can be enlarged to nanometer scale by using XSW induced fluorescence measurements at grazing incidence angles [97–100]. XRR is a widely used non-destructive tool for the microstructural characterisation of thin film structure. For the analysis of x-ray reflectivity data, a large variety of software packages have been designed with specific aims and are reported in the literature [35, 101–107]. Some of these software packages are also freely available to the scientific community. However, all these softwares utilise XRR technique alone to evaluate microstructural parameters of a thin film medium. GIXRF technique has been used as a sensitive probe [38, 108–114] to determine the location of an impurity atom inside a thin film medium. It has also been employed for determination of roughness and density variations in thin film structures, although the GIXRF technique is less sensitive for surface roughness effects in thin layered materials, as compared to the XRR technique. Similarly, small density variations in thin layer structures cannot be truly described by using GIXRF technique alone. The various potential features of combined XRR and GIXRF analysis are described in detail in Chapter 2. The most significant advantage of the combined XRR and GIXRF analysis is that it reduces the uncertainties of the individual techniques thereby drastically improving the reliability of the estimated structural parameters of a thin film medium [34, 35, 39, 115].

Considering the various attractive features and relative advantages of both the GIXRF and XRR techniques, we have developed a GUI-CATGIXRF program for the

simultaneous analysis of angle dependent XRR profile and fluorescence intensities emitted from a thin film specimen or a substrate. In this chapter, we will describe the salient features and potential applicability of GUI-CATGIXRF computer program. The GUI-CATGIXRF program is capable of performing computations for both XRR and GIXRF profiles, simultaneously. The combined analysis of XRR and GIXRF data allows us to determine a consistent set of microstructural parameters (*i.e.*, thickness, roughness, density variations and interface diffusion) of the thin film medium, with improved accuracies.

4.2 Standing wave - grazing incidence x-ray fluorescence

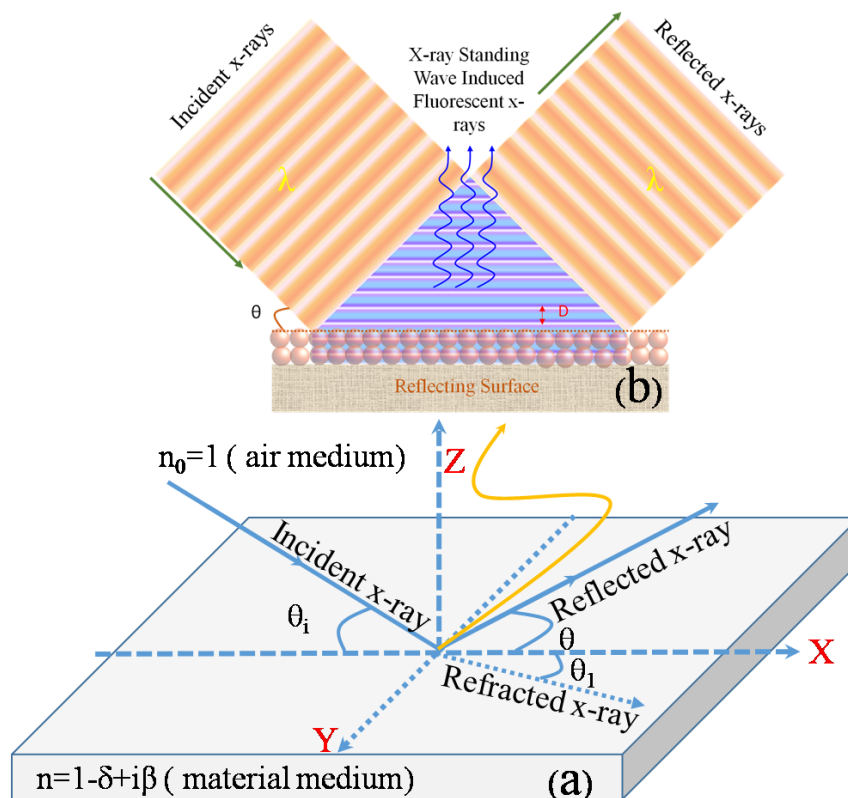


Figure 4.1: (a) Refraction of x-rays through an inhomogeneous medium (material). (b) The formation of x-ray standing wave on top of a reflecting surface due to the interference of incident and reflected x-ray beams of wave length λ . Enhanced fluorescence x-rays are emitted from those parts of the sample volume that present at the locations of XSW field antinodes.

An x-ray standing wave field is produced above the reflector surface due to the interference of incoming and reflected beam. As can be seen from Figs. 4.1(a), when a primary x-ray beam impinges on a smooth reflecting surface, a part of the radiation is specularly reflected and part of it is refracted and transmitted inside the sample surface. In the condition of total external reflection ($\theta < \theta_c$), the incoming and reflected beams interfere and form x-ray standing wave (XSW) field on the surface. The periodicity (D) of the standing wave can be defined as $D = \lambda/2\sin\theta$, for $\theta < \theta_c$, where λ is the wavelength of the incident x-ray beam. In the Fig. 4.1(a) the incidence angle θ and refracted angle θ_1 for the incoming and refracted x-ray beams are defined with respect to the sample surface respectively. These angles are related to each other by the equation $\sin\theta_{1,j} = \text{Re}[(\tilde{n}_j^2 - \cos^2\theta)^{1/2}]$, where \tilde{n}_j is the refractive index of the j^{th} medium. Fig. 4.1(b), demonstrates such a superposition of the incident and reflected x-ray beams on a mirror surface. It can be seen from this figure that the maxima and minima of interference fringe pattern generated, are planes parallel to the mirror surface. The maximum intensity of a bright fringe can be increased as large as ~ 4 times. For small value of θ , the phase shift between incident and reflected X-ray beam is $\sim 180^\circ$. In this condition, node of the X-ray standing wave field coincides at the surface of a substrate. At critical angle, the phase shift is close to zero, and we have an anti node near the surface.

The node to anti node distance and their position with respect to the substrate surface can be moved by changing the incidence angle between zero to critical angle. In this way, one can use the x-ray standing wave field as a probe to find out the location of an impurity atom near the surface. One can observe the fluorescence intensity from an impurity atom excited by the x-ray standing wave field as a monitor for the location. The fluorescence intensity will be larger when position of an impurity atom coincides with the position of an anti node where as a very low fluorescence signal is observed if node of the x-ray standing wave field coincides with the position of impurity atom. Beyond the critical angle, the reflected intensity becomes weak thereby decreasing contrast of the

x-ray standing wave field on substrate surface. This situation has been demonstrated in Fig. 4.1. In this condition, only a small modulation in the fluorescence intensity can be observed and the fluorescence excitation is mainly performed by the incident beam.

The smallest period of the x-ray standing wave field formed at critical angle. Usually the period of the x-ray standing wave field generated on a flat surface under total external reflection condition range in nanometer. When a sample residue is deposited on it, the fluorescence yield from an element increases due to increased value of electromagnetic field intensity available for excitation in TXRF region. In residue materials, the size of particles normally range in μm (i.e. larger than the period of X-ray wave field) thus several x-ray standing wave periods excites a particle. Moreover at the same time the x-ray field intensity at antinode and node positions of XSW field can be as high as 4 times of incident intensity and zero respectively therefore in case of droplet residue materials one obtains average x-ray fluorescence yield ~ 2 times in TXRF region.

4.3 Development of a GUI-CATGIXRF program

In order to perform the microstructural analysis of thin films, multilayer, substrates, etc. a computer program 'GUI-CATGIXRF', has been developed in FORTRAN 77 for the calculation of x-ray fluorescence intensities from a thin layered specimen or a substrate. Details of the methodology and several features of the program developed have been described in these subsections.

4.3.1 Program Methodology

For the computation of x-ray fluorescence intensities emitted from layered materials, both recursive formalism and matrix formalism have been described in the literature [54, 97, 116, 117]. We have followed recursive methodology to calculate electric field intensities in different layer mediums [34]. In order to estimate angle dependent

fluorescence intensities from a layered specimen, it is important that the electromagnetic field intensity at each position of the layered medium should be known explicitly. The GIXRF intensities originated from a complex thin layered material, like a periodic multilayer system, strongly depend on the structural parameters of the multilayer medium. These micro-structural parameters of the layered specimen (or substrates) can be derived from the combined analysis of XRR and GIXRF profiles.

Reflection and refraction in a layered specimen

In this section the reflection and refraction phenomenon occurring in a thin layered medium are described in detail for the sake of simplicity. We have considered a multiple thin film structure deposited on an infinitely thick substrate, as shown in Fig. 4.2. Layers of two materials (with high and low atomic numbers) having the thicknesses $d_1, d_2, \dots, d_{n1}, d_n$ are assumed to be stacked on a substrate surface. The layer index '0' represents the medium for the incoming x-ray wave; this may be either vacuum or air. In case when all the interfaces of the multilayer system are parallel to each other, one can write the equation of a plane electromagnetic wave travelling with frequency ω in a medium j , at a position r as

$$E_j(r) = E_j \exp[i(\omega t - \vec{k}_j \cdot \vec{r})] \quad (4.1)$$

where E_j is the electromagnetic field amplitude at the top of layer j . For the j^{th} layer, the wave vector k_j can be expressed as $k_j = k'_j - ik''_j$ and its components in the x-z plane are expressed by $k_{j,x} = \frac{2\pi}{\lambda} \cos\theta$, $k_{j,z} = \frac{2\pi}{\lambda} (\epsilon_j - \cos^2\theta)^{1/2}$, where θ is the glancing angle of incidence, λ is the wavelength of the incident x-ray field. The complex dielectric constant ϵ_j of a medium j can be expressed as

$$\epsilon_j = \tilde{n}_j^2 \approx 1 - 2\delta_j - i2\beta_j \quad (4.2)$$

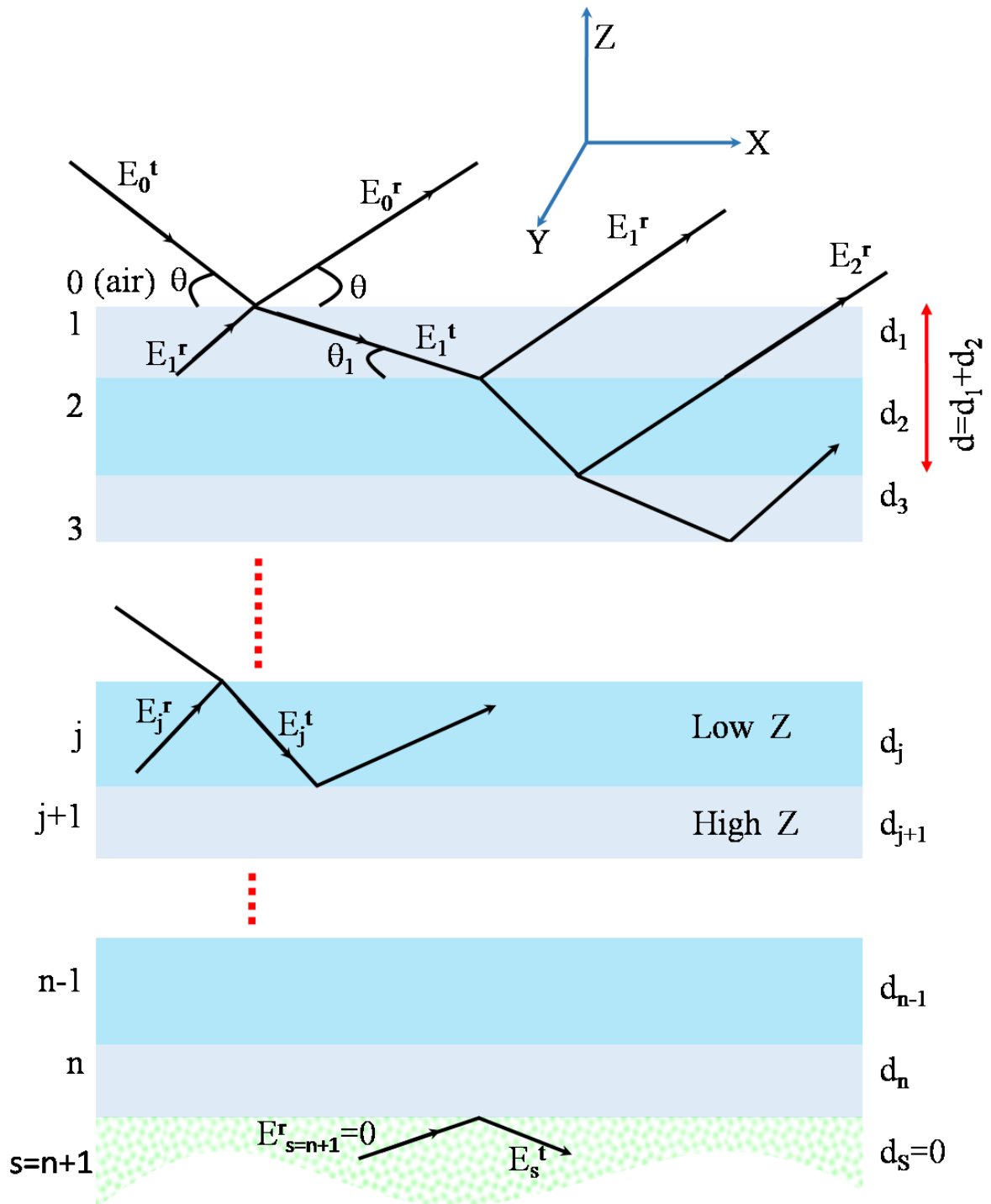


Figure 4.2: Multiple refraction and reflection of x-rays in a multilayer thin film structure on a thick infinite substrate. The transmitted and reflected field intensity in different media has been demonstrated by respective subscripts.

where δ is decrement term, which describes the deviation of real part of the refractive index \tilde{n} from unity, while β denotes the absorption of x-rays into the medium. The values of δ and β are expressed as $\delta = \frac{N_A r_e \lambda^2 \rho \times f'}{2\pi A}$ and $\beta = \frac{\lambda}{4\pi} \left(\frac{\mu}{\rho}\right) \rho$, where N_A is Avogadro's number, r_e is the classical electron radius, ρ is the density of the material (in g/cm^3), which relates to the electron density (n_e) by the formula $n_e = Z \times \frac{N_A}{A} \times \rho$. Here, A is the atomic weight of an element having atomic number Z , f' is the real part of average atomic scattering factor (equal to atomic number Z if anomalous dispersion can be neglected), (μ/ρ) is the mass absorption coefficient (in cm^2/g).

The electric field intensity inside a layered medium can be calculated for both s and p polarizations. However, in hard x-ray region (i.e. in small δ_j, β_j approximations), the formulas remain more or less identical for both polarizations. Here, we discuss the case for s-polarization. For the electric field parallel to the interface (s-polarization), the complex coefficients of reflection r_j and transmission t_j at the j and $j+1$ interface can be calculated from Fresnel's formulas

$$r_j = \frac{k_{j,z} - k_{j+1,z}}{k_{j,z} + k_{j+1,z}} \quad (4.3)$$

and

$$t_j = \frac{2k_{j,z}}{k_{j,z} + k_{j+1,z}} \quad (4.4)$$

These formulas (4.1-4.4) do not include the effect of substrate and interlayer roughness. Various methods are reported in the literature [55, 118, 119], to incorporate effects of roughness in the calculation of XRR and GIXRF profiles of a layered specimen. Moreover, the interface roughness (σ) of a thin film medium cannot be considered as a single quantity. This parameter basically defines the interface width of a thin film medium using an Error function. The density of a thin film medium at the interface region varies according to the Error function profile. In one approach, r_j is multiplied by a factor (the Debye-Waller factor), given by $S_j = \exp[-2\sigma_j^2 k_{j,z} k_{j+1,z}]$, where σ_j represents the root mean square deviation of the interface atoms from the ideal condition

(i.e. situation of perfectly smooth interface medium). However, the Debye-Waller factor approximation is valid only for small roughness values ($\sim 0 - 2$ nm). In a more practical approach, (the Nevot-Croce model [55]), r_j is multiplied by a factor S_j , and t_j is multiplied by a factor T_j , which can be expressed as $T_j = \exp[\sigma_j^2(k_{j,z} - k_{j+1,z})^2]/2$. Nevot-Croce model provides better results for incidence angles below θ_c as well as above θ_c . However, in the case of higher roughness values ($\sigma > 2$ nm), one needs to vary or approximate the density of the thin film medium as well. In our GUI-CATGIXRF program, surface roughness effects in the range of 3-6 nm can also be successfully treated by splitting a thin film medium into several layers and subsequently varying (or approximating) the density of the individual sub-layers, as described by H. Schwenke et al [119].

The transmitted and reflected x-ray field amplitudes, E_j^t and E_j^r at the top of j^{th} layer can be determined from recursion relations as $E_j^r = a_j^2 X_j E_j^t$, $E_{j+1}^t = \frac{a_j E_j^t T_j}{1 + a_{j+1}^2 X_{j+1} r_j S_j}$, $X_j = \frac{r_j S_j + a_{j+1}^2 X_{j+1}}{1 + a_{j+1}^2 X_{j+1} r_j S_j}$, and $a_j = \exp(-ik_{j,z} d_j)$, where d_j is the thickness of the layer j. Using the above relations, the electric field amplitudes E_j^t and E_j^r can be calculated in a layer medium from the knowledge of λ , θ , ϵ_j , the thickness d_j of layer j and its interface roughness σ_j . In the substrate medium, there is no reflection, thus $E_s^r = X_s = 0$. The calculation is performed in the reverse order, i.e. we first calculate the electric field amplitudes in the n^{th} layer and then progressively the field amplitudes are obtained for 0^{th} layer.

The ratio of electric fields at $j=0$ (air-film) interface, gives the reflectivity R, i.e.

$$R(\theta) = |E_0^r / E_0^t|^2 \quad (4.5)$$

Replacing E_0^t with 1.0, provides normalized XRR for a layered specimen.

Calculation of electric field intensity and fluorescence intensity

The total electric field intensity at a point r in the j^{th} layer medium is the vector sum of transmitted contribution $E_j^t(r) \downarrow$ and reflected contribution $E_j^r(r) \uparrow$ and is given by [28, 33, 34, 116, 120]

$$E_j^T(r) = E_j^t(r) \downarrow + E_j^r(r) \uparrow \quad (4.6)$$

where $E_j^t(r) \downarrow = E_j^t \exp(-ik_{j,z} \times z) \exp[i(\omega \times t - k_{j,x} \times x)]$ and $E_j^r(r) \uparrow = E_j^r \exp(-ik_{j,z} \times z) \exp[i(\omega \times t - k_{j,x} \times x)]$ represent equations for transmitted incident and reflected plane x-ray waves respectively. E_j^t and E_j^r are the amplitudes of transmitted and reflected electric fields at the top of layer j , which can be calculated using the recursion relations. The average x-ray field intensity $I_j(\theta, z)$, in the j^{th} layer medium at depth z is given by the following equation

$$I_j(\theta, z) = \frac{|E_j^t + E_j^r|^2}{|E_j^t|^2} = [\exp(-2k_{j,z}'' \times z) + \left| \frac{E_j^r}{E_j^t} \right|^2 \exp(2k_{j,z}'' \times z) + 2 \left| \frac{E_j^r}{E_j^t} \right| \cos([\nu(\theta) + 2k_{j,z}' \times z])] \quad (4.7)$$

where $\frac{E_j^r}{E_j^t} = \left| \frac{E_j^r}{E_j^t} \right| e^{i\nu(\theta)}$. Here, the term $\nu(\theta)$ represents the phase of the E-field ratio at the top of layer j . Using fundamental parameter approach, the equation for fluorescence intensity emitted from an element X , distributed in a layer j can be written as

$$I_{j,X}(\theta) = F(\theta) = I_0 G \times S_{X,E_0} \epsilon_{det} T_{air} \times \int_0^{d_j} C_X(z) \times I_j(\theta, z) \times \exp\left(-\left[\frac{(\mu/\rho)_E}{\sin\phi}\right] \rho \times z\right) dz \quad (4.8)$$

where S_{X,E_0} is the x-ray fluorescence production cross section for element X at incident x-ray energy E_0 . This quantity can be calculated theoretically as $S_{X,E_0} = \tau_X(E_0) \times \bar{\omega}_{k,L} \times g \times f$, where $\tau_X(E_0)$ is the photoelectric cross section of element X at incident energy E_0 . $\bar{\omega}_{k,L}$ represents average fluorescence yield for L or M shell. f is the jump factor of the respective absorption edge and g is the relative emission rate of the respective fluorescence line in its series. ϕ is the take off angle of the emitted fluorescence x-rays from layered specimen surface ($\phi \sim 90^\circ$). Various concentrations profile, as shown in Fig. 4.3 can be

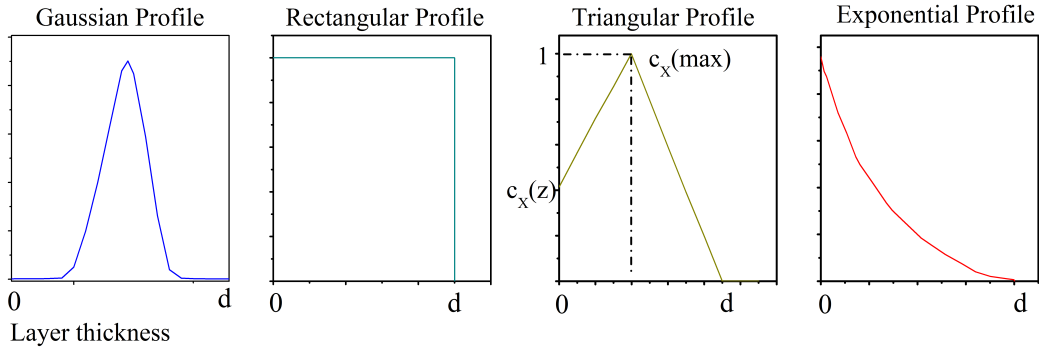


Figure 4.3: Schematic of various concentration profiles for an impurity element in a layer of thickness d .

assumed for an element X in layer j for the depth profile analysis. In such case, eqn. (4.7) needs to be solved numerically. If concentration of element X in layer j over its thickness d_j is constant (homogeneous layer) $C_X(z) \approx C_X$, then this quantity can be taken outside the integral and solution of eqn. (4.7) yields

$$I_{j,X}(\theta) = I_0 G \times C_X \times S_{X,E_0} \epsilon_{det} T_{air}(M_1 + M_2 + M_{12}) \quad (4.9)$$

where

$$M_1 = |E_j^t|^2 \times \frac{1 - \exp(-[(\mu/\rho)_{j,E_0}/\sin\theta_{1j} + (\mu/\rho)_{j,E}]\rho_j \times d_j)}{[(\mu/\rho)_{j,E_0}/\sin\theta_{1j} + (\mu/\rho)_{j,E}]} \quad (4.10)$$

$$M_2 = |E_j^r|^2 \times \frac{1 - \exp(-[-(\mu/\rho)_{j,E_0}/\sin\theta_{1j} + (\mu/\rho)_{j,E}]\rho_j \times d_j)}{[-(\mu/\rho)_{j,E_0}/\sin\theta_{1j} + (\mu/\rho)_{j,E}]} \quad (4.11)$$

and

$$M_{12} = 2 \times \text{Re}[E_j^* \times E_j^r \frac{1 - \exp(-[-2ik_0 \sin\theta_{1j}/\rho_j + (\mu/\rho)_{j,E}]\rho_j \times d_j)}{[-2ik_0 \sin\theta_{1j}/\rho_j + (\mu/\rho)_{j,E}]}] \quad (4.12)$$

where I_0 represents the primary intensity and G is a geometrical factor. The factor G takes care of the effect of footprint variation of the x-ray beam on the sample surface, at different incidence angles. $(\mu/\rho)_{j,E_0}$ and $(\mu/\rho)_{j,E}$ represent mass attenuation coefficients of layer j at primary x-ray energy E_0 and at characteristics energy E of the detected element X . C_X is the mass concentration of element X in the layer j . ϵ_{det} represents the

detector efficiency and T_{air} is the transmission of fluorescence x-ray in the air path from sample to detector. ρ_j is the density of layer j. In order to calculate GIXRF intensity from a repetitive layer structure, for example, in a multilayer medium, the net fluorescence intensity is calculated by summing the contribution from all layers and taking into account the absorption correction of upper layers. The fluorescence intensity emitted from an element X, present in all high Z and low Z layers are given, respectively, by

$$I_{high.x}(\theta) = \sum_{j,high.Z} \left(exp \left[- \sum_{n=1}^{j-i} \frac{(\mu/\rho)_{j,E} \times \rho_j \times d_j}{\sin\phi} \right] \times I_{A,x}(\theta) \right) \quad (4.13)$$

and

$$I_{low.x}(\theta) = \sum_{j,low.Z} \left(exp \left[- \sum_{n=1}^{j-i} \frac{(\mu/\rho)_{j,E} \times \rho_j \times d_j}{\sin\phi} \right] \times I_{B,x}(\theta) \right) \quad (4.14)$$

Here A and B represents the atomic numbers of high Z and low Z layers, respectively. The above formulas for XRR and GIXRF yield are valid for perfectly parallel or collimated incident x-ray beam. However, if the incident x-ray beam has certain divergence, expressed as α , then the reflectivity R [eqn. (4.5)] and fluorescence yield F [eqn. (4.8)], can be expressed as a convolution of the reflectivity/fluorescence function and the primary x-ray beam intensity distribution $I(\alpha)$.

$$R(\theta) = \frac{\int R(\theta - \alpha) \times I(\alpha) d\alpha}{\int I(\alpha) d\alpha} \quad (4.15)$$

and

$$F(\theta) = \frac{\int F(\theta - \alpha) \times I(\alpha) d\alpha}{\int I(\alpha) d\alpha} \quad (4.16)$$

In the CATGIXRF program, the shape of the primary incident x-ray beam has been considered as a Gaussian profile under $\pm 3\sigma$ limits.

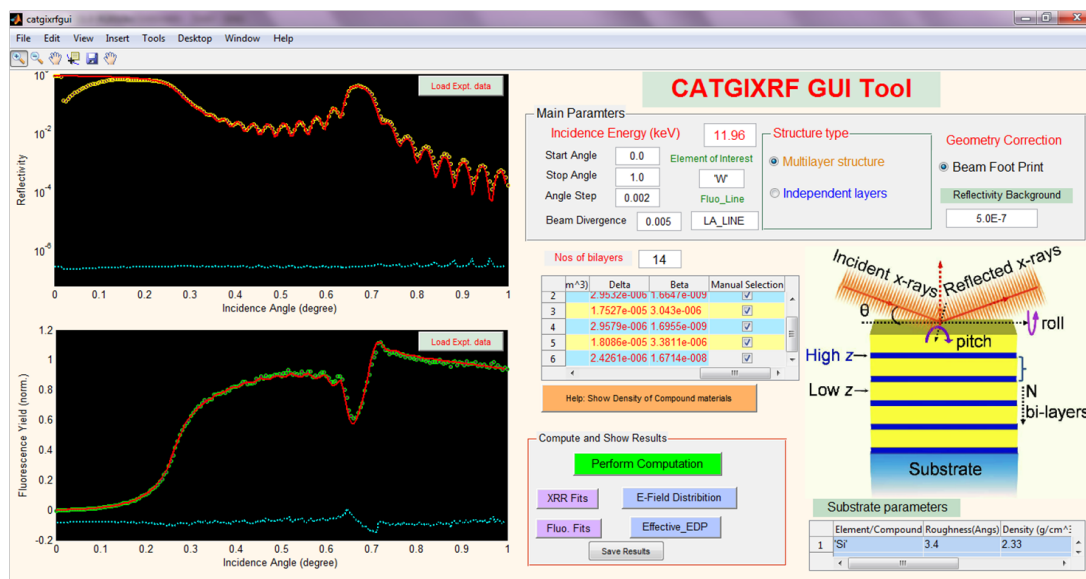


Figure 4.4: A snapshot of the main window of the GUI-CATGIXRF program, showing different command tools and buttons for input and output of the data. To allow model based fitting of the thin film medium, one can define the structure type by selecting options; ‘multilayer structure’ or ‘independent structure’, as described in the text.

4.3.2 GUI-CATGIXRF Interface

The CATGIXRF program runs in a standalone GUI window, as can be seen from the Fig. 4.4 and requires minimal inputs from a user. The structure type of a thin film medium, either ‘*Independent layers*’ or ‘*Multilayer Structure*’ can be selected using radio buttons selection. Depending upon the structure type, it is possible to provide inputs for the number of layers that contribute in a multilayer thin film structure. The inputs for the constituent’s layers such as layer index, element symbol or chemical compound formula for the layer material, thickness, roughness, density can be supplied through a GUI table that appears in the program window after the selection of thin film structure type. The experimental conditions such as energy of the incident x-rays, start angle, stop angle, angle step and beam divergence of the incident x-ray beam or instrumental resolution factor can be defined under the section of ‘Main Parameters’ panel. For the calculation of grazing incidence angle dependent x-ray fluorescence profile of an element it is important to provide inputs such as element symbol and appropriate characteristics fluorescence lines; K-alpha or L-alpha for the element of

interest. To ensure ease of use, we have defined another table to feed substrate parameters exactly below the schematic representation of the multilayer structure that appears in the GUI-CATGIXRF window. In this table, it is also possible to describe the element symbol or chemical compound formula for the substrate material. After providing all appropriate inputs in the GUI window, it is possible to compute XRR and GIXRF profiles using the push button 'Perform Computation'. The results of calculations appear in the respective XRR and GIXRF plot windows on the GUI panel. For the fitting of experimental data, it is necessary to load the measured XRR and GIXRF data prior to the computation of the theoretical XRR and GIXRF profiles.

4.3.3 Program internals

The GUI window of the CATGIXRF program is designed in the MATLAB (R2010b) platform while the core computation code for the calculation of XRR and GIXRF profiles is developed on the FORTRAN 77 platform. As an input, CATGIXRF program requires energy of incident radiation E_0 , thickness of layer d_j , density of the layer ρ_j , atomic number of the detected element Z and its characteristics fluorescence energy E , angular range namely start angle, end angle and the angular step. One can also specify the divergence of the primary x-ray beam, if primary beam divergence effects need to be corrected, or otherwise it can be set equal to the angular step. Primary beam divergence effects in GIXRF analysis of multilayer structures have been described elsewhere [72]. Furthermore, the interfacial roughness σ_j for each interface can be specified in angstrom units. The program needs the values of δ_j and β_j for layer and substrate materials. The program also requires the value of photo electric absorption coefficient of the detected element at incident primary energy E_0 and mass absorption coefficients of the layer (in cm^2/g) at incident energy E_0 , and at the characteristics fluorescence energy of the detected element E . The CATGIXRF program utilizes x-ray library (*xraylib*) functions [121] for the computation of fundamental parameters for x-ray - matter interactions. The

GUI-CATGIXRF program can be successfully run on any Windows (32-bit) machine after installing a command line utility of the *xraylib* (*xraylib-3.1.0-win32-cli.exe*) on the Windows machine. This allows the GUI-CATGIXRF to automatically obtain the optical constants for the different materials or elements at a given incident x-ray energy. The *xraylib* utility eliminates the requirement to prepare or use look up x-ray data tables for the optical constants of different materials and their compounds. Moreover to help a user we have also provided a look up table for density (gm/cm^3) of most common materials. One can start with an input guess of layer parameters thicknesses d_j , concentration c_j , density ρ_j and roughness σ_j . These values are changed manually until a good fit with the experimental data is obtained. A normalized fluorescence profile can be obtained by normalizing the GIXRF intensity at higher incidence angle.

4.3.4 Main features and utilities of the CATGIXRF program

GUI-CATGIXRF program calculates the XRR and GIXRF profiles simultaneously. It takes into account the interfacial roughness effects, the inter element absorption effects and the effect of primary beam divergence. The program can be used for several diverse applications: for calculation of the XRR and GIXRF intensities from thin films and multilayer structures, examination of XSW effects in multilayers, characterisation of metal nanoparticles on substrates and mirrors. It can also be used to study x-ray waveguide structures using marker fluorescence measurements. The GUI-CATGIXRF program offers various salient features and capabilities for fitting and visualization of XRR and GIXRF data. Some of them are listed in the following subsections:

Reflectivity background

It is possible to include background counts during the calculation of XRR profile for a thin film medium. The background in the reflectivity profile can be either measured

experimentally or can be estimated theoretically using the reflectivity counts at an incidence angle far above the critical angle where Kiessig oscillations almost disappear in the measured XRR profile. Inclusion of reflectivity background gives an opportunity to reliably estimate roughness effects in a thin film structure.

Calculation of Electron density profile

The in-depth electron density profile (EDP) of a thin layered medium can be computed from the best fitted parameters of a thin film medium. An '*Effective-EDP*' push button is provided in the *compute and show results* window of the CATGIXRF to generate in depth electron density profile of a thin film structure.

Calculation of Electric field distribution

The CATGIXRF has provided an option to compute x-ray electric field distribution in the different layered medium as well as above the reflector surface (in air or vacuum) as a function of angle and depth. The '*E-Field Distribution*' push button in the *compute and show results* window of the CATGIXRF gives the electric field distribution.

Beam foot print

X-ray beam foot print or geometrical effects markedly modify the measured XRR and GIXRF patterns of a thin film structure. In XRR, the geometrical effects dominantly appear in the vicinity of critical angle and it changes the nature of flat-top in the vicinity of total external reflection region. Since, this region does not contain any useful information about a thin film medium, it may be ignored during fitting of the measured XRR profile. Inclusion of a knife edge arrangement on the sample surface provides an alternative experimental approach to eliminate beam foot print effect in the XRR measurements. However, in case of the GIXRF measurements, the beam foot print

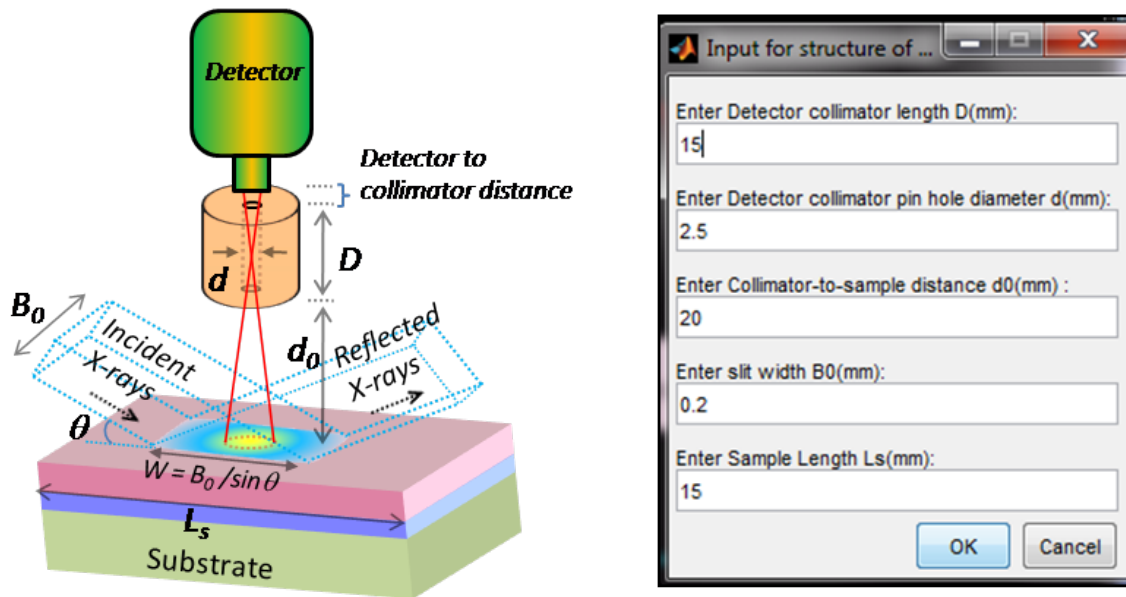


Figure 4.5: A schematic illustration for the beam foot print effect in the grazing incidence x-ray fluorescence measurements. On the right hand side, a snapshot of the sub-program window of the GUI-CATGIXRF program is shown that takes different input parameters from a user to define excitation geometry for a thin film specimen for the correction of beam foot print effect in the computed GIXRF profile.

effects become noticeably visible at higher incidence angles. The GUI-CATGIXRF program, corrects beam foot print effects in the computed GIXRF profile using the analytical formalism presented in the literature [48]. Fig. 4.5 depicts a schematic representation for the x-ray reflectivity measurement from a thin film structure along with the details of experimental geometry for fluorescence assisted GIXRF measurements. On the right side of the figure a snapshot of the sub-window of GUI-CATGIXRF program is shown that asks the inputs from a user for the correction of beam foot print effect in the measured GIXRF profile.

Append layer functionality

The structure of a thin periodic multilayer medium may not be truly periodic. There is always a possibility for the presence of a buried layer interface medium or thickness inhomogeneity of the bilayer period inside the multilayer structure. In such cases it is quite useful to describe the in-depth distribution profile of a thin film medium using

append layer functionality. The GUI-CATGIXRF program provides the option to add an append layer structure at any depth inside a thin film medium during the computation of XRR and GIXRF profiles.

Fit residuals

In the GUI-CATGIXRF program χ^2 (χ^2) minimization procedure is used for the simultaneous fitting of XRR and GIXRF data. The fit residuals of individual XRR and GIXRF profiles directly indicate the goodness of the fits. It is possible to obtain precise and reliable estimate for the microstructural parameters of a thin film medium when XRR and GIXRF fit residuals are minimised within the range of 2-6 %.

Manual Selection

Although various website and individual programs provide the x-ray data sets for optical constants and mass absorption coefficients for most common materials in the x-ray region (300 eV - 30 keV) [35, 101–107]. However, in some specific cases the availability of reliable optical constants and absorption database is still limited. For example, value of the optical constants (δ, β) especially in the vicinity of absorption edge of an element may vary or fluctuate \sim 20-30 % or more. To overcome this problem in the GUI-CATGIXRF program, we have provided a freedom (or an option) to user: initially, start fitting with the tabulated values of x-ray optical constants (δ, β) using the xraylib utility and then check “Manual Selection” box to vary them manually in order to derive more accurate values corresponding to the best fit results of the measured XRR and GIXRF profiles. This specific utility of the GUI-CATGIXRF facilitates an opportunity for the user to adopt and evaluate even unknown thin layered materials for which the optical constants at specific x-ray are not available in the literature.

Compute and show results

Compute and show results panel of the GUI-CATGIXRF program allows a user to calculate both the XRR and GIXRF profiles simultaneously using a push button ‘*Perform Computation*’ after providing all relevant input parameters in the main GUI window. Using the ‘XRR fit’ and ‘Fluo. Fit’ push buttons, it is possible to display fitted XRR and GIXRF profiles along with experimental data and fit residuals ($\chi_{expt.} - \chi_{theo.}$) in separate figure windows. The GUI-CATGIXRF program also provides an ability to compute electromagnetic x-ray field intensity distribution inside a thin layer medium using the recursive method [97, 117]. The push button ‘E-field distribution’ displays the computational results in a separate figure window. The push button ‘Effective_EDP’ provides an opportunity to determine effective electron density distribution inside the thin film medium as a function of film depth. The computed results for the effective electron density distribution appear in a separate window. For the fitting of the experimental XRR and GIXRF profiles one needs to provide an initial guess for the microstructural parameters such as thicknesses (d), density (ρ) and roughness (σ) of a thin film medium. The GUI-CATGIXRF program automatically obtains various optical constants for the thin film medium using its xraylib functionality. The structural parameters are then slowly varied to obtain the best fit XRR or GIXRF profiles corresponding to the measured data. It may be interesting to mention here that the angle dependent XRR and GIXRF profiles, which are complementary in nature, help each other in a self-consistent feedback manner to find out a precise and reliable estimate for the microstructural parameters of a thin layered structure. This is a general statement which would be applicable to all types of thin layered systems utilizing combined XRR and GIXRF analysis approach for the structural characterisation. The GUI-CATGIXRF program offers this unique functionality for the fitting of XRR and GIXRF profiles of a thin film structure. In the GUI-CATGIXRF program as such no specific criterion is implemented at which the fitting procedure can be stopped, however, it is purely left on

the satisfaction and judgement of the user. Usually, when fit residuals in both XRR and fluorescence are minimized within the range of 2-6%, one can terminate the fitting procedure.

4.4 Some example studies

In this section, various potential features of the GUI-CATGIXRF program have been demonstrated using some example calculations.

4.4.1 An x-ray wave guide structure

For a simple case, a multilayer structure consisting of three independent layers (trilayer structure) Cr (55 Å) / B₄C (400 Å) / Cr (250 Å) on top of a Si substrate was considered. Here, a low Z layer (Boron carbide) is sandwiched between two high Z (Chromium) layers. Such a trilayer structure is usually considered as x-ray wave guide. Figure 4.6 depicts the computed XRR profile and angle dependent GIXRF profile for the Cr-K α fluorescence intensity. For these computations, the incident x-ray energy of 12 keV was assumed. It can be seen from Fig. 4.6(a) that, the XRR profile shows a distinct and systematic interference fringes (Kiessig oscillations). The relative amplitude and width of these Kiessig oscillations strongly depend on the thickness and interface roughness of the Cr and B₄C layers. Furthermore, one can also observe a few small dips in the XRR profile below the critical angle (θ_c). These dips in the XRR appear due to the formation of selective excitation modes inside the B₄C layer medium. These excitation modes will be described with more details in the later figure (Fig. 4.7). Figure 4.6(b) demonstrates the variation of Cr-K α fluorescence intensity, emitted from the Cr (55 Å) / B₄C (400 Å) / Cr (250 Å) trilayer structure as a function of grazing incidence angles. It can be seen from Fig. 4.6(b) that several peaks corresponding to the resonant excitation modes (TE₀, TE₁, TE₂, etc.) appear in the computed Cr-K α fluorescence profile below critical angle

(θ_c) of the thin film medium. These peaks occur due to the formation of XSW field in the Cr / B₄C / Cr trilayer medium. The relative peak heights of these resonant modes strongly depend on the XSW field intensity distribution inside the trilayer medium as well as on the surface-interface properties of the high and low Z layers. Fig. 4.7(a) describes the contour plot for the electric field intensity (EFI) distribution inside the Cr (55 Å) / B₄C (400 Å) / Cr (250 Å) waveguide structure, calculated at an incident x-ray energy of 12 keV, as a function of incidence angle and film depth in the trilayer medium. From Fig. 4.7(a), it can be seen that various transverse electric field modes (TE₀, TE₁, TE₂, etc.) are excited in the B₄C layer medium at definite incidence angles. At large incidence angles (for higher modes), the x-ray field intensity moves towards the interface boundaries of the layered medium, this provides a possibility to determine the interface properties of the high and low Z layers by measuring Cr-K α fluorescence intensity emitted from respective top and bottom Cr layers. The effective electron density for the Cr / B₄C / Cr trilayer structure is also calculated using GUI-CATGIXRF program and is shown in Fig. 4.7(b). Table 4.1 summarizes the structural parameters of the trilayer thin film medium that were used during the computation of curves presented in Figs. (4.6 and 4.7).

Table 4.1: Structural parameters used in the GUI-CATGIXRF program for the computation of XRR and GIXRF (Cr-K α fluorescence) profiles for a Cr/B₄C/Cr trilayer structure.

Element/Compound	Thickness d (Å)	Roughness σ (Å)	Density ρ (gm/cm ³)
Cr	60.0	3.0	7.18
B ₄ C	400.0	3.3	2.50
Cr	250.0	4.0	7.18

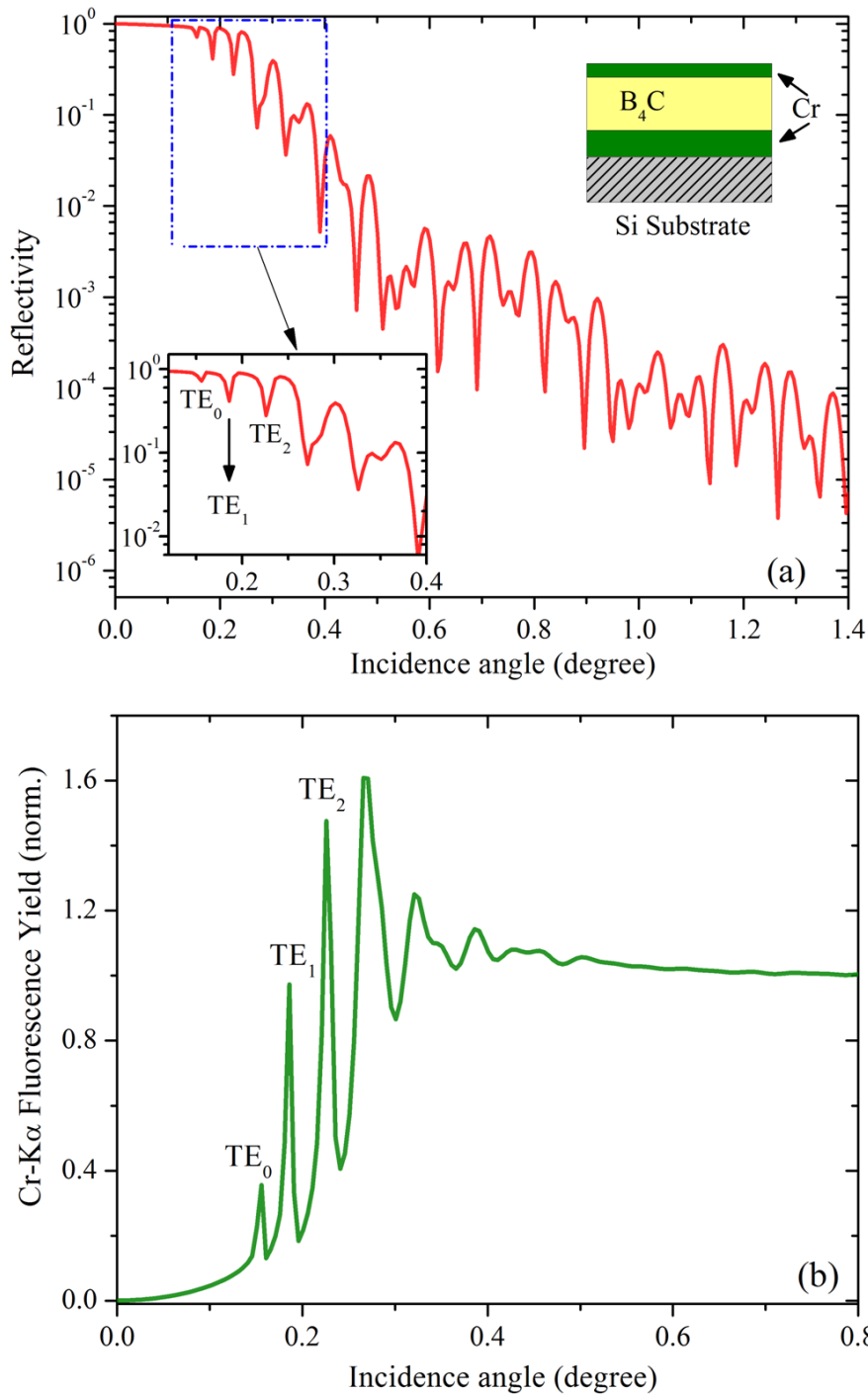


Figure 4.6: Computed XRR and GIXRF (Cr-K α fluorescence) profiles of a Cr (55 Å) / B₄C (400 Å) / Cr (250 Å) trilayer structure, deposited on a Si substrate surface. The computations are performed using the GUI-CATGIXRF program assuming an incident x-ray energy of 12 keV. (a) XRR profile, (b) GIXRF (Cr-K α fluorescence) profile, showing various transverse electric field excitation modes (TE₀, TE₁ and TE₂) that excite inside low Z material (B₄C) at specific incidence angles. In the inset of figure (a) we have also shown an extended view of the XRR profile in the vicinity of critical angle, showing location of the incidence angle for various excited modes.

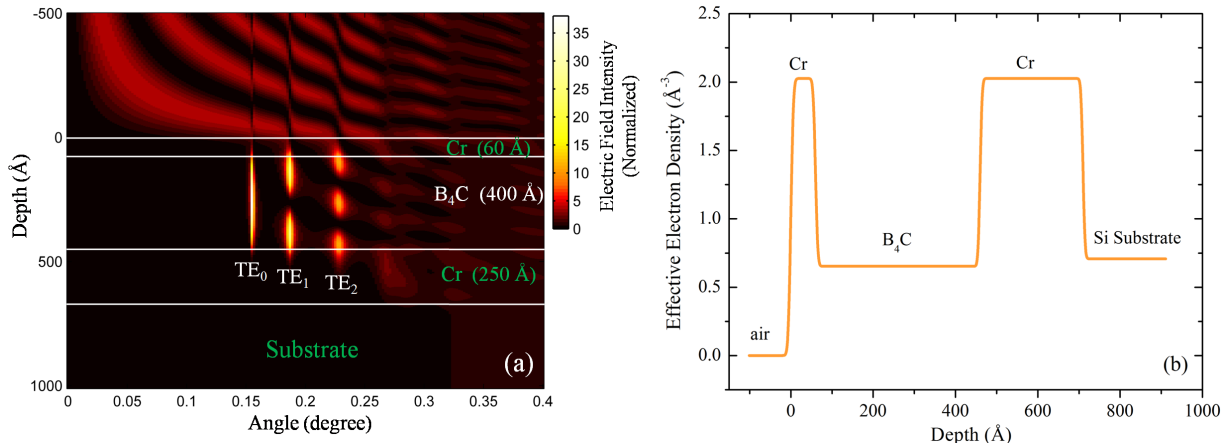


Figure 4.7: Electric field intensity (EFI) distribution computed inside the Cr (55 Å) / B₄C (400 Å) / Cr (250 Å) trilayer structure on a Si substrate surface using GUI-CATGIXRF program. The formation of different transverse electric field modes (TE₀, TE₁ and TE₂) can be clearly observed in the B₄C medium at distinct incidence angles. (b) Computed effective electron density profile for the trilayer medium.

4.4.2 Applicability of GUI-CATGIXRF for the characterisation of thin layered materials

To demonstrate the applicability of the GUI-CATGIXRF program, experimental measurements for a few thin layered structures of different surface-interface properties were carried out and determined their microstructural properties were determined using combined analysis of XRR and GIXRF profiles.

W-B₄C bilayer structure

Bilayer structure consisting of B₄C and W materials was fabricated on the polished Si (100) substrates at room temperature using a magnetron sputtering system [50]. Figure 4.8(a) shows measured and fitted XRR and GIXRF profiles obtained for the W (275 Å)-B₄C (300 Å) bilayer structure at incident x-ray energy of 12 keV. In the figure, W-L α fluorescent radiation emitted from the W-B₄C bilayer sample at different grazing incidence angles is plotted along with the measured x-ray reflectivity data. From Fig. 4.8(a), it can be seen that one finds an encouraging level of agreement between the

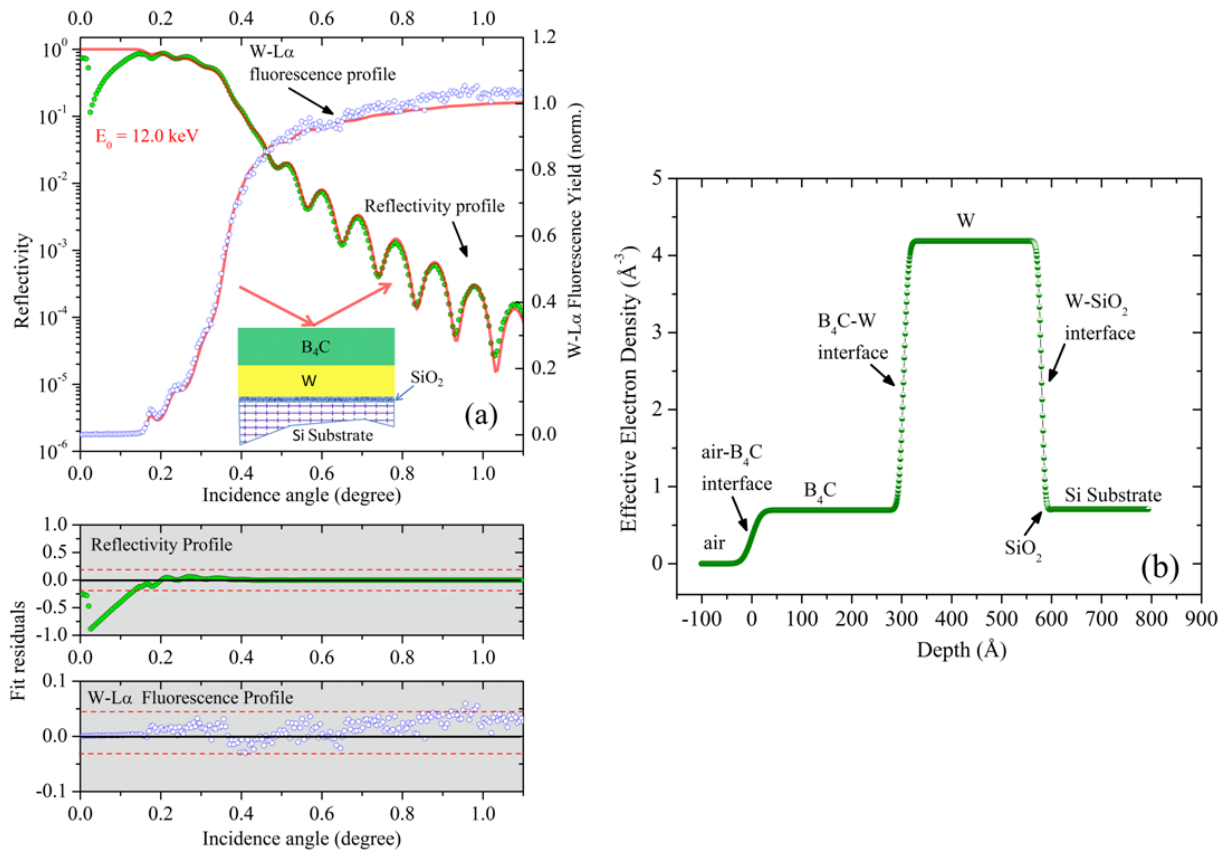


Figure 4.8: (a) Measured XRR and GIXRF (W-L α fluorescence) profiles along with fitted curves for the W (276 Å) - B₄C (304 Å) bilayer structure at incident x-ray energy of 12 keV. The fitted results also reveal the presence of a SiO₂ layer of thickness ~ 12.7 Å at the interface of W layer and Si substrate, as illustrated in the inset of the figure. Scattered points are the measured data while solid lines represent best fit curves to the experimental data. The fit residuals of the respective profiles are shown below. (b) Effective electron density profile for the bilayer medium computed from the best fit results.

experimental and computed profiles. It can also be noticed from Fig. 4.8(a), that the reflectivity and W-L α fluorescence profiles are anticorrelated in nature. One observes maximum fluorescence intensity of the W-L α line especially at those locations where x-ray reflectivity is minimum. This feature of the combined XRR-GIXRF method can be clearly recognized below critical angle $\theta_c \approx 0.32^\circ$. At higher incidence angles, the reflected intensity of the W-B₄C bilayer structure reduces rapidly ($R \propto \frac{1}{\theta^4}$), as a result, one does not observe small fluorescence oscillations corresponding to the Kiessig fringes that appear in the reflectivity profile at higher incidence angles. Thus, the W-L α fluorescence yield at higher incidence angles remains more or less constant. The best

fitted XRR and GIXRF profiles obtained from GUI-CATGIXRF program provide a thickness of the B₄C layer $\sim 304 \pm 3 \text{ \AA}$ and for the W layer $\sim 276 \pm 2 \text{ \AA}$. The roughness of B₄C (W) layers was found to be 14.5 \AA (7.7 \AA) respectively. The combined XRR and GIXRF analysis also reveals the presence of a SiO₂ layer of thickness $\sim 12.7 \pm 0.8 \text{ \AA}$ with a roughness value of $\sim 6 \pm 0.6 \text{ \AA}$ at the interface between tungsten and Si substrate. The fitted microstructural parameters of the W-B₄C bilayer structure at incident x-ray energy of 12 keV are summarized in Table 4.2. In Fig. 4.8(a), we have also plotted the fit residuals for the fitted XRR and GIXRF profiles, obtained using GUI-CATGIXRF program. The small fit residuals ($<5 \%$) provide an encouraging level of confidence for the computed micro structural parameters of the bilayer medium. Figure 4.8(b) depicts effective electron density profile (EDP) computed for the W-B₄C bilayer structure corresponding to the best fit experimental results. It can be seen from Fig. 4.8(b), the sharpness of the electron density profile at the interface boundary decreases if the interface roughness of the medium increases and vice-versa.

Table 4.2: Fitted microstructural parameters of the W-B₄C bilayer structure, determined from the GUI-CATGIXRF program using combined XRR and GIXRF (W-L α fluorescence) analysis at incident x-ray energy of 12 keV.

Element/Compound	Thickness d (Å)	Roughness (Å)	σ	Density ρ (gm/cm ³)
B ₄ C	304.0 ± 3.0	14.5 ± 1.5		2.4 ± 0.1
W	276.0 ± 2.0	7.7 ± 0.8		18.3 ± 0.6
SiO ₂	12.7 ± 0.8	6.0 ± 0.6		2.1 ± 0.2

W-B₄C multilayer structure

Multilayer structure consisting of B₄C and W materials was fabricated on the polished Si (100) substrates at room temperature using a magnetron sputtering system [50]. In this section the structural characterisation of a W-B₄C multilayer structure is presented. Simultaneous GIXRF and XRR measurements of the bilayer and multilayer structures

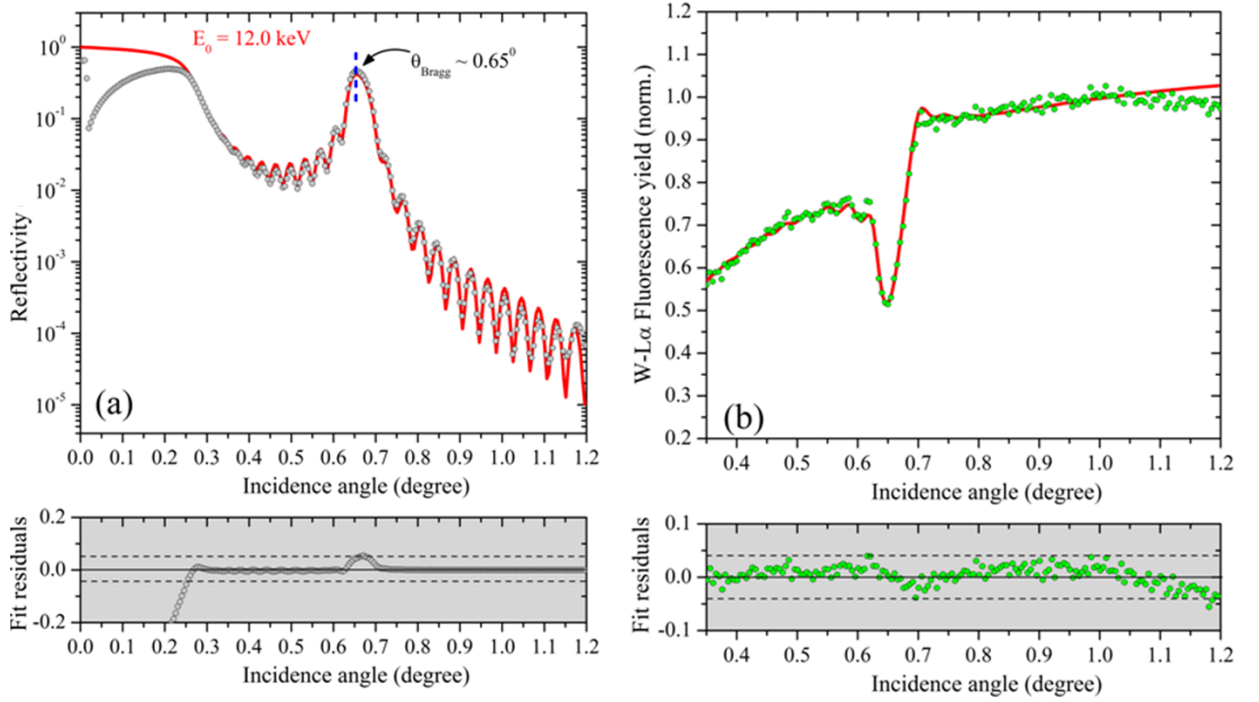


Figure 4.9: Measured and fitted XRR and GIXRF (W-L α fluorescence) profiles along with the fit residuals for a W-B $_4$ C periodic multilayer structure of parameters $d = 48.5 \pm 0.8$ Å and, number of bilayers $N = 15$ on a Si (100) substrate surface at incident x-ray energy of 12 keV. (a) XRR profile, (b) GIXRF (W-L α fluorescence) profile in the vicinity of Bragg region. Scattered points are the measured data while solid lines represent best fit curves to the experimental data.

were carried out in $\theta - 2\theta$ geometry using BL-16 reflectometer station [46, 47, 115, 122] at Indus-2 synchrotron facility, in the ambient air environment. Figure 4.9, describes measured XRR and W-L α fluorescence profiles along with the fitted curves for the W-B $_4$ C periodic multilayer structure consisting of $N = 15$ bilayer periods on the Si substrate surface. The XRR and fluorescence experimental data were fitted simultaneously using the GUI-CATGIXRF program. The layer thickness and roughness values of the high-Z and low-Z layer were allowed to vary during the fitting procedure. The density of the high-Z medium (W layers) was also allowed to change during the fitting in order to find a close match with the measured XRR data, especially in the vicinity of the critical angle of the multilayer structure. During the fitting process, the optical constants (δ and β) of the Henke's tabulation [123], were obtained using xraylib utility, and deposited thickness values of the multilayer structure were taken as the initial

guess. Both the XRR (Fig. 4.9(a)) and W-L α fluorescence (Fig. 4.9(b)) profiles were fitted consistently to derive the microstructural parameters of the W-B₄C multilayer structure such as thickness of the layers, surface roughness, and the interface diffusion between the high-Z and low-Z layers. The fitting procedure was repeated until both the XRR and W-L α fluorescence profiles are best fitted to the experimental data. The best fitted results to the measured XRR and W-L α fluorescence profiles of the W-B₄C multilayer give a value of the multilayer bilayer period thickness $d = d_W + d_{B_4C} = 48.5 \pm 0.8 \text{ \AA}$ with individual thickness of W and B₄C layers to be $d_W = 25.9 \pm 0.5 \text{ \AA}$, $d_{B_4C} = 22.6 \pm 0.6 \text{ \AA}$, and $\sigma_W = 5.0 \pm 0.6 \text{ \AA}$ and $\sigma_{B_4C} = 5.0 \pm 0.6 \text{ \AA}$ respectively for the roughness values. The estimated thickness of W and B₄C layer were 30 \AA and 25 \AA . The thickness of the W layer in the last bilayer period, near to the Si substrate was found to be slightly high ($d_W = 45.0 \pm 1.0 \text{ \AA}$), compared to the average thickness of the W layer in the other bilayer periods. This extended W layer was created inadvertently during the plasma stabilization in the magnetron sputtering system. The non-uniformity of thickness in a multilayer structure needs to be analysed. Detailed analysis of non-uniformity of thickness or buried layer of W inside a multilayer structure is described in the later section (4.5). In addition, we could also reveal the presence of a low density SiO₂ interface layer of thickness $\sim 20 \text{ \AA}$ between Si substrate and W-B₄C multilayer stack. In Fig. 4.9, we have also plotted the fit residuals for the XRR and W-L α fluorescence profiles to show the goodness of the theoretical fits. Table 4.3 summarizes fitted microstructural parameters of the W-B₄C multilayer structure determined using GUI-CATGIXRF program. The net errors in the determined microstructural parameters of the bilayer and multilayer thin film samples were obtained from the experimental measurement accuracies (*e.g.* counting statistics, repeatability, angular step resolution, and angular repeatability of the experimental data etc.) and found to be between 5 to 12 %.

Table 4.3: Microstructural parameters of the W-B₄C periodic multilayer structure consisting of N = 15 bilayers of the B₄C and W materials. These parameters were determined from the GUI-CATGIXRF program using combined XRR and GIXRF (W-L α fluorescence) analysis.

Element/Compound	Thickness d (Å)	Roughness σ (Å)	Density ρ (gm/cm ³)
B ₄ C	22.6 ± 0.6	3.6 ± 0.4	2.16 ± 0.1
W	25.9 ± 0.5	5.0 ± 0.6	16.8 ± 0.6
SiO ₂	20.0 ± 2.0	5.0 ± 0.6	2.1 ± 0.2

4.5 Analysis of interface morphology of a deeply buried layer in a multilayer structure

Long term durability of a thin film device is strongly correlated with the nature of the interface structure associated between different constituent layers. The reflection efficiency of synthetic periodic multilayer structures, which are primarily employed as artificial x-ray Bragg reflectors in many applications, is predominantly dictated by the nature of the buried interfaces between different layers. Recently, an increasing interest has been observed in case of characterisation of the buried interfaces in thin layered materials, as they significantly amend the physical properties of a thin film device [85–87, 93, 124]. The applicability of combined XRR-XSW analysis approach for probing deep buried interfaces inside a W-B₄C periodic multilayer structure have been demonstrated in this section. To understand the influence and underlying degradation pathways of buried interface layers on the measured XRR and GIXRF profiles, numerical simulations were carried out by considering a buried layer of W at different depths inside the W-B₄C multilayer structure. The results clearly show that the combined XRR and XSW analysis allows one to explore the location and structural morphology of a buried interface layer inside the periodic multilayer structure. The cross sectional transmission electron microscopy (TEM) measurements obtained on the same specimen support the observations of XRR and XSW analysis. The results also reveal that the present approach has the capability to determine slight density variations or any

atomic migration occurring in any layer deep inside a thin layered medium.

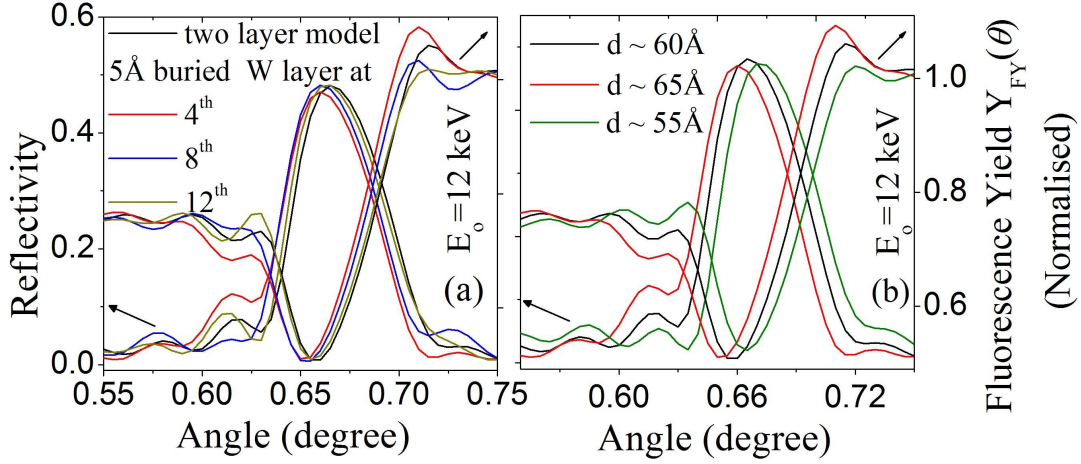


Figure 4.10: (a) calculated XRR and GIXRF profiles of a W-B₄C multilayer structure at 12.0 keV incident x-ray energy assuming a thickness asymmetry in the bilayer period of $\sim 5 \text{ \AA}$ at 4th, 8th, and 12th bilayer location respectively. (b) Simulated XRR and GIXRF profiles of the W-B₄C multilayer structure assuming a thickness variation of $\pm 5 \text{ \AA}$ in the W layer at 4th bilayer location.

4.5.1 Numerical simulation to understand the depth profiling of buried layer

During the numerical simulations, we have considered a W-B₄C multilayer structure consisting of N=15 bilayers on top of a Si(100) substrate surface. The bilayer period thickness of the multilayer structure was assumed to be $d \sim 60 \text{ \AA}$ with an individual thickness of W (B₄C) layer to be $d_W \sim 25 \text{ \AA}$ ($d_{B_4C} \sim 35 \text{ \AA}$). The roughness values of the W and B₄C layers were assumed to be $\sim 5 \text{ \AA}$ and $\sim 4 \text{ \AA}$ respectively. Figure 4.10(a) shows the computed XRR and W-L α fluorescence profiles of the W-B₄C multilayer after assuming an additional buried layer of W of thickness $\sim 5 \text{ \AA}$ at different locations (4th, 8th, and 12th bilayer position respectively) inside the multilayer structure. In this figure, the XRR and GIXRF profiles of W-B₄C multilayer structure computed in the ideal condition (i.e., without assuming any inclusion of buried W layer) at the incident x-ray energy of 12.0 keV were also compared. It can be seen from Fig. 4.10(a), that XRR and GIXRF

profiles differ significantly as the location of the buried layer of W changes inside the multilayer structure. XSW induced modulations in the XRR and GIXRF profiles are usually very weak, if a buried layer is present deep inside the multilayer structure. This is mainly because of the small phase changes that occur between incident and outgoing (reflected) wave.

The sensitivity of the combined XRR and GIXRF measurements was also quantitatively demonstrated in a condition when, the bilayer period of a multilayer is not uniform at various depths. Figure 4.10(b) depicts computed XRR and W-L α fluorescence profile of the W-B₄C multilayer structure by accounting a very small variation in thickness of W layer ($\Delta d \sim \pm 5 \text{ \AA}$) at the 4th bilayer position. It can be seen from the computed results (Fig. 4.10(b)), W-L α fluorescence profile is fairly sensitive to the small variation of the bilayer period thickness at a particular depth inside the multilayer structure.

4.5.2 Probing buried interfaces

Figures 4.11(a), and 4.11(b) show the measured and fitted XRR profiles of the W-B₄C multilayer structure at 10.0 keV and 12.0 keV x-ray energies respectively. During the model fitting [120] of the experimental XRR data two distinct cases were considered; in one case, a perfect bilayer structure (without any buried layer) for the W-B₄C multilayer structure with a number of bilayers N=15 with a period thickness $\sim 50 \text{ \AA}$ was assumed. In the other case, a similar structure for the W-B₄C multilayer along with a buried layer of W at 15th bilayer location was considered. From Figs. 4.11(a), and 4.11(b), it can be observed that if we assume a buried layer of W in our fit model the location and the amplitude of the Kiessig oscillations as well as respective Bragg reflections match quite well with the measured XRR profile. On the other hand, if the XRR profile is computed assuming a perfect bilayer model, it differs significantly from the experimental data especially in the incidence angle regime between the first and second Bragg peaks, as depicted in the inset of the Figs. 4.11(a) and 4.11(b). However, a subtle difference can be

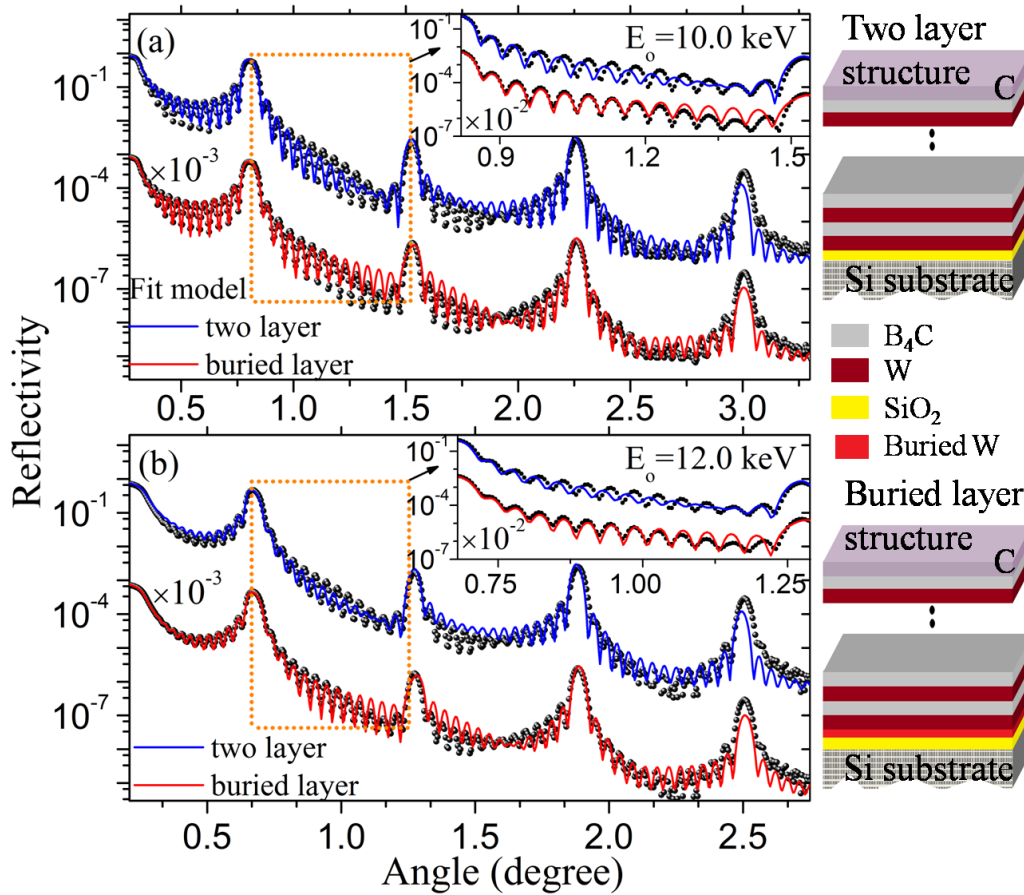


Figure 4.11: Measured (scattered points) and fitted (solid lines) x-ray reflectivity profiles of W-B₄C multilayer structure at two different incident x-ray energies of (a) 10.0 keV and (b) 12.0 keV. On the right hand side, a schematic illustrations depict two layer and buried layer model of the W-B₄C multilayer. In this layer model, a low-density C layer is also marked on top of the W-B₄C multilayer medium.

seen at 4th Bragg peak. This deviation probably can be attributed to the nonlinear diffuse scattered background produced from the multilayer sample. The thickness and roughness values of the individual layers, as well as the buried layer of the multilayer structure, were determined from the best fitted XRR profiles and are summarized in Table 4.4.

To validate the conclusions drawn from XRR measurements, combined XSW induced fluorescence and XRR measurements at 12.0 keV x-ray energy were carried out. An extended view of the combined XRR and GIXRF profiles in the vicinity of the 1st Bragg peak is shown in the inset of Fig. 4.12(a). It can be seen here that the reflectivity profile computed assuming a buried layer structure matches quite well with experimental data at both the high and low angle sides of the 1st Bragg peak. On the contrary, the fitted XRR

profile does not follow the experimental data points especially at the higher angle side of the Bragg peak in a situation when computations are performed using the two layer model. We arrive at a similar conclusion after fitting XSW induced W-L α and W-L β profiles in the vicinity of the 1st Bragg reflection peak, as illustrated in the inset of Fig. 4.12(a). In Fig. 4.12(b), we have shown computed electric field intensity (EFI) distribution inside the W-B₄C periodic multilayer structure as a function of incidence angle and film depth (z).

Table 4.4: Fitted microstructural parameter of the W-B₄C multilayer structure obtained by using XRR and XSW analysis. d = thickness (Å), ρ = density (g/cm³), σ = roughness (Å). All the error values in the determined microstructural parameters of multilayer structure are lies between 2-6 %.

Layer Material	10 keV XRR			12 keV XRR			12 keV XSW		
	d	σ	ρ	d	σ	ρ	d	σ	ρ
C	32.0	6.5	1.3	31.3	6.0	1.2	30.0	6.0	1.2
B ₄ C	24.0	3.6	2.2	23.6	3.2	2.1	22.3	3.2	2.1
W	26.0	5.0	17.4	26.4	4.6	17.3	25.4	4.6	17.3
buried W	18.0	5.0	17.4	18.0	4.6	17.3	16.6	4.6	17.3

4.5.3 Determination of in depth Electron density profile

Transmission electron microscopy (TEM) measurements on the W-B₄C multilayer structure were also carried out to verify the results obtained using XRR and XSW induced fluorescence measurements. The cross-sectional transmission electron microscopy measurements were performed at Philips CM200 transmission electron microscope with a W-filament cathode operating at 200 KV. Figure 4.13(a) depicts measured cross-section TEM micrograph, showing alternating W (dark fringe) and B₄C (light gray fringe) layers of the W-B₄C multilayer structure with a sharp interface boundary. Figure 4.13(b) shows the line scan profile derived from measured TEM micrograph. It can also be noticed from Fig. 4.13(b) that the 15th bilayer period is slightly asymmetric. This is due to the presence of an additional buried layer of W of thickness ~ 14.0 Å, which was formed unintentionally during the deposition process.

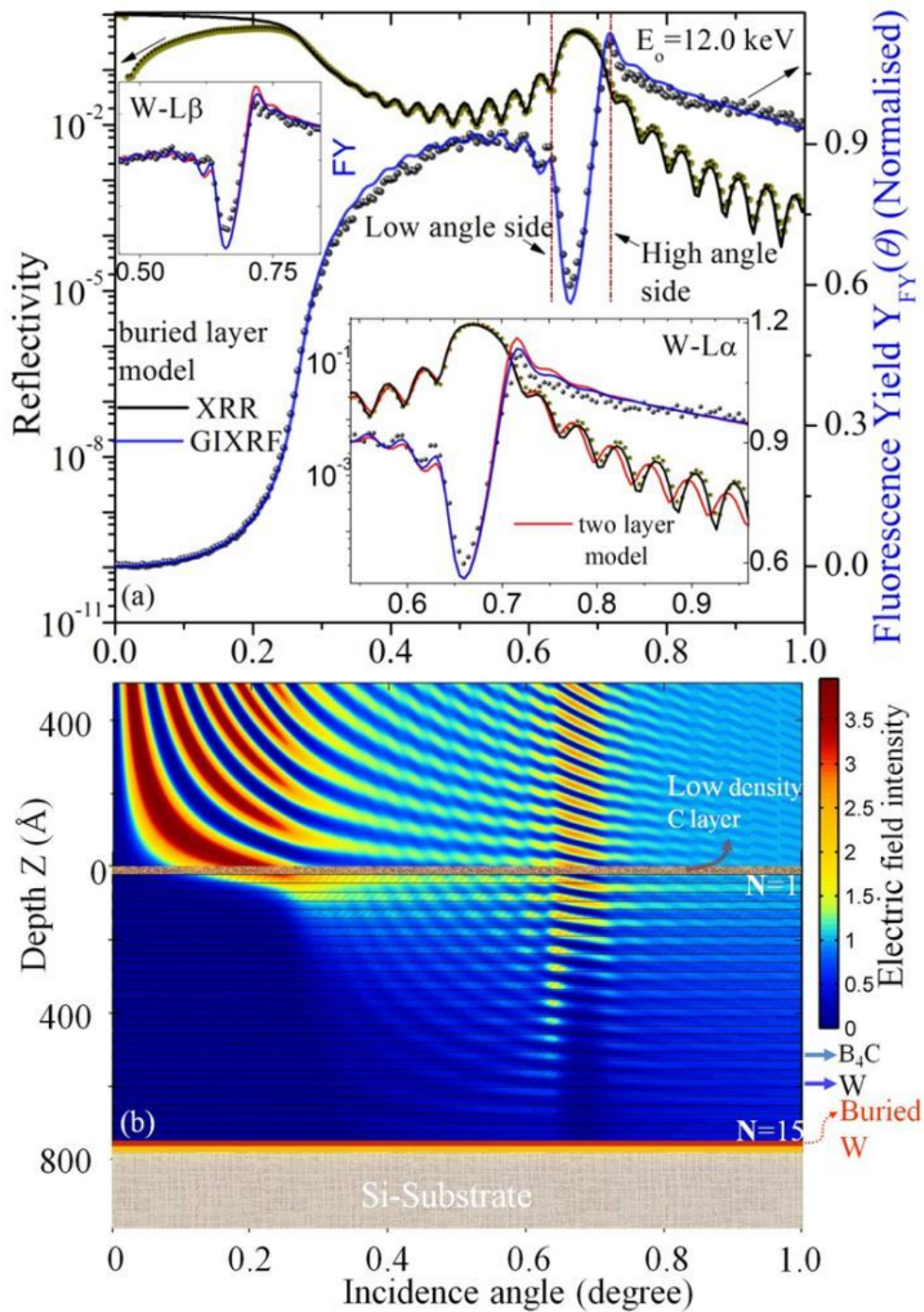


Figure 4.12: (a) Measured and fitted W-L α fluorescence and XRR profiles for the W-B₄C multilayer structure at an incident x-ray energy of 12.0 keV. The inset shows an extended view of the XRR and GIXRF profiles in the vicinity of the 1st order Bragg peak. (b) Computed x-ray field intensity (EFI) distribution inside a W-B₄C periodic multilayer structure at 12.0 keV x-ray energy.

The calculated period thickness of the W layer in the last asymmetric bilayer was found to be $\sim 51.0 \pm 2.5 \text{ \AA}$, which is in good agreement with the results obtained using effective electron density profile (EDP). The EDP profile, (Fig. 4.13(c)) of the W-B₄C multilayer structure was obtained from the best fit results of the XRR and GIXRF profiles as shown in Fig. 4.12(a). In the Fig. 4.13(c), the EDP profile of W-B₄C multilayer structure was also compared and plotted by considering an ideal case, after neglecting interface roughness effects ($\sigma = 0$) and assuming bulk densities of the W and B₄C layers. On the right side of Figs. 4.13(b) and 4.13(c), an enlarged view of the TEM line scan profile and EDP profile were given, where one could clearly distinguish a slight diffusion of W in the last B₄C layer (as shown by thick arrows). The diffusion of W increases the density of the B₄C layer ($\rho \sim 3.9 \text{ g/cm}^3$) and therefore reduces density contrast between W and B₄C layers in the 15th bilayer period (see Fig. 4.13(a)). One could also observe formation of a low density SiO₂ layer (thickness $\sim 22 \text{ \AA}$) between the multilayer structure and Si substrate, which is distinctly visible through the fitted EDP and TEM line scan profiles (see Fig. 4.13). These results clearly demonstrate the compelling abilities of the combined XRR and GIXRF analysis approach for the non-destructive determination of deeply buried interface layer structure inside a multilayer structure. Tungsten has an outer shell electronic configuration of $5d^4 6s^2 6p^0$. Its 5d band remains partially filled in case of divalent, trivalent, tetravalent, pentavalent compounds and completely empty in the case of the hexavalent compounds. Since the 5d, 6s and 6p electronic levels are very close to each other, hybridization of these orbitals is energetically favourable in many tungsten compounds. Such hybridization eventually modulates the nature of these higher shell energy levels [125–131]. Hence, depth resolved chemical speciation is often desirable to understand the underlying degradation pathways (*if any*) and its influence on the interfacial chemical changes in the case of a multilayer structure. The depth resolved chemical analysis of a multilayer structure is described in the later section (4.6).

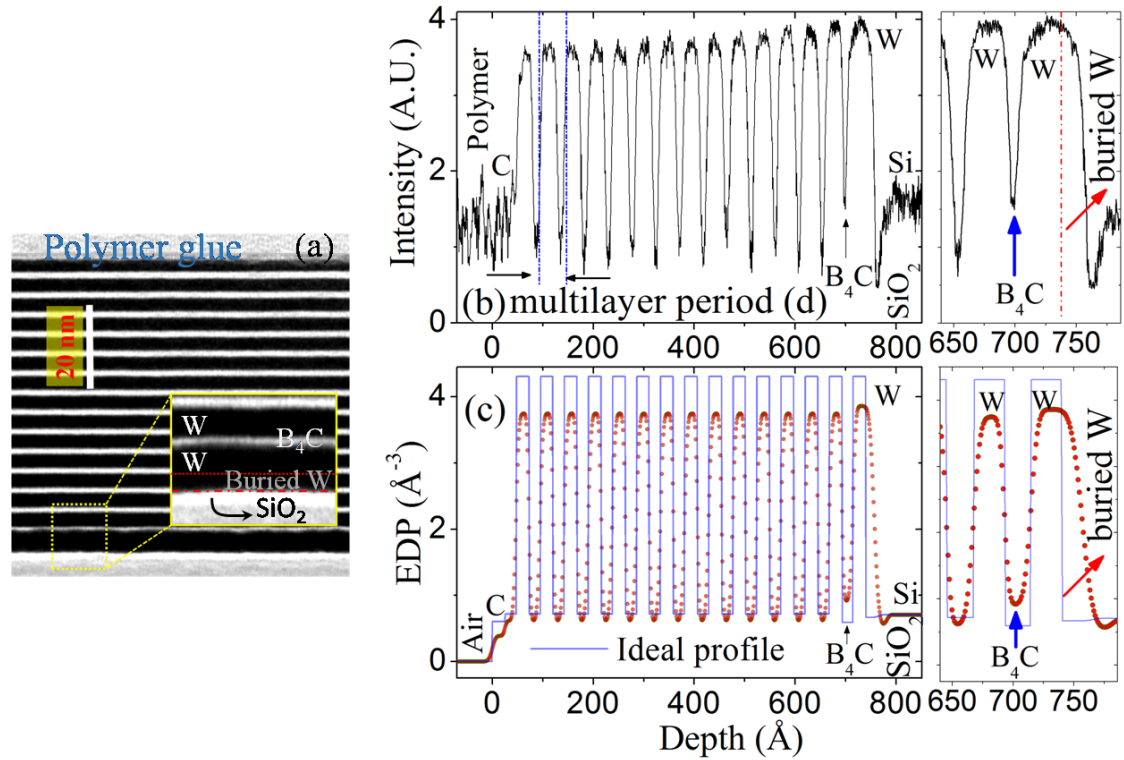


Figure 4.13: (a) Cross-sectional TEM micrograph of the W-B₄C multilayer structure. (b) A line scan profile derived from the cross section TEM micrograph. (c) Derived effective electron density profile (EDP) of the multilayer structure.

4.6 Depth resolved chemical speciation in a multilayer structure

Electronic states at the surface and interface boundary of a thin film medium significantly differ from that of the bulk due to strong orbital reconstruction or hybridization of near surface atoms [132]. Such a hybridization extensively modulates the physical properties of a thin film medium. Despite the recent advances in thin film growth methodology the interface boundary between two materials in a thin film can not be realised distinctly due to atomic migration [133]. Surface and interface alteration due to atomic scale modulation of the orbital occupation is an active area of research to unravel insights on many correlated and uncorrelated physical phenomena, such as, electronic and magneto transport properties, interlayer exchange coupling properties of various thin layered materials in condensed matter physics research [134–140]. In order

to achieve a detailed understanding about the electronic mechanism responsible for the observed physical properties in thin layered materials it is often necessary to investigate and compare the unusual behaviour of orbital electrons in surfaces, interfaces and bulk [132, 134, 141–143]. Probing surfaces and interfaces in a superlattice structure [93, 124] can lead to new opportunity to reveal unusual physical properties associated with a thin layered material. Despite immense interest in this field, no appropriate technique is available that can provide depth resolved localised chemical information about a thin layered material. The conventional absorption techniques suffer from the inherent technical limitations as they do not provide depth resolved information about physical and chemical properties of nanostructured materials and their localization with respect to the substrate surface. Surface interface studies had many surprises in the past and are still not fully understood [144–149]. For example, a recent work discovers unknown origin of interfacial magnetism and superconductivity [150]. Similarly electronic properties such as density of states, change of valance states at surface interface boundaries of thin film medium can be significantly different from bulk.

Fluorescence assisted x-ray standing wave (XSW) technique has become the workhorse for the surface-interface aspects of condensed matter research. As a nondestructive probe, the XSW induced fluorescence measurements at grazing incidence angles offer atomic scale depth resolution inside a thin film medium [38, 100, 151–159]. Recent advancements in various combined x-ray spectroscopy approaches have made it possible to obtain depth resolved chemical information on surfaces and interfaces in a non-destructive manner. It has been shown that x-ray reflectivity (XRR) together with grazing incidence x-ray fluorescence (GIXRF) measurements can be used as a sensitive probe to evaluate depth resolved microstructural parameters of a buried layer inside a W-B₄C multilayer structure [124]. The recent advances in the field of surface-interface analysis of thin layered materials have spurred new experimental efforts to develop methods that are far more accurate as compared to that of the conventional absorption methods.

Depth resolved chemical speciation of a W-B₄C multilayer structure has been demonstrated using combined XRR and GIXRF measurements along with the XSW assisted depth resolved x-ray absorption near edge structure (XANES) measurements. The depth selectivity of the XSW wave field inside the multilayer structure was controlled by precisely tuning the grazing incidence angle of the impinging x-ray wave field. We have carried out x-ray reflectometry measurements to investigate the anomalous behaviour of the optical constants (δ, β) of W in the vicinity of W-L₃ characteristics absorption edge. Such measurements are highly useful for obtaining quantitative information on stoichiometric chemical nature and electronic distribution of the probed atom in the material. XSW assisted depth resolved XANES measurements near the W-L₃ absorption edge energy ($E_o \sim 10207$ eV) are carried out for two sets of W-B₄C multilayer structure comprising of 10 and 15 bilayer repetitions, respectively. Our results show existence of unusual electronic states for the W atoms that are present at interface boundary as compared to those present in the bulk thin film medium in case of the W-B₄C multilayer structure. The grazing incidence x-ray diffraction (GIXRD) measurements performed on the same multilayer structure supports results of the XSW investigations.

4.6.1 Probing various depth of a multilayer structure

W-B₄C periodic multilayer structures, comprising of N=15 and N=10 bilayers, used in the present analysis were prepared on a polished Si(100) substrate at room temperature using a DC magnetron sputtering system [50]. A schematic illustration of the x-ray reflection from a periodic multilayer structure comprising of bilayer repetitions N=15 is shown in Fig. 4.14. The combined x-ray reflectivity and grazing incidence x-ray fluorescence measurements for W-B₄C multilayer consisting of 15 bilayer repetitions were carried out at the x-ray reflectometer station of BL-16 beamline of Indus-2 synchrotron facility [115, 122]. Figures 4.15(a) and 4.15(b) respectively show the

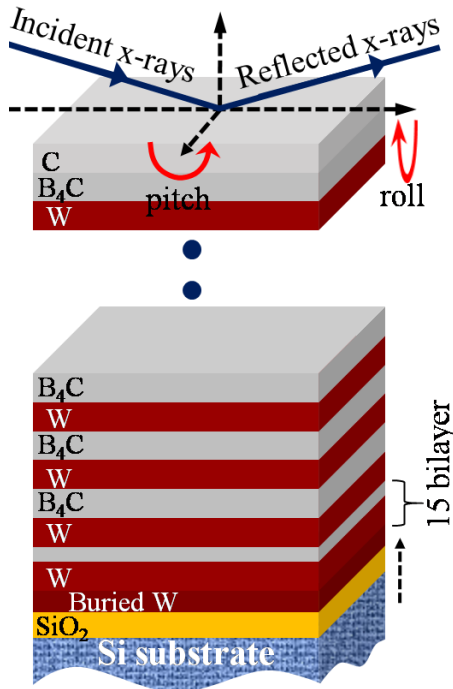


Figure 4.14: A schematic representation showing the x-ray reflection from a W-B₄C periodic multilayer structure consisting of N=15 bilayer repetitions. In this figure we have also depicted a buried interface layer of W inside the multilayer medium, on top of a Si substrate.

measured and fitted XRR and GIXRF profiles in the vicinity of the 1st Bragg peak for the W-B₄C multilayer structure consisting of 15 bilayer repetitions at 10230 eV incident x-ray energy (above the W-L₃ absorption edge energy $E_o \sim 10207$ eV). Simultaneous fitting of the measured XRR and GIXRF data was carried out using the CATGIXRF program [120]. During the model fitting of the experimental XRR and GIXRF profiles we have considered a thin buried layer of W of thickness 16.6 Å, inside the multilayer structure. A schematic illustration showing the location of the buried layer of W is given in Fig. 4.14. The microstructural parameters of the W-B₄C multilayer structures comprising of number of bilayer repetitions N=15 and N=10 were determined using the combined XRR-GIXRF measurements. The best fit results give an average multilayer bilayer period thickness $d = d_w + d_{B_4C} = 47.7$ Å with individual thicknesses of W and B₄C layers $d_w \sim 25.4$ Å, $d_{B_4C} \sim 22$ Å respectively. The detailed microstructural analysis of the W-B₄C multilayer structure is described in section (4.6) [124]. Figure 4.16 depicts computed electric field intensity (EFI) distribution at 10230 eV x-ray energy inside the

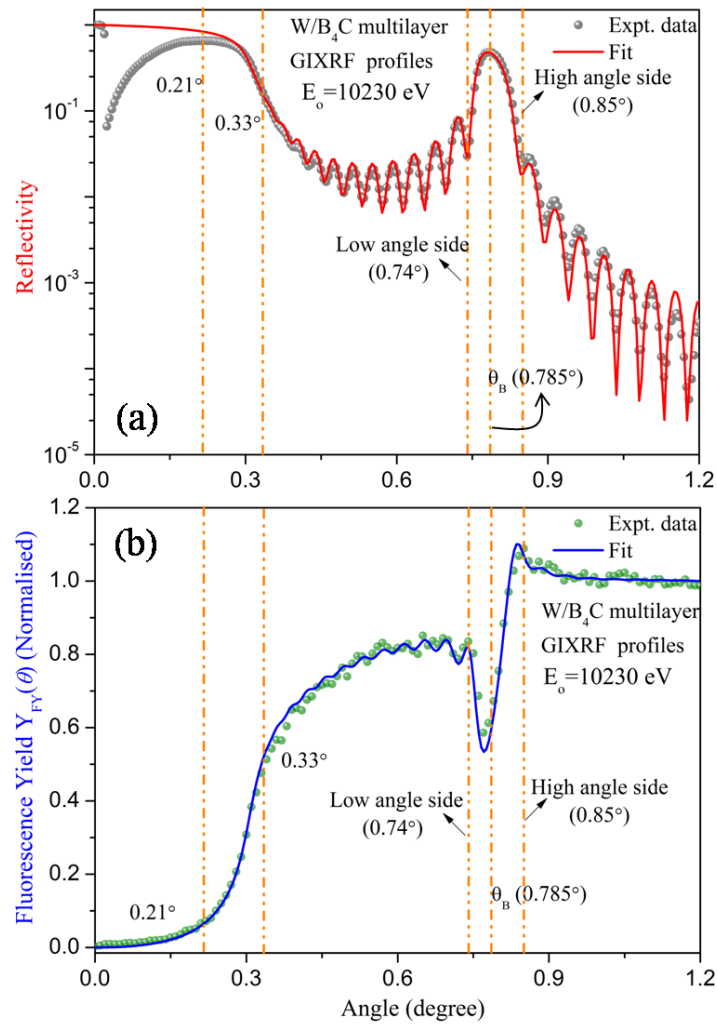


Figure 4.15: Measured and fitted (a) XRR and (b) W-L α fluorescence profiles for W-B₄C multilayer structure comprising of N=15 bilayer repetitions at an incident x-ray energy of 10230 eV.

W-B₄C periodic multilayer structure as a function of incidence angle and film depth (z). The EFI was computed taking into account the microstructural parameters determined from the best fit results obtained using combined XRR and GIXRF analysis. From Fig. 4.16, it can be observed that the positions of XSW antinodes vary inside the multilayer medium as grazing incidence angles of the primary x-ray beam are changed. The observed periodic Kiessig interference fringes in the XRR and GIXRF profiles are anticorrelated in nature. It can be seen from the Fig. 4.15(b) that the W-L α fluorescence intensity profile shows a strong XSW modulation especially at the low and high angle sides of the Bragg region. The W-L α fluorescence intensity is minimum at very low

grazing incidence angles and starts increasing rapidly as the grazing incidence angle just crosses the critical angle ($\theta_c \approx 0.29^\circ$) of the film medium. This variation of W-L α fluorescence intensity mainly arises due to the movement of XSW wave field in the thin film structure. At very low grazing incidence angles or below the critical angle ($\theta_c \approx 0.29^\circ$), there is no appreciable x-ray intensity inside the multilayer medium, but it exists only on top of the multilayer surface in the form of XSW fringes due to strong reflection (total external reflection region) from the sample surface. So, a very few W atoms, situated 2-5 nm below the top surface of the multilayer, is excited by the evanescent wave and the corresponding fluorescence intensity is very weak. As the incidence angle advances through the critical angle boundary, the x-ray field starts to penetrate in different layers of the multilayer medium and consequently W-L α fluorescence intensity increases very rapidly. At the Bragg angle ($\theta_{Bragg} \approx 0.785^\circ$), an XSW field of periodicity equal to the multilayer period ($D = d$) is set-up inside the multilayer medium. At the low angle side ($\theta_{Low} \approx 0.74^\circ$) of the Bragg peak, the antinodes of the XSW field remain in the low Z layer (B₄C layer). As the incidence angle advances across the Bragg region, these antinodes move towards the high Z layer (W layer). However, at the Bragg peak the antinodes stand exactly at the interfaces of the low Z and high Z layer. At the high angle side ($\theta_{High} \approx 0.85^\circ$) of the Bragg peak, XSW antinodes completely coincide with the position of the high Z layers (W layer). Because of this movement of the XSW antinodes intensity, the W-L α fluorescence intensity is strongly modulated over the Bragg region. As a result, at the high angle side of the Bragg peak, one obtained relatively higher W-L α fluorescence yield as compared to that of the low angle side. At higher incidence angles (after the 1st Bragg peak) the W-L α fluorescence yield more or less remains constant because the W atom is excited only with the direct x-ray beam as there is no formation of XSW field due to very weak reflected x-ray beam at high incidence angles. One may expect a light XSW modulation of the W-L α fluorescence yield near the 2nd Bragg peak. These control depth selectivity of XSW field in combination with x-ray absorption fine structure analysis provides a

possibility to determine the depth selective chemical speciation of a thin film medium. This can be achieved by measuring the XSW assisted fluorescence intensity from a thin layered medium across the characteristics absorption edge of a layered material. Various grazing incidence angles were selected for the XSW assisted depth resolved x-ray absorption measurements near the W-L₃ absorption edge energy ($E_o \sim 10207$ eV). These angles are marked by the dotted vertical lines in Figs. 4.15 and 4.16. It may be important to mention here that the probed depth volume estimated from XSW field is usually not constant across the absorption edge of a material due to anomalous behaviour of the complex refractive indices or optical constants of the layered material.

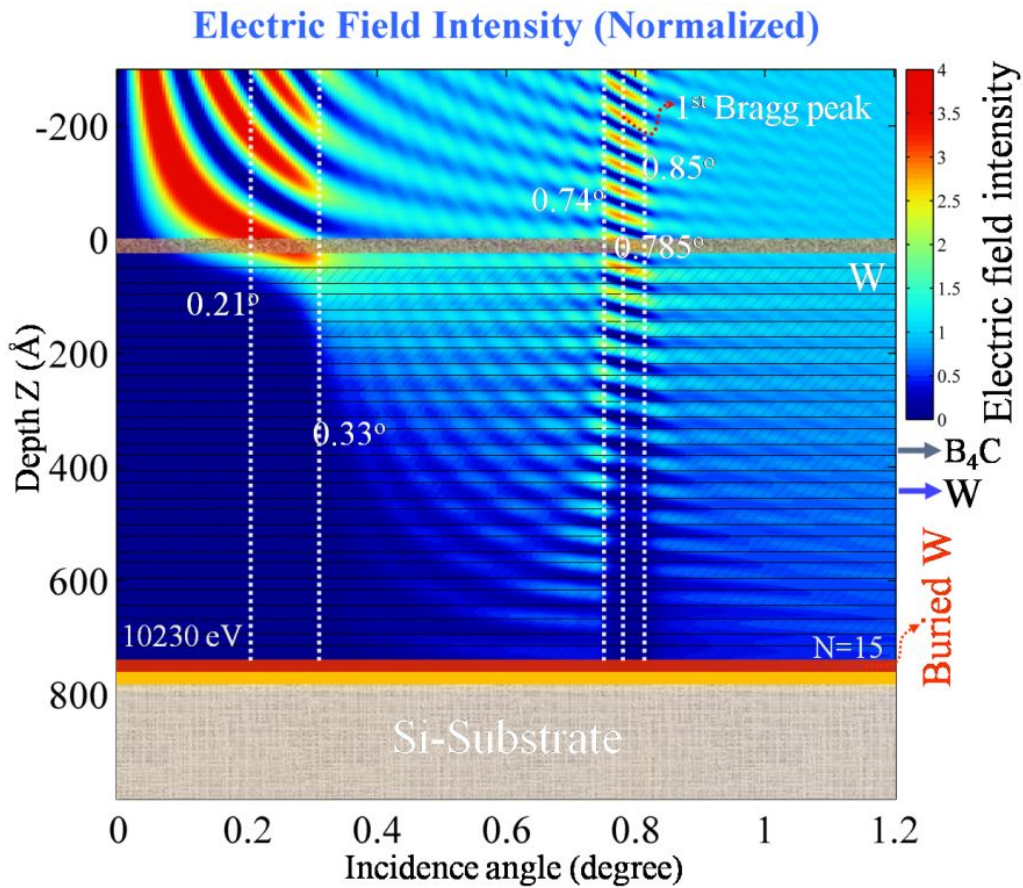


Figure 4.16: X-ray field intensity (EFI) distribution inside a W-B₄C periodic multilayer structure computed using best fitted parameters obtained from the XRR and W-L α fluorescence measurements at an incident x-ray energy of $E= 10230$ eV. In this figure, we have also marked various dotted vertical lines showing different incident angles that have been opted for depth selective XANES measurements of W-B₄C multilayer structure.

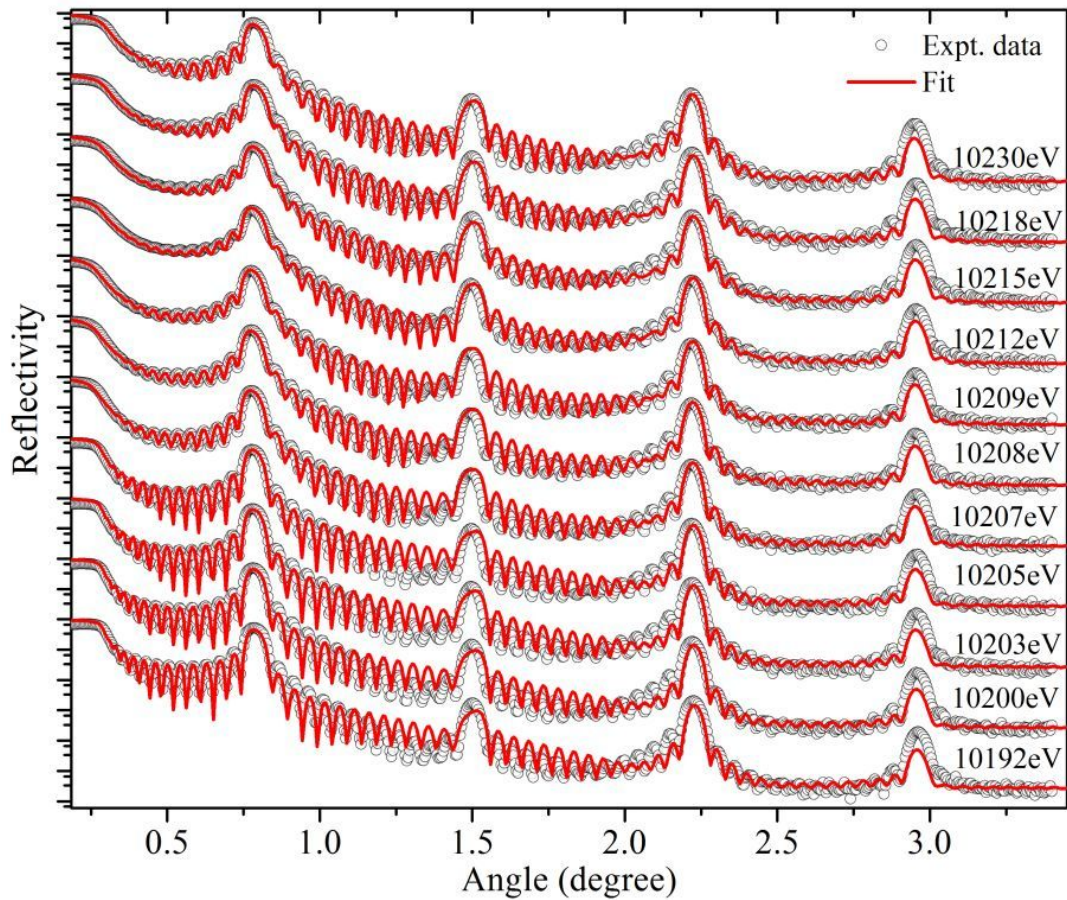


Figure 4.17: Measured and fitted XRR profiles for W-B₄C multilayer structure comprising of N=15 bilayer repetitions in the incident x-ray energies of 10192-10230 eV.

4.6.2 Determination of optical constant of W near the absorption edge

In order to investigate the anomalous behaviour of the optical constants (δ, β) of W near the characteristics L₃ absorption region, we have performed x-ray reflectivity measurements of the W-B₄C multilayer structure near the W-L₃ absorption energy region. Figure 4.17 shows the measured and fitted specular reflectivity profiles of the W-B₄C multilayer structure in the energy region of 10192 eV to 10230 eV. The x-ray reflectivity data were recorded with an angular step size of $\theta \approx 0.005^\circ$ using reflectometer station of BL-16 beamline of Indus-2 synchrotron facility. Before XRR measurements, incident x-ray energies emitted from the BL-16 beamline were calibrated

by performing absorption edge measurements of a pure W foil as well as a W thin film of thickness 270 Å. While fitting XRR profiles in the energy region of 10192 eV- 10230 eV, as an initial guess we have considered measured optical constants (δ, β) of a pure W thin film. In addition, we fixed the microstructural parameters of the W-B₄C multilayer structure and allowed to vary optical constants of W in a controlled manner until one obtains best fit curves to the measured XRR data. It can be seen from Fig. 4.17 that the measured XRR patterns match quite well with the fitted profiles except a subtle difference at the 2nd and 4th Bragg peak locations. This deviation can be attributed to the non-linear diffused scattering background produced from the multilayer sample. In addition, we also recognized that the 15th bilayer period of W-B₄C multilayer structure (N=15) is slightly asymmetric, since an additional buried layer of W was created unintentionally during the deposition process. This non-uniformity in bilayer period thickness results in a subtle difference between the measured and fitted XRF profiles at the 2nd and 4th Bragg peaks. A detailed discussion is presented elsewhere [124]. The reflectivity of the 1st Bragg peak decreases significantly near the L₃ absorption edge region of W due to strong anomalous absorption effects.

The average optical constants of W in the energy region of 10192 eV - 10230 eV have been determined experimentally by fitting the measured angle dependent specular x-ray reflectivity profiles of the W-B₄C multilayer structure. Measured values of the optical constants (δ, β) of W are plotted in the Figs. 4.18(a) and 4.18(b) respectively. For comparison, we have also plotted Henke tabulated values of optical constants of W in Fig. 4.18 considering a density of W ~ 17.3 g/cm³. It can be seen from Fig. 4.18 that the measured optical constants (δ, β) in the energy region of 10192 eV to 10230 eV show a good agreement with the Henke tabulated values [123]. A maximum deviation $\sim 5 - 7$ % was observed between measured and tabulated values of δ where as in case of β values, a maximum deviation $\sim 10 - 15$ % was realized. In the case of x-ray reflectivity analysis, the measurement accuracies of the optical constants usually depend on the β/δ ratio for all the materials [160, 161]. The optical constants can be uniquely determined in a

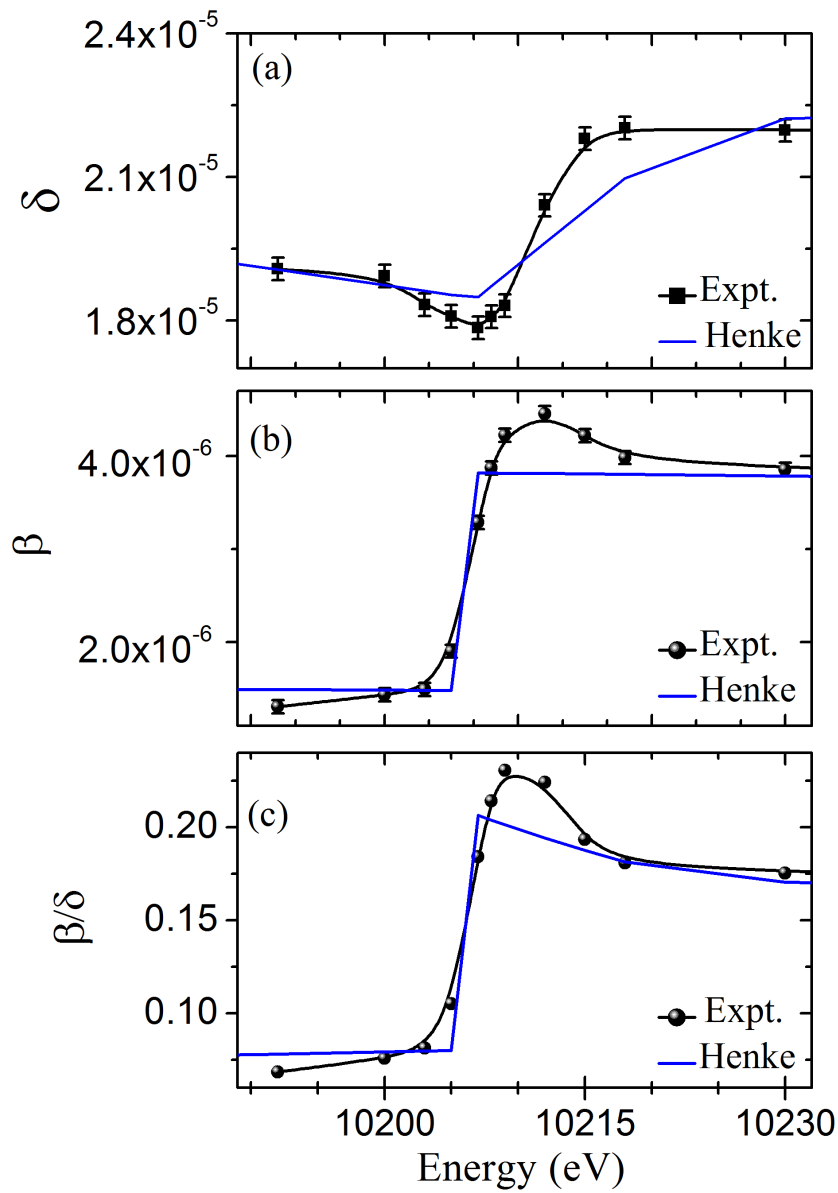


Figure 4.18: Determined optical constants (a) δ , (b) β , and (c) the ratio β/δ of W from the x-ray reflectivity measurements in a W-B₄C multilayer structure comprising of N=15 bilayer repetitions in x-ray energy region of 10192 -10230 eV. The values of optical constants calculated from the Henke table are also given for comparison.

situation when $\beta/\delta \leq 0.5$. Figure 4.18(c) shows the variation of β/δ ratio of W in our case for the energy region of 10192 eV to 10230 eV. At a first glance, this variation seems to be in close agreement with the Henke tabulated values. We observe a maximum variation in the β/δ ratio of $W \sim 0.23$. In order to investigate the dependency of probed depth volume of the XSW field at different incident x-ray energy and grazing incidence angles, we have computed EFI distribution in the vicinity of the L_3 absorption edge of W. Figure 4.19 represents the computed EFI distribution at (a) 10205 eV, (b) 10207 eV, (a) 10212 eV, and (a) 10218 eV x-ray energies inside the W-B₄C multilayer structure as a function of incidence angle and film depth (z). The EFI was computed taking into account the fitted microstructural parameters of the multilayer structure and derived optical constants obtained from the XRR analysis at x-ray different energies. From Fig. 4.19, it can be observed that the probed depth of the x-ray field inside the multilayer structure remains more or less constant in case when the incident x-ray energies are varying in the vicinity of W- L_3 absorption edge. However, the locations of XSW antinodes shift by an angle of 0.01° for x-ray energies above the L_3 absorption edge ($E \sim 10218$ eV).

4.6.3 Depth resolved chemical analysis of a multilayer structure

XSW assisted depth resolved XANES measurements at W- L_3 absorption edge energy ($E_o \sim 10207$ eV) for W-B₄C multilayer of 15 bilayer repetitions was performed at the same reflectometer station [115]. An x-ray beam of size $100 \mu\text{m}(v) \times 10 \text{ mm}(h)$, generated using a crossed-slits aperture, was allowed for the GIXRF-XANES measurements. Figures 4.20(a) and 4.20(b) respectively show the measured and normalised XSW assisted depth resolved x-ray absorption near edge structure measurements for two different W-B₄C multilayer structures consisting of 15 and 10 bilayer repetitions at various grazing incidence angles in the vicinity of L_3 edge energy of tungsten. In these figures, measured XANES profile (in the fluorescence mode) of a

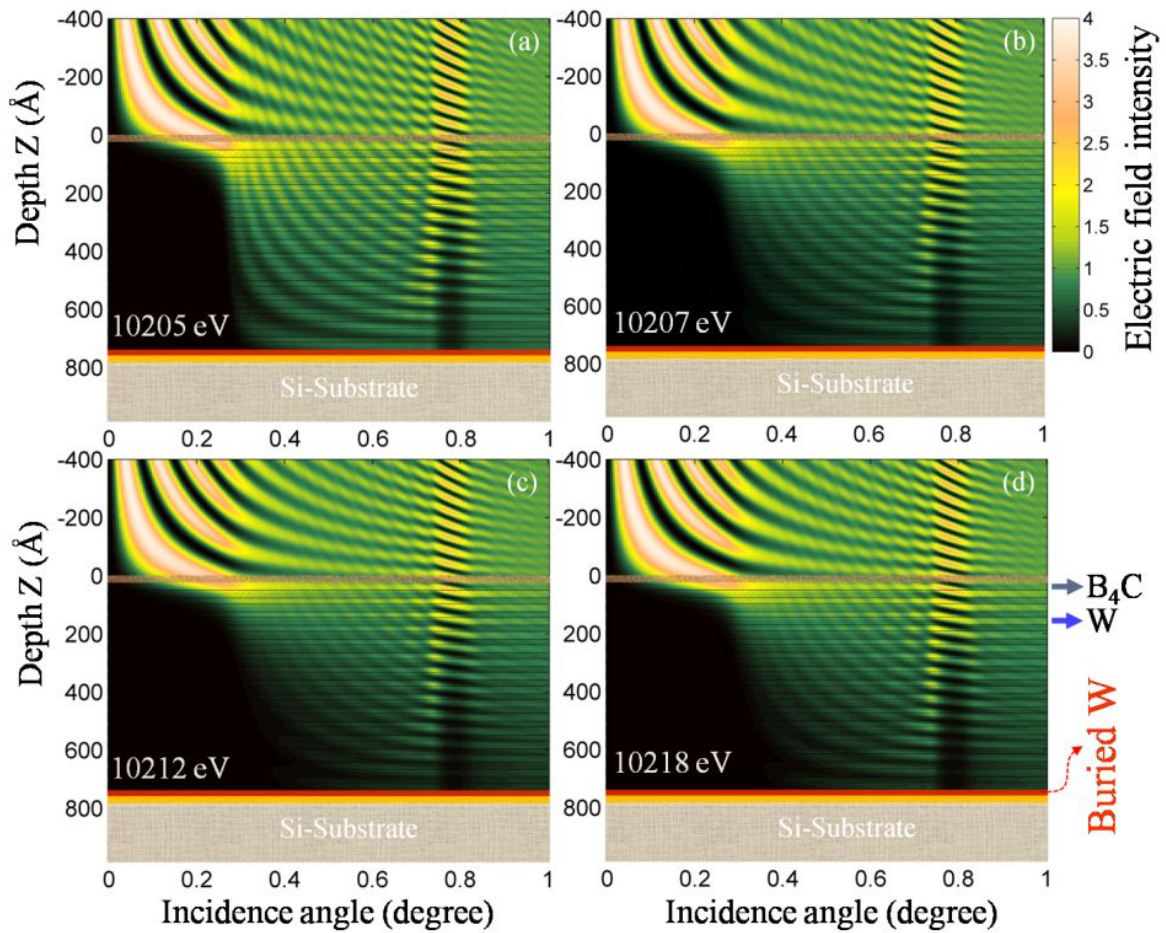


Figure 4.19: X-ray field intensity (EFI) distribution inside a W-B₄C periodic multilayer structure computed using best fitted parameters obtained from the XRR and W-L α fluorescence measurements and determined optical constants (δ, β) at incident x-ray energy of (a) 10205 eV, (b) 10207 eV, (c) 10212 eV and (d) 10218 eV. One clearly observed the probing depth volume of XSW wave field inside W-B₄C multilayer structure across the W-L₃ absorption edge energy preserves a more or less constant volume, except a angular shift $\theta \sim 0.01^\circ$ at high energy side ($E \sim 10230\text{eV}$) of the W-L₃ edge.

pure tungsten metal foil was also plotted. The main absorption peak (white line) in Fig. 4.20(a) and 4.20(b) is visible due to strong transition of 2p_{3/2} electrons to the partially filled 5d levels. White spectrum or line is defined by an intensity distributed continuously over a broad range of energy or wavelength. It can also be seen here that the peak intensity of the white line varies at various grazing incidence angles. This is mainly attributed to different probing depths (*i.e.* extinction lengths) of the x-ray wave field inside the W-B₄C multilayer structure at different grazing incidence angles. The observed white line features in measured XANES profiles of W-B₄C multilayer structure

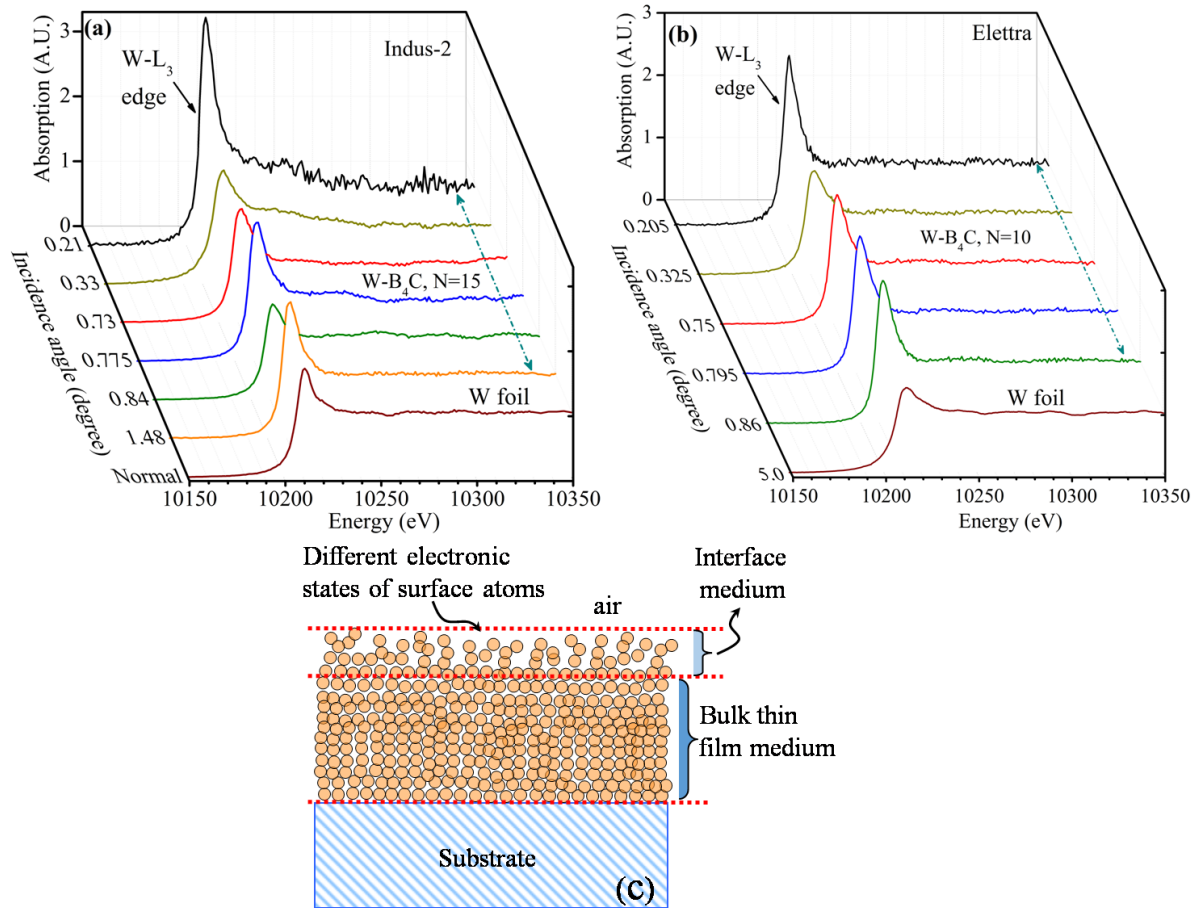


Figure 4.20: X-ray standing wave induced XANES profiles of the W-B₄C multilayer structures measured at L₃ edge of W. (a) Measured XANES profile of a multilayer structure consisting of N=15 bilayer repetitions using BL-16 beamline of Indus synchrotron facility, and (b) W-B₄C multilayer structure with N=10 bilayer repetitions measured at the International Atomic Energy Agency (IAEA) GIXRF-XRR experimental facility operated at the XRF beamline of Elettra Sincrotrone Trieste (BL-10.1L).

(N=15) at different grazing incidence angles, e.g., $\theta=0.73^\circ$ (at low angle side), $\theta=0.775^\circ$ (at 1st Bragg peak) and $\theta=0.84^\circ$ (at high angle side) correspond to different probing depths of the x-ray wave field. At these incidence angles, antinodes of XSW field exist in the low Z layers (B₄C), at the interface of B₄C-W layers and in the high Z layers (W) respectively. The white line intensity at an incidence angle of $\theta=1.48^\circ$ (at 2nd Bragg peak) describes a normal excitation of the W-B₄C multilayer structure. This is due to the fact that at such a high incidence angle XSW field does not exist inside the multilayer structure because of very weak reflection of the primary x-ray beam. In this condition, all the W layers of the multilayer are excited only by the primary x-ray beam. It can also

be seen that the characteristic features of the white line at $\theta=1.48^\circ$ is similar to that of the pure W metal foil. On the other hand, a subtle shift of the edge energy position ($E_o=10207$ eV) can be observed in the measured XANES profiles at grazing incidence angles of 0.21° and 0.33° . This occurs mainly due to the small probing depth of the XSW wave field inside the multilayer medium at these angles. In such conditions only few W atoms sitting at the top surface of a tungsten layer are excited. These top sub-surface W atoms experience a highly asymmetric crystal environment, which in turn decreases their binding energy as compared to those W atoms, situated at deep inside the multilayer medium. It can also be noticed from Fig. 4.20 that at lower grazing incidence angles, the peak intensity of white line is relatively larger as compared to that of the higher incidence angles. This can be explained by understanding the origin of white line that arises as a result of electron transition from W-2p_{3/2} orbitals to partially filled 5d orbitals in addition to the transitions that occur from W-2p_{3/2} to unoccupied localised states near 5d states. These localised states emerge because of the bulk defects as well as due to surface effects (see Fig. 4.20(c)). In case of bulk, an atom remains in a homogeneous structured environment. This causes an overlap of electron wave functions of adjacent neighbouring atoms in all 3-directions uniformly. As a result, the dipolar coupling between two orbitals that leads to origin of white line intensity is distributed nearly isotropically. On the other hand, in the case of surface or interface states the atomic densities may be localized to its position because of lack of bulk symmetries. This would lead to sharp dipolar transitions between core levels and unoccupied surface states. The contribution of the surface effects are usually very large in the case of a thin film structure of thickness ranging in few tens of angstrom. At grazing incidence angle, the relative contribution of surface states will be larger as compared to that of the bulk defects, which in turn enhance the peak intensity of white line in the normalised XANES spectra. XSW-XANES measurements for a W-B₄C multilayer consisting of N=10 bilayer repetitions were also carried out the at the International Atomic Energy Agency (IAEA) GIXRF-XRR experimental facility operated at the XRF beamline of Elettra

Sincrotrone Trieste (BL-10.1L). Figure 4.20(b) shows the normalized XANES spectra measured at XRR-GIXRF experimental station of IAEA- Elettra beamline (BL-10.1L) for a W-B₄C multilayer consisting of number of bilayer periods N=10. We arrive at similar conclusion after analysing the XSW-XANES profiles presented in Fig. 4.20(b). These XANES profiles do not provide any signature of change of chemical state of W in the W-B₄C multilayer structures.

In order to further validate our conclusions drawn from the XANES analysis of the

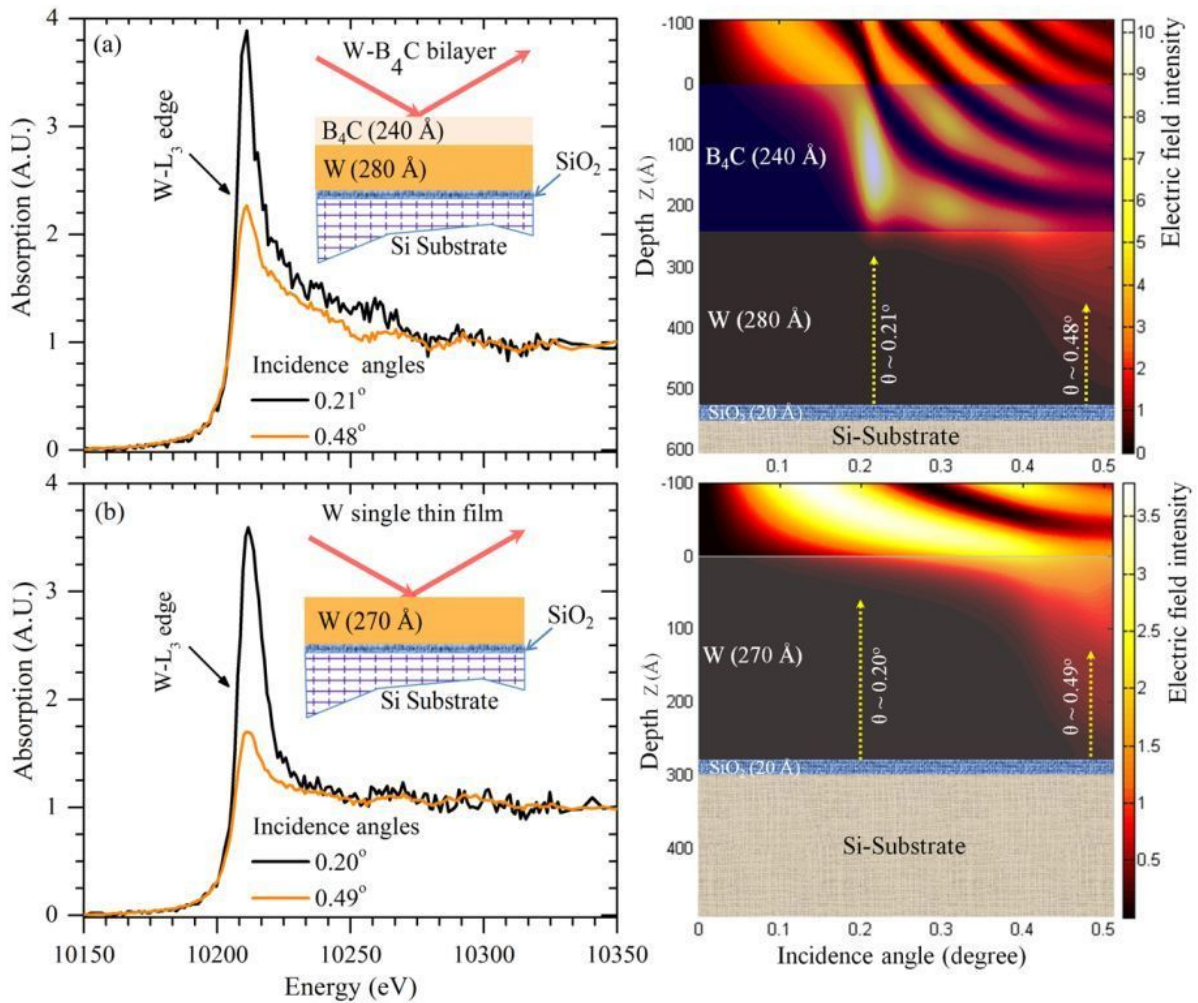


Figure 4.21: X-ray standing wave induced XANES profiles of (a) W-B₄C bilayer and (b) W single thin film structures at L₃ edge of W. In the inset of Figs. (a) and (b) a schematic model structure of the W-B₄C bilayer and W single thin film structures are given. On the right hand side, computed x-ray field distribution near W-L₃ edge energy ($E \sim 10208$ eV) is shown inside the two mediums.

multilayer structures, we have carried out XSW assisted XANES measurements on a W

single thin film structure (thickness $d \sim 270 \text{ \AA}$), as well as of a W-B₄C bilayer structure (bilayer thickness $d = d_W + d_{B_4C} = 280+240 \text{ \AA}$) to determine the formation of various chemical phases (if any) inside the thin film medium. Figure 4.21 shows the measured XANES profiles for (a) W-B₄C bilayer and (b) W single thin film structures at various grazing incidence angles. It can be noticed from Fig. 4.21 that the XANES profiles of W-B₄C bilayer and W single thin film structures resemble the formal XANES nature of multilayer structures at various grazing incidence angles. On the right hand side of Fig. 4.21, we have depicted the XSW field distribution inside the bilayer and single thin film structures. In these figures the probed depths of x-rays at various grazing incidence angles are marked by arrows. It confirms that the enhanced white line intensity at very low grazing incidence angles arises mainly due to the surface states and self absorption effect does not play any significant role in this particular scenario [162, 163]. In conventional XANES measurements it has already been shown that the peak intensity of white line remains more or less unchanged in case of different oxidation states of W [125, 126, 164]. The results are found to be consistent with the investigations reported by Rao *et al.*, [165]. They have shown that W and B₄C in the W-B₄C multilayer remain stable up to an annealing temperature of 800°C. Beyond this temperature (above $\sim 1000^\circ \text{C}$), B₄C layer starts to decompose into free C or B atoms, which then react with the W atoms to produce more stable chemical phases of the tungsten [166].

4.6.4 X-ray diffraction study

GIXRD measurement was carried out at angle dispersive x-ray diffraction (ADXRD) beamline [167, 168] (BL-12) of Indus-2 synchrotron facility for the W-B₄C multilayer at 15.5 keV x-ray energy to determine formation of various crystalline phases (if any) inside the multilayer medium. Figure 4.22 shows the measured GIXRD pattern of the W-B₄C multilayer consisting of N=15 bilayer repetitions at a fixed grazing incidence

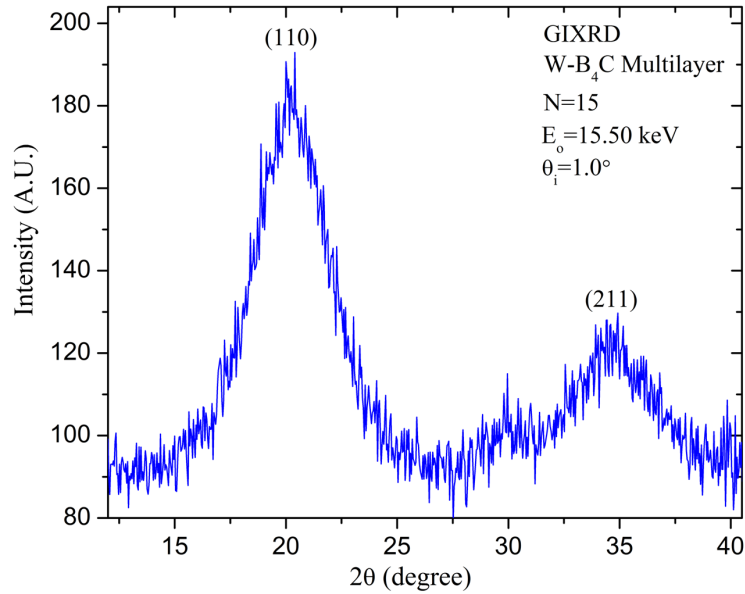


Figure 4.22: Measured GIXRD pattern of W-B₄C multilayer consisting of N=15 bilayer repetitions at incident x-ray energy of 15.5 keV. During the measurements the incidence angle of the primary x-ray beam was fixed at 1.0°.

angle of 1°. It may be noted here that the attenuation length of the incident x-ray at 15.5 keV is greater than the total thickness of the W-B₄C multilayer stack. The GIXRD measurements show two broad peaks corresponding to the W(110) and W(211) planes, which suggest that W is present in the polycrystalline phase with a very small grain size boundary. We could also observe a very small peak at ~29.9° that arises due to asymmetric reflection from the Si substrate. The GIXRD measurement does not provide any evidence of formation of any other chemical phases of W inside the W-B₄C multilayer structure.

In practice, it is very difficult to map depth resolved chemical information on thin layered materials by using conventional x-ray absorption fine structure (XAFS) measurements (transmission or fluorescence mode). The combined XSW-XAFS analysis approach offers an opportunity to study depth resolved local structure of thin layered materials with atomic scale resolution.

4.7 Summary

We have described a “GUI-CATGIXRF” is as an easy-to-use computational tool capable of simulating grazing incidence x-ray reflectivity and x-ray standing wave induced fluorescence emission from a thin film structure, simultaneously. It is specially designed to meet the increasing demand of reliable and precise evaluation of microstructural parameters of a thin film medium using both synchrotron and conventional laboratory x-ray sources. The program also allows model based fitting procedures, which can be implemented simply by selecting options; independent layered structure or periodic multilayer structure, thus enabling us to resolve structures of more complex heterogeneous thin film systems.

The structural morphology of a W-B₄C multilayer structure have been investigated at angstrom resolutions using combined XRR and grazing incidence x-ray fluorescence measurements. It is realized that XRR investigation together with the GIXRF measurements can be used as a sensitive probe to quantitatively evaluate a buried layer structure or any thickness inhomogeneity of the bilayer period inside a periodic multilayer structure. The combined XRR and GIXRF measurements are therefore especially suitable in correlating electronic and magnetic properties of a nanoscale thin film semiconductor device or a magnetic multilayer structure with their structural properties.

The XANES characterisation along with the combined XRR-GIXRF analysis have been used to perform depth resolved chemical speciation of a thin film structure. Two sets of W-B₄C multilayer structures consisting of N=15 and N=10 bilayer periods have been analysed independently using Indus-2 synchrotron and Elettra Sincrotrone Trieste facilities. XSW-XANES results reveal significant changes in the chemical nature of W atoms that are present at the surface and interface boundaries as compared to those present in the bulk thin film medium. This is mainly due to the surface electronic states of the W atoms. On the other hand, the electronic behaviour of the W atoms that are

present deep inside the bulk W layer remains unchanged, which represents the bulk electronic states of W. The grazing incidence x-ray diffraction results also support the above mentioned conclusions. The understanding of distribution of surface states as a function of depth for thin films is often necessary to correlate electronic, magnetic and transport properties of a thin film device.

Chapter 5

Analysis of nanoparticles using XSW

In this chapter applicability of the x-ray fluorescence technique in combination with the x-ray reflectivity technique has been described for the reliable and precise characterisation of surface morphology of metal nanoparticles, dispersed on a flat surface. Theoretical models have been developed that takes into account the effect of average particle size, particle's shape, nature of particle's dispersion and their agglomeration on top of a substrate surface during the calculation of XSW assisted fluorescence profile of the nanostructured materials. The effect of longitudinal (or temporal) coherence property of the primary x-ray beam on the total reflection assisted x-ray standing wave (TR-XSW) analysis of nanoscale materials is also quantitatively evaluated.

In the subsequent sections of the chapter, XSW assisted fluorescence methodology has been applied to study the surface morphology of different types of nanostructured materials *e.g.* Au nanoparticles and TiO₂ nanoparticles deposited on top of a Si substrate surface. A novel synthesis procedure for the fabrication of low dimensional TiO₂ nanoparticles on polished Si substrates using gas phase CO₂ laser pyrolysis method is described in detail. Atomic force microscopy measurements along with the transmission electron microscopy measurements were also carried out to correlate the findings of the XSW investigations.

5.1 Introduction

Dispersion of metal nanoparticles on flat surfaces has attracted considerable interest in many technological applications. Numerous advantages of functionalised patterned nanostructures especially in medical physics, chemistry, biology and semiconductor quantum dot applications have rapidly driven the growth of this field in the last two decades. In particular, for applications involving biomedical imaging, the nanoparticles have attracted perhaps the greatest attention as these materials provide a direct interface at the sub-cellular length scale. Precise characterisation of nanostructured materials is becoming increasingly important as they find widespread applications in various fields of science and nanotechnology [169–171]. The performance of a nanostructured device strongly depends on its microstructural properties [172, 173]. Reliable characterisation methods are thus often needed to reveal their detailed structural properties *such as* average particle size, particle's shape, internal structure, surface morphology, particle's distribution and chemical composition. Presence of any unwanted impurity even at micro or trace level may lead to change in the physical properties and may deteriorate the overall performance of a nanostructured device [37]. The quantitative analysis of nanomaterials is often very difficult because currently available methods are not very robust, moreover, it requires high spatial resolution for a nano-probe method (of the order of sub-nanometer length scale) in order to distinguish the internal structure of a nanomaterial. At present most commonly available surface microscopy techniques (*e.g.* - scanning electron microscopy, scanning tunneling microscopy, atomic force microscopy, etc.) allow nanometer length scale resolution for probing of the materials, however, these techniques suffer from the serious disadvantages of relatively poor energy resolution as well as relatively modest detection sensitivities for elements present at low concentrations. Moreover, these techniques do not provide any depth dependent information about physical and chemical nature of the nanostructured material and their localisation with respect to the substrate surface.

X-ray standing wave assisted grazing incidence fluorescence technique is one of the most powerful and versatile tools to unfold depth resolved physical and chemical properties of the nanoparticles [174–176], as it combines the features of both x-ray reflectivity (XRR) and x-ray fluorescence (XRF) techniques. In the condition of total external reflection of x-rays on a mirror surface or Bragg reflection from a multilayer structure, the incoming and reflected beams interfere and form an XSW field on top of the mirror surface. This XSW field also extends below the mirror surface up to a certain depth. Enhanced fluorescence radiation is emitted from those parts of the sample volume that are present at the locations of XSW field antinodes. By changing the grazing incidence angle in the vicinity of the critical angle or Bragg reflection region, the position of XSW antinodes can be moved inside the sample material and the corresponding changes in the fluorescence intensity can be recorded as a function of grazing incidence angles [34]. So, the GIXRF profile contains the information about the nanoparticles dispersed on the substrate surface. GIXRF technique offers high accuracy for the determination of the density variation in a thin film medium [177]. GIXRF analysis not only provides dimensional visualization for the nanostructures but also offers depth dependent localisation for a foreign impurity element (if any) embedded inside a nanostructured material. XRR technique suffers from an intrinsic difficulty of analysing non-reflecting (non-continuous) layers. On the other hand, GIXRF technique provides information about the non-reflecting layers as well as for the reflecting layers. Here, the nanoparticles dispersed on a mirror surface act as a nonreflecting layer for the incident x-ray beam. Therefore, in many cases it is not possible to completely reveal the structure of a complex nanostructured thin film medium that comprises both reflecting and nonreflecting layers, using only one of the techniques (XRR or GIXRF) [34, 35, 37, 38, 178–180]. The inherent characteristic features of GIXRF allow us to even analyse multielement nanostructured materials and obtain useful information on the nature of dispersion, agglomeration, average particle size, shape of the particles as well as internal structure and chemical composition of the nanostructured materials over a

large surface area (~ 4 to 5 orders larger in magnitude) as compared to that of the conventional surface microscopy technique [38, 113, 154, 181, 182]. The various attractive features of the combined XRR-GIXRF analysis have been described in detail in Chapter 2. A few research groups have recently demonstrated that XSW assisted XRF measurements can be used successfully for the determination of average particle size of mono-dispersive nanoparticles over a flat reflecting surface as well as for those embedded in a complex sample matrix [183–186].

In this chapter, surface morphology of various nanomaterials using combined XRR-GIXRF analysis technique has been investigated. The results show that GIXRF measurements along with the x-ray reflectivity analysis can be used as a sensitive probe for the reliable and precise determination of surface morphology of the metal nanoparticles, dispersed on a substrate surface. Numerical simulations were also carried out to demonstrate striking capabilities of GIXRF technique for the determination of average size, shape, nature of dispersion of the particles and their agglomeration on a substrate surface. Given example includes the analysis of Au nanoparticles and TiO_2 dispersed on Si substrate surface. The relative advantages of GIXRF analysis have been discussed by comparing the results obtained using atomic force microscopy and transmission electron microscopy measurements.

5.2 Analysis of Au nanoparticle on flat substrate

In this section, surface morphology and microstructural analysis of Au nanoparticles using GIXRF technique will be described. Often, nature of dispersion of nanoparticles on a flat surface is governed by many complex short range forces. Depending upon the surface chemistry and available cohesive and adhesive forces between different particles as well as between particle and substrate, the dispersion of the nanoparticle usually follows a complex distribution profile on the Si surface. It might be poly-dispersive in nature or may follow a complex distribution of particles in the form of agglomerations.

The quantitative analysis of such complex nanostructured materials is very important, but still a largely unexplored issue. Currently available surface analysis techniques are not particularly suitable for the morphological analysis of nanostructured materials. The XRR measurements in combination with the GIXRF [178] investigations can be used as a sensitive probe to characterize the nature of dispersion of nanostructured materials on top of a flat surface. Observing the characteristic intensity modulations in the GIXRF profile below the critical angle (*e.g.* in the TXRF region), it is possible to explore the fractional concentrations of the nanoparticle clusters that are formed by the aggregated nanoparticles on a substrate. If the distribution of the nanoparticles is purely mono-dispersive in nature on top of a surface, then one observes several peaking modulations in the GIXRF profile. Their peak heights usually approach to ~ 4 times with respect to the fluorescence intensity at higher incidence angles. These peaking oscillations in the GIXRF profile arise due to the coincidence of an XSW antinode (XSW field that appears below the critical angle, see Fig. 5.2(d)) with the volume of the Au nanoparticles. The peak intensity of these GIXRF modulations reduces to ~ 2 times, if the mono-dispersive nature of the nanoparticles is lost on the substrate surface and the particles are present in the form of agglomerates (micro cluster). The intensity of GIXRF modulations further reduces to a value of ~ 1.2 times in a situation when large size clusters of the nanoparticles or a continuous thin film are present on the substrate surface.

Figure 5.1 shows a systematic representation of this agglomeration procedure of Au nanoparticles grown on Si substrate. The computation is performed at incident x-ray energy of 15.0 keV. The XRR and GIXRF profiles display a formal illustration as the density of the layer of Au nanoparticles increases from 0.005 to 19.3 g/cm³ and a continuous layer is formed on top of a Si substrate. The XRR profile does not show any signature of the presence of Au nanoparticles having densities from 0.005 to 2.0 g/cm³, which are likely due to the fact that the Au layer is quite thin ($d \sim 10$ nm) having a very low density (0.005 g/cm³) as compared to its bulk density (19.3 g/cm³). Thus, the

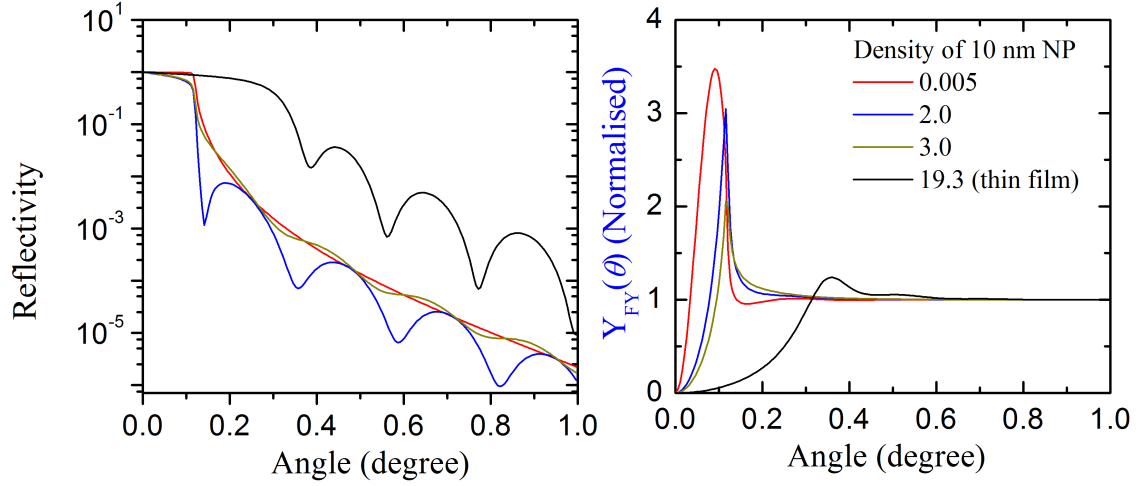


Figure 5.1: Computed XSW assisted (a) XRR and (b) Au-L α fluorescence profiles for 10 nm Au nano-spheres of various densities (0.005 to 19.3 g/cm³). During the calculation we have assumed Au nano-spheres dispersed on top of a Si surface at incident x-ray energy of 15.0 keV.

surface area concentration [ρ (g/cm³) \times d(cm)] of the Au nanoparticle on a Si surface is assumed to vary between 5 ng/cm² and 19.3 μ g/cm² [113, 38]. In addition, these GIXRF intensity modulations are also significantly affected by the shape factor of a particle. In the subsequent sections, these effects were explored in detail.

Effect of particle size distribution

In this section, the effect of particle size distribution on the GIXRF analysis has been studied. Numerical simulations have been carried out by taking into account a fixed average size of (dia.~30 nm) the Au nanoparticles and their different particle size distribution profiles. Figures 5.2(a), (b), and (c) show the computed GIXRF profiles for the Au nanospheres at 15.0 keV incident x-ray energy assuming different r. m. s. variations in the particle size distribution (σ ~2 nm, σ ~8 nm and σ ~12 nm, respectively). During the calculation of GIXRF intensity, we have considered a Gaussian size distribution profile for the Au nanospheres on a Si substrate. From Fig. 5.2, it can be clearly observed, that the GIXRF profile undergoes a systematic modification if the r. m. s. variation (σ) as the size of Au nanospheres changes from 2 to 12 nm. The Au-L α

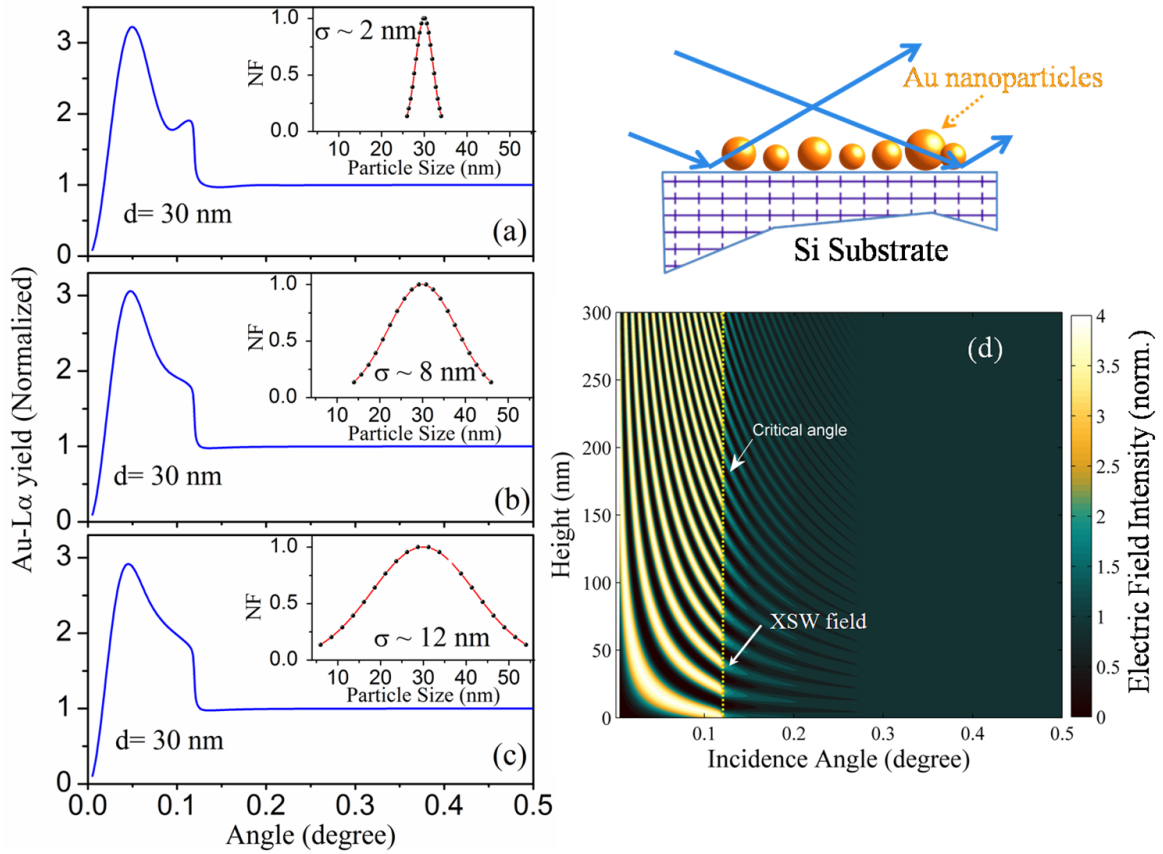


Figure 5.2: Computed Au-L α fluorescence profiles for the Au nano-spheres dispersed on top of a Si surface at incident x-ray energy of 15.0 keV. The Au-L α fluorescence yield has been calculated by assuming an average particle size of ~ 30 nm and considering different r. m. s. variations (σ) in the particle size distribution (a) $\sigma = 2$ nm, (b) $\sigma = 8$ nm, and (c) $\sigma = 12$ nm respectively. The insets show the computed distribution profiles of the Au nanoparticles (NF) vs. their size. On the upper right location of the figure we have depicted a schematic illustration for the distribution of nanoparticles on a Si surface. (d) Computed contour plot for x-ray field intensity distribution at 15 keV x-ray energy on a Si substrate.

intensity modulations in the GIXRF profiles below $\theta_c \approx 0.12^\circ$, change rapidly and merge together if one increases the r. m. s. variation in the particle size. In the insets of Fig. 5.2 we have also shown distribution profiles of the Au nanoparticle as a function of their size (normalized frequency-NF vs. particle size). In Fig. 5.2(d), we have shown computed electric field intensity (EFI) distribution above the Si surface as a function of incidence angle and height (z). During the EFI computations, incident x-ray of energy 15 keV was assumed. In Fig. 5.2(d), one clearly observes a boundary for the critical angle of the Si substrate ($\approx 0.12^\circ$). Below θ_c , the x-ray wave field on the Si surface exists in the form of

standing wave field. This standing wave field interacts with the Au nanoparticles and produces intensity modulations in the GIXRF profile below θ_C . On the top right location of Fig. 5.2, we have depicted a schematic illustration for the XSW induced fluorescence excitation of Au nanospheres on a Si substrate at grazing incidence angles.

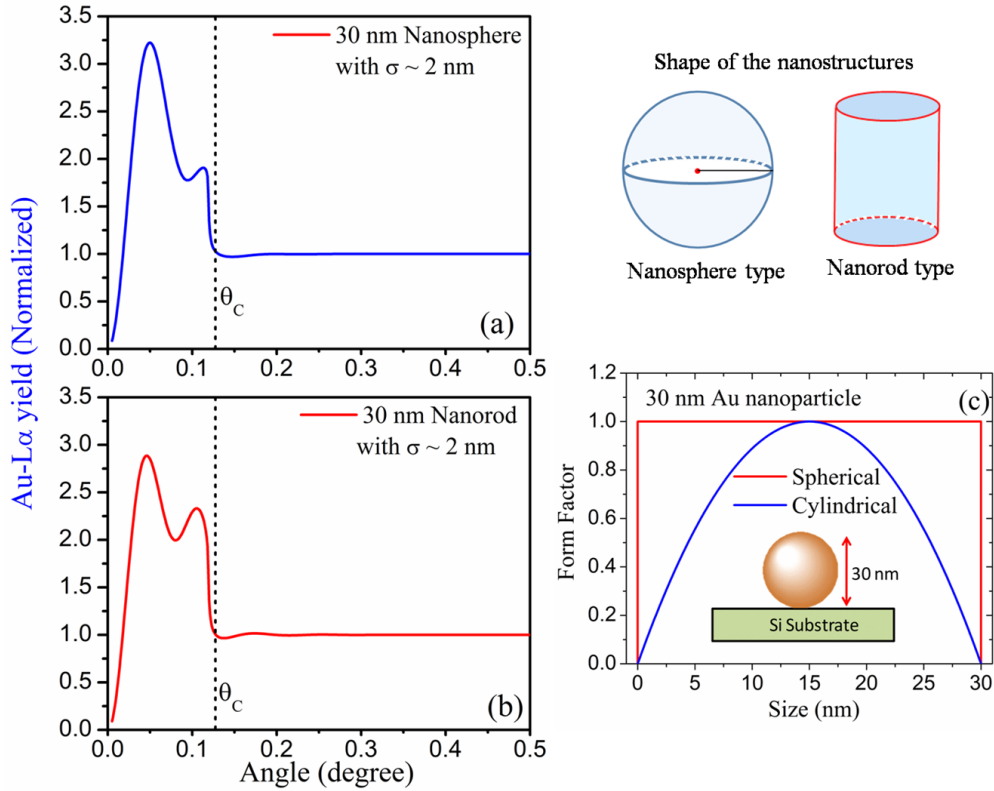


Figure 5.3: Computed GIXRF profiles (Au-L α fluorescence yields) for different shapes of Au nanoparticles distributed on the Si surface at 15.0 keV x-ray energy. (a) Nano-sphere (dia.= 30 nm), (b) Nanorod (height = 30 nm). In the above calculations, we have assumed a r. m. s. variation (σ) in the particle size distributions $\sigma = 2$ nm. (c) Computed form factor profiles for the spherical and cylindrical shapes nanoparticles.

Effect of particle shape

Numerical simulations were also carried out to study the effect of shape of a nanostructure in the GIXRF analysis. To maintain a consistency in the interpretation of our results with respect to previous sections, similar size of the Au nanoparticles (average diameter $d \sim 30$ nm) was considered during the numerical computations. In one

case (Fig. 5.3(a)), we have considered spherical shape of the nanoparticles. In another case (Fig. 5.3(b)), we have considered cylindrical shape (i.e. nanorod type) of the Au nanoparticles. In both the cases, we have assumed an r. m. s. variation (σ) in the particle size distribution of ~ 2 nm. The calculations were done at incident x-ray energy of 15 keV. The form factor ($F(z)$) for spherical and cylindrical nanoparticle can be given as $F(z) = [4z(d-z)/d^2]$ for $z \leq d$; 0 for $z > d$ and $F(z) = 1$ for $z \leq d$; 0 for $z > d$ respectively [181, 182]. From Figs. 5.3(a) and 5.3(b), it can be seen that the Au- $L\alpha$ fluorescence yield shows strong variations in the computed GIXRF profile especially below θ_C , if the shape of the nanoparticles changes from spherical to cylindrical. These results clearly show that the shape parameter (i.e. form factor profile) considerably modulates the GIXRF profile of a nanoparticle. The computed form factor profiles for the spherical and cylindrical nanoparticles have been depicted in Fig. 5.3(c). On the top right corner of Fig. 5.3, we have also shown schematic illustrations for the different shapes of nanoparticles. It can be seen from Fig. 5.3, that GIXRF investigations are fairly sensitive to the shape of the nanoparticles. Such measurements can be successfully employed to distinguish different shapes of the metal nanoparticles (e.g. nanosphere, nanorod, etc.).

Analysis of surface morphology of the nanoparticles

Assembled nanostructures on flat surface have recently attracted considerable interest in many nanotechnology, biotechnology and semiconductor quantum dot applications. Adequate characterisation of such patterned nanostructure is thus often needed to infer and characterize detailed surface morphology and chemical composition of the nanostructured materials. In the present case the surface morphology of self assembled Au nanoparticles were analysed using GIXRF measurements. Figure 5.4(a) depicts measured and fitted Au- $L\alpha$ fluorescence profile for the Au nanoparticles on the Si surface at incident x-ray energy of 15.0 keV. During the fitting, we have assumed a Gaussian profile for the particle size distribution of Au nanoparticles with a

polydispersity factor (σ/N_{av}) ~ 0.07 . Here, σ is the r. m. s. variation in the particle size whereas N_{av} describes the average diameter of the particles. Best fitted GIXRF curve to the measured data yields a value of $N_{av} \sim 30 \text{ nm} \pm 2 \text{ nm}$ with $\sigma \sim 2.1 \text{ nm}$. In Fig. 5.4(b), we have plotted the size distribution profile of the Au nanoparticles that has been taken into account during the computation of GIXRF profile. An AFM system (Danish Micro Engineering Ltd) operating in IC (intermittent contact) mode was employed to study the surface topography of the samples over the regions of $\sim 2 \mu\text{m} \times 2 \mu\text{m}$. Different regions of the sample surfaces were probed using computer-controlled sample translation stages. On the right hand side of Fig. 5.4, we have shown measured AFM images for the Au nanoparticles on the Si surface. The AFM results reveal an average vertical size of the Au nano-sphere $\sim 30 \text{ nm}$. However, the lateral dimension was found to be $\sim 200 \text{ nm}$. This is mainly because of the fact that the lateral resolution in the AFM investigations is often limited by the tip size of the AFM instrument [187].

5.3 Effect of temporal coherence on surface x-ray standing wave measurements

Over several decades, the X-ray standing wave (XSW) technique has been developed as a nondestructive element-specific probe yielding structural analysis over length-scales ranging from 0.1 to 100 nanometers. The method, which is reviewed elsewhere [100, 112, 188–190], has been widely exploited for a variety of applications including determination of positions of impurities in crystals [108, 109, 191–193], chemically-bound atoms at single crystal surfaces [152, 194, 195], metallic atoms in molecular multilayer films [98], ions at electrified liquid/solid interfaces [111], distributions of metallic nanoparticles on surfaces [38, 113, 181, 182] as well as studies of interface structures and density variations in synthetic periodic multilayer structures [196–198]. In terms of x-ray wavelength λ and scattering angle 2θ the probed

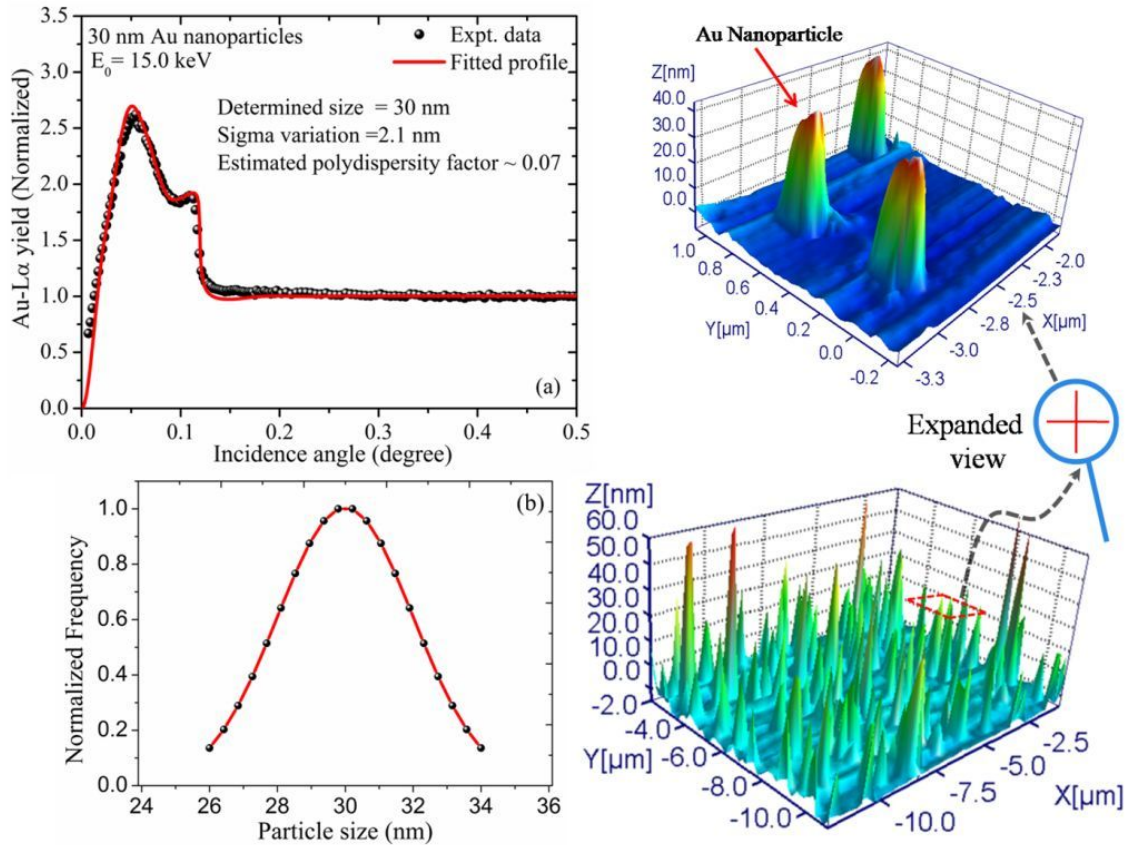


Figure 5.4: (a) Measured and fitted Au-L α fluorescence profiles obtained for the Au nanoparticles, deposited on top of the Si surface at 15.0 keV x-ray energy. The scattered points show the experimental data while the solid line is the best fitted profile to the measured data. The Au-L α fluorescence yield has been normalized at an incidence angle of $\theta = 0.5^\circ$. (b) Particle size distribution profile obtained for the Au nanoparticles on top of the Si surface using GIXRF measurements. On the right side, measured AFM images for the distribution of Au nanoparticles on the Si surface acquired at different locations are shown.

length-scale is directly linked to the XSW period $D = \lambda/2S \sin\theta = 2\pi/Q$, which is 0.1 to 1 nm for an XSW generated by single crystal Bragg diffraction, and 8 to 100 nm for an XSW generated by total reflection from a mirror surface.

While understanding of the XSW technique has witnessed considerable progress there remain a number of unexplored effects that can influence this 2-beam interference phenomenon. One such effect is the influence of the coherence properties of the incoming x-ray wave field on the XSW field intensity distribution above a reflector surface. In conventional XSW analysis the incident wave field is assumed perfectly monochromatic plane-wave with zero wavelength dispersion ($\delta\lambda = 0$), hence assuming

an infinite longitudinal coherence length of the incoming x-rays. As previously demonstrated [100, 199], this simplifying assumption has no significant effect on the analysis until the optical path length difference ($\Delta = n2zS \sin\theta$) between the two interfering waves is significantly smaller than the longitudinal coherence length ($L_L \approx \lambda^2/\delta\lambda$), where n is the index of refraction, z is the height of the probed atomic layer above the mirror surface and $\delta\lambda$ is the FWHM of the spectral distribution. Beyond this constraint, XSW analysis will not match well with the measurements, if the longitudinal coherence properties of the incoming x-ray field are not properly taken into account in the model calculations.

In this section, we extend the analysis method beyond the zero-bandwidth approximation to include the influence of longitudinal coherence properties of the incoming x-ray field on XSW measurements. The results show that the derived numerical solutions developed to account for the coherence properties of a source can be directly adapted in the computation of the angle-dependent XSW field pattern produced by a partially coherent x-ray beam, characterized with a Gaussian distribution in intensity and a finite spectral bandwidth. The new approach allows one to perform XSW analysis with improved reliability using most of the x-ray sources currently available, which offer finite spectral resolutions for the incoming x-rays. To explicitly demonstrate the applicability of our modified XSW approach, XSW analysis was performed on several nanostructured materials, deposited on Si or Au mirror surfaces using different incident x-ray beams with different longitudinal coherence properties.

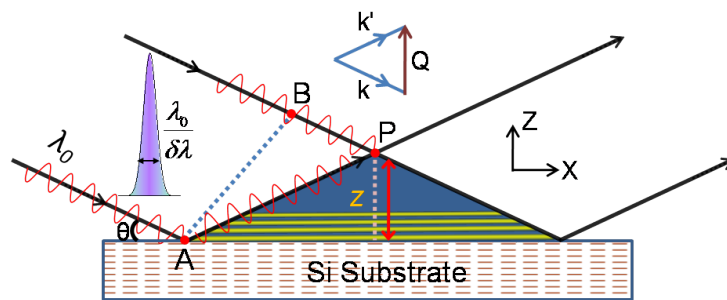


Figure 5.5: A schematic illustration describing formation of XSW field under total external reflection of x-rays on a mirror surface.

5.3.1 Theoretical background

It is convenient to express the electric field intensity at height z above a reflecting surface (refer Fig. 5.5) by [97]

$$I(\theta, z) = |\mathbf{E}_o^i + \mathbf{E}_o^r|^2 = I_o \{1 + R + 2\sqrt{R} \cdot \text{Re}[\gamma(\Delta)]\} \quad (5.1)$$

where $R = |E_o^r/E_o^i|^2$ represents the reflectivity above the Si mirror surface, $I_o = |E_o^i|^2$ is the incident intensity, \mathbf{E}_o^i and \mathbf{E}_o^r respectively describe amplitudes of the incident and reflected x-ray wave fields, the complex degree of coherence $\gamma(\Delta) = |\gamma_{ir}(\Delta)| \cdot \exp(i[\nu(\theta) - Q_z z])$ accounts for the interference between the incident and reflected wave fields, $Q_z = 4\pi S \sin\theta/\lambda$ represents z -component of scattering vector $\vec{Q} = \vec{k}^i - \vec{k}^r$, $\nu(\theta)$ is the phase of the E-field amplitude ratio and θ is the glancing incidence angle on the mirror surface. In the above expression, we have introduced an additional term $|\gamma_{ir}(\Delta)|$ that signifies the modulus of the degree of mutual coherence [200, 201] between incident and reflected x-ray waves above the mirror surface. Its value changes from 0 to 1 and strongly depends on the optical path length difference $\Delta = n(AP - BP) \approx n2zS \sin\theta$ between two wave fields at point P with a vertical height z above the substrate surface. It is expressed by

$$\gamma(\Delta) = \frac{\langle \mathbf{E}_o^i(P, t) \cdot \mathbf{E}_o^r(P, t) \rangle}{\left[\langle |\mathbf{E}_o^i(P, t)|^2 \rangle \cdot \langle |\mathbf{E}_o^r(P, t)|^2 \rangle \right]^{1/2}} \quad (5.2)$$

Figure 5.6(a) depicts simulation for the term $\text{Re}[\gamma(\Delta)]$ as a function of path length difference, (represented in terms of height z) above the substrate surface at incidence angle of $\theta \approx 0.114^\circ$. Fig. 5.6(b) shows the contour plot for the x-ray field intensity distribution computed as a function of height z and incidence angle θ on top of the Si substrate surface. In the contour plot (Fig. 5.6(b)), one clearly observes a boundary for the critical angle of the Si substrate. The visibility contrast of XSW interference fringes is significantly higher below the critical angle $\theta_c \approx 0.114^\circ$. The results presented in Figs

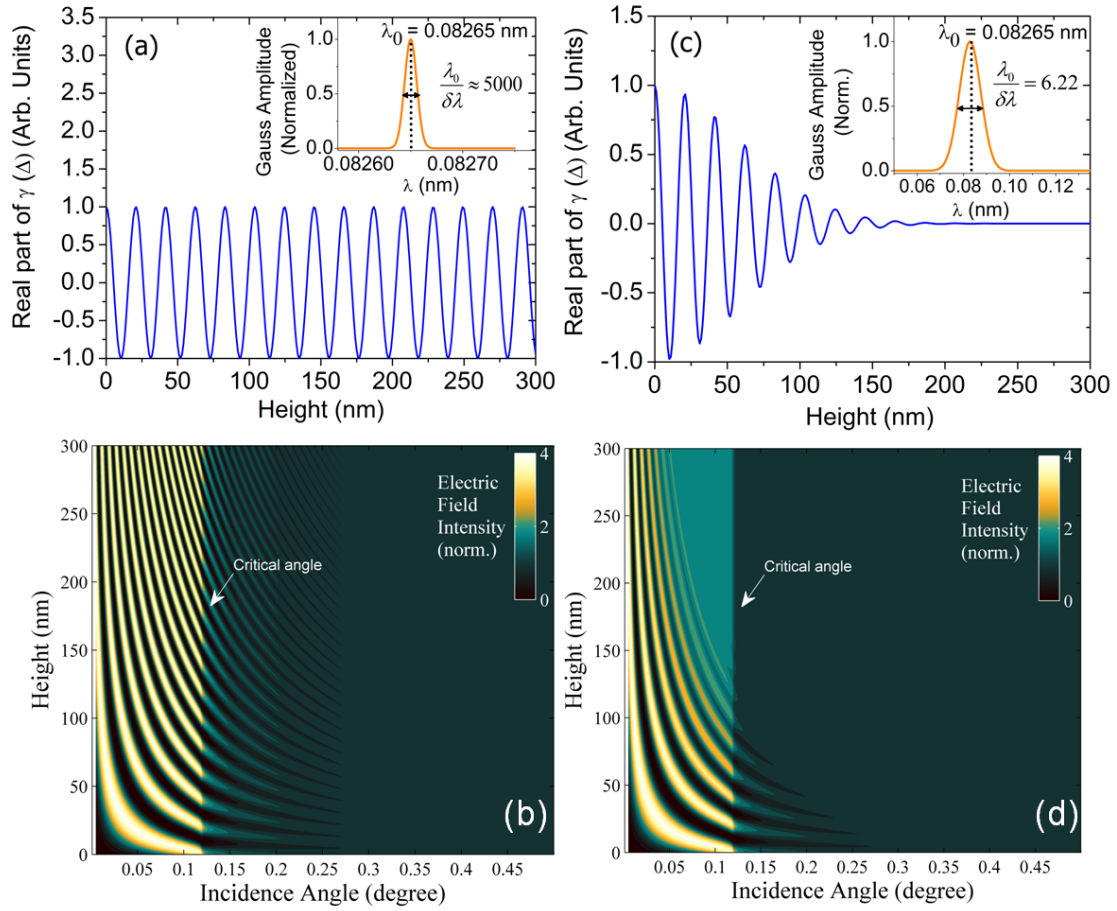


Figure 5.6: Variation of $Re [\gamma(\Delta)]$ and computed x-ray field intensity distribution above the Si substrate surface for the 15 keV x-rays at two different spectral resolutions. (a) and (b) show simulation results obtained at spectral resolution of $\lambda_0/\delta\lambda \approx 5000$. While (c) and (d) depict simulation results obtained at low spectral resolution of $\lambda_0/\delta\lambda \approx 6.22$. (a) and (c) are calculated at the critical angle $\theta_c \approx 0.114^\circ$.

5.6(a) and 5.6(b) have been simulated for incident x-rays of 15 keV and considering a spectral resolution of $\lambda_0/\delta\lambda \approx 5000$, described by a Gaussian distribution profile $I(\lambda) = \frac{I_0}{\sqrt{2\pi}(\delta\lambda/2.35)} \exp[-\frac{(\lambda - \lambda_0)^2}{2(\delta\lambda/2.35)^2}]$ as shown in the inset of the Fig. 5.6(a). It can be further observed from Fig. 5.6(a), at a large value of spectral resolution, the amplitude of real part $\gamma(\Delta)$ remains unchanged up to the height $z = 300$ nm above the substrate surface. This is because at this incident angle the optical path length difference between the incident and reflected waves at $z = 300$ nm is $\Delta \sim 1.2$ nm, which is much smaller than the longitudinal coherence length (~ 413 nm).

Figures Fig. 5.6(c) and Fig. 5.6(d) respectively report simulations obtained for the

incident x-rays energy of 15 keV comprising a spectral resolution of $\lambda_o/\delta\lambda \approx 6.22$. From Fig. 5.6(c), it can be seen that at large height above the substrate surface, for example, at $z \geq 150$ nm, the incident and reflected beams hardly remain coherent with each other. As a result, the interference term in eqn. (5.1) vanishes and the total x-ray intensity above the substrate simply represents the sum of the intensity of the incident and reflected x-rays beams (refer to Fig. 5.6(d)). Furthermore, it can also be noticed from Fig. 5.6(d) that the XSW interference modulations below critical angle are strongly correlated with the $\gamma(\Delta)$ value. If path length difference Δ (for a given height z), between two interfering beams, is significantly smaller than the coherence length (i.e. $\Delta \ll L_L$), then a XSW with high fringe visibility, $V = (I_{max} - I_{min})/(I_{max} + I_{min})$, is produced in the total reflection region. As the path length (Δ) is increased, the XSW fringe visibility is reduced. For example, for incident x-rays of energy ~ 15 keV comprising of spectral resolution of $\lambda_o/\delta\lambda \approx 6.22$, the coherence length $L_L \approx 0.51$ nm (FWHM), which corresponds to a height of $z \approx 129$ nm above the substrate surface. At this height, the visibility of the XSW fringe has reduced by $\sim 50\%$. For large heights ($z \gg L_L$), the interference effect completely vanishes and the net intensity below the critical angle attains maximum value of $\approx 2I_o$.

5.3.2 Numerical simulations

In this section, we describe the applicability of the XSW methodology by analysing a few nanostructured materials using a well-characterized partial coherent x-ray radiation. Figure 5.7(a) depicts simulation results for the Au nanoparticles distribution on the Si(100) surface, that clearly reveals deeper insights on how the monochromaticity of the partially coherent x-ray radiation affects the sensitivity of the TR-XSW assisted angle dependent Au-L α fluorescence yield of the Au nanoparticles. The TR-XSW assisted Au-L α fluorescence profiles were computed at different spectral widths of the incident x-ray radiation assuming spherical shape of the Au nanoparticles (dia. ≈ 250 nm). It can be noted from Fig. 5.7(a) that the XSW assisted Au-L α fluorescence profile of the

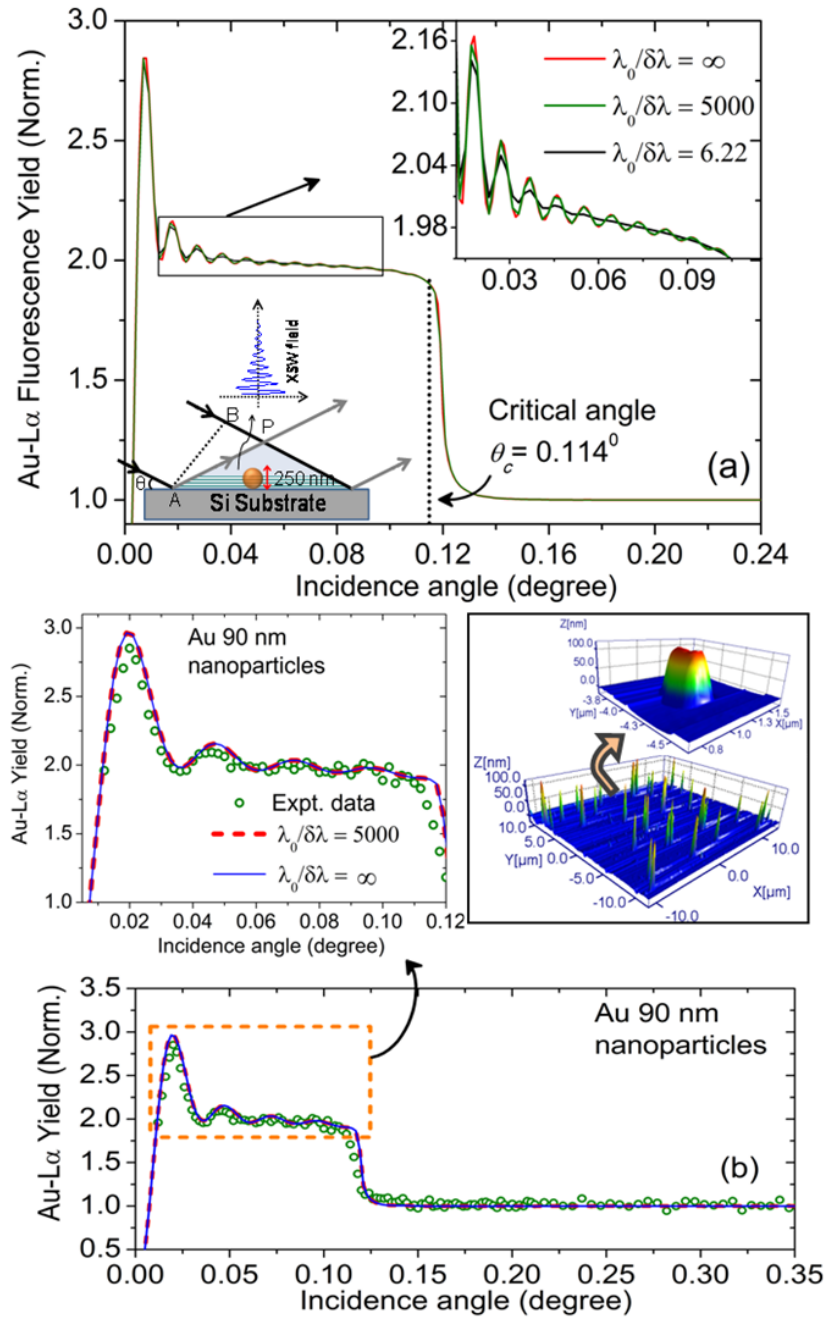


Figure 5.7: (a) Computed XSW induced fluorescence profiles for spherical Au nanoparticles distribution on a Si substrate surface at different spectral resolution widths of the incoming x-ray beam. The angle dependent fluorescence profiles are simulated using eqn. (5.1) and the formula $I_{FY}(\theta) = \int_0^d I(\theta, z) \times \exp\left(-\frac{\mu_{Au}}{S \sin\phi}\right) \times F(z) dz$, where μ_{Au} describes the linear absorption coefficient of Au for the outgoing fluorescent x-ray photons, ϕ is the take off angle of emitted fluorescent photons and d is the diameter of the nanoparticle, $F(z) = 4z \frac{(d-z)}{d^2}$ represents the normalized density profile for a spherical nanoparticle as a function of height z above the substrate surface. (b) Comparison of measured to calculated Au fluorescence yields. AFM image of Au nanoparticles distribution on Si surface is shown in upper right along with enlarged image of a single nanoparticle.

nanoparticles undergoes slowly with a distinct and systematic variation as we allow to vary the monochromaticity of the incident x-ray radiation ($\lambda_0/\delta\lambda = \infty$ to 6.22). The visibility contrast of the XSW induced Au-L α fluorescence oscillations decreases gradually in the total reflection region ($\theta < 0.114^\circ$) at the lower spectral resolutions. Even, many XSW oscillations vanish completely in the computed Au-L α fluorescence profile at spectral resolution $\lambda_0/\delta\lambda \approx 6.22$, which can be clearly seen from the expanded view as shown in the inset of Fig. 5.7(a)).

5.3.3 Analysis of Au nanoparticles and Langmuir-Blodgett thin film structure using partially coherent SR radiation

The experimental measurements for the Au nanoparticle distribution comprising an average particle size $d \sim 90$ nm (dia.), dispersed on a Si(100) substrate surface were carried out at the BL-16 beamline of Indus-2 synchrotron radiation facility [46]. The angular resolution of the BL-16 reflectometer station (KOHZU 2-circle goniometer) was found to be $\sim 0.002^\circ$. Incident x-rays of energy 15 keV from bending magnet source, monochromatized with a fixed exit Si (111) double-crystal monochromator were used to excite nanoparticle samples at grazing incidence angles. A vortex spectroscopy detector (SDD) comprising an active surface area of 50 mm² and an energy resolution of ~ 140 eV at 5.9 keV (Mn K α x-rays) was placed in the plane of sample substrate (*i.e.*, in the plane of s-polarized electric vector of the synchrotron beam) in order to obtain better signal to noise ratios for the emitted fluorescent x-rays. The SDD was placed at ~ 30 mm distance from the centre of the beam footprint on the sample surface. Au-L α fluorescence x-rays emitted from the gold nanoparticles were collected by a Vortex spectroscopy detector. Figure 5.7(b) depicts experimentally measured XSW induced Au-L α fluorescence profile for the Au nanoparticles along with the computed TR-XSW profiles at different spectral resolutions. The counting statistics of Au-L α intensity was ensured in the range of (1-3)%. In the computation, we have considered a polydispersity

factor (σ/N_{av}) ≈ 0.05 for the Au nanoparticles, where N_{av} is the average particle size and σ is the r. m. s. variation in particle size. In Fig. 5.7(b), one observes a couple of interference oscillations in the measured XSW induced Au-L α fluorescence profile below the critical angle of the Si substrate ($\theta_c \approx 0.114^\circ$). These peaking interference oscillations in the fluorescence profile emerge due to the coincidence of the XSW antinodes within the volume of the Au nanoparticles. The left side inset of the Fig. 5.7(b) shows an expanded view for the total external reflection region. It can be seen that the computed fluorescence profile at spectral resolution $\lambda_o/\delta\lambda \approx 5000$ closely agrees with the profile that was obtained assuming an ideal monochromatic x-ray source (*i.e.* $\lambda_o/\delta\lambda = \infty$). This is due to the fact that at higher spectral resolutions, the incident and reflected x-ray beams remain fully coherent, up to a height of several hundred of nanometers above the substrate surface. If the size of the nanostructure is considerably smaller than the coherence length, for example, in our case of 90 nm Au nanoparticles, then full volume of a nanostructure is excited by the XSW field created with a 100% coherent superposition of the incident and reflected x-ray beams. In conditions, if spectral resolution of the incident x-rays deteriorates or if the height of a nanostructure increases on top of the substrate surface, then the measured fluorescence profile will show deviation from the ideal behavior ($\lambda_o/\delta\lambda = \infty$). On the top right inset of Fig. 5.7(b) we have shown the measured AFM image for the Au nanoparticles, which clearly demonstrates a mono-dispersed surface topography for the Au nanoparticle distribution on the Si substrate surface. We have also performed TR-XSW analysis for a LB thin film structure deposited on top of a Au mirror surface using 10 keV incident x-rays of different spectral resolutions. This experiment used the hard-bend radiation from the D-line at the Cornell High Energy Synchrotron Source. Figures 5.8(a-c) show measured Zn-K α fluorescence profiles originated from the trapped Zn atomic layer (thickness ≈ 3.0 nm) at a height $z \sim 90.3$ nm in the LB film structure using incident x-ray beam with differing longitudinal coherence lengths and a fixed angular divergence $\approx 0.003^\circ$. Figure 5.8(a) shows Zn-K α fluorescence profile measured using a nearly ideal plane wave

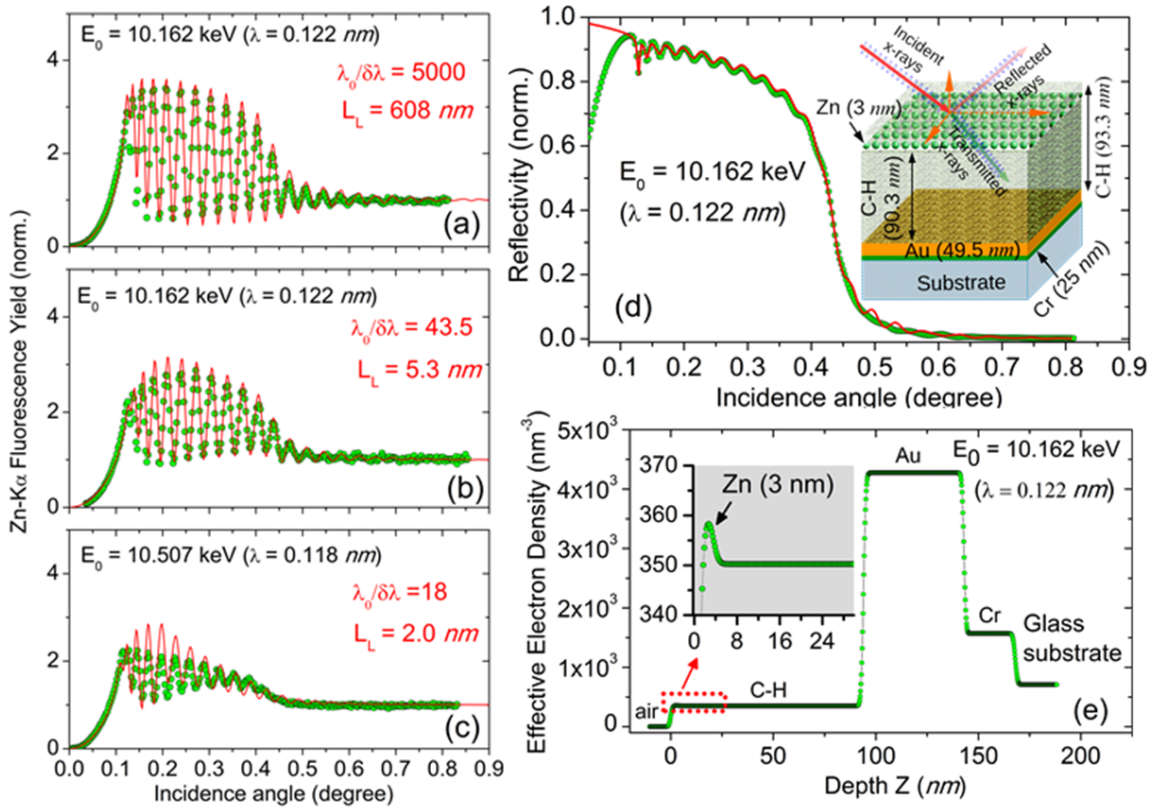


Figure 5.8: Experimental demonstration of the applicability of the partially coherent radiation for TR-XSW analysis. (a-c) Measured and fitted angle-dependent x-ray fluorescence profiles for the Zn atomic layer embedded in a LB film structure at different spectral widths of the incident x-ray photons. The relative uncertainty in the Zn yield is less than 5% for data above 0.45° and less than 2% below 0.45° . (d) Measured and fitted x-ray reflectivity profiles for the LB thin film structure at x-ray energy of 10.162 keV with spectral resolution of $\lambda_0/\delta\lambda \approx 5000$ corresponding to (a). (e) Effective electron density profile of the LB thin film structure determined from the best fit results using combined XRR and TR-XSW analysis, which clearly reveals the presence of Zn atomic layer at a mean height $\langle z \rangle = 90.3$ nm, from Au surface layer.

condition of spectral width $\lambda_0/\delta\lambda \approx 5000$, ($L_L \approx 608$ nm) obtained by a Si(111) monochromator. Figs. 5.8(b) and 5.8(c) demonstrate measured Zn-K α fluorescence profiles obtained using relatively wider band-pass incident x-ray beams produced by synthetic Bragg multilayer monochromators, providing spectral resolutions of $\lambda_0/\delta\lambda \approx 43.5$ and $\lambda_0/\delta\lambda \approx 18$, respectively, which were determined by using the measured angular width of the reflectivity curves from two different hkl planes of a Si analyser crystal in the sample position. The details about preparation of LB thin film structure and experimental conditions used for the measurements described in Fig. 5.8

are given elsewhere [98, 188, 199, 202]. It can be seen from Figs. 5.8(a-c), the visibility of the XSW induced oscillations in the Zn-K α fluorescence profile reduces dramatically as the monochromaticity ($\lambda_0/\delta\lambda$) of the incident x-ray photons varies from 5000 to 18. The theoretically computed curves shown by red solid lines closely predict the experimental observations even in the cases when spectral resolution of the incident x-ray photons changes by large magnitudes (≈ 200 times). This encouraging level of agreement between the experimental and computed TR-XSW profiles convinces the validity of our modified XSW approach. In Fig. 5.8(d), we have shown the measured and fitted x-ray reflectivity profiles obtained for the LB thin film structure at incident x-ray photon energy of 10.162 keV at the highest spectral resolution corresponding to the Fig. 5.8(a). In this figure, we have also shown a schematic layout for the LB thin film structure. Fig. 5.8(e) shows effective electron density profile (EDP) for the LB thin film structure determined from combined x-ray reflectivity (XRR) and TR-XSW analysis using the best fit results obtained in all three cases. The EDP clearly reveals the presence of Zn atomic layer at location $z \approx 90.3$ nm, from the Au layer surface.

5.4 Characterization of TiO₂ nano-composites

Nanostructures of titanium oxide are currently being investigated for variety of potential applications, such as solar photovoltaics, solar water splitting for H₂ fuel generation etc., as they offer excellent photo-catalytic properties. Recently, several motivated research programs are being pursued for the development of advanced solar absorber materials for efficient utilization of solar energy as a long term sustainable energy resource [186, 203–207]. Titanium oxide (TiO₂) nanostructures, are considered to be the most promising photo-catalysts for this purpose, because these have a bandgaps in the ultraviolet region which can be readily tuned to the visible region after proper band-gap tailoring [208–212]. TiO₂ is being used in solar photovoltaics, solar water splitting for H₂ fuel generation, and environmental pollutant purification etc.

applications [174, 206, 213, 214]. In addition, TiO₂ nanomaterials are also used for biochemical, sensors, self-cleaning applications [215–217]. All these advanced technological applications require highly pure, low dimensional crystalline TiO₂ nanostructures of specific sizes. Precise knowledge about the growth kinetics of nucleation, formation of layer structure, crystalline nature, etc. help us in understanding the physical properties of TiO₂ nanostructure for the practical device applications. The microstructural characterisation of TiO₂ nanostructures is also very essential as their catalytic properties are greatly influenced by the structural defects and associated surface-interface characteristics. One, therefore, needs suitable processes to synthesize different types of nanostructures effectively on a large surface with a high production rate and reliable means to analyse them in an efficient manner [218].

Presently deposition of TiO₂ nanoparticles (NP) on a flat smooth surface is being carried out by using various liquid phase, and gas phase chemical synthesis processes [219–227]. Most of these synthesis processes are very time consuming and based on the chemical process. In addition, during the synthesis process, a lot of precautions are required to avoid any impurity contamination in the deposited sample. Laser pyrolysis is an efficient deposition technique to grow low dimension nanomaterials over a large surface area of the substrate [228–233]. It is very fast and single step process with a very high production rate.

In this section, we describe the synthesis of the TiO₂ nanomaterial using CW CO₂ laser pyrolysis method and their non-destructive surface characterisation using XRR and GIXRF techniques. The growth conditions have been extensively studied using GIXRF measurements. We have also performed grazing incidence x-ray diffraction (GIXRD) measurements to investigate the crystalline nature of the deposited NP on the Si substrate. Detailed surface morphological analysis of the TiO₂ nanostructure has been performed using combined XRR and GIXRF measurements. Electron diffraction (ED) and transmission electron microscopy (TEM) measurements were also carried out to validate the findings of the XSW analysis on the TiO₂ nanostructures.



Figure 5.9: A photograph of the deposition set up (based on the laser pyrolysis process).

5.4.1 Synthesis of TiO₂ nanoparticles

TiO₂ nanostructures were synthesized in an in-house developed continuous wave (CW) CO₂ laser based gas phase pyrolysis system. Figure 5.9 shows the photograph of the deposition chamber. The basic synthesis process is based on the resonant absorption process. In this process, C₂H₄ is used as a sensitizer gas. C₂H₄ absorbs the laser energy resonantly and transfers this energy to the precursor material Ti(OC₃H₇)₄ or TTIP via molecular collisions for the formation of TiO₂ by breaking the bonds of TTIP. Synthesized TiO₂ NP were collected on a Si (100) substrate on the top of the reaction zone of laser beam and Ti(OC₃H₇)₄ gas. We have also made an arrangement that allows C₂H₄ gas to flow through the TTIP in the vapour phase to the reaction zone through a round-nozzle of diameter 4 mm. The typical diameter of the laser beam was 5 mm (FWHM). The samples were deposited using argon, as a cooling gas medium, which also confines the flow of the NP at a constant pressure of ~ 650 mbar into the reaction chamber. We have employed a constant temperature of 80°C to the chamber tube, through which the vapours of TTIP and C₂H₄ flow to the reaction zone to avoid any condensation of vapour inside the tube. Different experimental parameters of the deposition process have been optimized to obtain high quality NP formation on a substrate surface. The optimum deposition parameters for the generation of highly pure, nearly mono-dispersed TiO₂ NP are given in Table 5.1.

Prior to the deposition of the nanostructures, the r.m.s roughness, metal impurity (if any) and presence of the any native oxide on top of the Si substrate have been analysed by the XRR and XRF measurements. The r.m.s roughness and the thickness of the SiO₂ layer were found to be $\sim 0.48 \pm 0.05$ nm and 2.4 ± 0.2 nm respectively. TiO₂ NP were deposited on Si (100) substrates for the surface characterisation. A Cu grid support (a TEM grid comprising films of formvar/carbon) was also placed in close proximity with the Si substrate on top of the reaction zone for the collection of nanoparticles for TEM analysis. The collection time for NP on top of the Cu grid was ~ 4 second.

Table 5.1: Optimum parameters for the low dimensional TiO₂ nanoparticle deposition.

SI. No.	Parameter	Value
1	Laser power (after reactor)	80W
2	Reactor pressure	650 mbar
3	Argon flow rate	0.4 slpm*
4	Flow rate of Ethylene	0.2 slpm*
5	Temperature of precursor materials (or Bub- bler temperature)	40 °C
6	Temperature of the substrate	300K

* slpm : standard liters per minute.

5.4.2 Studies on growth kinetics and crystalline phase of TiO₂ nanoparticles

To elaborately study the growth conditions of TiO₂ nanoparticles several samples were prepared at precursor temperature 40°C, 50°C, 60°C, 70°C, and 80°C respectively. However, the temperature of the tube was kept fixed at $\sim 80^\circ\text{C}$. The TXRF measurements were carried out at BL-16 beamline of Indus-2 synchrotron radiation facility for all the samples [46, 53] to obtain quantitative information on the growth mechanism of TiO₂ nanoparticles using laser assisted pyrolysis fabrication process. In Fig. 5.10, we have plotted the vapour pressure of precursor material (TTIP) and Ti fluorescence intensities emitted from the TiO₂ NP samples at different temperature of the

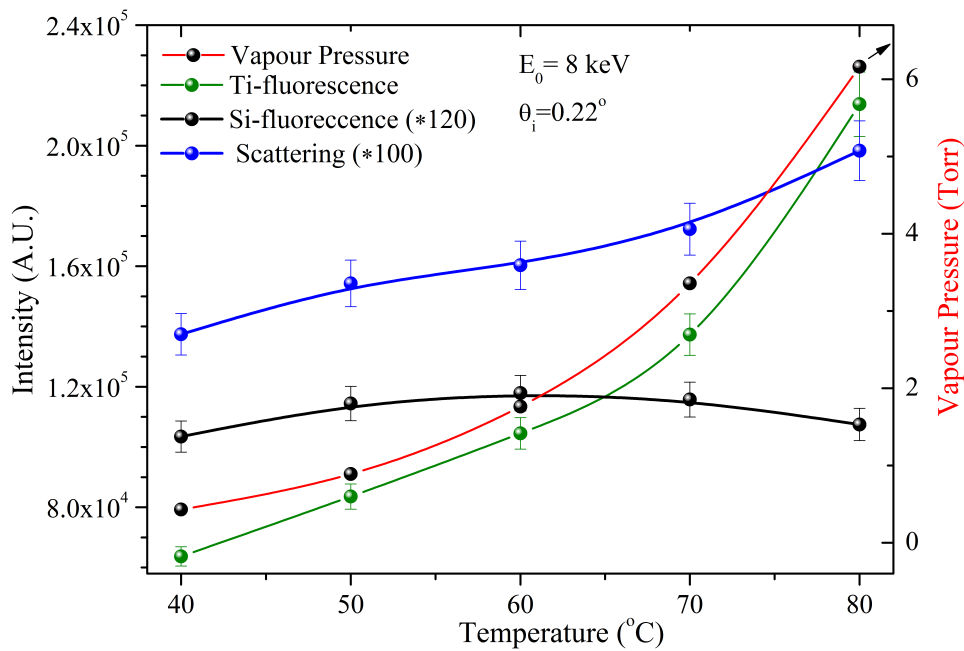


Figure 5.10: Total reflection x-ray fluorescence (TXRF) measurements were performed at incident x-ray energy of 8 keV. The grazing incidence angle $\theta \sim 0.22^\circ$ was fixed during the measurements. Si, Ti-fluorescence intensity, and Scattered light intensity are plotted with vapour pressure of TTIP as a function of temperature.

precursor materials. The variation of Compton scattered intensity observed in different NP samples with temperature is also plotted in Fig. 5.10. It can be seen from Fig. 5.10 that the variation of Ti fluorescence intensity follows the variation of vapour pressure of the precursor material at different temperatures. This is because the amount of TiO_2 deposited on the Si substrate is strongly correlated to the vapour pressure of TTIP. Therefore, if one increases the temperature of TTIP, it increases the deposition of NP on the substrate surface. It can also be noticed from Fig. 5.10 that variation of Compton scattered x-ray follows the variation of Ti fluorescence intensity at different vapour temperature of TTIP. Similar nature was also observed for Si fluorescence intensity. The laser pyrolysis process provides high production rate for the fabrication of the nanoparticles. It is also possible to fabricate doped nanoparticle structures with a narrow particle size distribution over the broad surface area of a substrate.

The crystalline nature of the TiO_2 nanoparticles were analysed using powder x-ray diffraction measurements in grazing incidence geometry at the room temperature

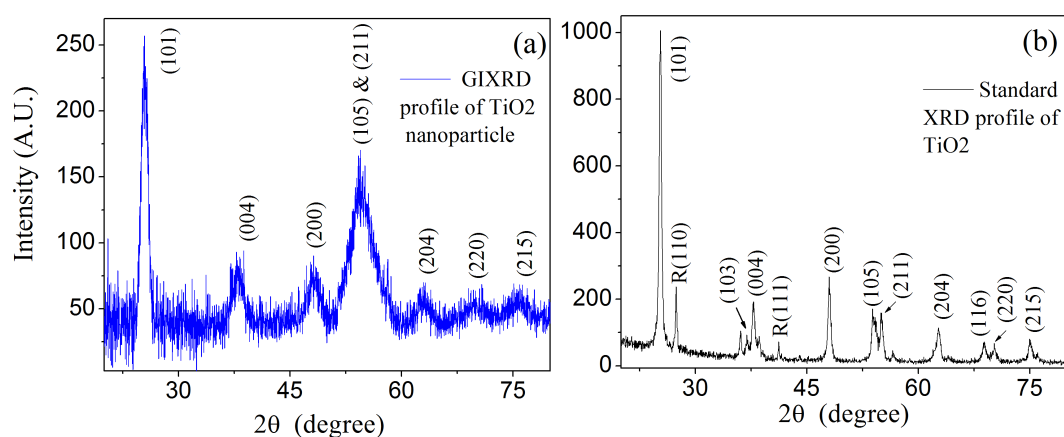


Figure 5.11: (a) Grazing incidence x-ray diffraction profile of synthesised TiO₂ nanoparticles deposited on Si substrate. (b) XRD profile of standard TiO₂ powder (P25) at Cu-K α wavelength ($\lambda=1.54$ Å).

condition. The x-ray diffraction (XRD) measurements were carried out using a commercial BRUKER D-8 x-ray reflectometer station at Cu-K α wavelength ($\lambda=1.54$ Å). Figure 5.11(a) demonstrates the XRD profile of the fabricated TiO₂ nanostructures. During the measurement the grazing incidence angle was fixed at 1.0° . The TiO₂ nanoparticles were deposited on a Si substrate using laser pyrolysis process for a deposition time of 15 minute. In Fig. 5.11(b), measured XRD profile of a standard TiO₂ powder (P25) at room temperature is provided for the comparison purpose [234, 235]. The characteristics peaks observed in the profile (5.11(a)) predict the structure of the sample to be tetragonal with the $I4_1/amd$ space group. It can also be concluded from Fig. 5.11 that the TiO₂ nanoparticles are polycrystalline in nature and are having an anatase phase. The particle size of the TiO₂ nanoparticles, evaluated from the grazing incidence x-ray diffraction pattern using Scherrer's formula [236] was found to be $\sim 8-10$ nm (corresponding to the (101) reflection).

5.4.3 Determination of surface morphology of TiO₂ nano-composites

Surface morphology of the nanocomposite materials can be determined using XSW method. XSW induced GIXRF measurements are extremely sensitive to the nature of

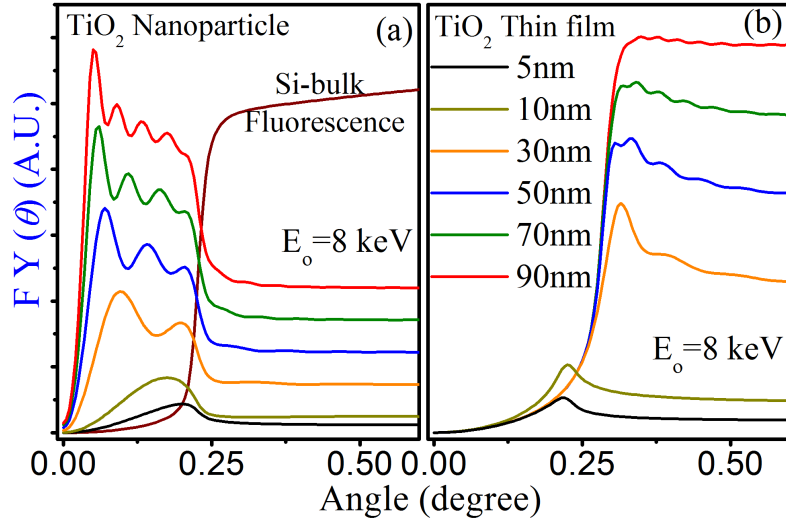


Figure 5.12: Calculated XSW assisted GIXRF profiles at 8 keV incident x-ray energy for two cases: (a) TiO_2 nano-spheres of various sizes, and (b) TiO_2 thin films of different thicknesses on top of Si substrate.

surface structure of a nanomaterial (i.e. if it is a thin film, nanoparticles, macroparticles or buried layer etc). Figure 5.12(a) depicts computed GIXRF profiles for the TiO_2 nano-spheres comprising of an average particle size ranging from 5 nm to 10 nm, whereas Fig. 5.12(b) shows the simulated GIXRF profiles for TiO_2 thin film structures of various thicknesses ranging from 5 nm to 10 nm. The simulations were carried out assuming an incident x-ray energy of 8 keV. In Fig. 5.12(a) Si- $K\alpha$ fluorescence intensity emitted from the Si substrate is also plotted. It can be seen from Figs. 5.12(a) and 5.12(b) that fluorescence yields (FY) emitted in the case of nanoparticles and in the case of thin film structures are markedly different from one another. Distinct differences observed in the nature of the GIXRF profiles in case of nanoparticles and in the case of thin film structure can be understood from the XSW wave field distribution computed as a function of grazing incidence angle and depth z on top of a Si substrate surface at 8 keV incident x-ray energy (see Fig. 5.14(c)). The nanoparticles are excited by the x-ray field present in the form of XSW wave field below the critical angle on top of the Si substrate surface. On the other hand in the case of TiO_2 thin film structure one observes the Ti- $K\alpha$ fluorescence yield at incidence angles above $\theta \approx 0.25^\circ$ (critical angle of Ti at 8 keV). The Ti- $K\alpha$ fluorescence yield increases monotonically if one increases the

thickness of TiO₂ thin film medium (5.12(b)). From the simulations presented in Figs. 5.12(a) and 5.12(b) it can be concluded that by observing the fluorescence intensity emitted in the vicinity of the critical angle it is possible to predict the structures of the nanomaterials (nanoparticle type or continuous thin film structure type).

In order to validate the capability of the combined XRR and GIXRF analysis

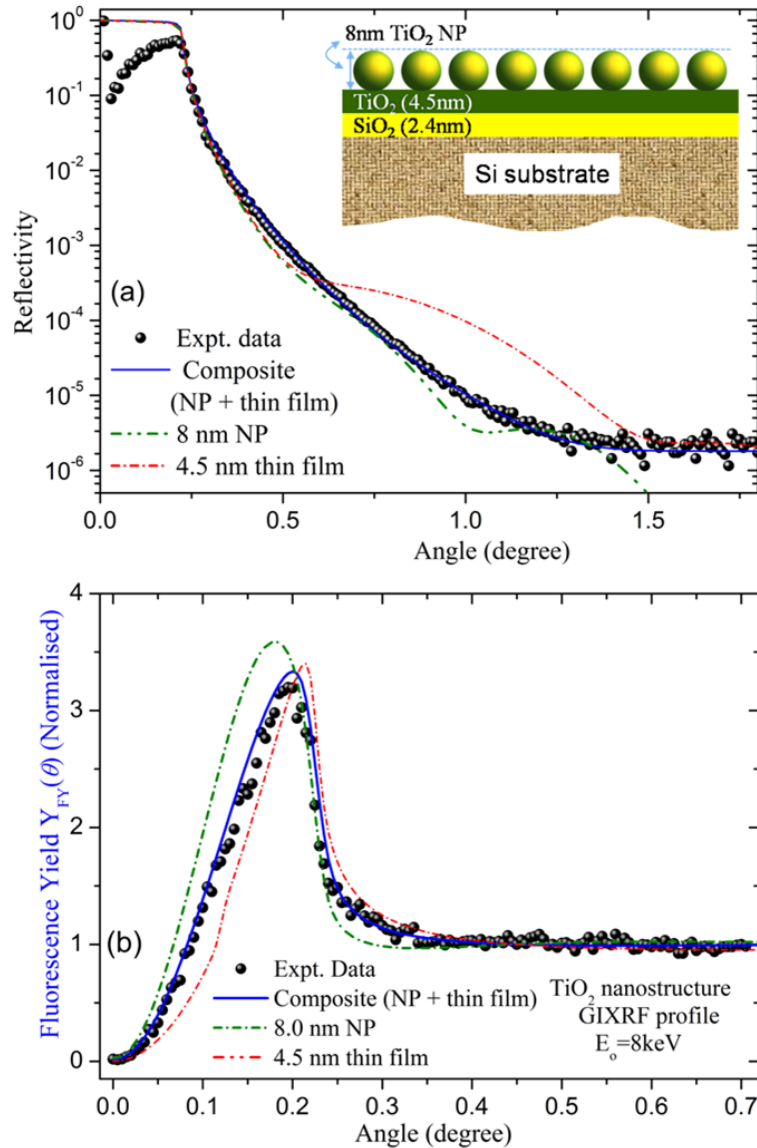


Figure 5.13: Measured and simulated (a) XRR and (b) XSW induced GIXRF profiles of TiO₂ nanostructures at 8 keV incident x-ray energy. The inset shows a three layer model of TiO₂ nano-structure opted for the fitting of measured experimental data.

technique for the analysis of nanoparticle matter we have analysed the distribution of composite TiO₂ nanostructures on top of a Si substrate surface. The simultaneous XRR

and GIXRF measurements were carried out at reflectometer station of BL-16 beamline at 100 mA ring current. The angular resolution of the BL-16 reflectometer station (KOHZU 2-circle goniometer) was found to be $\sim 0.002^\circ$. Figures 5.13(a) and 5.13(b) respectively represent the measured and fitted XRR and GIXRF profiles of the composite TiO₂ nanostructures on top of the Si substrate surface at 8 keV incident x-ray energy. It can be seen from Fig. 5.13(b) that the measured fluorescence profile of Ti-K α matches quite well with the simulated profile when a three layer model comprised of a SiO₂ layer on top of Si substrate, a bare TiO₂ thin layer, and a low density TiO₂ NP layer on top of the TiO₂ thin film is assumed for the fitting of experimental Ti-K α yield (see the inset of Fig. 5.13(a)). For the comparison purpose computed GIXRF profiles for the individual cases (either nanoparticles or a continuous thin film) are also provided in Fig. 5.13(a). It can be seen that these computed profiles significantly differ from the measured Ti-K α GIXRF profiles. However, the XRR profile presented in Fig. 5.13(a) was fitted considering a low density SiO₂ over-layer of thickness ~ 2.4 nm. The XRR profile provides the critical angle of Si ($\sim 0.22^\circ$), which corresponds to critical value of Si at 8 keV energy. The XRR profile does not show any signature of the presence of TiO₂ NP or pure TiO₂ thin layer medium. This can be attributed to the fact that the TiO₂ layer is quite thin ($d \sim 4.5$ nm) having a very low density (0.4 gm/cm³) as compared to its bulk density (4.23 gm/cm³). The XRR profile is unable to distinguish the low electron density contrast between the low density TiO₂ layer and Si substrate. On the other hand, the GIXRF profile shows a strong peaking behaviour near the critical angle of Si substrate ($\theta_c=0.22^\circ$) due to the coincidence of the XSW antinodes with the location of NP (see the inset of Fig. 5.14(a)). The measurements presented in Fig. 5.13(a) clearly show that the combined analysis provides us a novel capability to completely resolve the structure of a complex thin layered medium comprising of both particles as well as reflecting layer structure. In our case, the best fit results indicate the presence of TiO₂ nano-spheres of average diameter $\approx 8.0 \pm 1.0$ nm with an average density of $\rho \approx 0.04$ gm/cm³ (surface area concentration ~ 0.032 μ g/cm²) with a underneath TiO₂ thin film layer of thickness \sim

4.5 nm, and density $\approx 0.4 \text{ g/cm}^3$ on top of the Si substrate. The roughness values for NP layer and TiO₂ thin film medium were found to be $\sim 0.6 \text{ nm}$ and $\sim 0.8 \text{ nm}$ respectively.

We have also carried out characterisation of surface morphology (i.e., particle size, shape, nature of dispersion, particle agglomeration, presence of wetting layer, etc.) of another TiO₂ nanostructure using combined simultaneous XRR and GIXRF measurements at 8 keV x-rays. Figures 5.14(a) and 5.14(b) respectively represent the measured and fitted combined XRR and GIXRF profiles of the TiO₂ nanostructure on top of a Si substrate surface. It can be seen from Fig. 5.14(a) that the simulated XRR profile closely follows the measured profile if we assume a three layer model (as shown in the inset of Fig. 5.14(a)) comprising of a thin SiO₂ layer on top of Si substrate, a bare TiO₂ thin layer, and a low density TiO₂ NP layer on top of the TiO₂ thin film medium. On the other hand, the simulated XRR profiles in the individual cases (only nanoparticles layer or a thin film etc.) differ significantly from the measured one. One arrives at a similar conclusion after fitting XSW induced Ti- $k\alpha$ GIXRF profile. GIXRF profile shows a strong peaking behaviour in the vicinity of the critical angle of Si substrate ($\theta_c=0.22^\circ$) due to the coincidence of the XSW antinodes (see Fig. 5.14(c)) with the NP layer (see inset of Fig. 13(c)). In Fig. 5.14(c) we have shown computed normalized x-ray field intensity distribution on the Si substrate at the 8 keV incident x-ray energy corresponding to the best-fit parameters obtained from the combined XRR and GIXRF measurements. The variation of Ti- $k\alpha$ fluorescence intensity as a function of grazing incidence angles θ can be understood with the help of XSW wave field distribution on top of a Si substrate at 8 keV x-ray energy. In Fig. 5.14(c), one clearly observes the boundary for critical angle $\theta_c=0.22^\circ$ (dashed line). Below the critical angle, the x-ray field on top of the Si substrate surface exists in the form of XSW fringes. As one increases the incidence angle θ , the x-ray field starts penetrating onto the Si substrate medium. The penetration of the incident x-ray field further increases at higher incidence angles. The best-fitted microstructural parameters of the TiO₂ nanostructure obtained from the combined XRR and GIXRF analysis at 8 keV incident x-ray energy are summarized in Table 5.2.

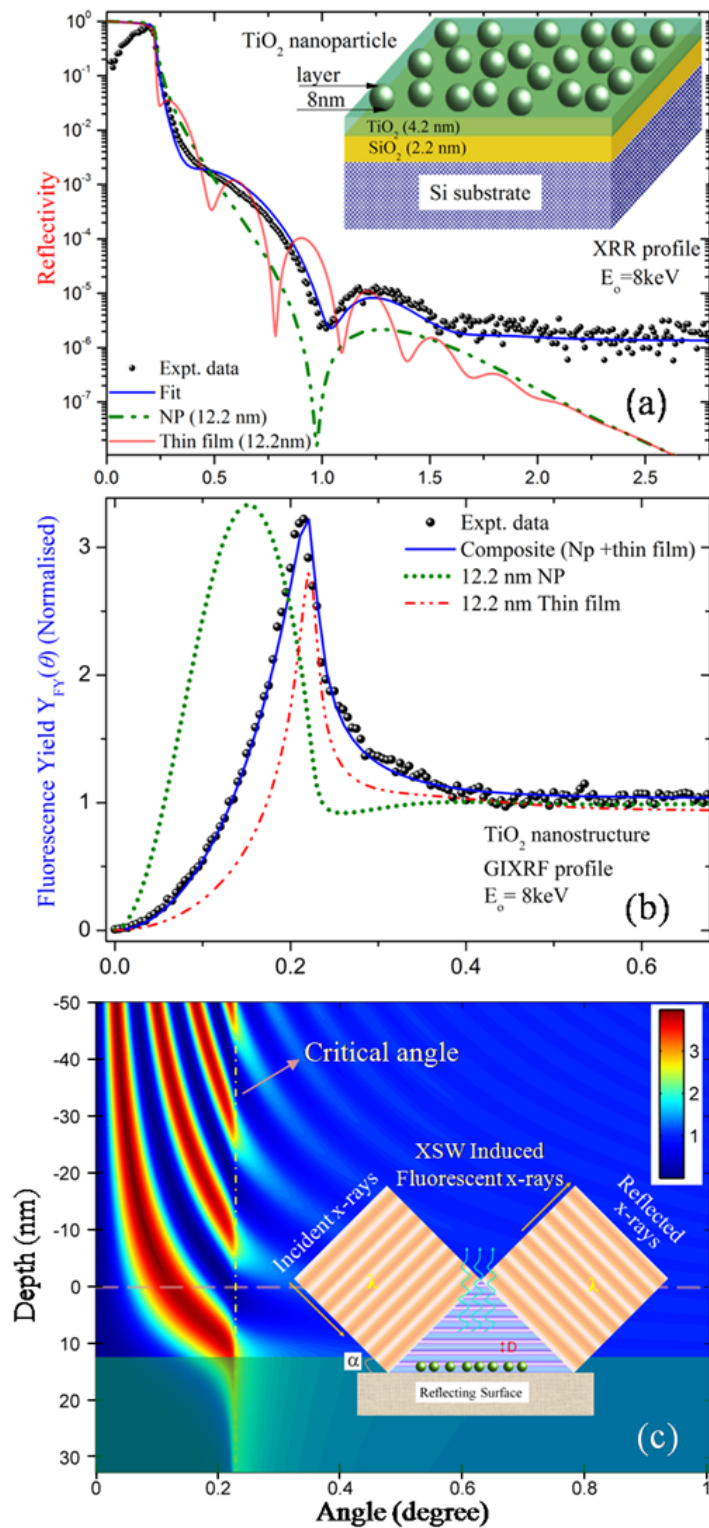


Figure 5.14: Combined XRR and GIXRF measurements at 8 keV incident x-ray energy. Measured and fitted (a) XRR , and (b) XSW induced GIXRF profiles of the TiO₂ nanostructure. (c) The contour plot of x-ray field intensity distribution on a Si substrate as a function of depth of layer medium and incidence angle calculated with the best fit results of XRR and Ti-K α fluorescence measurements. The scatter points are the experimental data and the solid lines are the simulated data. The fluorescence yield of Ti- K α has been normalized at $\theta = 0.45^\circ$.

To increase the dynamical range and sensitivity of the GIXRF analysis for the

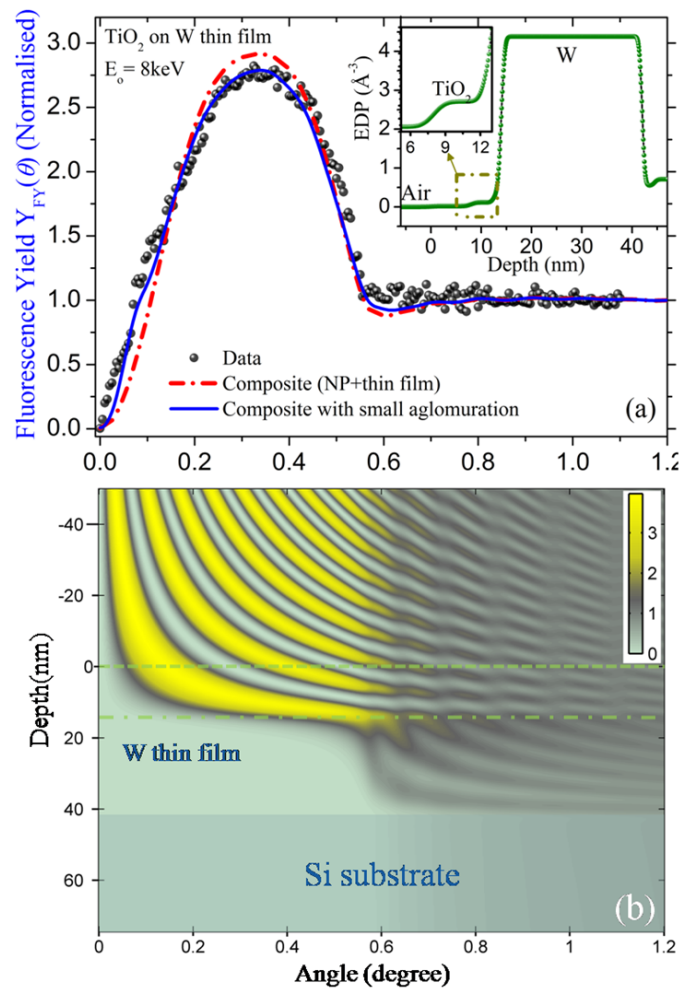


Figure 5.15: (a) Measured and fitted GIXRF profiles of TiO₂ nanostructures deposited on a W thin film at 8 keV incident x-ray energy. (b) The contour plot of x-ray field intensity distribution on a W thin film as a function of depth of layer medium and incidence angle. The EFI was calculated from best fit results of GIXRF. The scatter points are the experimental data and the solid lines are the fitted data. The fluorescence yield of Ti-K α has been normalized at $\theta = 0.85^\circ$.

investigation of small feature size, TiO₂ nanostructures, were synthesized on top of a W thin film at similar deposition conditions as mentioned in Table 5.1. Large critical angle values of W thin film ($\theta_c=0.55^\circ$) at 8 keV x-ray energy allows us to obtain improved accuracy of the estimated microstructural parameters of the small size nanoparticles using GIXRF measurements. To further re-evaluate the microstructural parameters of TiO₂ nanostructure, they were dispersed on top of a W thin film structure (~thickness 200 \AA) prepared using magnetron sputtering system. Figure 5.15(a) demonstrates the

Table 5.2: Best fitted microstructural parameters of the TiO₂ nanostructured obtained from the combined XRR and GIXRF measurements.

Substrate	Layer Material	Thickness d (nm)	Roughness σ (nm)	Density ρ (g/cm ³)	chi ²
Si	TiO ₂ NP	8.0±1.0	0.8±0.2	0.065±0.01	0.07
	TiO ₂	4.2±0.3	0.6±0.2	2.15±0.05	
	SiO ₂	2.2±0.3	0.6 ±0.1	1.6 ±0.1	
W thin film	TiO ₂ NP	8.0±1.0	0.8±0.2	0.04±0.01	0.08
	TiO ₂	5.0±0.3	0.6±0.2	2.15±0.05	
	W	28.0±0.6	0.55±0.2	19.0±0.5	
	SiO ₂	2.4±0.3	0.6 ±0.1	1.6 ±0.1	

measured and fitted GIXRF profiles of the TiO₂ nanostructure on top of W thin film medium. The measured profile was fitted by assuming a three layer model as opted in the previous case (see the inset of Fig. 5.14(a)). In Fig. 5.15(b), we have shown contour plot of electric field intensity (EFI) distribution on top of a W thin film as a function of depth z of film medium and incidence angle. From Fig. 5.15(a) it can be seen that the GIXRF profile shows strong peaking behaviour in the vicinity of critical incidence angle of $\theta_c \sim 0.55^\circ$. Below the critical angle the x-ray wave field remains in the form of interference fringes above the W film medium (see Fig. 5.15(b)). As one increases the incidence angle above $\theta \sim 0.55^\circ$, the x-ray wave field starts penetrating in the W film medium. In the vicinity of θ_c the fluorescence yield of the TiO₂ nanoparticles decreases abruptly and remains more or less constant at further higher incidence angle values. From the EFI profile (Fig. 5.15(b)) one can clearly visualise the boundary of x-ray wave field, for the W thin film medium. From Fig. 5.15(a) it can be seen that there is a slight discrepancy in the fitted and measured profile at low incidence angle ($\theta = 0 - 0.2^\circ$). This deviation arises mainly because of the presence of some bigger size particles on top of the W thin film medium. The variation in the particle size distributions and presence of a continuous thin layer of TiO₂ usually occur due to the non-uniform interaction of the Gaussian profile of the laser beam intensity with the parabolic-laminar profile of gas

velocity in the reaction zone. This provides a fair chance that some unreacted TTIP may also deposited on Si substrate surface. So, when the effect of bigger size nanoparticles were included in our model calculation then we observed a significant improvement in the fitted GIXRF profile.

To validate the findings of the XSW investigation on TiO_2 nanostructures, TEM

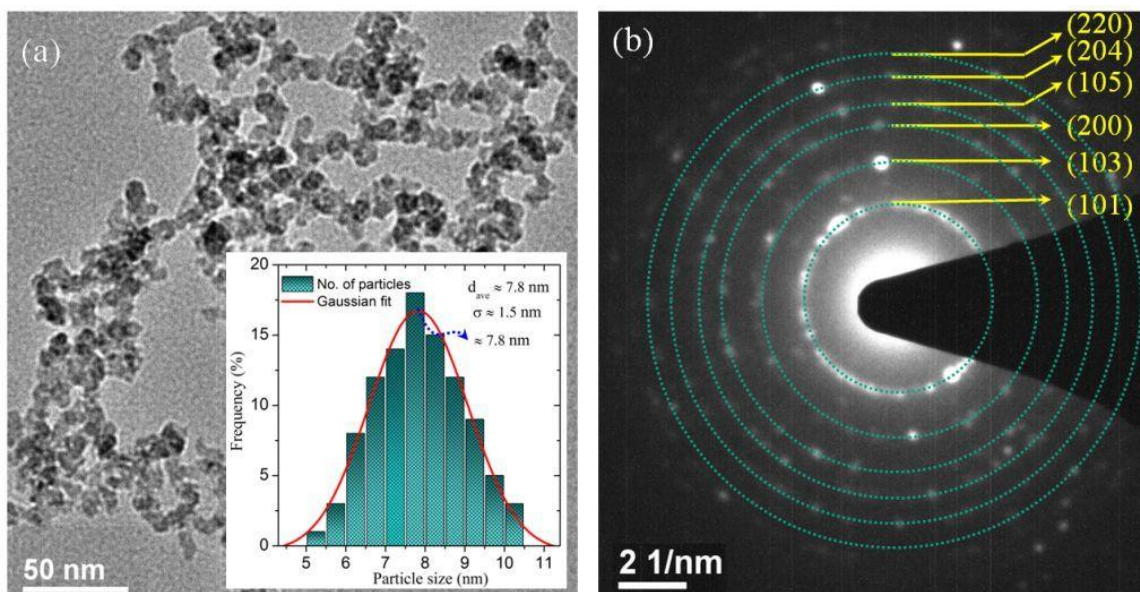


Figure 5.16: (a) TEM micrograph, and (b) Electron diffraction (ED) profile of TiO_2 nanoparticle deposited on Cu grid.

measurements were carried out using a commercial TEM (Philips, CM200) instrument. In this instrument, W-filament was used as the cathode material at an accelerating anode voltage of 200 kV. Figure 5.16(a) shows the TEM image of the TiO_2 nanoparticle distribution on top of a Cu grid. In the inset of the Fig. 5.16(a) a histogram for the TiO_2 nanoparticle size distribution is given. It can be seen from the Fig. 5.16(a) that deposited nanoparticles have very narrow particle size distribution. The average particle size of the TiO_2 nanoparticles was also determined using transmission electron microscope images. The estimated average particle size of the TiO_2 nanoparticles was found to be between 7-10 nm with r. m. s. size variation of 1.5 nm. The shape of the TiO_2 particles was found to be spherical which can be clearly observed from the measured TEM image (Fig. 5.16(a)). In the same TEM set up electron diffraction measurements were also carried

out. Figure 5.16(b) shows the measured electron diffraction profile of the TiO₂ nanoparticles. Selected area electron diffraction shows lattice fringes that confirm the crystalline nature of the TiO₂ nanostructures. One can clearly identify various reflection peaks in the measured ED pattern. These reflection peaks were found to closely match with the peaks obtained using XRD measurements. However, the (103) reflection could not be detected in the XRD profile. This may be due to the easy growth direction of TiO₂ nanoparticles on top of the Si substrate.

5.5 Summary

The feasibility and effectiveness of the combined XRR-GIXRF analysis approach has been demonstrated for the determination of microstructural parameters of different types of nanoparticles. The developed theoretical models allow one to directly evaluate the average particle size, particle shape, nature of particle dispersion and their agglomeration on top of substrate surface using XSW assisted fluorescence measurements. Most significant advantages of the XSW assisted fluorescence analysis is that it allows non-destructive quantitative mapping of the surface morphology of nanostructured materials dispersed on top of a surface or embedded inside a continuous bulk matrix.

It has been shown that longitudinal coherence properties of a partially coherent x-ray source have an ability to efficiently modulate the XSW field intensity pattern under total reflection condition on a mirror surface. We have implemented the source properties such as spectral resolution and its intensity distribution to account for longitudinal coherence in the model computation of fluorescence-induced XSW profile of a nanostructured material. There are two technical outcomes from our findings that connects the TR-XSW fringe visibility to coherence properties of SR photons. (1) The spectral resolution of the upstream monochromator can be designed to maximize the incident intensity and therefore fluorescence sensitivity from an atomic layer without significantly compromising the spatial resolution of the measured atomic height

distribution profile. For example, certain TR-XSW measurements can be performed on a conventional X-ray tube or rotating anode source using wide-band-pass multilayer optics. (2) The TR-XSW measurement can be designed to measure the longitudinal (or temporal) coherence properties of the incident beam.

TiO₂ nanoparticles on top of the Si substrate surface have been synthesized by gas phase laser pyrolysis process. Nearly mono-dispersed, highly pure TiO₂ nanoparticles of ~ 7-10 nm sizes were obtained on large area of Si substrate at optimum operating conditions. Depth resolved element sensitive analysis of TiO₂ nanostructure has been carried out using combined XRR & GIXRF analysis technique. The XSW analysis demonstrates that the nanoparticles are embedded in a thin TiO₂ layer medium on top of the substrate. The particle sizes of the TiO₂ nanoparticles determined by the XSW analysis have also been confirmed by the TEM measurements. The methodology discussed in this Chapter has a potential to provide depth-resolved and element-specific information about low dimensional metal nanoparticles.

Chapter 6

Summary and Future scope

This chapter summarizes the results and conclusions part of the present thesis work. Future directions to carry out further research work both in the fields of characterisation of nanostructured material analysis as well as their applications for harvesting solar energy and depth resolution chemical speciation of buried interfaces in thin film structure are described.

The present thesis work clearly demonstrates the immense capability of synchrotron radiation based x-ray spectroscopy techniques for the depth resolved structural characterisation of nanostructured materials. Recently, precise characterisation of nanostructured materials are becoming increasingly important as they find widespread applications in various fields of science and nanotechnology. We report the development of new methodologies for probing of surface-interface of the nanostructured materials in a non-destructive manner. The subject of this thesis work was the analysis of nanomaterials using x-ray standing wave generated using total reflection on a mirror surface as well as Bragg reflection of multilayer structure.

6.1 Development of an x-ray reflectometer

A grazing incidence x-ray reflectometer station has been developed and set-up on the BL-16 microfocus x-ray fluorescence beamline of Indus-2 synchrotron facility. The reflectometer station facilitates surface-interface characterisation of nanostructured materials using x-ray reflectivity and XSW induced x-ray fluorescence measurements. The performance of the reflectometer has been evaluated by analysing several thin film structures comprising of different surface interface properties. The details of the BL-16 x-ray reflectometer are presented in Chapter 2. The reflectometer has been employed for variety of studies, for examples, analysis of nanoparticles, surface-interface characterisation of nanocomposite, XSW characterisation of thin films, depth resolved structural and chemical analysis of a W-B₄C multilayer structure.

6.2 Grazing incidence x-ray fluorescence studies

In Chapter 3, we have described effect of synchrotron beam polarization in grazing incidence excited x-ray fluorescence analysis. Theoretical computations have been

carried out to explain how scattering probability densities of the Compton and elastic scattering radiations depend on the scattering angle (θ) and azimuthal angle (ϕ) in the polarization plane of the synchrotron radiation beam. Our computation results closely corroborate with the experimental total reflection x-ray fluorescence (TXRF) measurements, carried out on several standard reference materials (SRMs). Interestingly, the azimuthal anisotropy of the scattered photons shows its vital role on the significance of observed x-ray fluorescence detection sensitivities.

6.3 XSW analysis of thin layered medium

In Chapter 4, we have described the applicability of combined XRR-GIXRF analysis approach for probing of deep buried interfaces inside a W-B₄C periodic multilayer structure. It has been shown that XRR investigation together with the GIXRF measurements can be successfully used to quantitatively evaluate the presence of a buried interface structure or any thickness non-uniformity inside a periodic multilayer structure. It has also been shown that the combined XRR-GIXRF technique allows one to distinguish minimal density variations of the order of $\sim 6\%$ or any atomic migration taking place in a layer medium, deep inside a multilayer structure. The cross-section TEM analysis unveil a much deeper insight of the interface diffusion phenomena and supports the conclusion drawn from the XSW characterisation. To study chemical speciation inside the W-B₄C periodic multilayer structure, XSW assisted depth resolved near edge x-ray absorption measurements have been carried out. Interestingly, the results presented in Chapter 4 show existence of some unusual electronic states for W at the surface-interface boundary of the W-B₄C multilayer structure as compared to that of the bulk W.

6.4 XSW analysis of nanocomposite

In Chapter 5, we have discussed the unique ability of the combined XRR-GIXRF approach for the reliable and precise characterisation of surface morphology of metal nanoparticles, dispersed on a flat surface. Appropriate theoretical models have been developed that take into account the effect of average particle size, particle's shape, nature of particle's dispersion and their agglomeration on top of a substrate surface during the computation of XSW assisted fluorescence profile of the nanoparticles. We have studied in detail the effect of temporal coherence properties of the primary x-ray beam on the total reflection assisted x-ray standing wave fluorescence analysis of nanostructured materials. The applicability of the XSW assisted fluorescence methodology for the determination of surface morphology of different types of nanostructured materials (e.g. Au nanoparticles and TiO₂ nanoparticles dispersed on top of a Si substrate surface) has been described in detail in Chapter 5. A novel synthesis procedure for the fabrication of low dimensional TiO₂ nanoparticles using gas phase CO₂ laser pyrolysis method has been described. Atomic force microscopy, transmission electron microscopy, grazing incidence x-ray diffraction and electron diffraction measurements were also carried out to correlate findings of the XSW investigations. Our results show that TiO₂ nanostructure on top of a Si substrate follow a composite distribution. Using slicing analysis it was found that a certain fraction of nanoparticles are present in the form of continuous thin layer medium. Whereas, some of the nanoparticles follow a particulate type of distribution.

6.5 Future scope

For the future scope, we anticipate that the new developments in the instrumentation as well as analysis methodology will enable us to study a large variety of low atomic number nanostructure (*such as*- graphane nanostructure). Two developments that seem

promising are: I) vacuum compatibility of the BL-16 reflectometer station for light element detection and, II) in-situ and in-operando studies of nanostructured materials at various sample environments.

In the present thesis work, it has been shown that polarization properties of the synchrotron beam significantly affect the elemental detection sensitivities in grazing incidence x-ray fluorescence analysis. A more careful study can be planned to understand the nature of polarization dependent grazing incidence x-ray fluorescence emission from a SRM or nanostructure material. The scattered polarised x-rays can be measured using the position-sensitive detector. Such measurements would be able to provide useful information about the azimuthal anisotropy of the scattered photons (Compton and elastic scattered photons). It is expected that polarization dependent scattering measurements from a nanostructure material would greatly help us in understanding in-plane and out-of-plane correlation of scattered photons.

XSW assisted depth resolved chemical speciation in periodic multilayer structure can be used as a sensitive probe to investigate interface intermixing phenomena in thin film. Therefore, some interesting applications that can be pursued using combined XSW-XANES analysis are - depth resolved chemical speciation of electrolyte interfaces in solid state batteries, and chemical speciation of buried interfaces in thin film solar cell structures etc. Furthermore, the combined XRR-GIXRF technique can also be applied to study structural and chemical properties of the core-shell nanoparticles. Such kinds of studies have not been performed so far and therefore may yield valuable informations on novel physical aspects of the core-shell nanostructures.

During the thesis work, we have also synthesised and studied in detail the structure of low dimensional TiO_2 nanocomposites on top of Si substrate. It is worth mentioning here that TiO_2 nanostructures find vital importance for various practical applications. Composite TiO_2 nano-structures, doped with Ag, Au elements can be studied to understand their absorption response in visible light range for various practical applications.

References

- [1] Attwood, D. *Soft x-rays and extreme ultraviolet radiation Principles and applications*; Cambridge University Press, New York, 1999.
- [2] Nielsen, J. A.; McMorrow, D. *Elements of Modern X-ray Physics*; Wiley, United Kingdom, 2011.
- [3] Mao, Y.; Li, G.; Guo, Y.; Li, Z.; Liang, C.; Peng, X.; Lin, Z. *Nature Communications* **2017**, 8:14628.
- [4] Hwang, H. Y.; Iwasa, Y.; Kawasaki, M.; Keimer, B.; Nagaosa, N.; Tokura, Y. *Nature Materials* **2012**, 11, 103.
- [5] Cuenya, B. R. *Thin Solid Films* **2010**, 518, 3127–3150.
- [6] Major, J. D.; Turkestani, M. A.; Bowen, L.; Brossard, M.; Li, C.; Lagoudakis, P.; Pennycook, S. J.; Phillips, L. J.; Treharne, R. E.; Durose, K. *Nature Communications* **2016**, 7:13231.
- [7] Senanayak, S. P.; Yang, B.; Thomas, T. H.; Giesbrecht, N.; Huang, W.; Gann, E.; Nair, B.; Goedel, K.; Moya, S. G. X.; McNeill, C. R.; Docampo, P.; Sadhanala, A.; Friend, R. H.; Sringhaus, H. *Sci. Adv.* **2017**, 3, 1601935.
- [8] Su, W. C.; Chang, T. C.; Liao, P. Y.; JiaChen, Y.; Chen, B. W.; Hsieh, T. Y.; Yang, C. I.; Huang, Y. Y.; Chang, H. M.; Chiang, S. C.; Chang, K. C.; Tsai, T. M. *Appl. Phys. Lett.* **2017**, 110, 103502.

- [9] Frisk, A.; Hase, T.; Svedlindh, P.; Johansson, E.; Andersson, G. *J. Phys. D: Appl. Phys.* **2017**, *50*, 085009.
- [10] Collins, S. M.; Garcia, S. F.; Calvino, J. J.; Midgley, P. A. *Scientific Reports* **2017**, *7*:5406.
- [11] Yeu, I. W.; Park, J.; Han, G.; Hwang, C. S.; Choi, J. *Scientific Reports* **2017**, *7*:10691.
- [12] Timm, C.; Schnyder, A. P.; Agterberg, D. F.; Brydon, P. M. R. *Phys. Rev. B* **2017**, *96*, 094526.
- [13] Rupp, G. M.; Opitz, A. K.; Nenning, A.; Limbeck, A.; Fleig, J. *Nature Materials* **2017**, *16*, 640–646.
- [14] Zheng, D.; Jin, C.; Li, P.; Wang, L.; Feng, L.; Mi, W.; Bai, H. *Scientific Reports* **2016**, *6*:24568.
- [15] Paganin, D. M. *Coherent X-Ray Optics*; Oxford University Press, Oxford, 2006.
- [16] Tiwari, M. K.; Sawhney, K. J. S. *Spectrochimica Acta Part B* **2003**, *58*, 1895–1900.
- [17] Kelly, B. G.; Loether, A.; Unruh, K. M.; DeCamp, M. F. *Phys. Rev. B* **2017**, *95*, 064301.
- [18] Charilaou, M.; Bordel, C.; Berche, P.; Maranville, B. B.; Fischer, P.; Hellman, F. *Phys. Rev. B* **2016**, *93*, 224408.
- [19] Kravets, A. F.; Polishchuk, D. M.; Dzhezherya, Y. I.; Tovstolytkin, A. I.; Golub, V. O.; Korenivski, V. *Phys. Rev. B* **2016**, *94*, 064429.
- [20] Riviere, J. C.; Myhra, S. *Handbook of Surface and Interface Analysis: Methods for Problem Solving*; CRC Press, New York, 2009.
- [21] Saha, D.; Ajimsha, R. S.; Rajiv, K.; Mukherjee, C.; Gupta, M.; Misra, P.; Kukreja, L. M. *App. Surf. Sci.* **2014**, *315*, 116–123.

- [22] Hippert, F.; Geissler, E.; Hodeau, J. L.; Berna, E. L.; Regnard, J. R. *Neutron and X-ray Spectroscopy*; Springer, The Netherlands, 2006.
- [23] Hufner, S. *Photoelectron Spectroscopy*; Springer, New York, 1996.
- [24] Cullity, B. D. *Elements of X-ray Diffraction*; Addison Wesley Publishing, Massachusetts, 1956.
- [25] Bunker, G. *Introduction to XAFS: A Practical Guide to X-ray Absorption Fine Structure Spectroscopy*; Cambridge University Press, New York, 2010.
- [26] Bhattacharya, G.; Giri, R. P.; Saxena, H.; Agrawal, V. V.; Gupta, A.; Mukhopadhyay, M. K.; Ghosh, S. K. *Langmuir* **2017**,
- [27] Ju, G.; Tabuchi, M.; Takeda, Y.; Amano, H. *Appl. Phys. Lett.* **2017**, *110*, 262105.
- [28] Klockenkamper, R.; von Bohlen, A. *Total Reflection X-Ray Fluorescence Analysis and Related Methods*; Wiley: Dortmund and Berlin, Germany, 2015.
- [29] Grieken, R. E. V.; Markowicz, A. *Handbook of X-ray Spectrometry*; Marcel Dekker, New York, 2002.
- [30] Sauer, M.; Hofkens, J.; Enderlein, J. *Handbook of Fluorescence Spectroscopy and Imaging*; Wiley-VCH, Singapore, 2011.
- [31] Lakowicz, J. R. *Principles of Fluorescence Spectroscopy*; Springer, Singapore, 2006.
- [32] Albani, J. R. *Principles and Applications of Fluorescence Spectroscopy*; Blackwell Science, Oxford, 2007.
- [33] Becker, R. S.; Golovchenko, J. A.; Patel, J. R. *Phys. Rev. Lett.* **1983**, *50*, 153–156.
- [34] Tiwari, M. K.; Lodha, G. S.; Sawhney, J. S. *X-ray Spectrum*. **2010**, *39*, 127–134.

- [35] Ingerle, D.; Schiebl, M.; Strel, C.; Wobrauschek, P. *Rev. Sci. Instrum.* **2014**, *85*, 083110.
- [36] Ingerle, D.; Meirer, F.; G. Pepponi,; Demenev, E.; D. Giubertoni,; Wobrauschek, P.; Strel, C. *Spectrochim. Acta B.* **2014**, *99*, 121–128.
- [37] Tiwari, M. K.; Sawhney, K. J. S.; Lodha, G. *Surf. Interface Anal.* **2010**, *42*, 110–116.
- [38] Tiwari, M. K.; Sawhney, K. J. S.; Lee, T. L.; Alcock, S. G.; Lodha, G. S. *Phys. Rev. B* **2009**, *80*, 035434.
- [39] Lubeck, J.; Beckhoff, B.; Fliegau, R.; Holfelder, I.; Honicke, P.; Muller, M.; Pollakowski, B.; Reinhardt, F.; Weser, J. *Rev. Sci. Instrum.* **2013**, *84*, 045106.
- [40] Yano, Y. F.; Uruga, T.; Tanida, H.; Toyokawa, H.; Terada, Y.; Yamada, H. *J. Synchrotron Rad.* **2010**, *17*, 511–516.
- [41] Sakurai, K.; Uehara, S.; Goto, S. *J. Synchrotron Rad.* **1998**, *5*, 554–556.
- [42] Paulus, M.; Lietz, D.; Sternemann, C.; Shokuie, K.; Evers, F.; Tolan, M.; Czeslik, C.; Winter, R. *J. Synchrotron Rad.* **2008**, *15*, 600.
- [43] Athiray, P.; Sudhakar, M.; Tiwari, M.; Narendranath, S.; Lodha, G.; Deb, S.; Sreekumar, P.; Dash, S. *Planet. Space Sci.* **2013**, *89*, 183.
- [44] Misra, N. L.; Tiwari, M. K.; Kumar, S. S.; Dhara, S.; Singh, A. K.; Lodha, G. S.; Deb, S. K.; Gupta, P. D.; Aggarwal, S. K. *X-Ray Spectrom.* **2013**, *42*, 4.
- [45] Misra, N. L.; Tiwari, M.; Vats, B. G.; Kumar, S. S.; Singh, A. K.; Lodha, G.; Deb, S.; Gupta, P.; Aggarwal, S. *X-Ray Spectrom.* **2014**, *43*, 152.
- [46] Tiwari, M. K.; Gupta, P.; Sinha, A. K.; Kane, S. R.; Singh, A. K.; Garg, S. R.; Garg, C. K.; Lodha, G. S.; Deb, S. K. *J. Synchrotron Rad.* **2013**, *20*, 386–389.

- [47] Das, G.; Tiwari, M. K.; Singh, A. K.; Ghosh, H. *J. Anal. At. Spectrom.* **2014**, *29*, 2405.
- [48] Li, W.; Zhu, J.; Ma, X.; Li, H.; Wang, H.; Sawhney, K. J. S.; Wang, Z. *Rev. Sci. Instrum.* **2012**, *83*, 053114.
- [49] Nayak, M.; Rao, P. N.; Lodha, G. S. *Asian Journal of Physics* **2010**, *19*, 1–14.
- [50] Lodha, G. S. *RRCAT News Lett.* **2009**, *22*, 7.
- [51] Meirer, F.; Singh, A.; Pepponi, G.; Streli, C.; Homma, T.; Pianetta, P. *J. Anal. At. Spectrom.* **2010**, *29*, 479–496.
- [52] Perez, C. A.; Radthe, M.; Sanchez, H. J. *X-Ray Spectrom.* **1999**, *28*, 320–326.
- [53] Tiwari, M. K.; Singh, A. K.; Das, G.; Chowdhury, A.; Lodha, G. S. *AIP Conference Proceedings* **2014**, *1591*, 642–643.
- [54] Parratt, L. G. *Phys Rev.* **1954**, *95*, 359.
- [55] Nevot, L.; Croce, P. *Appl. Phys. Rev.* **1980**, *15*, 761.
- [56] Tiwari, M. K.; Lodha, G. S.; Sawhney, K. J. S.; Gowrisankar, B.; Singh, A. K.; Bhalerao, G. M.; Sinha, A. K.; Das, A.; Verma, A.; Nandedkar, R. V. *Curr. Sci.* **2008**, *95*, 6031–7609.
- [57] Zawisza, B.; Skorek, R.; Theato, T.; Queralt, I.; Hidalgo, M.; Sitko, R. *Spectrochimica Acta Part B* **2013**, *88*, 192.
- [58] Streli, C.; Wobrauschek, P.; Meirer, F.; Pepponi, G. *J. Anal. At. Spectrom.* **2008**, *23*, 7921.
- [59] Streli, C.; Wobrauschek, P.; Beckhoff, B.; Ulm, G.; Fabry, L.; Pahlke, S. *X-Ray Spectrom.* **2001**, *30*, 241.

- [60] Ortega, L.; Comin, F.; Formoso, V.; Stierle, A. *J. Synchrotron Radiat.* **1998**, *5*, 1064–1066.
- [61] Comin, F.; Navizet, M.; Mangiagalli, P.; Apostolo, G. *Nucl. Instrum. Methods Phys. Res., Sect. B* **1999**, *150*, 538–542.
- [62] Pella, P. A.; Dobbyn, R. C. *Anal. Chem.* **1988**, *60*, 684–687.
- [63] Embong, Z.; Wagiran, H. *Proceedings of International Nuclear Conference: a new era in Nuclear Science and Technology the challenge of the 21st century*, **1997**, *29*, 111–118.
- [64] Spolnik, Z.; Belikov, K.; Meel, K. V.; Adriaenssens, E.; Roeck, F. D.; Grieken, R. V. *Appl. Spectrosc.* **2005**, *59*, 1465–1469.
- [65] Klein, O.; Nishina, Y. *Z. Phys.* **1929**, *52*, 853.
- [66] Hanson, A. L. *Nucl. Instrum. Methods Phys. Res., Sect. A* **1986**, *243*, 583–598.
- [67] Hanson, A. L. *Nucl. Instrum. Methods Phys. Res., Sect. A* **1986**, *249*, 515–521.
- [68] Peplow, D. E.; Verghese, K. *Phys. Med. Biol.* **1998**, *43*, 2431–2452.
- [69] Latha, P.; Abdullah, K. K.; Unnikrishnan, M. P.; Varier, K. M.; Babu, B. R. S. *Phys. Scr.* **2012**, *85*, 035303.
- [70] Francis, P. *J. Phys. Radium* **1926**, *7*, 390–401.
- [71] Sakurai, K.; Eba, H.; Goto, S. *Jpn. J. Appl. Phys., Part 1* **1998**, *38*, 3321.
- [72] Tiwari, M. K.; Naik, S. R.; Lodha, G. S.; Nandedkar, R. V. *Anal. Sci.* **2005**, *21*, 757.
- [73] Margui, E.; Zawisza, B.; Skorek, R.; Theato, T.; Queralt, I.; Hidalgo, M.; Sitko, R. *Spectrochim. Acta, Part B* **2013**, *88*, 192–197.

- [74] Windt, D. L.; Donguy, S.; Hailey, C. J.; Koglin, J.; Honkimaki, V.; Ziegler, E.; Christensen, F. E.; Chen, H.; Harrison, F. A.; Craig, W. W. *Appl. Opt.* **2003**, *42*, 2415.
- [75] Pietsch, U.; Hol, V.; Baumbach, T. *High-Resolution X-Ray Scattering From Thin Films to Lateral Nanostructures*; New York: Springer-Verlag Berlin, Heidelberg, 2004.
- [76] Zahn, P.; Papanikolaou, N.; Erler, F.; Mertig, I. *Phys. Rev. B* **2002**, *65*, 134432.
- [77] Revaz, B.; Cyrille, M. C.; Zink, B. L.; Schuller, I. K.; Hellman, F. *Phys. Rev. B* **2002**, *65*, 094417.
- [78] Wellock, K.; Theeuwen, S. J. C. H.; Caro, J.; Gribov, N. N.; van Gorkom, R. P.; Radelaar, S.; Tichelaar, F. D.; Hickey, B. J.; Marrows, C. H. *Phys. Rev. B* **1999**, *60*, 10291.
- [79] Costa, A. T.; de Castro, B.; Jr., A. C.; d Albuquerque e Castro, J.; Muniz, R. B. *J. Phys.: Condens. Matter* **2001**, *13*, 1827.
- [80] Kim, J. H.; Vrejoiu, I.; Khaydukov, Y.; Keller, T.; Stahn, J.; Rhm, A.; Satapathy, D. K.; Hinkov, V.; Keimer, B. *Phys. Rev. B (R)* **2012**, *86*, 180402.
- [81] Barbee, T. W. *Synthetic Modulated Structure Materials*; New York: Academic Press, 1985.
- [82] Spiller, E. *Appl. Phys. Lett.* **1972**, *20*, 365.
- [83] Holy, V.; Kubena, J.; Ohlidal, I.; Lischka, K.; Plotz, W. *Phys. Rev. B* **1993**, *47*, 15896.
- [84] Holy, V.; Baumbach, T. *Phys. Rev. B* **1994**, *49*, 10669.

- [85] Eisenhauer, D.; Pollakowski, B.; Baumann, J.; Preidel, V.; Amkreutz, D.; Rech, B.; Back, F.; Voigt, E. R.; Beckhoff, B.; Kanngießer, B.; Becker, C. *Phys. Status Solidi A* **2015**, *212*, 529.
- [86] Unterumsberger, R.; Pollakowski, B.; Müller, M.; Beckhoff, B. *Anal. Chem.* **2011**, *83*, 8623.
- [87] Amkreutz, D.; Haschke, J.; Haring, T.; Ruske, F.; Rech, B. *Sol. Energy Mater. Sol. Cells* **2014**, *123*, 13.
- [88] Kortright, J. B.; Awschalom, D. D.; Sthr, J.; Bader, S. D.; Idzerda, Y. U.; Parkin, S. S. P.; Schuller, I. K.; Siegmann, H. C. *J. Magn. Magn. Mater.* **1999**, *207*, 7.
- [89] Jonker, B. T. *Magnetic Ultrathin Films: Multilayers and Surfaces, Interfaces and Characterization*; Materials Research Society, Pittsburgh, 1993; Vol. 313.
- [90] Chen, Y.; Gramlich, M. W.; Hayden, S. T.; Miceli, P. F. *Phys. Rev. Lett.* **2015**, *114*, 035501.
- [91] Kim, S. K.; Kortright, J. B. *Phys. Rev. Lett.* **2001**, *86*, 1347.
- [92] MacKay, J. F.; Teichert, C.; Savage, D. E.; Lagally, M. G. *Phys. Rev. Lett.* **1996**, *77*, 3925.
- [93] Church, J. R.; Weiland, C.; Opila, R. L. *Appl. Phys. Lett.* **2015**, *106*, 171601.
- [94] Miyata, N.; Ishikawa, S.; Yanagihara, M.; Watanabe, M. *Jpn. J. Appl. Phys., Part I* **1999**, *38*, 6476.
- [95] Reichert, H.; Honkimäki, V.; Snigirev, A.; Engemann, S.; Dosch, H. *Physica B* **2003**, *336*, 46.
- [96] Chen, K.; Yang, G. R.; Nielsen, M.; Lu, T. M.; Rymaszewski, E. J. *Appl. Phys. Lett.* **1997**, *70*, 399.
- [97] Boer, D. K. G. *Phys. Rev. B* **1991**, *44*, 498.

- [98] Bedzyk, M. J.; Bommarito, G. M.; Schildkraut, J. S. *Phys. Rev. Lett.* **1989**, *62*, 1376.
- [99] Tsuji, K.; Injuk, J.; Grieken, R. V. *X-Ray Spectrometry: Recent Technological Advances*; Wiley, 2004.
- [100] Zegenhagen, J.; Kazimirov, A. *The X-Ray Standing Wave Technique: Principle and Applications*; World Scientific, 2013.
- [101] Braun, C. *Parratt32*; HMI Berlin, Germany, 1997.
- [102] Sergey, S. **1997**,
- [103] Windt, D. W. *Computer in Physics* **1998**, *12*, 360–370.
- [104] Nelson, A. *J. Appl. Cryst.* **2006**, *39*, 273–276.
- [105] Björck, M.; Andersson, G. *J. Appl. Cryst.* **2007**, *40*, 1174–1178.
- [106] Danauskas, S. M.; Li, D. M.; M., B.; Lin,; Lee, K. Y. C. *J. Appl. Cryst.* **2008**, *41*, 1187–1193.
- [107] Karimov, P.; Harada, S.; Kawai, J. *Surf. Interface Anal.* **2003**, *35*, 76.
- [108] Batterman, B. W. *Phys. Rev. A* **1964**, *133*, A759.
- [109] Golovochenko, J. A.; Batterman, B.; Brown, W. L. *Phys. Rev. B* **1974**, *10*, 4239.
- [110] Bedzyk, M. J.; Materlik, G.; Kovalchuk, M. V. *Phys. Rev. B* **1984**, *30*, 2453.
- [111] Bedzyk, M. J.; Bilderback, D. H.; Bommarito, G.; Caffrey, M.; Schildkraut, J. S. *Science* **1988**, *241*, 1788.
- [112] Woodruff, D. P. *Rep. Prog. Phys.* **2005**, *68*, 743.
- [113] Tiwari, M. K.; Bhalerao, G. M.; Babu, M.; Sinha, A. K.; Mukherjee, C. *J. Appl. Phys.* **2008**, *103*, 054311.

- [114] Honicke, P.; Detlefs, B.; Muller, M.; Darlatt, E.; Nolot, E.; Grampeix, H.; Beckhoff, B. *Phys. Status Solidi A* **2015**, *212*, 523–528.
- [115] Das, G.; Kane, S. R.; Khooha, A.; Singh, A. K.; Tiwari, M. K. *Rev. Sci. Instrum.* **2015**, *86*, 055102.
- [116] Krol, A.; Sher, C. J.; Kao, Y. H. *Phys. Rev. B* **1988**, *38*, 8579.
- [117] Ghose, S. K.; Dev, B. N. *Phys. Rev. B* **2001**, *63*, 245409.
- [118] Stoev, K.; Sakurai, K. *The Rigaku Journal* **1997**, *14*, 22.
- [119] Schwenke, H.; Gutschke, R.; Knoth, J.; Kock, M. *Appl. Phys. A* **1992**, *54*, 460.
- [120] Tiwari, M. K.; Das, G. *X-Ray Spectrom.* **2016**, *45*, 212.
- [121] Schoonjans, T.; A. Brunetti, B. G.; del Rio, M. S.; Sol, V. A.; Ferrero, C.; Vincze, L. *Spectrochimica Acta Part B* **2011**, *66*, 776–784.
- [122] Das, G.; Khooha, A.; Kane, S. R.; Singh, A. K.; Tiwari, M. K. *AIP Conference Proceedings* **2016**, *1728*, 020142.
- [123] Henke, B. L.; Gullikson, E.; Davis, J. *Atomic Data and Nuclear Data Tables* **1993**, *54*, 181–342.
- [124] Das, G.; Khooha, A.; K.Singh, A.; K.Srivastava, A.; K.Tiwari, M. *Appl. Phys. Lett.* **2016**, *108*, 263109.
- [125] Oakton, E.; Siddiqi, G.; Fedorov, A.; Coperet, C. *New J. Chem.* **2016**, *40*, 217–222.
- [126] Jayarathne, U.; Chandrasekaran, P.; Greene, A. F.; Mague, J. T.; DeBeer, S.; Lancaster, K. M.; Sproules, S.; Donahue, J. P. *Inorg. Chem.* **2014**, *53*, 8230–8241.
- [127] Garcia-Garcia, F. J.; Rostra, J. G.; Yubero, F.; s, J. P. E.; Elipe, A. R. G. *J. Phys. Chem. C* **2015**, *119*, 644–652.

- [128] Luca, V.; Blackford, M. G.; Finnie, K. S.; Evans, P. J.; James, M.; Lindsay, M. J.; Kazacos, M. S.; Barnes, P. R. F. *J. Phys. Chem. C* **2007**, *111*, 18479–18492.
- [129] Clinton, D. E.; Tryk, D. A.; Bae, I. T.; Urbach, F. L.; Antonio, M. R.; Scherson, D. A. *J. Phys. Chem.* **1996**, *100*, 18511–18514.
- [130] Yamazoe, S.; Hitomi, Y.; Shishido, T.; Tanaka, T. *J. Phys. Chem. C* **2008**, *112*, 6869–6879.
- [131] GAUNS., S. A. *Department of Physics-Goa University, India* **1996**,
- [132] Chakhalian, J.; Freeland, J. W.; Habermeier, H.; Cristiani, G.; Khaliullin, G.; van Veenendaa, M.; Keimer, B. *Science* **2007**, *318*, 1114–1117.
- [133] Nakagawa, N.; Hwang, H. Y.; Muller, D. A. *Nature Materials* **2006**, *5*, 204–209.
- [134] Benckiser, E. et al. *Nature Materials* **2011**, *10*, 189–193.
- [135] Rata, A. D.; Herklotz, A.; Nenkov, K.; Schultz, L.; Drr, K. *Phys. Rev. Lett.* **2008**, *100*, 076401.
- [136] Jackeli, G.; Khaliullin, G. *Phys. Rev. Lett.* **2008**, *101*, 216804.
- [137] Tebano, A.; Aruta, C.; Sanna, S.; Medaglia, P. G.; Balestrino, G.; Sidorenko, A. A.; Renzi, R. D.; Ghiringhelli, G.; Braicovich, L.; Bisogni, V.; Brookes, N. B. *Phys. Rev. Lett.* **2008**, *100*, 137401.
- [138] Aruta, C.; Ghiringhelli, G.; Bisogni, V.; Braicovich, L.; Brookes, N. B.; Tebano, A.; Balestrino, G. *Phys. Rev. B* **2009**, *80*, 014431.
- [139] Salluzzo, M.; Cezar, J. C.; Brookes, N. B.; Bisogni, V.; Luca, G. M. D.; Richter, C.; Thiel, S.; Mannhart, J.; Huijben, M.; Brinkman, A.; Rijnders, G.; Ghiringhelli, G. *Phys. Rev. Lett.* **2009**, *102*, 166804.
- [140] Bera, S.; Bhattacharjee, K.; Kuri, G.; Dev, B. N. *Phys. Rev. Lett.* **2007**, *98*, 196103.

- [141] Zwiebler, M.; Hamann-Borrero, J. E.; Vafaei, M.; and S. Macke, P. K.; He, R. S. F.; Bchner, B.; Sawatzky, G. A.; Alff, L.; Geck, J. *New J. Phys.* **2015**, *17*, 083046.
- [142] Mannhart, J.; Schlom, D. G. *SCIENCE* **2010**, 327.
- [143] Okumura, T.; Nakatsutsumi, T.; Ina, T.; Orikasa, Y.; Arai, H.; Fukutsuka, T.; Iriyama, Y.; Uruga, T.; Tanida, H.; Uchimoto, Y.; Ogumi, Z. *J. Mater. Chem.* **2011**, *21*, 10051–10060.
- [144] Kortright, J. B.; Colbrie, A. F. *J. Appl. Phys.* **1987**, *61*, 1130.
- [145] Wang, Y.; Narayanan, S.; Liu, J.; Shu, D.; Mashayekhi, A.; Qian, J.; Wang, J. *J. Synchrotron Rad.* **2007**, *14*, 138.
- [146] Wang, H.; Dhesi, S. S.; Maccherozzi, F.; Cavill, S.; Shepherd, E.; Yuan, F.; Deshmukh, R.; Scott, S.; van der Laan, G.; Sawhney, K. J. *S. Rev. Sci. Instrum.* **2011**, *82*, 123301.
- [147] MacDonald, M. A.; Schaefer, F.; Pohl, R.; Poole, I. B.; Gaupp, A.; Quinn, F. M. *Rev. Sci. Instrum.* **2008**, *79*, 025108.
- [148] Pradhan, P. C.; Gangir, D.; Majhi, A.; Nayak, M.; Biswas, A.; Bhattacharyya, D.; Lodha, G. S. *J. Phys. D: Appl. Phys.* **2016**, *49*, 135305.
- [149] Windt, D. L.; Gullikson, E. M.; Walton, C. C. *J. Phys. D: Appl. Phys.* **2002**, *27*, 2212.
- [150] Joshua, A.; Pecker, S.; Ruhman, J.; Altman, E.; Ilani, S. *Nature Communications* **2012**, *3*, 1129.
- [151] Tiwari, M. K.; Wang, H.; Sawhney, K. J. S.; Nayak, M.; Lodha, G. S. *Phys. Rev. B* **2013**, *87*, 235401.
- [152] Emery, J. D.; Detlefs, B.; Karmel, H. J.; Nyakiti, L. O.; Gaskill, D. K.; Hersam, M. C.; Zegenhagen, J.; Bedzyk, M. J. *Phys Rev Lett.* **2013**, *111*, 215501.

- [153] Libera, J. A.; Cheng, H.; de la Cruz, M. O.; Bedzyk, M. J. *J. Phys. Chem. B* **2005**, *109*, 23001–23007.
- [154] Kayser, Y.; Sa, J.; Szlachetko, J. *Anal. Chem.* **2015**, *87*, 10815–10821.
- [155] Meyer, D. C.; Richter, K.; Paufler, P.; Gawlitza, P.; Holz, T. *J. Appl. Phys.* **2000**, *87*, 7218–7226.
- [156] Meyer, D. C.; Gawlitza, P.; Richter, K.; Paufler, P. *J. Phys. D: Appl. Phys.* **1999**, *32*, 3135–3139.
- [157] Pollakowski, B.; Beckhoff, B.; Reinhardt, F.; Braun, S.; Gawlitza, P. *Phys. Rev. B* **2008**, *77*, 235408.
- [158] Pollakowski, B.; Hoffmann, P.; Kosinova, M.; Baake, O.; Trunova, V.; Unterumberger, R.; Ensinger, W.; Beckhoff, B. *Anal. Chem.* **2013**, *85*, 193.
- [159] Sanyal, K.; Khooha, A.; Das, G.; Tiwari, M. K.; Misra, N. L. *Anal. Chem.* *89*, 871–876.
- [160] Andre, J. M.; Barchewitz, R.; Maquet, A.; Marmoret, R. *Phys. Rev. B* **1984**, *29*, 6576–6585.
- [161] Soufli, R.; Gullikson, E. M. *Appl. Opt.* **1997**, *36*, 5499–5507.
- [162] Pfalzer, P.; Urbach, J. P.; Klemm, M.; Horn, S.; denBoer, M. L.; Frenkel, A. I.; Kirkland, J. P. *Phys. Rev. B* **1999**, *60*, 9335.
- [163] Li, W.; Yuan, X.; Zhu, J.; Zhu, J.; Wang, Z. *Phys. Scr.* **2015**, *90*, 015804.
- [164] Pradhan, P. C.; Majhi, A.; Nayak, M.; Nand, M.; Rajput, P.; Shukla, D. K.; Biswas, A.; Rai, S. K.; Jha, S. N.; Bhattacharyya, D.; Phase, D. M.; Sahoo, N. K. *J. Appl. Phys.* **2016**, *120*, 045308.
- [165] Rao, P. N.; Rai, S. K.; Nayak, M.; Lodha, G. S. *Appl. Opt.* **2013**, *52*, 6126.

- [166] Siffalovic, P.; Jergel, M.; Chitu, L.; Majkova, E.; Matko, I.; Luby, S.; Timmann, A.; Roth, S. V.; Keckes, J.; Maier, G. A.; Hembd, A.; Hertlein, F.; Wiesmann, J. *J. Appl. Crystallogr.* **2010**, *43*, 1431.
- [167] Singh, G.; Banerji, A.; Barpande, K.; Bhatnagar, V.; Bhujle, A. G.; Fakhri, A. A.; Fatnani, P.; Ghodke, A. D.; Hannurkar, P. *Proceedings of Indian Particle Accelerator Conference* **2006**, *94*.
- [168] Sinha, A. K.; Sagdeo, A.; Gupta, P.; Upadhyay, A.; Kumar, A.; Singh, M. N.; Gupta, R. K.; Kane, S. R.; Verma, A.; Deb, S. K. *Journal of Physics: Conference Series* **2013**, *425*, 072017.
- [169] Antoniak, C.; Lindner, J.; Spasova, M.; Sudfeld, D.; Acet, M.; Farle, M.; Fauth, K.; Wiedwald, U.; Boyen, H. G.; Ziemann, P.; Wilhelm, F.; Rogalev, A.; Sun, S. *Phys. Rev. Lett.* **2006**, *97*, 117201.
- [170] Ruda, H. E. et al. *Nanoscale Res. Lett.* **2006**, *1*, 99.
- [171] Henley, S. J.; Carey, J. D.; Silva, S. R. P. *Appl. Phys. Lett.* **2006**, *89*, 183120.
- [172] Waitz, T.; Karnthaler, H. P. *Acta Mater* **2004**, *52*, 5461–5469.
- [173] Waitz, T.; Kazykhanov, V.; Karnthaler, H. P. *Acta Mater* **2004**, *52*, 137–147.
- [174] Katayama, M.; Ikesaka, S.; J.Kuwano,; Yamamoto, Y.; Koinuma, H.; Matsumoto, Y. *Appl. Phys. Lett.* **2006**, *89*, 242103.
- [175] von Bohlen, A. *Spectrochimica Acta B* **2009**, *64*, 821.
- [176] Tiwari, M. K.; Das, G.; Bedzyk, M. J. *Appl. Phys. Lett.* **2015**, *107*, 103104.
- [177] Tsuji, K.; Wagatsuma, K. *Jpn. J. Appl. Phys.* **1996**, *35*, 1535.
- [178] Das, G.; Kumar, M.; Biswas, A. K.; A.Khooha,; Mondal, P.; Tiwari, M. K. *e-print arXiv: 1609.09261 [cond-mat.mtrl-sci]*

- [179] Das, G.; Kumar, M.; Biswas, A. K.; Khooha, A.; Mondal, P.; Tiwari, M. K. *AIP Conference Proceedings* **2017**, 1832, 050025.
- [180] Ingerle, D.; Pepponi, G.; Meirer, F.; Wobrauschek, P.; Strelt, C. *Spectrochimica Acta Part B* **2016**, 118, 20–28.
- [181] von Bohlen, A.; Krmer, M.; Sternemann, C.; Paulus, M. *J. Anal. At. Spectrom.* **2009**, 24, 792–800.
- [182] von Bohlen, A.; Brucher, M.; Holland, B.; Wagner, R.; Hergenroder, R. *Spectrochim. Acta Part B* **2010**, 65, 409–414.
- [183] Reinhardt, F.; Osn, J.; T, S.; Pap, A.; Kolbe, M.; Beckhoff, B. *J. Anal. At. Spectrom.* **2012**, 27, 248–255.
- [184] Levard, C.; Michel, F. M.; Wang, Y.; Choi, Y.; Eng, P.; Brown, G. E. *J. J. Synchrotron Rad* **2011**, 18, 871–878.
- [185] Borowik, T.; Przybylo, M.; Pala, K.; Otlewski, J.; Langner, M. *Spectrochim. Acta Part B* **2011**, 66, 726–732.
- [186] Brher, M.; Chakif, M.; Gurevich, E. L.; Hergenrder, R. *Spectrochimica Acta Part B* **2014**, 98, 601–764.
- [187] Wilson, N. R.; Macpherson, J. V. *Nature Nanotechnology* **2009**, 4, 483–491.
- [188] Zegenhagen, J. *Surf. Sci. Rep.* **1993**, 18, 202.
- [189] Vartanyants, I. A.; Kovalchuk, M. V. *Rep. Prog. Phys.* **2001**, 64, 1009.
- [190] Bedzyk, M. J.; Cheng, L. W. *Rev. Mineral. Geochem.* **2002**, 49, 221.
- [191] Cheng, L.; Fenter, P.; Bedzyk, M. J.; Sturchio, N. C. *Phys. Rev. Lett.* **2003**, 90, 255503.

- [192] Bokhoven, J. A. V.; Lee, T. L.; Drakopoulos, M.; Lamberti, C.; Thiess, S.; Zegenhagen, J. *Nat. Mater.* **2008**, *7*, 551.
- [193] Lee, T. L.; Bihler, C.; Schoch, W.; Limmer, W.; Daeubler, J.; Thiess, S.; Brandt, M. S.; Zegenhagen, J. *Phys. Rev. B* **2010**, *81*, 235207.
- [194] Golovchenko, J. A.; Patel, J. R.; Kaplan, D. R.; Cowan, P. L.; Bedzyk, M. J. *Phys. Rev. Lett.* **1982**, *49*, 560.
- [195] Qian, Y. L.; Sturchio, N. C.; Chiarello, R. P.; Lyman, P. F.; Lee, T. L.; Bedzyk, M. J. *Science* **1994**, *265*, 1555.
- [196] Kawamura, T.; Takenaka, H. *J. Appl. Phys.* **1994**, *75*, 3806.
- [197] Kohli, V.; Bedzyk, M. J.; Fenter, P. *Phys. Rev. B* **2010**, *81*, 054112.
- [198] Matsushita, T.; Iida, A.; Ishikawa, T.; Nakagiri, T.; Sakai, K. *Nucl. Instrum. Methods Phys. Res. A* **1986**, *246*, 751.
- [199] Bedzyk, M. J. *arXiv:0908.2115-cond-mat.mtrl-sci* **2009**,
- [200] Born, M.; Wolf, E. *Principles of Optics*; Cambridge University Press, United Kingdom, 1999; pp 554–630.
- [201] Tiwari, M. K.; Das, G. *arXiv:1406.3581v1- cond-mat.mes-hall* **2014**,
- [202] Wang, J.; Bedzyk, M. J.; Penner, T. L.; Caffrey, M. *Nature* **1991**, *354*, 377.
- [203] Marshal, J. *Nature* **2014**, *510*, 22.
- [204] Liu, S.; Meng, F.; Xie, W.; Zhang, Z.; Shen, L.; Liu, C.; He, Y.; W.Guo.; Ruan, S. *Appl. Phys. Lett.* **2013**, *103*, 233303.
- [205] Motellier, S.; Derrough, S.; Locatelli, D.; Amdaoud, M.; Lhaute, K. *Spectrochimica Acta Part B* **2013**, *88*, 1–9.
- [206] Gupta, S. M.; Tripathi, M. *Chinese Sci. Bull.* **2011**, *56*, 1639–1657.

- [207] Sentein, C.; B.Guizard,; Giraud, S.; Y, C.; Tngal, F. *Journal of Physics: Conference Series* **2009**, *170*, 012013.
- [208] Cho, I. S.; Lee, C. H.; Feng, Y.; Logar, M.; Rao, P. M.; Cai, L.; Kim, D. R.; Sinclair, R.; Zheng, X. *Nature Communications* **2013**, *4*:1723.
- [209] Bagheri, S.; Ramimoghadam, D.; Yousefi, A. T.; Hamid, S. B. A. *Int. J. Electrochem. Sci.* **2015**, *10*, 3088 – 3097.
- [210] Hattori, M.; Einaga, H.; Daio, T.; Tsuji, M. *J. Mater. Chem. A* **2015**,
- [211] Mi, Y.; Weng, Y. *Scientific Reports* **2015**, *5*:11482.
- [212] Li, L.; Yan, J.; Wang, T.; Zhao, Z.; Zhang, J.; Gong, J.; Guan, N. *Nature Communications* **2015**, *6*:5881.
- [213] Ma, Y.; Wang, X.; Jia, Y.; Chen, X.; Han, H.; ; Li, C. *Chem. Rev.* **2014**, *114*, 9987–10043.
- [214] Sudhagar, P.; Devadoss, A.; Nakata, K.; Terashima, C.; Fujishima, A. *Journal of The Electrochemical Society* **2015**, *162*, H108–H114.
- [215] Kulkarni, M.; Mazare, A.; Gongadze, E.; Perutkova,; Iglıc, V. K.; Milov, I.; Schmuki, P.; Iglıc, A.; Mozetic, M. *Nanotechnology* **2015**, *26*, 062002.
- [216] Li, J.; Cushing, S. K.; Zheng, P.; Senty, T.; Meng, F.; Bristow, A. D.; Manivanan, A.; Wu, N. *J. Am. Chem. Soc.* **2014**, *136*, 8438–8449.
- [217] Shi, H.; Magaye, R.; V.Castranova,; Zhao, J. *Particle and Fibre Toxicology* **2013**, *10*, 1–33.
- [218] Hussain, M.; Ceccarelli, R.; Marchisio, D. L.; Fino, D.; Russo, N.; Geobaldo, F. *Chemical Engineering Journal* **2010**, *157*, 45–51.
- [219] Abou-Helala, M.; Seeberb, W. *App. Surf. Sci.* **2002**, *195*, 53–62.

- [220] Reetz, M. T.; Helbig, W. *J. Am. Chem. Soc.* **1994**, *116*, 7401–7402.
- [221] Zhang, L.; Manthiram, A. *Journal of Materials Chemistry* **1996**, *6*, 999–1004.
- [222] Brinker, C. J.; Scherer, G. W. *Sol-Gel Science: The Physics and Chemistry of Sol-Gel processing* **1990**,
- [223] Alain, C. P. *Introduction to Sol-Gel Processing* **1998**,
- [224] Singh, A.; Vihinen, J.; Franberg, E.; Hyvarinen, L.; Honkanen, M.; Levanen, E. *Nanoscale Research Letters* **2016**, *11*:447.
- [225] Vollath, D. *Journal of Nanoparticle Research* **2002**, *33*, 369–389.
- [226] Schwyn, S.; Garwin, E.; Ott, A. S. *Journal of Aerosol Science* **1988**, *19*, 639–642.
- [227] Marchisio, D. I.; Omegna, F.; Barresi, A. A. *Chem. Eng. J.* **2009**, *146*, 456–465.
- [228] Cannon, W. *Journal of the American Ceramic Society* **1982**, 324–330.
- [229] Cannon, W. *Journal of the American Ceramic Society* **1982**, 330–335.
- [230] Bouhadoun, S.; Guillardb, C.; Dapozzeb, F.; Singh, S.; Amans, D.; Boucl, J.; Boime, N. H. *Applied Catalysis B: Environmental* **2015**, *174*, 367–375.
- [231] Pignon, B.; Maskrot, H.; Ferreol, V. G.; Leconte, Y.; Coste, S.; Gervais, M.; Pouget, T.; Reynaud, C.; Tranchant, J. F.; Herlin-Boime, N. *Eur. J. Inorg. Chem.* **208**, *6*, 883.
- [232] Figgemeier, E.; Kylberg, W.; Constable, E.; Scarisoreanu, M.; Alexandrescu, R.; Morjan, I.; Soare, I.; Birjega, R.; Popovici, E.; Fleaca, C.; Gavrilă-Florescu, L.; Prodan, G. *Appl. Surf. Sci.* **2007**, *254*, 1037.
- [233] van Erven, J.; Munao, D.; Fu, Z.; Trzeciak, T.; Janssen, R.; Kelder, E.; Marijnissen, J. C. M. *KONA Powder and Particle Journal* **2009**, *27*, 157–173.
- [234] Khan, M. N.; Bashir, J. *Journal of Modern Physics* **2011**, *2*, 962–965.

[235] Burdett, J.; Hughbanks, T.; Miller, G. J.; Jr., J. W. R.; Smith, J. V. *J. Am. Chem. Soc.* **1987**, *109*, 3639–3646.

[236] Scherrer, P. *Mathematisch-Physikalische Klasse* **1918**, *2*, 98–100.